Penta-Twinned Bipyramidal Au Microcrystallites: Unraveling non-Cubic Phases and Investigating Phase Transformations

A Thesis
Submitted for the Degree of
Doctor of Philosophy
By
Chaitali Sow

JNCASR

Chemistry and Physics of Materials Unit
Jawaharlal Nehru Centre for Advanced Scientific Research
(Deemed- to-be-University)
Bengaluru-560064 (India)

November 2020

Dedicated to My Parents

Declaration

I hereby declare that the thesis entitled **"Penta-Twinned Bipyramidal Au Microcrystallites: Unraveling non-Cubic Phases and Investigating Phase Transformations"** is an authentic record of research work carried out by me at the Chemistry and Physics of Materials Unit, Jawaharlal Nehru Centre for Advanced Scientific Research, Bengaluru, India under the supervision of Prof. Giridhar U. Kulkarni and that it has not been submitted elsewhere for the award of any degree or diploma.

In keeping with the general practice in reporting scientific observations, due acknowledgement has been made whenever the work described in based on the findings of other investigators. Any omission that might have occurred due to oversight or error in judgment is regretted.

Chaitali Sow

Certificate

Certified that the work described in this thesis titled "**Penta-Twinned Bipyramidal Au Microcrystallites: Unraveling non-Cubic Phases and Investigating Phase Transformations**" has been carried out by Chaitali Sow at the Chemistry and Physics of Materials Unit, Jawaharlal Nehru Centre for Advanced Scientific Research, Bengaluru, India under my supervision and that it has not been submitted elsewhere for the award of any degree or diploma.

Professor Giridhar U. Kulkarni

(Research Supervisor)

Acknowledgements

Preface

The thesis work pertains to the stabilization of Au microcrystallites in unconventional lattices, mapping the spatial distribution of the lattices in the crystallite volume and their stability aspects under various chemical and physical perturbants. It is organized into ten chapters.

Chapter I introduces the concept of nanoscale materials, their length scale dependent properties and depicts various synthetic routes of preparation with specific examples from the literature reports. In the later part of this chapter, a brief discussion on unconventional lattices of noble metal nanostructures and the associated lattice strain, is provided along with the crystal structure dependent properties. At the end, the scope of the thesis is presented. **Chapter II** summarizes the various instruments and characterization techniques used in the thesis work.

Chapter III deals with stabilization of Au microcrystallites in unconventional lattices by a chemical route, *i.e.*, thermolysis of a metal-organic precursor in presence of a shape-directing agent. The variations in the precursor composition and thermolysis temperature of the precursor allow to maximize the unconventional lattices contribution to ~ 92% with large reproducibility (~ 90%). The unconventional lattices, *i.e.*, body-centered orthorhombic (bco) and body-centered tetragonal (bct) mixed phases, together called as bc(o,t) are kinetically arrested in the crystallite volume due to geometrically induced constraint and are ambient stable for years. The crystallites are majorly bipyramidal in shape.

Chapter IV presents the results obtained from scanning X-ray diffraction microscopy (SXDM) study of a non-cubic Au bipyramid, revealing the spatial distribution of different lattices in the crystallite volume. The crystallites are ~ 200-400 nm thick and not suitable to study by TEM and the associated techniques (SAED and tomography). The study confirms the presence of metastable lattices and their spatial distributions, specifically bco-rich body and fcc-rich tips. The crystal domains are twisted ~ 6° along the length and the growth directions are bco<010> and fcc<110>. The diffraction data has confirmed the presence of penta-twinned geometry throughout the crystallite volume. Importantly, the study allows to visualize the planes and their orientations, for instance, bco(002)/fcc(002) being along the crystal growth axis. The study reveals the co-presence of compression (6.06%) and expansion (4.21%) along with anisotropic strain throughout the length.

Chapter V demonstrates the stability of the bc(o,t) crystallites under ion beam (Ar$^+$) irradiation with a moderate beam energies in the range, 1.2-5 keV. Interestingly, exposure of Ar$^+$ ion with this low beam energy enables to stabilize new bct phases (bct-I). The Ar$^+$ exposure seems to engineer the lattice strain altering the *c/a* ratio of bct-I *via* uniaxial expansion along the *c*-direction and eventually causing phase transformation to fcc. During the transformation, the pristine bco disappears, followed by the bct phases leaving behind only residuals. Several distinct bct-I phases are produced depending on the time of exposure of the energetic beam. The stability of these phases has been studied at ambient as well as at high temperatures.

Chapter VI presents the observations from thermal annealing induced phase transformation in bc(o,t) Au crystallites made using *in-situ* SXDM measurements. The kinetically frozen bc(o,t) lattices undergo phase transformation to fcc by stress relaxation during high temperature annealing. The pre-existed twist of the domains along the length in the pristine crystallite undergo untwisting in the annealing process. The study allows visualization of the untwisting of the domains following the phase transformation.

Chapter VII deals with the effect of various adsorbents on the surface and the crystal structure of the Au crystallites. Treatment with hexadecanethiol enhances the crystallinity by the reduction in mosaicity, whereas treatment with Na$_2$S introduces phase transformation to fcc with preferential orientation of {111} *via* strong Au-S interaction. Presence of surfactants such as quaternary ammonium salts causes oxidative etching assisted phase transformation to fcc with {002} orientation. Effect of various metal-organic precursors (M-ToABr, where M = Pt, Pd, Ag and Cu and ToABr = tetraoctylammonium bromide) on the stability of bc(o,t) Au is also shown. For example, Ag$^+$ acts as blocking agent and Cu^{2+} as synergistic agent in the phase transformation process. Treatment with Au(III)/ToABr reveals a crystal structure dependent dissolution which consequently unveils a core-shell bc(o,t)-fcc structure. The fcc sheath protects the metastable bc(o,t) core and thereby explains the extraordinary ambient stability of the bc(o,t) Au crystallite.

Chapter VIII represents the stability of bc(o,t) Au in comparison with fcc Au in certain harsh chemical environments, *i.e.*, electroless deposition of Cu, treatment with Hg and aqua regia. For instance, selective deposition of Cu at the fcc rich tips and nearly bare bc(o,t) rich body displays nobler behavior of bc(o,t) Au in comparison with fcc Au, portraying crystal structure

dependent chemical stability. The reactivity difference is understood considering the lattice anisotropy associated with the bc(o,t) lattices in contrast to isotropic fcc lattice.

Chapter IX illustrates electroless deposition of Cu as a simple, cost effective chemical probe to identify the presence of polymorphic domains in a collection of crystallites. The deposition of Cu is selective towards the fcc enriched regions and very sensitive to the presence of small proportion of bc(o,t) lattices. The anisotropic deposition of Cu on bc(o,t) crystallites is used as template for the anisotropic deposition of metals and metal sulfide overlayers in the crystallite volume.

Chapter X summarizes the thesis work and provides a brief outlook.

*   *   *

Table of Contents

<p style="text-align:center">*   *   *</p>

Acronyms

FESEM	Field-emission scanning electron microscopy
EDX	Energy Dispersive X-ray Spectroscopy
BSE	Back-scattered-electron
HRTEM	High-resolution transmission electron microscopy
SAED	Selected area electron diffraction
FIB	Focused ion beam
IBID	Ion beam induced deposition
STEM	Scanning transmission electron microscopy
HAADF	High-angle annular dark-field
LAADF	Low-angle annular dark-field
XRD	X-ray diffraction
SXDM	Scanning X-ray Diffraction Microscopy
XRF	X-ray fluorescence
XFM	X-ray fluorescence microscopy
CXD	Coherent X-ray diffraction
NFL	Nanofocusing refractive X-ray lens
AFM	Atomic force microscopy
TGA	Thermogravimetric analysis
UV-vis NIR	Ultra violet-visible near-infrared
fcc	Face-centered cubic
hcp	Hexagonal close-packed
bcc	Body-centered cubic
bct	Body-centered tetragonal
bco	Body-centered orthorhombic
bc(o,t)	bco + bct

FWHM	Full width at half maximum
PVP	Poly-vinyl pyrrolidone
CTAB	Hexadecyltrimethylammonium bromide
ToABr	Tetraoctylammonium bromide
UPD	Under-potential deposition
DFT	Density function theory
MD	Molecular dynamics
HER	Hydrogen evolution reaction
SAM	Self-assembled monolayer
LSPR	Localized Surface Plasmon Resonance
DMSO	Dimethyl sulfoxide
BSA	Bovine serum albumin
EG	Ethylene glycol

*   *   *

Nanomaterials[*]

I.1 About the Length Scale and Size Dependent Properties

Materials with one of the dimensions in nanometer scale typically in the range of ~ 1-100 nm are considered as nanomaterials. With reduction of size down to the nano regime, the properties of the materials change drastically. For example, instead of a continuous band, discrete bands are obtained in metals due to the non-overlapping of the bands. The gap between the discrete bands is considered as Kubo gap (δ). Depending on the gap, a metal can be non-metal/insulator at nanoscale (see **Figure I.1**) [1].
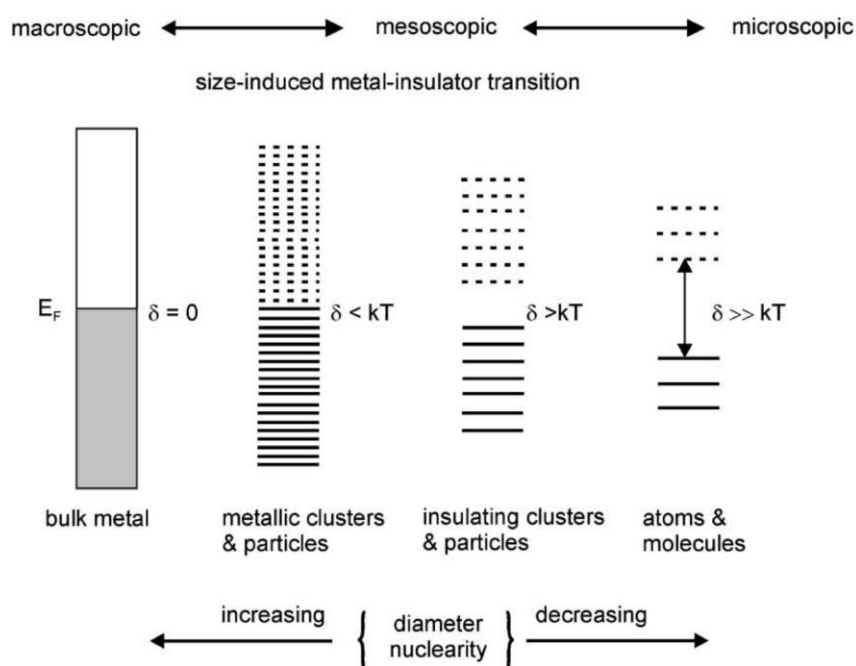
Figure I.1. Schematic illustration of development of band gap and the density of states as the number of atoms in a system decreases (from left to right). δ is the so-called Kubo gap. Figure reprinted with permission from Reference 1; copyright 2006 Royal Society of Chemistry.

With reduction in size, the contribution of the surface atoms increases which results in enhancement in overall area while the volume is retained constant, as shown in **Figure I.2**a [1]. The increased fraction of the surface atoms reduces the probability of coordination fulfilment which thereby facilitates reactivity, for example as a better catalyst. A famous title from a paper by Uzi Landman can be recalled here, "When gold is not noble: Nanoscale gold catalyst" [2]. Similarly, depression in the melting point with reduction in size can be understood by

---

considering the highly un-coordinated surface atoms or drop in cohesive energy (see **Figure I.2**b).
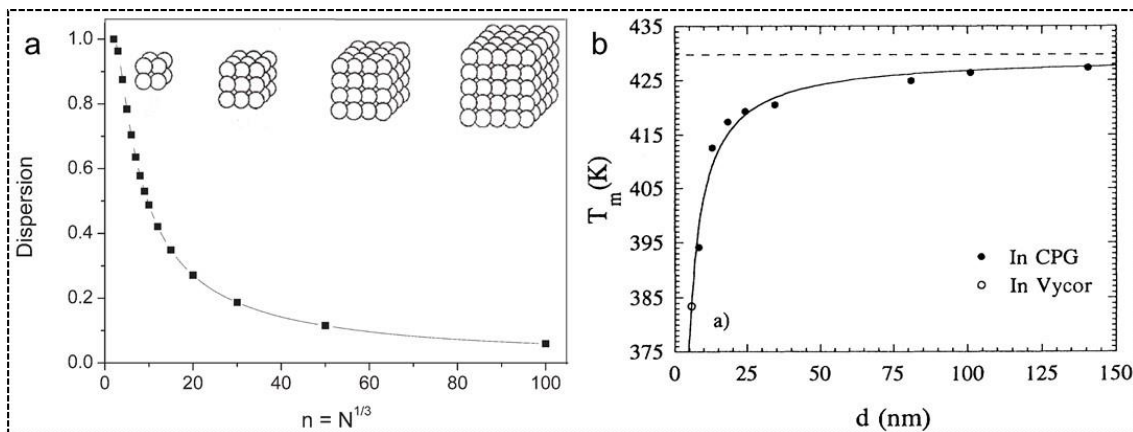
Figure I.2. (a) Evolution of the dispersion as a function of n for cubic clusters up to n = 100 (N = 10^6). The structure of the first four clusters is displayed. (b) Melting temperature as a function of pore diameter. The broken line represents the bulk melting point. Figure reprinted with permission from Reference 1; copyright 2006 Royal Society of Chemistry.
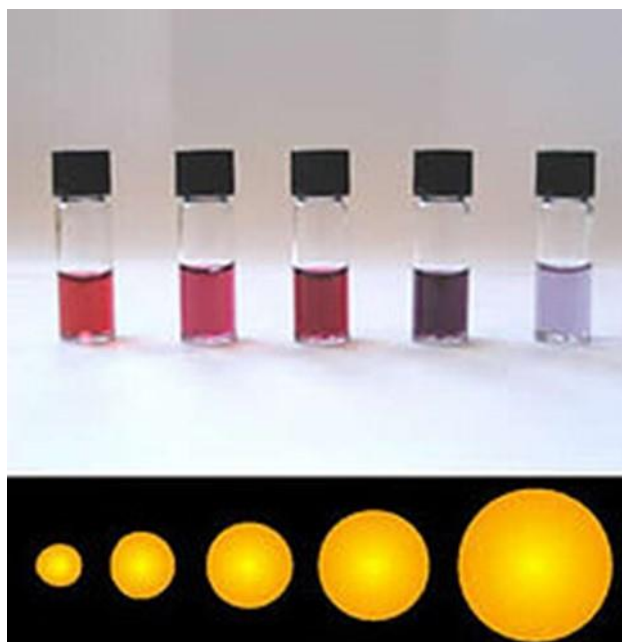
Figure I.3. Variation in color of Au colloidal solution with reduction in size of Au crystallites (right to left). Image source: Colloidal gold-Wikipedia (by Aleksandar Kondinski).

The reduction in size and the resulting quantum confinement introduce change in the optical color of the metals [1]. For example, gold is no more golden at the nanoscale. This can be understood considering the surface plasmon resonance (SPR), a collective oscillation of the

charge carrier at the metal-dielectric interface. In nanoparticles, the SPR is localized due to the size constraints (particle in a box problem), which is known as localized SPR (LSPR). The LSPR related with Au and Ag interacts with the electromagnetic radiation in the range of visible light which causes enhanced absorption of matching wavelength. Thus, the complementary reflection gives color. Smaller sized Au absorbs green light and reflects red. Although in addition to absorption, scattering also contributes toward color in bigger sized nanoparticles (~ 40 nm) [3]. With increasing size, the Au colloidal sol exhibits different color from red to blue as shown in **Figure I.3**.

I.2 Shape Dependent Properties

Metal nanocrystallites can be broadly categorized as isotropic (spherical) and anisotropic based on geometrical consideration. Surface plasmon of the metal nanocrystallites is shape dependent. For instance, spherical Ag nanoparticles (~ 40 nm) exhibit a single absorption peak at ~ 410 nm [4,5]. With introduction of anisotropy in the morphology, the oscillations of e-density are along and perpendicular to the length of the crystallites in contrast to isotropic and thereby the dipolar plasmon contribution splits into transverse and longitudinal modes. One-dimensional nanosystems, for example, nanowires, nanorods and bipyramids demonstrate both the transverse and longitudinal modes [6] as shown in **Figure I.4**.
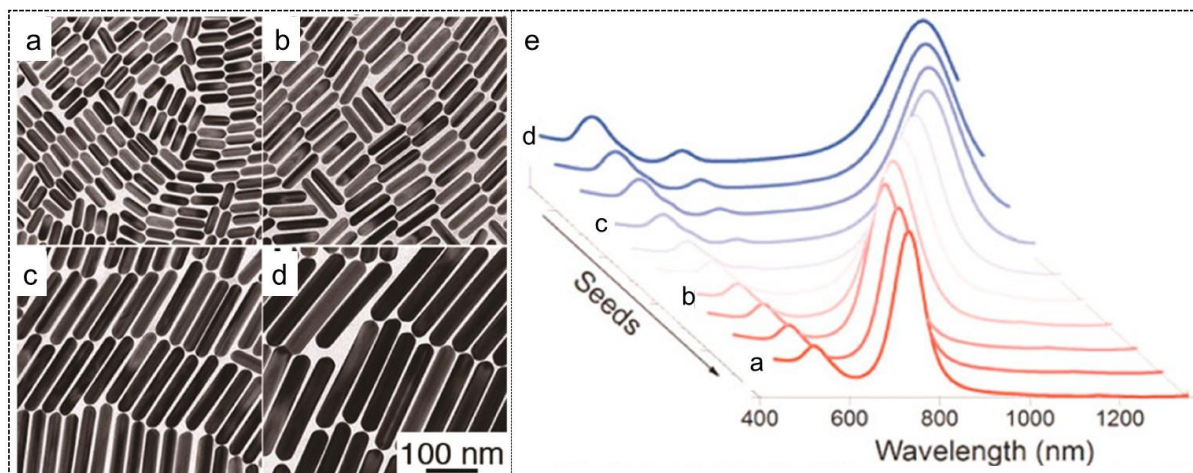
Figure I.4. (a–d) Transmission electron microscopy (TEM) images of Au nanorods prepared from different amounts of seeds and (e) UV-vis-NIR spectra of Au colloids prepared with different seed concentrations. Figure reprinted with permission from Reference 6; copyright 2017 American Chemical Society.

Noble metal nanostructures have been widely used in various catalytic reactions due to high surface area and their extraordinary stability under harsh chemical conditions. For example, Au which is otherwise inactive in the bulk state [7,8] exhibits a superior catalytic activity in the form of nanoparticles (< 5 nm) supported on oxides [7,9]. In addition, size- and shape-controlled nanostructures introduce highly un-coordinated/active sites and thereby the enhanced activity [10]. Besides, crystallographic orientation or surface energy of the exposed facets also alter the performance of a catalyst [11,12].

I.3 Synthesis of Metal Nanocrystallites

Synthesis of well-controlled metal nanocrystallites has been the subject of interest since the last two decades. Owing to the wide range of applications of the nanocrystallites in various fields, the syntheses of well-dispersed, size-/shape-controlled and surfactant-free crystallites are in demand. Among the well-known chemical, physical and biological techniques, the former provides an easy, less cumbersome but cost effective route with multiple controllable parameters.

I.3.A Chemical Synthetic Process

Some of the synthetic processes commonly used in successfully stabilizing fine-tuned morphology of the nanocrystallites are discussed below.
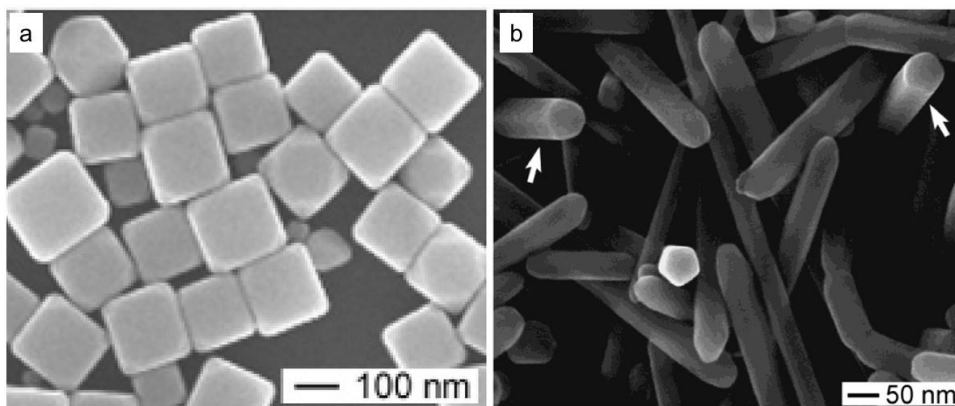
Figure I.5. (a) TEM and (b) scanning electron microscopy (SEM) images of various Ag nanostructures prepared by polyol method. Panel a reprinted with permission from Reference 16; copyright 2005 American Chemical Society. Panel b reprinted with permission from Reference 13; copyright 2003 American Chemical Society.

Polyol synthesis. Reduction of metal cations in the presence of polyol and capping agent at a moderate temperature is known as polyol method. For example, Ag nanocubes were synthesized by AgNO$_3$, poly-vinyl pyrrolidone (PVP) and ethylene glycol (EG) [13]. Heating of EG provides the continuous source of reductant, glycolaldehyde [14]. The reduction efficiency of EG is dependent of reaction temperature and therefore, the latter acts as a controlling parameter to tune the morphology as well as size of it. Additionally, the presence of additives such as Cl$^-$, O$_2$ [15] and Fe(II) [16] is also known to direct the shape of the nanocrystallites. Various morphologies prepared by this method are shown in **Figure I.5.**

Thermal decomposition. Thermal reduction of the metal-organic complex allows to synthesize nano, micro and sub-millimeter sized crystallites on a chosen substrate. The reduction is depended on the thermolysis temperature which facilitates simply variable shapes and sizes of the crystallites. Single crystalline sub-millimeter ranges of Au microcrystallites (see **Figure I.6**a) were achieved by the thermal decomposition of M-ToABr, a metal-organic precursor, where the M = Au and ToABr (tetraoctylammonium bromide) is a phase transferring agent [17]. The size controlled crystallites were obtained by varying the thermolysis temperature and concentration of the reactants. For example, thermolysis of the same precursor composition at 130 °C and 250 °C results in ~ 400 and ~ 30 µm sized Au microcrystallites, respectively [18,19]. The M can also be Ag, Pd, Pt and Cu and therefore different metal crystallites (see **Figure I.6**b,c) [20].
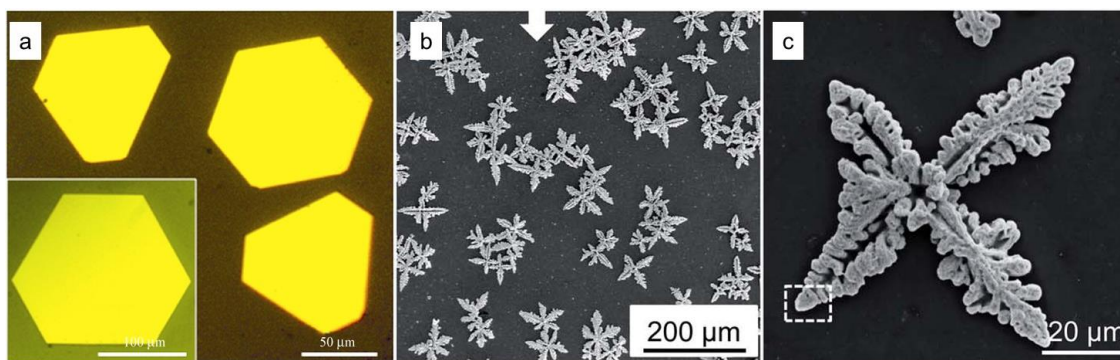
Figure I.6. Thermal decomposition of metal-organic precursor results in microcrystallites. (a) Optical images of Au microplates. (b,c) SEM images of Ag microflowers. Panel a reprinted with permission from Reference 17; copyright 2010 Springer Nature. Panels b and c reprinted with permission from Reference 20; copyright 2014 Royal Society of Chemistry.

Galvanic replacement. Galvanic replacement is a redox reaction, where oxidation (or sacrifice) of a metal and reduction (or deposition) of another metal occurs in a solution and thereby facilitates the growth of framework or cage or tube like structure. The difference in the reduction potential drives this reaction where the second metal necessarily possesses a higher potential than that of the first one [21]. For example, Au nanorings assisted growth of Pt framework [22], where the Au act as sacrificial template. The frames/cages with higher surface area and highly un-coordinated surfaces provide a large platform for applications, such as in catalysis.
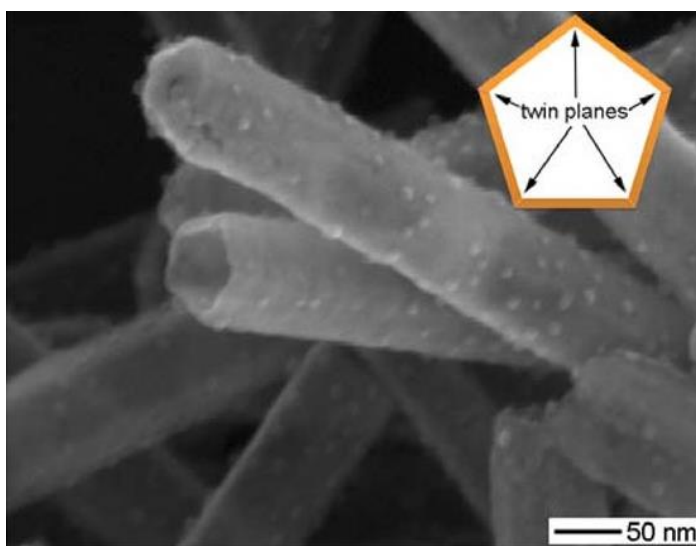
Figure I.7. SEM image of Ag-Au alloy nanotubes that were synthesized through the galvanic replacement reaction between the Ag nanowires and an aqueous solution of $HAuCl_4$ at 100 °C. The open nanotubes clearly show the 5-fold symmetry as same as that of the Ag nanowires. Inset is the schematic illustration to highlight the pentagonal cross section of the nanotubes and the existence of five twin planes in each nanotube. Figure adapted with permission from Reference 22; copyright 2012 Springer Nature.

The galvanic replacement provides a wide range of advantages over other synthetic methods, such as in unraveling the spatial distribution of mixed crystal lattices in an individual nanostructure, such as treatment of $HAuCl_4$ to the Ag nanowires (stabilized in unconventional body-centered tetragonal (bct) lattice) introduces Ag-Au alloyed penta-twinned nanotubes [23]. In the nanotubes, the 5-fold geometry retains while the penta-twinned boundaries do not cross (*i.e.*, disappearance of the apex, see **Figure I.7**). This dissolution of

the core results in the vanishing of the bct phase, revealing the presence of bct at the core protected by the fcc sheath.

Seed-mediated/Templated-based growth. The seed mediated growth provides a uniform dispersion of the final morphology simply by tuning the reaction concoctions [24,25]. In presence of seed, the growth can be epitaxial/non-epitaxial, as shown in **Figure I.8**a–e. In case, the lattice mismatch is < 5%, the outgrowth can be conformal, whereas with large lattice mismatch, it will be non-conformal, *i.e.*, no epitaxial relation [4]. Similarly, 1-D Au nanowires (< 2 nm in diameter) were stabilized by the AuCl-oleylamine polymeric 1-D structured strand as a template [26].
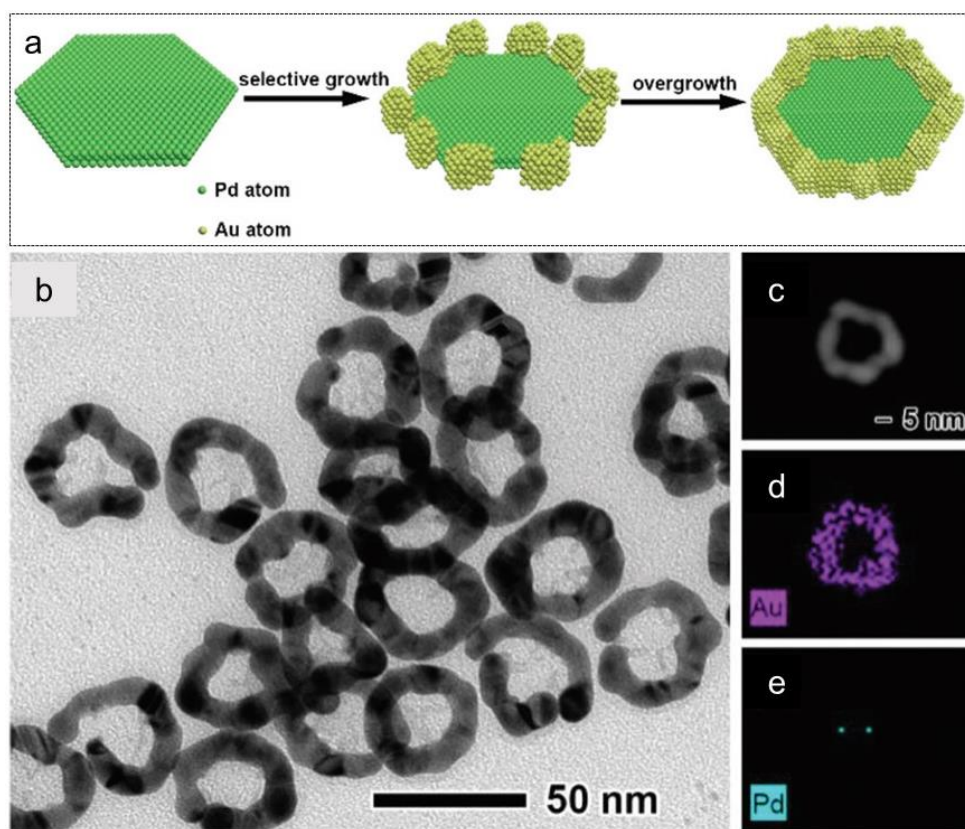
Figure I.8. Seed mediated growth. (a) Schematic illustrating the formation mechanism of the Pd ultrathin nano-sheet supported Au nanorings. (b) TEM, (c) High-angle annular dark-field- scanning TEM (HAADF-STEM), and (d,e) Energy Dispersive X-ray Spectroscopy (EDX) mapping images of the Au nanorings after chemical etching of the Pd nanosheets in the interior. Figure reprinted with permission from Reference 25; copyright 2016 Royal Society of Chemistry.

Besides, the presence of seed may help in visualization of the presence of symmetry as well as the growth direction. For example, visualization of the apex of the 5-fold symmetry in

a penta-twinned Au nano-decahedron/bipyramid/rod starting with a Pd seed in it is shown in **Figure I.9** [27]. The difference in the atomic number of Pd and Au allows to differentiate the seed (at the core) and shell (the grown Au bipyramid) using transmission electron microscopy (TEM). The Pd core allows to locate the apex of the 5-fold axis and thereby, the growth direction [6,27].
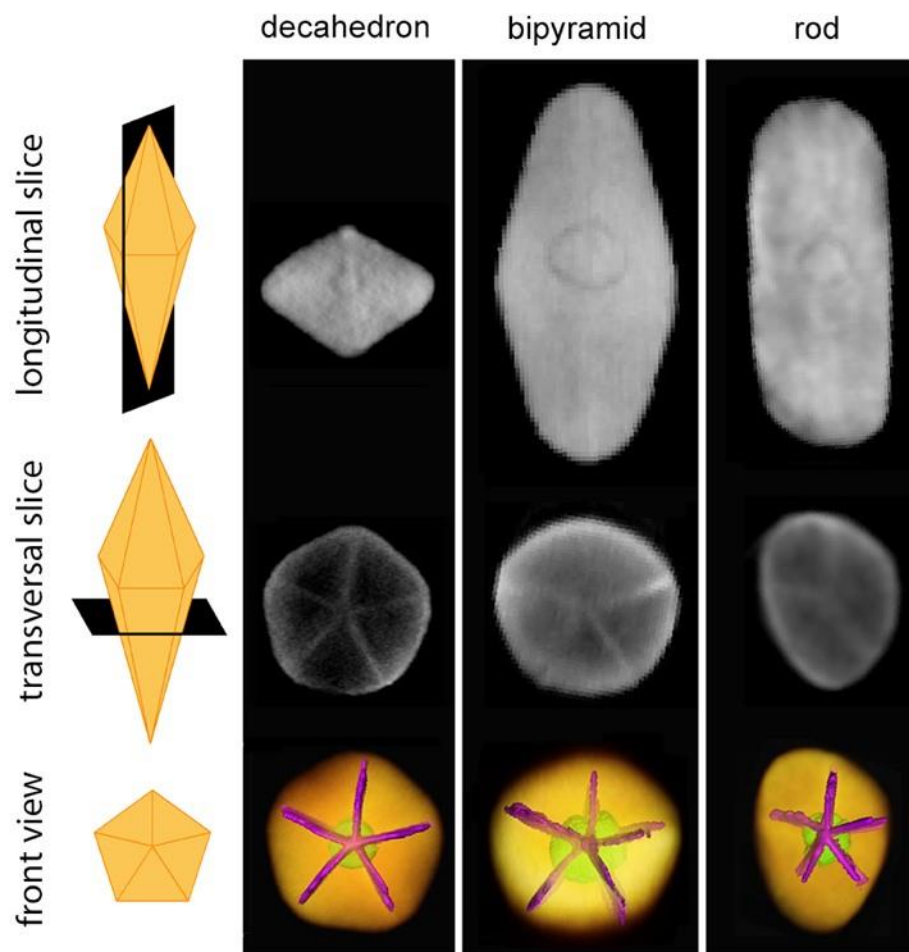
Figure I.9. Seed mediated growth. Top row: Longitudinal orthoslices through the HAADF-STEM reconstruction of a decahedron, a bipyramid and a nanorod grown from Au/Pd seeds. Middle row: Transversal orthoslices through the low-angle annular dark-field (LAADF)-STEM reconstruction, from which the twins can be segmented. Bottom row: The segmented seed and twin planes superimposed with the HAADF-STEM reconstruction. At the left, different ways of slice were shown. Figure reprinted with permission from Reference 27; copyright 2018 American Chemical Society (For further permissions related to the material excerpted should be directed to the ACS).

Post-synthetic modification. The variation in morphology can also be achieved at the post-synthetic process by exchanging the surface capping agents which results in deformation in

morphology *via* the different interaction strength of the capping agents with the surface of the nanostructures. Some cases, the interaction may introduce different periodicity of the atoms [28,29]. Among the well-known modulators, widely used ones are oxidative etching, laser irradiation, thermal treatment and e-beam exposure. For example, micelle coated Au nanorods undergo morphological transformation to nanoparticles upon thermal annealing at ~ 110 °C [30] or upon femtosecond laser irradiation [31]. Similarly, the presence of Cu^{2+}, an oxidizing agent assists in the morphological transformation [32] as shown in **Figure I.10**a,b. Br^-/O_2 etches the convex facets of Au nanostars and redeposits at the concave places resulting deformation in morphology [33]. Oxidative etching assisted growth of hetero-phase Au nanowires starting with Au stars is another example (see **Figure I.10**c,d) [34].
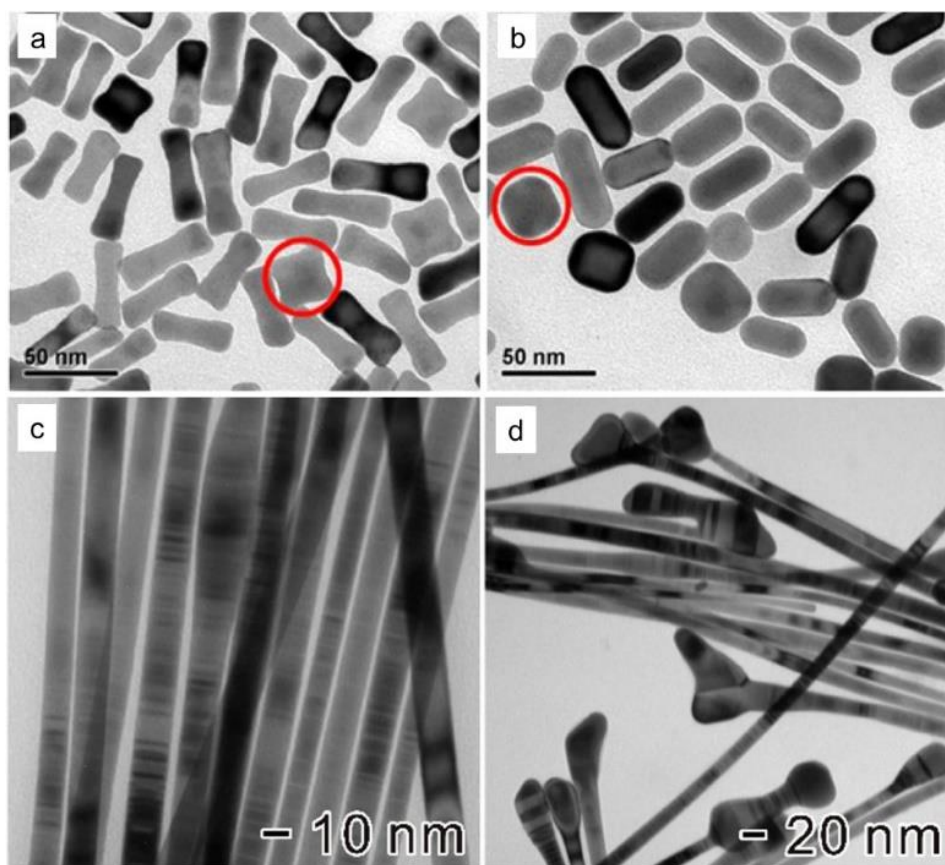
Figure I.10. TEM images of Au nanorods as (a) original dog-bone shape and (b) after shape conversion in presence of Cu^{2+} and CTAB. (c,d) TEM images of etching-assisted growth of hetero-phase Au nanowires. Panels a and b reprinted with permission from Reference 32; copyright 2013 American Chemical Society. Panels c and d reprinted with permission from Reference 34; copyright 2019 American Chemical Society.

I.3.B Other Processes

Physical method. Laser ablation [35,36] and evaporation and condensation [37] assisted growth provides ligand free metal nanocrystallites. However, the required high energy and temperature for the synthesis are not easily affordable. The method is not suitable to the well-controlled growth of morphologies and sizes.

Biological method. Au microcrystallites can also be synthesized with the aid of proteins where the latter controls the nuclei and kinetically the growth process. For instance, Au plates with lateral dimension exceeding 2 mm were achieved by bovine serum albumin (BSA) [38].

I.4 Reaction Kinetics in Presence of Capping Agents

The surface energy of the exposed facets depends on the surface coordination number. Among many known parameters, contribution of surface energy directs the thermodynamically controlled morphology directed by the Wulff polyhedron. Thus, the thermodynamically favorable morphology is the one which exposes the lower energy facets. For fcc metals, the increasing surface energy sequence is (110) > (100) > (111) due to the surface coordination no. 7, 8 and 9, respectively (instead of 12). Among the many obtained morphologies, the commonly occurred ones are octahedron, cuboctahedron, cube, plates, rods and sheets. Although, many other shapes exposing the higher energy facets are seen which can be understood by considering the kinetically controlled growth.

In a reaction, both thermodynamics and kinetics play role. The kinetically controlled morphologies comprise of the energetically expensive facets whereas the Wulff polyhedral enriched with lower energy facets are the thermodynamically favored one [39].

The presence of capping agents can alter the morphologies, such as by preferentially blocking/allowing growth of certain facets. The adsorption of capping agents on a definite facet lowers the total energy of the facet compared to the other facets and thereby the growth proliferates exposing the stabilized facet. This growth is thermodynamically controlled/favored as shown in **Figure I.11**a [4]. For example, transformation of Pt rounded octahedra particulates to cubes by H_2S due to the lowering of (100) facets energy over (111) facets [40] (see **Figure I.12**). In contrast, adsorption of capping agents can block the growth on a particular facet (for example, lower energy facets) and thereby the growth may occur

selectively on the energetically expansive facets. This process facilitates the growth of the unfavorable facets which is kinetically controlled as shown in **Figure I.11**b [39].
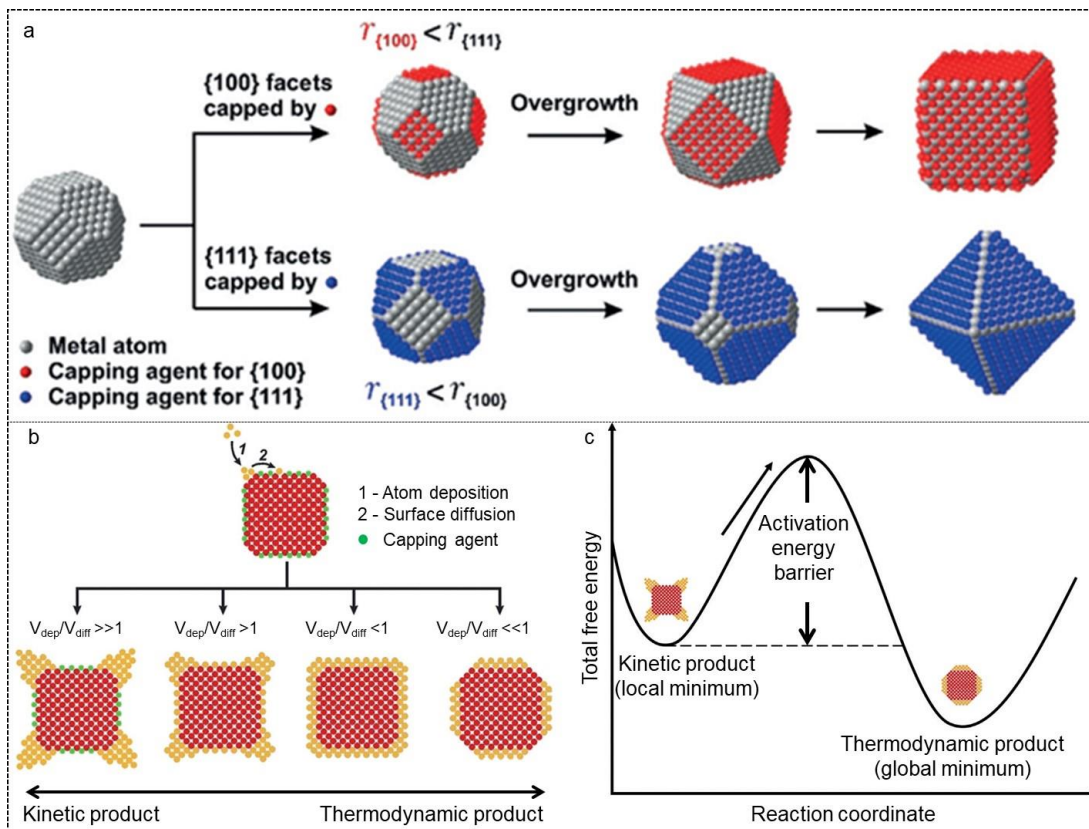
Figure I.11. (a) Schematic representation of the role of a capping agent in directing the growth of a single-crystal seed into nanocrystals with different shapes. (b) Schematic representation of the various products formed under different conditions in presence of a capping agent and starting with a 2D square seed. The capping agent covers side faces of the seed. Reaction kinetics. (c) Schematic illustration of the total free energy associated with the kinetic and thermodynamic products along with the activation energy barrier to transform a kinetic product to a thermodynamic product (indicated by the arrow). Figure reprinted with permission from Reference 39; copyright 2020 John Wiley and Sons.

The thermodynamically controlled morphology exhibits an absolute minimum energy while the kinetic state is at a local minimum energy (see **Figure I.11**c). The energy barrier governs the transformation of the kinetically locked morphology to the thermodynamically one. Depending upon the barrier, the transformation can be very fast or slow, for instance, although the graphite is energetically favored over diamond, the formed diamond remains at the kinetically locked state forever due to the higher energy barrier. Thus, perturbants induced

deformation in the morphologies is viewed as crossing the energy barrier required to achieve the thermodynamically favored morphologies [39].
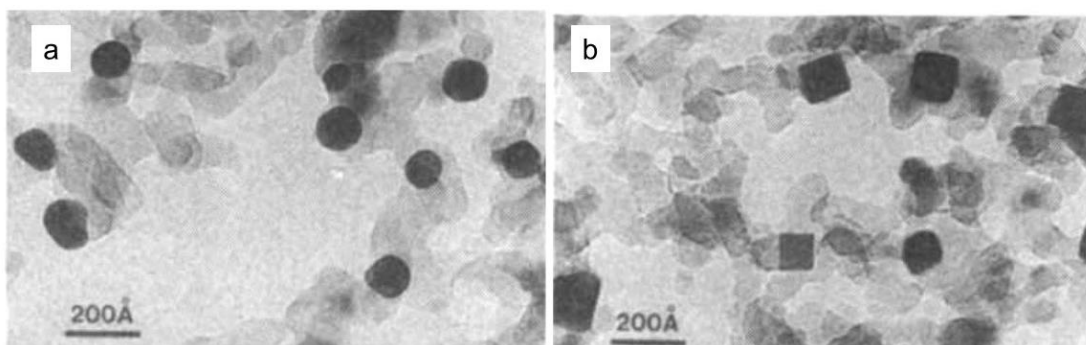
Figure I.12. TEM images of the Pt particulates with (a) (111) orientation and (b) adsorbate-induced faceted to (100) orientation. Figure reprinted with permission from Reference 40; copyright 1986 Springer Nature.

The anisotropic morphology in Au (as bipyramids) can be obtained by additional shape-directing agents, such as Ag^+ [17,41] (see **Figure I.13**a–c). The presence of ambidentate ligand, dimethyl sulfoxide (DMSO) helps in stabilizing the high-index (311) facets in the trapezohedral morphology [42], which was otherwise difficult to achieve (**Figure I.13**d). The trapezohedrals act as seed for the growth of octagonal bipyramids, a new class of bipyramids (see **Figure I.13**e). Hence, the presence of surfactants/ligands/capping agents for the growth and stabilization of higher energy facets and the anisotropic morphology (induced by shape-directing agents) is the essential component in a chemical reaction for shape-controlled growth.

The formation of icosahedron to decahedron to truncated octahedron is the favorable route for the growth of fcc metals. A decahedra inherently associates with a solid angle gap of ~ 7.35° which introduces geometrical constraints [43,44] as shown in **Figure I.14**a. The formation of decahedra is favored when the size is small due to the presence of 10 (111) facets (see **Figure I.14**c–d). During the growth process, the chemical potential governs the growth along the lateral direction causing the bigger sized decahedra associated with large sized (111) surfaces. However, the growth of larger sized decahedra is unfavorable due to the high energy associated with the defects and thereby the growth is along the 5-fold axis introducing anisotropic geometry. The growth along the 5-fold axis is favored due to the comparably small resultant growth strain associated with the penta-twin boundaries although at the expense of the energetically expensive (100) facets (see **Figure I.14**e,f). However for this unidirectional

growth, an additional capping agent is required to reduce down the energy of the (100) planes [45].
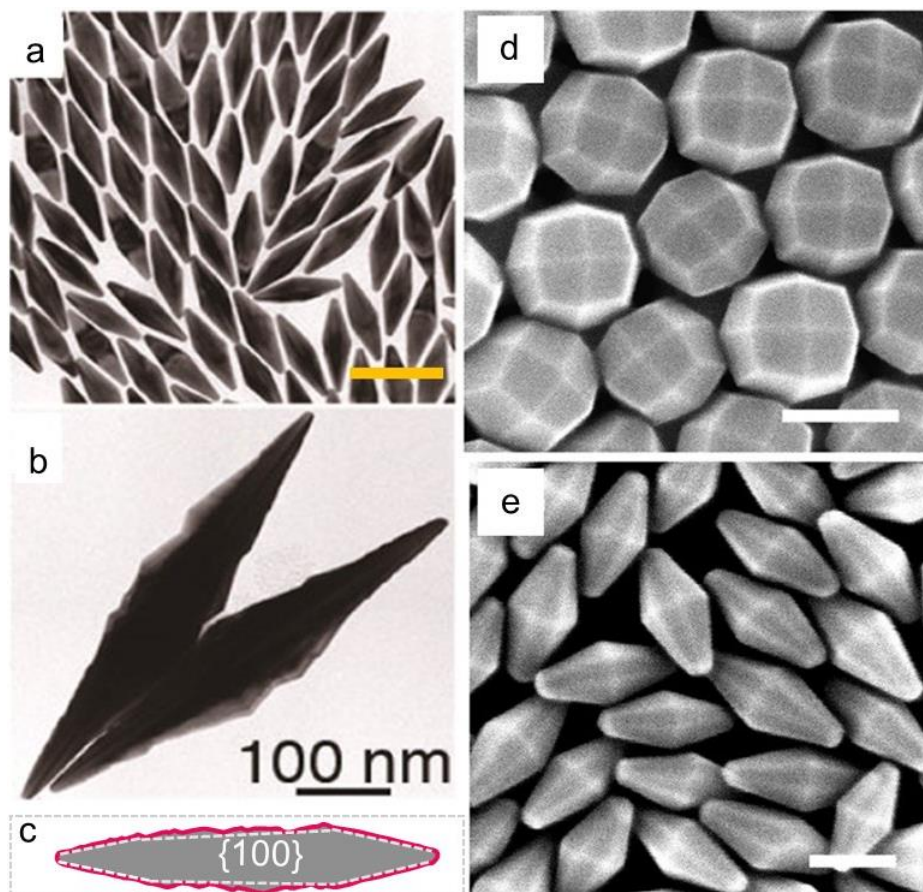
Figure I.13. (a,b) TEM images of Au bipyramids. Scale bar, 100 nm. (c) Schematic representation of a bipyramid with projected {100} facets (shown by white dashed lines). SEM images of (d) trapezohedral Au nanocrystals and (e) single-crystalline octagonal Au bipyramids in dimethyl sulfoxide (DMSO). Scale bars, (d) 100 nm and (e) 50 nm. Panels a and b reprinted with permission from Reference 6; copyright 2017 American Chemical Society. Panels d and e reprinted with permission from Reference 42; copyright 2017 American Chemical Society.

I.5 Strain in Metal Nanocrystallites

The Au (111) surface undergoes herringbone reconstruction due to the unsatisfactory coordination no. 9, instead of 12. At the nanoscale, the high surface energy of the small crystallites is associated with strain. The surface stress induced deformation may lead to the stabilization of other structures, such as an fcc metal favors lower bulk energy while at the nanoscale, the higher surface energy favors hcp or vice versa [46,47]. Geometrical constraints

induced due to the peculiar morphology as can be seen in **Figure I.14**a consequences strain which is in contradictory to the nano size effect can raise with the size of the crystallite [23].

Oxide-supported metal catalyst (Au/TiO$_2$) acts as very good catalyst and the main driving parameter in addition to the small size of the crystallite is the strain originated at the interface [48]. Similarly, the strain can originate at the interface of the overlayer and substrate in a template assisted grown crystallite.
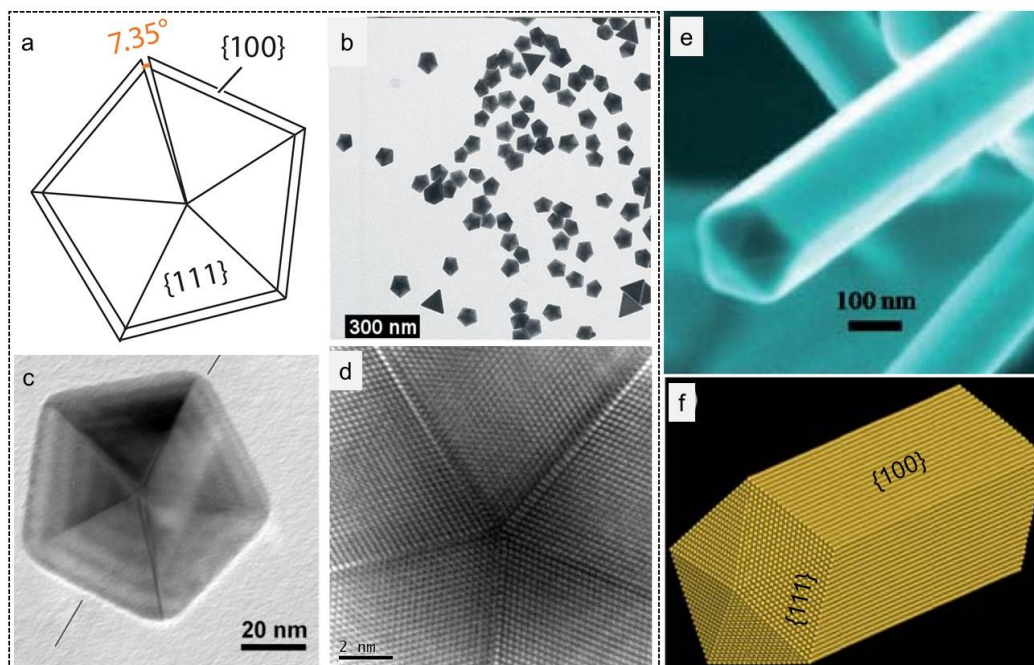
Figure I.14. (a) Schematic illustration of a decahedron with a geometrical constraint introducing a solid angle gap of approximately 7.35°. (b,c) TEM images of decahedral Au nanoparticles evidencing the pentagonal bipyramid geometry. (d) High-resolution transmission electron microscopy (HRTEM) image of a decahedra collected from the center, clearly showing the presence of five twin planes. (e) SEM image of a Au nanowire presenting a 5-fold symmetry axis. (f) Schematic representation of the nanowire. Panel a reprinted with permission from the Annual Review of Materials Research, Volume 50 © 2020 by Annual reviews, http://www.annualreviews.org/. Panels b−d reprinted with permission from Reference 44; copyright 2006 John Wiley and Sons. Panels e and f reprinted with permission from Reference 45; copyright 2010 Royal Society of Chemistry.

I.6 Unconventional Crystal Structures of Noble Metal Nanocrystallites

Nobility of metals−Ru, Os, Rh, Ir, Pd, Pt, Ag and Au−owe a lot to their internal crystal structures. All prefer close-packed structures, preferably face-centered cubic (fcc), except Ru

and Os which crystallize in hexagonal close-packed (hcp) structure. In both, the packing fraction (0.74) and first coordination number (12) are favorable; combined with their electronic structure, they render the metal noble. Indeed, the surface of the metal can be nobler than the bulk [7]. This being the scenario, any instance of occurrence of a noble metal in a non-native crystal structure generates much excitement in the research community.
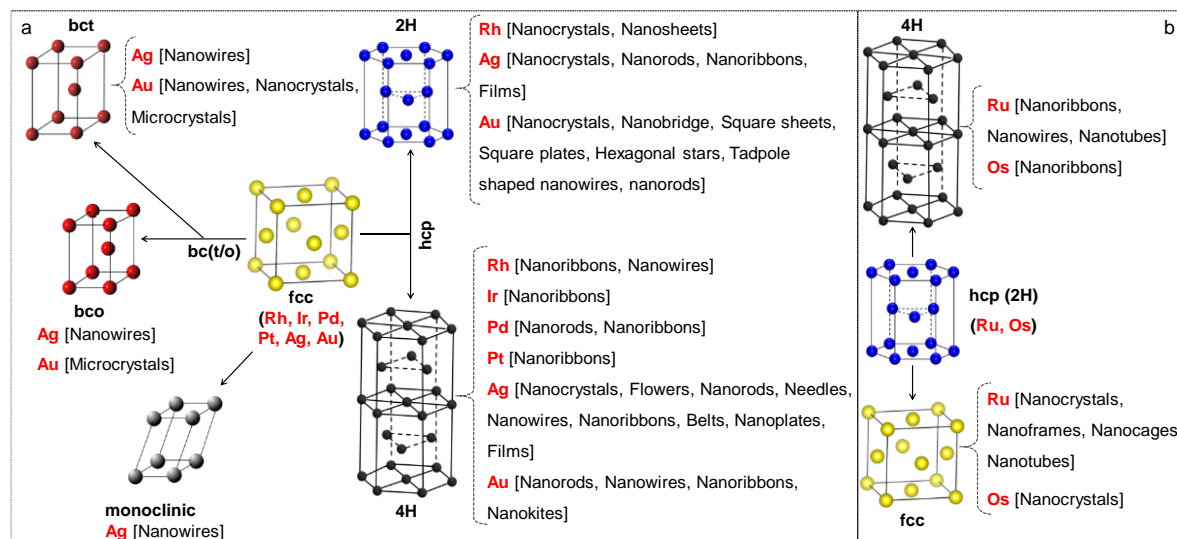
Figure I.15. Unit cells of unconventional crystal structures of noble metals reported in the literature, shown in relation to their conventional unit cells. (a) Conventionally face-centered cubic (fcc): Rh, Ir, Pd, Pt, Ag, and Au. (b) Conventionally hexagonal close-packed (hcp) (2H): Ru and Os. In the square brackets are listed possible morphologies of the crystallites in the non-native crystal structures, including body-centered tetragonal (bct), body-centered orthorhombic (bco), and monoclinic structures. Adapted with permission from the Annual Review of Materials Research, Volume 50 © 2020 by Annual reviews, http://www.annualreviews.org/.

The fcc and hcp structures exhibit distinct stacking sequences of the close-packed planes. In fcc, the {111} planes form a stacking sequence of ABCABC, whereas hcp consists of {001} planes stacking in a sequence of ABAB along the <001> direction. In the latter, the packing period can extend even longer, as in ABCBABCB (4H) and ABCACBABCACB (6H) and CBABABCBCBABABCB (8H) structures. Thus far, only 2H and 4H phases of Au, Ag, and Rh have been reported, while 6H and 8H structures reported only in Au [34,49]. The hcp structure is also termed 2H and the fcc 3C, where the number preceding refers to the number of planes in the packing sequence. **Figure I.15** contains a detailed survey of the literature from the past two decades represented in the form of schematic unit cells of various noble metals in

their native and non-native crystal structures. The metals Rh, Ir, Pd, Pt, Ag, and Au, which commonly occur in fcc, are reported as belonging to other closely related cells–body-centered cubic, bct, and body-centered orthorhombic (bco), as well as the monoclinic form. These metals can exist in the hcp 2H and 4H structures as well. Ru and Os, by contrast, may crystallize in 4H and fcc [50,51], away from the commonly known hcp (2H) forms as shown in **Figure I.16**.

I.7 Synthesis of Unconventional Crystal Structures

The occurrences of such crystal phases are closely tied to the morphologies exhibited by the respective crystallites, which are summarized in **Figure I.15**. The morphologies in turn depend crucially on synthetic conditions employed, such as the presence of shape-directing agents, nuclei with inherent defects, kinetics adopted, and the template used, as discussed below.

The presence of acetylacetonate ligand helps in the stabilization of Ru and Os nanocrystallites in fcc lattice (instead of conventional hcp) due to the coordination of the ligand to the surface of fcc Ru/Os atoms during the reaction [50,51]. The O-O distance (2.74–2.93 Å) in the acetylacetonate being nearly close to the nearest neighbor bond lengths of Ru-Ru (2.69 Å) and Os-Os (2.67 Å) leads to the stabilization of (111) facets in the form of decahedron and icosahedral morphologies, respectively [51,52].

In case a tiny nucleus is born, incorporating disorder by design, it may lead to unusual situations when it grows to larger sizes. The solid-angle deficiency introduces a lot of strain in the decahedra as illustrated in **Figure I.14**a, and under proper growth kinetics, this strain can be well-accommodated in the nucleus itself. The latter, when it grows into a bigger crystallite, retains the dislocations or twin defects, as observed in Ag [53] and Au decahedral particles [54]. At sufficiently large sizes (on the order of a few micrometers), the built-in disorder may even induce a lattice transformation, resulting in a lesser symmetry. Examples include the bct phases seen in Ag nanowires [23] and Au crystallites [55]. The composition of the precursor and the reaction kinetics may also dictate the resultant morphology and the crystal structure [4,56,57].

Synthesized nanomaterials in an unusual morphology and non-native structures introduced in them are sometimes found in template-driven growths, such as in the case of Ru

grown over a Pt substrate [58] by epitaxial deposition. The substrate in some cases is itself present in its non-native structure form, as in the case of 4H structures of Ir and Os grown over a 4H Au surface [59].

I.8 Specific Examples of Unconventional Crystal Structures

I.8.A A fcc Metal Crystallizing in hcp

Although both fcc and hcp possess similar packing fractions, the interplanar spacings along the closed packed planes, {111} and {0001}, respectively, differ, as do the unit cell volumes. The volume change can be as large as 29.4% from fcc to hcp [60]. Given this, it is difficult to stabilize the hcp phase under normal conditions. The 4H phase is a special case.
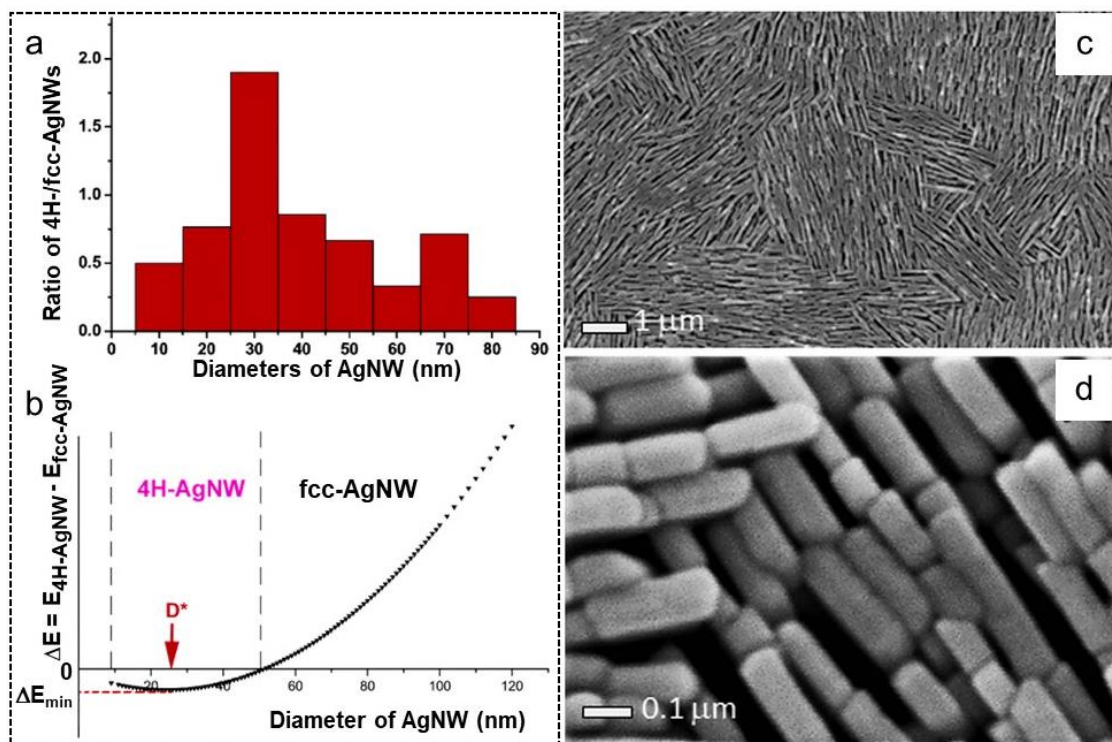
Figure I.16. Ag nanowires in hcp lattice (4H). (a) Histogram of the wire diameter from TEM data, with the 4H phase maximizing at approximately 30 nm. (b) Systemic energy difference between individual 4H and fcc with varying diameters of the nanowires. (c,d) SEM images at different magnifications of the Ag film hosting 4H phase and exhibiting rod-like microstructure. Panels a and b reprinted with permission from Reference 46; copyright 2006 American Chemical Society. Panels c and d reprinted with permission from Reference 64; copyright 2019 American Chemical Society.

4H Ag. The most stable polytype of Ag is 3C (fcc), although Ag in 4H structure (along with 2H) does occur naturally in mineral deposits from northeastern Russia [61]. The as-

prepared 4H (approximately 25% of the total) Ag nanowires by direct current electrodeposition possess uniform diameters of approximately 55 nm with a preferred [10–10] growth direction [62]. Reaction kinetics, size, and morphology are the critical factors that influence the formation and stabilization of the 4H phase. Extensive studies have been carried out addressing the role of size confinement in the formation and stabilization of the Ag 4H phase. One such study based on TEM reported that the 4H phase maximizes (approximately 65% of the total) at 30 nm diameter [46] and falls off at both smaller and larger values (see **Figure I.16**a).

Indeed, the theoretical plot of systemic energy difference in **Figure I.16**b shows that the value reaches its negative minimum at about 25.5 nm diameter. Interestingly, the persistence of 4H phase is seen in thick bulk Ag films (**Figure I.16**c) containing micrometer-size domains of oriented nanorods (approximately 100 nm long and 30 nm wide) [63,64] (**Figure I.16**d).

4H Au. Au has been stabilized into 4H hcp phase in the form of nanoribbons [65] a few micrometers long and a few tens of nanometers wide, with the growth direction being $[001]_{4H}$, as shown in **Figure I.18**a. Such a growth was facilitated by a 1D polymer-based soft-template, which first forms Au nanowires [26] that then grow into nanoribbons. The as-prepared 4H nanoribbons partially convert back to fcc when subjected to a moderate pressure cycle (see **Figure I.17**b) and irreversibly convert to fcc under higher pressures [66]. Flexing the prepared Au nanoribbons using sonication and further depositing Au on the bent nanoribbons chemically led to Au nanokites [67] (**Figure I.17**c), where the fcc is present only at the joining point of the two 4H arms. The latter are connected by a twin boundary (see **Figure I.17**d). The 4H Au can also be stabilized in the form of nanowires [68] (**Figure I.17**e) containing kinks, which consist of 5-fold fcc twins and the associated grain boundaries. The Au nanowires show extraordinary stability during heating at 800 °C.

I.8.B A hcp Metal Crystallizing in fcc

Ru nanoparticles possessing a 5-fold twinned decahedral structure have been crystallized into unconventional fcc structure [50] (see **Figure I.18**a). The nanoparticles exhibited a high degree of stability at up to 500 °C when heated under vacuum. Ru can also be stabilized in fcc structure *via* epitaxial growth over Pt [58] and Pd [69] substrates, resulting in core-shell structures. Upon removing the core, fcc Ru nanoframes [69] or nanocages [70] were

realized, as shown in **Figure I.18**b,c. Diversity in the shape and composition of the seeds, the site-selective growth at the corners and edges of the seed, and the reaction kinetics all seem to dictate the final shapes of the Ru nanocages.
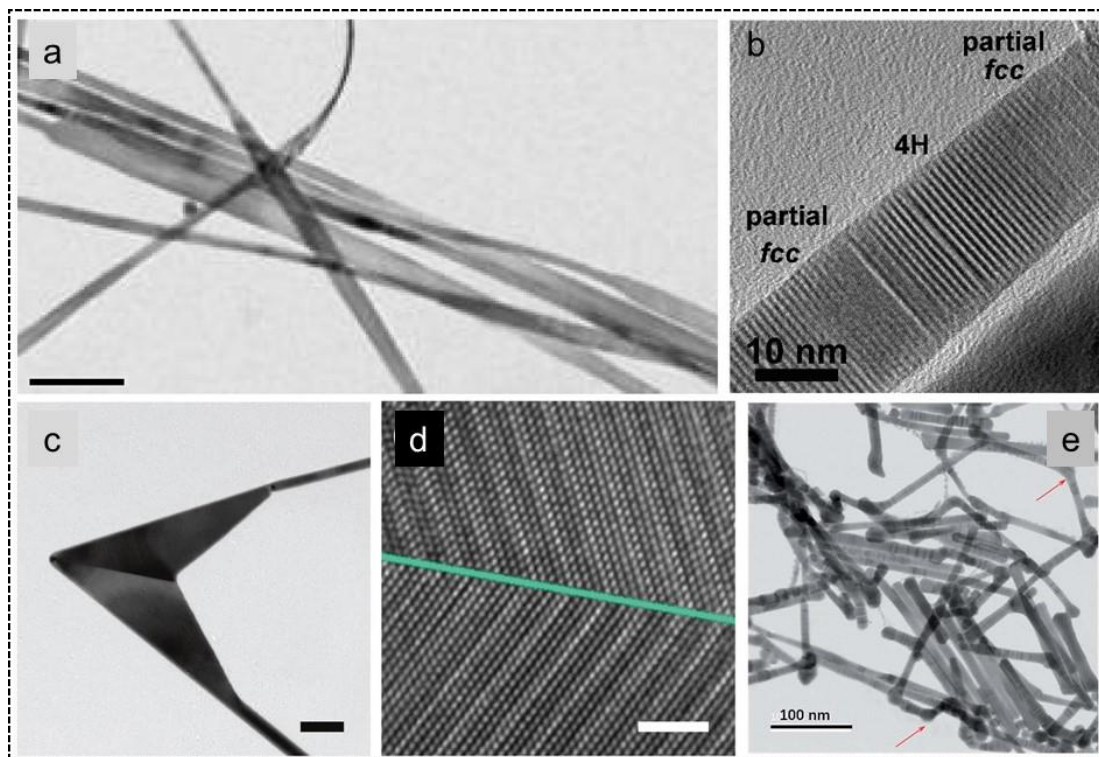
Figure I.17. Au nanostructures in hcp lattice (4H). (a) TEM image of 4H Au nanoribbons. (b) TEM image of a Au nanoribbon partially converted to fcc after decompression. (c) TEM image of a twinned nanokite and (d) HRTEM image of the corresponding twin boundary (green line). (f) Bright-field STEM image of the as-synthesized 4H Au wires. Panel a reprinted with permission from Reference 65; copyright 2015 Springer Nature. Panel b reprinted with permission from Reference 66; copyright 2018 American Chemical Society. Panels c and d reprinted with permission from Reference 67; copyright 2019 Springer Nature. Panel e reprinted with permission from Reference 68; copyright 2019 Royal Society of Chemistry.

I.8.C A fcc Metal Crystallizing in bco and bct

MD simulations have predicted a spontaneous fcc to bct phase transformation in metal nanowires, such as Au and Ag (diameter < 2 nm) in the presence of surface stress [71,72]. Individual cases are dealt with below.

bco and bct Ag. Ambient stable thick bct Ag nanowires were reported starting with decahedral nuclei [23]. The nuclei (**Figure I.19**a) grew along the [011] direction (see **Figure I.19**b),

forming nanowires of approximately 85 nm in diameter and lengths of a few micrometers (**Figure I.19**c). Occurrence of bct phase was only observed in strained decahedral particles and not in similarly sized nanocubes, further strengthening the observation that the internal strain induces the appearance of the bct phase. The proportion of bct was found to increase with increasing defects, meaning more bct phase in long nanowires. Conventionally, the proportion of a non-native phase should decrease with increasing size of the nanoparticles. In contrast, here, the persistent occurrence of the bct phase across the entire length of the nanowire is an exception, highlighting the effect of strain in stabilizing a non-native phase.
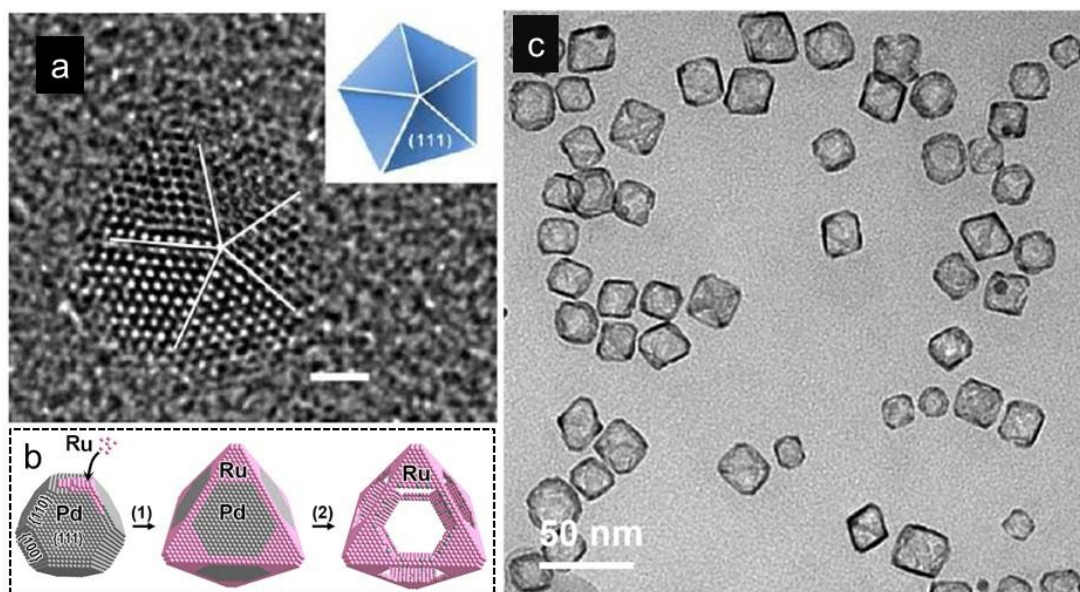
Figure I.18. Ru nanoparticles in fcc lattice. (a) HRTEM image of an fcc decahedral nanoparticle with the schematic in the inset. (b) Template driven growth of fcc Ru nanocages by the growth of Pd-Ru core-shell octahedral and followed by selective etching of the Pd core, resulting in a Rh octahedral nano-cage. (c) TEM image of Ru nanocages. Panel a reprinted with permission from Reference 50; copyright 2013 American Chemical Society. Panel b reprinted with permission from Reference 69; copyright 2016 American Chemical Society. Panels c reprinted with permission from Reference 70; copyright 2017 American Chemical Society.

Interestingly, the as-prepared bct phase was found to be ambient stable even after two years, perhaps due to the less strained sheath (fcc) protecting the strained core (bct). Thermal annealing in tetraethylene glycol resulted in nanowire fragmentation, initially into nanorods and eventually into nanoparticles [73]. Additionally, atomistic MD simulations have shown a possible fcc-to-bco (instead of bct) phase transformation [74] in penta-twinned Ag nanowires

because of the geometrical constraint at the twin boundaries and the side walls, shown in **Figure I.19**d. These regions are associated with elastic strain energies large enough to host extended defects purely under thermal activation. This energy can be roughly proportional to the area of the pentagonal cross-section; the larger the nanowire diameter, the more defective structures there will be.
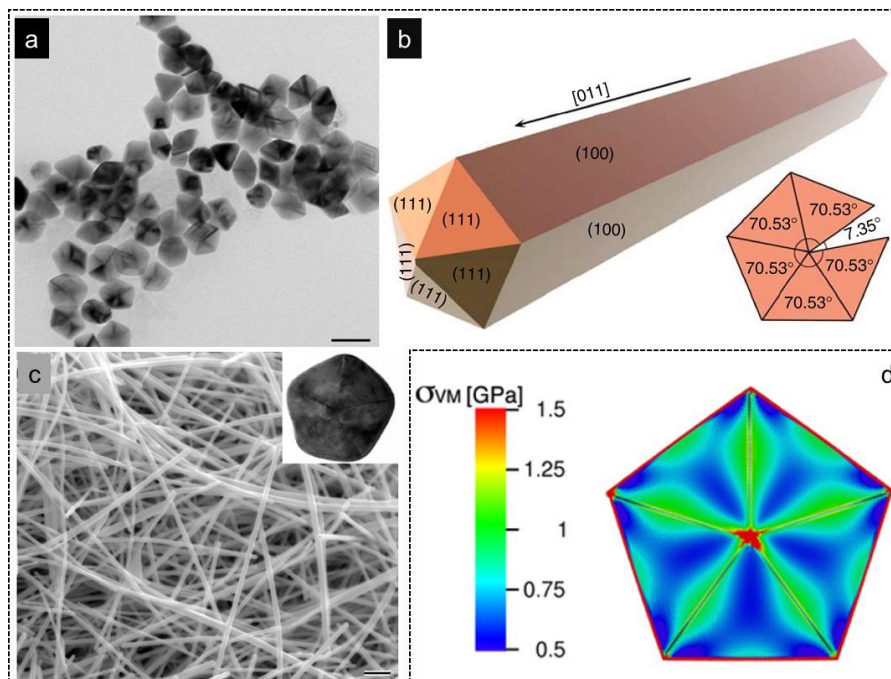
Figure I.19. Ag nanostructures in bco and bct lattices. (a) TEM image of decahedral Ag nanoparticles. (b) Ag nanowire with 5-fold symmetry. (c) SEM image of Ag nanowires and (inset) its cross-sectional TEM image viewed parallel to the longitudinal axis. (d) Distribution of intrinsic atomic stresses over a pentagonal cross-section of the 35 nm diameter nanowire, where σ_{VM} is the von Mises stress. Panels a–c reprinted with permission from Reference 22; copyright 2012 Springer Nature. Panel d reprinted with permission from Reference 74; copyright 2014 American Chemical Society.

bco and bct Au. A phase transformation to bct in a small part of a Au nanocrystal (approximately 10 nm) was monitored under TEM following a fracture in response to tensile loading [75]. Along the direction of the fracture (<001>), the length contracted by approximately 30% following the Bain model [76]. The model suggests that the compressive stress is inversely related to the size of the crystallite, leading to phase transformation (bct). Clearly, this is a size-dependent phenomenon. Unlike the example above, the formation of bct phase has been reported in a penta-twinned microcrystal [55], starting with a decahedral

nucleus. Microcrystallites of Au measuring a few micrometers in length have been stabilized, hosting as much as approximately 85% of the bco and bct structures [77].

I.9 Crystal Structure Dependent Properties

The metal surfaces exhibit bright luster in appearance. The free electrons lying beneath the Fermi level get excited by absorbing the exposed visible light and jump to the higher energy. Later, the excited electrons jump down to the lower energy levels by emitting radiation, which cover the full visible wavelength spectrum, thereby representing shiny silver color. Due to the presence of delocalized free electrons, metals are good electrical and heat conductors. Thus, alternation in the crystal structure can alter the Fermi level and thereby introduce surprises in terms of the behavior of a metal.

I.9.A Chemical stability

The as-prepared Au 4H nanoribbons are coated with oleylamine, and upon surface ligand exchange by 1-dodecanethiol, a phase transformation results to form $(001)_{fcc}$-oriented fcc [78]. The transformation at ambient conditions may arise owing to the flattening of the $(1\bar{1}0)_{4H}$ planes, with the prevailing Au-S interaction as a driving factor. In other instances, the strain induced by epitaxial layers (such as Ir, Rh, Ru, and Os) also causes partial phase transformation. Pristine $(110)_{2H}$-oriented Au square sheets transform into $(100)_{fcc}$-oriented nanosheets upon exchange of surface-capped oleylamine ligands by octadecanethiol (87), with an overall enhancement in the thickness (approximately 35%) because of the larger interlayer spacing of the basal (200) plane of fcc. The transformation is accompanied by a surface reconstruction of the $Au(100)_{fcc}$.

I.9.B Optical Property

The reflective color of a 4H Ag film was different from that of the fcc Ag [63]; the latter appeared shiny white as expected, whereas the former was golden yellow [63]. The corresponding spectral shift was approximately 5 nm (62 meV) toward blue, which disappeared upon annealing due to phase conversion. As is well-known, the monoatomic structure of fcc is associated with active acoustic modes while being Raman inactive, whereas the 4H structure with its four-atom basis hosts both acoustic and optical modes, making it Raman active (64 nm^{-1}).

I.9.C Electrical Property

The electrical properties also show interesting variations with the crystal structure. For example, a thick film of 4H Ag in the form of nanorod agglomerates showed a resistivity value approximately 130 times higher compared to its fcc counterpart [63], which decreased by 24 times on annealing accompanied by the partial conversion to the native fcc structures. The observed higher values are thought to be due to the modifications in the Fermi surface as well as the electronic structure.

I.9.D Catalytic Property

Metal crystallites hosting unconventional crystal structures have produced immense interest in the field of catalysis, where the performance of a catalyst is dictated mainly by the surface reactivity (*i.e.*, coordination number and surface energy) [9] and the active surface area. This property can be even more intriguing if the crystallites are in a different structure than the normal fcc [50,79,80].
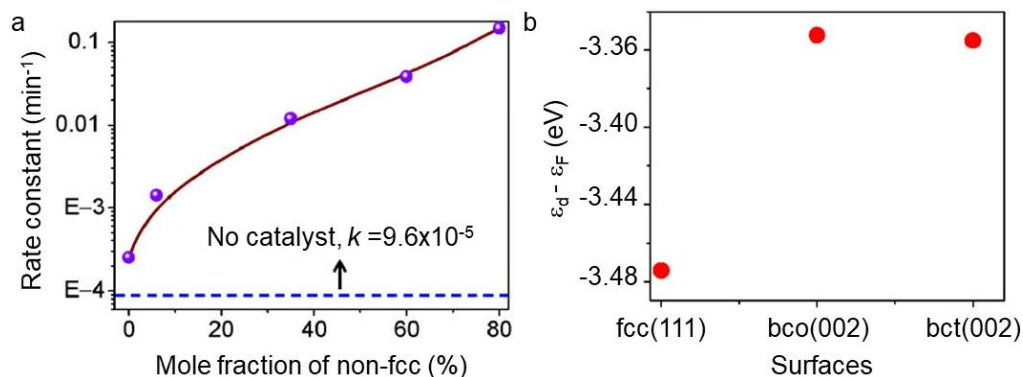
Figure I.20. Crystal structure-dependent catalytic property. (a) Variation in the rate constant of the *p*-nitrophenol to *p*-aminophenol reduction reaction at different fractions of the non-fcc (bco and bct) phases. The blue dashed line indicates the rate constant in the absence of the metal catalyst. (b) ε_d, the d-band center for atoms on the low index surfaces of fcc, bco, and bct phases of Au. Figure reprinted with permission from Reference 77; copyright 2017 Springer Nature.

A model reduction reaction, *p*-nitrophenol to *p*-aminophenol, was monitored using ultraviolet visible spectroscopy relying on the characteristic absorption peaks. The reaction rate constant increased monotonically with an increasing proportion of bco and bct in the microcrystallites, reaching a value nearly three orders higher than that from an uncatalyzed reaction [77] (**Figure I.20**a). The experimental observations were supported by the density function theory calculations, which predicted lower effective coordination numbers for the

surface atoms in the bco and bct phases. The theoretically calculated d-band positions (see **Figure I.20**b) follow the trend fcc < bco < bct, again emphasizing the higher reactivity of the bco and bct structures.

I.10 Advantages of Unconventional Lattices in Micro-Sized Crystallites

The stabilization of metals in the nanoscale with energetically expensive facets is comparatively easy due to the manifestation of lower volume energy and higher surface energy. The same phenomenon allows to arrest the unconventional lattices at the nanoscale (for example, reverse role of crystallization of fcc and hcp) which is otherwise impossible to achieve [50,51]. With increase in dimension, (for example nm to µm), the nanostructures prefer the conventional morphology as well as crystal structures [46]. The stabilization of anisotropic morphologies at the micrometer scale is possible by an additional shape-directing agent, such as, Ag(I) in Au (100), PVP in Ag(100) and thereby the formation of ~ few µms long bipyramids and nanowires [4]. Again, the ambient stable unconventional lattices at the micro-scale are possible due to the increase of the strain associated with the nuclei, in contrast to the conventional nano size effect [55]. The metastable lattices stabilized at the micro-scale may provide different properties deviated from the nanoscale. Additionally, the larger size of the crystallites provides ease in handling, for example, as optical wave-guide (of Au bipyramids) [41], top contact (Au microplates) [81] and electrodes in fabrication (2 mm sized Au plates) [38].

I.11 Scope of the Thesis

The wide range of applications of the unconventional crystal structures of noble metals has articulated immense interest among the community to successfully crystallize ambient stable non-native lattices with reproducible, scalable and ease in handling to the great extent. The literature reports narrate mostly the non-native structures at the nanoscale which undergo deformation or phase transformation under commonly used perturbants. The work reported in the thesis is an attempt to address the above mentioned issues in Au microcrystallites and provide boundary conditions within which the untraditional lattices of Au are stable. Additionally, the spatial distribution of the various lattices in the crystallite volume and stabilization of other lattices are also subjects of the investigation. Finally, the effect of crystal structure on template-based growth may also be explored.

References

[1]   E. Roduner, *Size Matters: Why Nanomaterials Are Different*, Chem. Soc. Rev. **35**, 583 (2006).

[2]   S. A. A. Sanchez U. Heiz, W.-D. Schneider, H. Ha1kkinen, R. N. Barnett, and Uzi Landman, *When Gold Is Not Noble: Nanoscale Gold Catalysts*, J. Phys. Chem. A **103**, 9573 (1999).

[3]   E. B. Guidez and C. M. Aikens, *Quantum Mechanical Origin of the Plasmon: From Molecular Systems to Nanoparticles*, Nanoscale **6**, 11512 (2014).

[4]   Y. Xia, Y. Xiong, B. Lim, and S. E. Skrabalak, *Shape-Controlled Synthesis of Metal Nanocrystals: Simple Chemistry Meets Complex Physics?*, Angew. Chem. Int. Ed. **48**, 60 (2009).

[5]   K. L. Kelly, E. Coronado, L. L. Zhao, and G. C. Schatz, *The Optical Properties of Metal Nanoparticles: The Influence of Size, Shape, and Dielectric Environment*, J. Phys. Chem. B **107**, 668 (2003).

[6]   A. Sánchez-Iglesias, N. Winckelmans, T. Altantzis, S. Bals, M. Grzelczak, and L. M. Liz-Marzán, *High-Yield Seeded Growth of Monodisperse Pentatwinned Gold Nanoparticles through Thermally Induced Seed Twinning*, J. Am. Chem. Soc. **139**, 107 (2017).

[7]   B. Hammer and J. K. Nørskov, *Why Gold Is the Nobelest of All the Metals*, Nature **376**, 238 (1995).

[8]   B. Hvolbaek, B. Hvolbaek, T. V. W. Janssens, T. V. W. Janssens, B. S. Clausen, B. S. Clausen, H. Falsig, H. Falsig, C. H. Christensen, C. H. Christensen, J. K. Norskov, and J. K. Norskov, *Catalytic Activity of Au Nanoparticles*, Nano Today **2**, 14 (2007).

[9]   H. Falsig, B. Hvolbæk, I. S. Kristensen, T. Jiang, T. Bligaard, C. H. Christensen, and J. K. Nørskov, *Trends in the Catalytic CO Oxidation Activity of Nanoparticles*, Angew. Chem. Int. Ed. **47**, 4835 (2008).

[10]   V. Bansal, V. Li, A. P. O'Mullane, and S. K. Bhargava, *Shape Dependent Electrocatalytic Behaviour of Silver Nanoparticles*, CrystEngComm **12**, 4280 (2010).

[11]   N. Tian, Z.-Y. Zhou, S.-G. Sun, Y. Ding, and Z. L. Wang, *Synthesis of Tetrahexahedral Platinum Nanocrystals with High-Index Facets and High Electro-Oxidation Activity*, Science **316**, 732 (2007).

[12]   Q. Zhang and H. Wang, *Facet-Dependent Catalytic Activities of Au Nanoparticles Enclosed by High-Index Facets*, ACS Catal. **4**, 4027 (2014).

[13]   Y. Sun, B. Mayers, T. Herricks, and Y. Xia, *Polyol Synthesis of Uniform Silver Nanowires: A Plausible Growth Mechanism and the Supporting Evidence*, Nano Lett. **3**, 955 (2003).

[14]   S. E. Skrabalak, B. J. Wiley, M. Kim, E. V. Formo, and Y. Xia, *On the Polyol Synthesis of Silver Nanostructures: Glycolaldehyde as a Reducing Agent*, Nano Lett. **8**, 2077

(2008).

[15] B. Wiley, T. Herricks, Y. Sun, and Y. Xia, *Polyol Synthesis of Silver Nanoparticles : Use of Chloride and Oxygen to Promote the Formation of Single-Crystal , Truncated Cubes and Tetrahedrons*, Nano Lett. **4**, 1733 (2004).

[16] B. Wiley, Y. Sun, and Y. Xia, *Polyol Synthesis of Silver Nanostructures: Control of Product Morphology with Fe(II) or Fe(III) Species*, Langmuir **21**, 8077 (2005).

[17] B. Radha, M. Arif, R. Datta, T. K. Kundu, and G. U. Kulkarni, *Movable Au Microplates as Fluorescence Enhancing Substrates for Live Cells*, Nano Res. **3**, 738 (2010).

[18] B. Radha and G. U. Kulkarni, *A Real Time Microscopy Study of the Growth of Giant Au Microplates*, Cryst. Growth Des. **11**, 320 (2011).

[19] B. Radha and G. U. Kulkarni, *Giant Single Crystalline Au Microplates*, Curr. Sci. **102**, 70 (2012).

[20] G. Mettela, S. Siddhanta, C. Narayana, and G. U. Kulkarni, *Nanocrystalline Ag Microflowers as a Versatile SERS Platform*, Nanoscale **6**, 7480 (2014).

[21] X. Xia, Y. Wang, A. Ruditskiy, and Y. Xia, *25th Anniversary Article: Galvanic Replacement: A Simple and Versatile Route to Hollow Nanostructures with Tunable and Well-Controlled Properties*, Adv. Mater. **25**, 6313 (2013).

[22] H. J. Jang, S. Ham, J. A. I. Acapulco, Y. Song, S. Hong, K. L. Shuford, and S. Park, *Fabrication of 2D Au Nanorings with Pt Framework*, J. Am. Chem. Soc. **136**, 17674 (2014).

[23] Y. Sun, Y. Ren, Y. Liu, J. Wen, J. S. Okasinski, and D. J. Miller, *Ambient-Stable Tetragonal Phase in Silver Nanostructures*, Nat. Commun. **3**, 971 (2012).

[24] N. R. Jana, L. Gearheart, and C. J. Murphy, *Seed-Mediated Growth Approach for Shape-Controlled Synthesis of Spheroidal and Rod-like Gold Nanoparticles Using a Surfactant Template*, Adv. Mater. **13**, 1389 (2001).

[25] W. Wang, Y. Yan, N. Zhou, H. Zhang, D. Li, and D. Yang, *Seed-Mediated Growth of Au Nanorings with Size Control on Pd Ultrathin Nanosheets and Their Tunable Surface Plasmonic Properties*, Nanoscale **8**, 3704 (2016).

[26] Z. Huo, C.-K. Tsung, W. Huang, X. Zhang, and P. Yang, *Sub-Two Nanometer Single Crystal Au Nanowires*, Nano Lett. **8**, 2041 (2008).

[27] N. Winckelmans, T. Altantzis, M. Grzelczak, A. Sánchez-Iglesias, L. M. Liz-Marzán, and S. Bals, *Multimode Electron Tomography as a Tool to Characterize the Internal Structure and Morphology of Gold Nanoparticles*, J. Phys. Chem. C **122**, 13522 (2018).

[28] H. Zhang, B. Gilbert, F. Huang, and J. F. Banfield, *Water-Driven Structure Transformation in Nanoparticles at Room Temperature*, Nature **424**, 1025 (2003).

[29] Y. Liu, C. Wang, Y. Wei, L. Zhu, D. Li, J. S. Jiang, N. M. Markovic, V. R. Stamenkovic, and S. Sun, *Surfactant-Induced Postsynthetic Modulation of Pd Nanoparticle Crystallinity*, Nano Lett. **11**, 1614 (2011).

[30] M. B. Mohamed, K. Z. Ismail, S. Link, and M. A. El-Sayed, *Thermal Reshaping of Gold Nanorods in Micelles*, J. Phys. Chem. B **102**, 9370 (1998).

[31] G. González-Rubio, P. Díaz-Núñez, A. Rivera, A. Prada, G. Tardajos, J. González-Izquierdo, L. Bañares, P. Llombart, L. G. Macdowell, M. A. Palafox, L. M. Liz-Marzán, O. Peña-Rodríguez, and A. Guerrero-Martínez, *Femtosecond Laser Reshaping Yields Gold Nanorods with Ultranarrow Surface Plasmon Resonances*, Science **358**, 640 (2017).

[32] T. Wen, H. Zhang, X. Tang, W. Chu, W. Liu, Y. Ji, Z. Hu, S. Hou, X. Hu, and X. Wu, *Copper Ion Assisted Reshaping and Etching of Gold Nanorods: Mechanism Studies and Applications*, J. Phys. Chem. C **117**, 25769 (2013).

[33] L. Rodríguez-Lorenzo, J. M. Romo-Herrera, J. Pérez-Juste, R. A. Alvarez-Puebla, and L. M. Liz-Marzán, *Reshaping and LSPR Tuning of Au Nanostars in the Presence of CTAB*, J. Mater. Chem. **21**, 11544 (2011).

[34] C. Wang, X. Li, L. Jin, P.-H. Lu, C. Dejoie, W. Zhu, Z. Wang, W. Bi, R. E. Dunin-Borkowski, K. Chen, and M. Jin, *Etching-Assisted Route to Heterophase Au Nanowires with Multiple Types of Active Surface Sites for Silane Oxidation*, Nano Lett. **19**, 6363 (2019).

[35] T. Tsuji, K. Iryo, N. Watanabe, and M. Tsuji, *Preparation of Silver Nanoparticles by Laser Ablation in Solution*, Appl. Surf. Sci. **202**, 80 (2002).

[36] S. Barcikowski and G. Compagnini, *Advanced Nanoparticle Generation and Excitation by Lasers in Liquids*, Phys. Chem. Chem. Phys. **15**, 3022 (2013).

[37] H. Förster, C. Wolfrum, and W. Peukert, *Experimental Study of Metal Nanoparticle Synthesis by an Arc Evaporation/Condensation Process*, J. Nanoparticle Res. **14**, 926 (2012).

[38] L. Lv, X. Wu, Y. Yang, X. Han, R. Mezzenga, and C. Li, *Trans-Scale 2D Synthesis of Millimeter-Large Au Single Crystals via Silk Fibroin Templates*, ACS Sustain. Chem. Eng. **6**, 12419 (2018).

[39] T.-H. Yang, Y. Shi, A. Janssen, and Y. Xia, *Surface Capping Agents and Their Roles in Shape-Controlled Synthesis of Colloidal Metal Nanocrystals*, Angew. Chem. Int. Ed. **59**, 15378 (2020).

[40] P. J. F. Harris, *Sulphur-Induced Faceting of Platinum Catalyst Particles*, Nature **323**, 792 (1986).

[41] G. Mettela, R. Boya, D. Singh, G. V. P. Kumar, and G. U. Kulkarni, *Highly Tapered Pentagonal Bipyramidal Au Microcrystals with High Index Faceted Corrugation: Synthesis and Optical Properties*, Sci. Rep. **3**, 1793 (2013).

[42] W. Niu, Y. Duan, Z. Qing, H. Huang, and X. Lu, *Shaping Gold Nanocrystals in Dimethyl Sulfoxide: Toward Trapezohedral and Bipyramidal Nanocrystals Enclosed by {311} Facets*, J. Am. Chem. Soc. **139**, 5817 (2017).

[43] A. Howie and L. D. Marks, *Elastic Strains and the Energy Balance for Multiply Twinned*

Particles, Philos. Mag. A **49**, 95 (1984).

[44] A. Sánchez-Iglesias, I. Pastoriza-Santos, J. Pérez-Juste, B. Rodríguez-González, F. J. García De Abajo, and L. M. Liz-Marzán, *Synthesis and Optical Properties of Gold Nanodecahedra with Size Control*, Adv. Mater. **18**, 2529 (2006).

[45] A. Mayoral, H. Barron, R. Estrada-Salas, A. Vazquez-Duran, and M. José-Yacamán, *Nanoparticle Stability from the Nano to the Meso Interval*, Nanoscale **2**, 335 (2010).

[46] X. Liu, J. Luo, and J. Zhu, *Size Effect on the Crystal Structure of Silver Nanowires*, Nano Lett. **6**, 408 (2006).

[47] J. L. Huang, Z. Li, H. H. Duan, Z. Y. Cheng, Y. D. Li, J. Zhu, and R. Yu, *Formation of Hexagonal-Close Packed (hcp) Rhodium as a Size Effect*, J. Am. Chem. Soc. **139**, 575 (2017).

[48] T. V. W. Janssens, B. S. Clausen, B. Hvolbæk, H. Falsig, C. H. Christensen, T. Bligaard, and J. K. Nørskov, *Insights into the Reactivity of Supported Au Nanoparticles: Combining Theory and Experiments*, Top. Catal. **44**, 15 (2007).

[49] H. Benaissa and M. Ferhat, *Polytypism-Induced Stabilization of Hexagonal 2H, 4H and 6H Phases of Gold*, Superlattices Microstruct. **109**, 170 (2017).

[50] K. Kusada, H. Kobayashi, T. Yamamoto, S. Matsumura, N. Sumi, K. Sato, K. Nagaoka, Y. Kubota, and H. Kitagawa, *Discovery of Face-Centered-Cubic Ruthenium Nanoparticles: Facile Size-Controlled Synthesis Using the Chemical Reduction Method*, J. Am. Chem. Soc. **135**, 5493 (2013).

[51] T. Wakisaka, K. Kusada, T. Yamamoto, T. Toriyama, S. Matsumura, G. Ibrahima, O. Seo, J. Kim, S. Hiroi, O. Sakata, S. Kawaguchi, Y. Kubota, and H. Kitagawa, *Discovery of Face-Centred Cubic Os Nanoparticles*, Chem. Commun. **56**, 372 (2020).

[52] N. Araki, K. Kusada, S. Yoshioka, T. Sugiyama, T. Ina, and H. Kitagawa, *Observation of the Formation Processes of Hexagonal Close-Packed and Face-Centered Cubic Ru Nanoparticles*, Chem. Lett. **48**, 1062 (2019).

[53] M. Tsuji, M. Ogino, R. Matsuo, H. Kumagae, S. Hikino, T. Kim, and S. H. Yoon, *Stepwise Growth of Decahedral and Icosahedral Silver Nanocrystals in DMF*, Cryst. Growth Des. **10**, 296 (2010).

[54] C. L. Johnson, E. Snoeck, M. Ezcurdia, B. Rodríguez-González, I. Pastoriza-Santos, L. M. Liz-Marzán, and M. J. H¨YTCH, *Effects of Elastic Anisotropy on Strain Distributions in Decahedral Gold Nanoparticles*, Nat. Mater. **7**, 120 (2008).

[55] G. Mettela, M. Bhogra, U. V Waghmare, and G. U. Kulkarni, *Ambient Stable Tetragonal and Orthorhombic Phases in Penta-Twinned Bipyramidal Au Microcrystals*, J. Am. Chem. Soc. **137**, 3024 (2015).

[56] Y. Sun and Y. Xia, *Shape-Controlled Synthesis of Gold and Silver Nanoparticles*, Science **298**, 2176 (2002).

[57] Y. Xia, X. Xia, and H. C. Peng, *Shape-Controlled Synthesis of Colloidal Metal*

Nanocrystals: Thermodynamic versus Kinetic Products, J. Am. Chem. Soc. **137**, 7947 (2015).

[58] H. Jin, K. W. Lee, N. T. Khi, H. An, J. Park, H. Baik, J. Kim, H. Yang, and K. Lee, *Rational Synthesis of Heterostructured M/Pt (M = Ru or Rh) Octahedral Nanoboxes and Octapods and Their Structure-Dependent Electrochemical Activity toward the Oxygen Evolution Reaction*, Small **11**, 4462 (2015).

[59] Z. Fan, Y. Chen, Y. Zhu, J. Wang, B. Li, Y. Zong, Y. Han, and H. Zhang, *Epitaxial Growth of Unusual 4H Hexagonal Ir, Rh, Os, Ru and Cu Nanostructures on 4H Au Nanoribbons*, Chem. Sci. **8**, 795 (2016).

[60] I. Chakraborty, D. Carvalho, S. N. Shirodkar, S. Lahiri, S. Bhattacharyya, R. Banerjee, U. Waghmare, and P. Ayyub, *Novel Hexagonal Polytypes of Silver: Growth, Characterization and First-Principles Calculations*, J. Phys. Condens. Matter **23**, 325401 (2011).

[61] A. I. M. A. V. Novgorodova, M. I. Gorshkov, *Native Silver and Its New Structural Modifications*, Int. Geol. Rev. **23**, 552 (1979).

[62] Y. Zhou, G. T. Fei, P. Cui, B. Wu, B. Wang, and L. De Zhang, *The Fabrication and Thermal Expansion Properties of 4H-Ag Nanowire Arrays in Porous Anodic Alumina Templates*, Nanotechnology **19**, 285711 (2008).

[63] I. Chakraborty, S. N. Shirodkar, S. Gohil, U. V Waghmare, and P. Ayyub, *A Stable, Quasi-2D Modification of Silver: Optical, Electronic, Vibrational and Mechanical Properties, and First Principles Calculations*, J. Phys. Condens. Matter **26**, 025402 (10PP) (2014).

[64] B. Sharma, B. Chalke, N. Kulkarni, J. Parmar, S. Gohil, and P. Ayyub, *Hexagonal → Cubic Transition in Ag : Prototype for a General Mechanism for Irreversible Solid−solid Structural Transformations*, J. Phys. Chem. C **123**, 23177 (2019).

[65] Z. Fan, M. Bosman, X. Huang, D. Huang, Y. Yu, K. P. Ong, Y. A. Akimov, L. Wu, B. Li, J. Wu, Y. Huang, Q. Liu, C. Eng Png, C. Lip Gan, P. Yang, and H. Zhang, *Stabilization of 4H Hexagonal Phase in Gold Nanoribbons*, Nat. Commun. **6**, 7684 (2015).

[66] Q. Li, W. Niu, X. Liu, Y. Chen, X. Wu, X. Wen, Z. Wang, H. Zhang, and Z. Quan, *Pressure-Induced Phase Engineering of Gold Nanostructures*, J. Am. Chem. Soc. **140**, 15783 (2018).

[67] W. Niu, J. Liu, J. Huang, B. Chen, Q. He, A.-L. Wang, Q. Lu, Y. Chen, Q. Yun, J. Wang, C. Li, Y. Huang, Z. Lai, Z. Fan, X.-J. Wu, and H. Zhang, *Unusual 4H-Phase Twinned Noble Metal Nanokites*, Nat. Commun. **10**, 2881 (2019).

[68] Q. Wang, Z. L. Zhao, C. Cai, H. Li, and M. Gu, *Ultra-Stable 4H-Gold Nanowires up to 800 °C in a Vacuum*, J. Mater. Chem. A **7**, 23812 (2019).

[69] H. Ye, Q. Wang, M. Catalano, N. Lu, J. Vermeylen, M. J. Kim, Y. Liu, Y. Sun, and X. Xia, *Ru Nanoframes with an fcc Structure and Enhanced Catalytic Properties*, Nano Lett. **16**, 2812 (2016).

[70] M. Zhao, A. O. Elnabawy, M. Vara, L. Xu, Z. D. Hood, X. Yang, K. D. Gilroy, L. Figueroa-Cosme, M. Chi, M. Mavrikakis, and Y. Xia, *Facile Synthesis of Ru-Based Octahedral Nanocages with Ultrathin Walls in a Face-Centered Cubic Structure*, Chem. Mater. **29**, 9227 (2017).

[71] J. Diao, K. Gall, and M. L. Dunn, *Surface-Stress-Induced Phase Transformation in Metal Nanowires*, Nat. Mater. **2**, 656 (2003).

[72] K. Gall, J. Diao, M. L. Dunn, M. Haftel, N. Bernstein, and M. J. Mehl, *Tetragonal Phase Transformation in Gold Nanowires*, J. Eng. Mater. Technol. **127**, 417 (2005).

[73] Z. Li, J. S. Okasinski, J. D. Almer, Y. Ren, X. Zuo, and Y. Sun, *Quantitative Determination of Fragmentation Kinetics and Thermodynamics of Colloidal Silver Nanowires by in Situ High-Energy Synchrotron X-ray Diffraction*, Nanoscale **6**, 365 (2014).

[74] Y. Zhou and K. A. Fichthorn, *Internal Stress-Induced Orthorhombic Phase in 5-Fold-Twinned Noble Metal Nanowires*, J. Phys. Chem. C **118**, 18746 (2014).

[75] H. Zheng, A. Cao, C. R. Weinberger, J. Y. Huang, K. Du, J. Wang, Y. Ma, Y. Xia, and S. X. Mao, *Discrete Plasticity in Sub-10-Nm-Sized Gold Crystals*, Nat. Commun. **1**, 144 (2010).

[76] W. C. M. Bowles J. S., *The Bain Strain, Lattice Correspondences, and Deformations Related to Martensitic Transformations*, Metall. Trans. **3**, 1113 (1972).

[77] G. Mettela, N. Mammen, J. Joardar, S. Narasimhan, and G. U. Kulkarni, *Non-fcc Rich Au Crystallites Exhibiting Unusual Catalytic Activity*, Nano Res. **10**, 2271 (2017).

[78] Z. Fan, M. Bosman, X. Huang, D. Huang, Y. Yu, K. P. Ong, Y. A. Akimov, L. Wu, B. Li, J. Wu, Y. Huang, Q. Liu, C. Eng Png, C. Lip Gan, P. Yang, and H. Zhang, *Stabilization of 4H Hexagonal Phase in Gold Nanoribbons*, Nat. Commun. **6**, 7684 (2015).

[79] M. Mavrikakis, B. Hammer, and J. K. Nørskov, *Effect of Strain on the Reactivity of Metal Surfaces*, Phys. Rev. Lett. **81**, 2819 (1998).

[80] A. Ruban, B. Hammer, P. Stoltze, and H. L. Skriver, *Surface Electronic Structure and Reactivity of Transition and Noble Metals*, J. Mol. Catal. A Chem. **115**, 421 (1997).

[81] B. Radha, D. Jayaraj, G. U. Kulkarni, S. Heun, D. Ercolani, and L. Sorba, *Large-Area Ohmic Top Contact to Vertically Grown Nanowires Using a Free-Standing Au Microplate Electrode*, ACS Appl. Mater. Interfaces **4**, 1860 (2012).

*   *   *

Characterization Techniques*

Several spectroscopic and microscopic techniques have been used to characterize the prepared samples reported in this thesis. In the following paragraphs, the details of instruments used and the sample preparation methods are described.

Scanning Electron Microscopy (SEM) and Energy Dispersive X-ray Spectroscopy (EDX). SEM was performed using a Nova NanoSEM 600 equipment (FEI Co., The Netherlands). EDX mapping was performed using EDX Genesis V4.52 (USA) attached to the SEM column operating at 15 kV. For imaging the crystallite and penta-twinned tips of the bipyramid (in the tilted view), the stage was tilted (-10° to 60°). In-situ heating was performed in a lab built set up (as shown in Figure II.1).
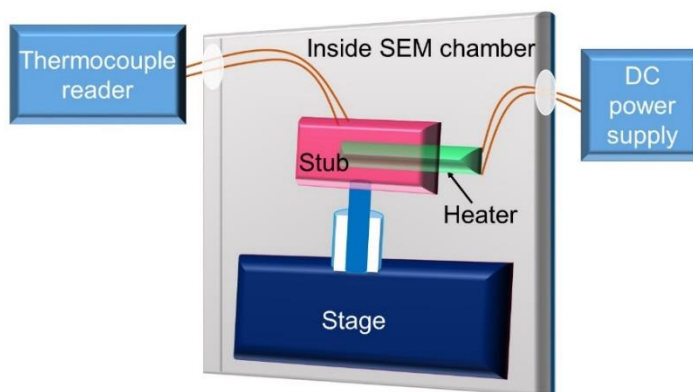
Figure II.1. In-situ heating setup within the SEM chamber.

Transmission Electron Microscopy (TEM) and Selected Area Electron Diffraction (SAED). Transmission electron microscopy (TEM) measurements were carried out with a JEOL-3010 instrument operating at 300 kV (λ = 0.0196 Å). SAED patterns were collected using Technai F30 UHR TEM operating at 200 kV. Samples for TEM were prepared by depositing a drop of the nanomaterial on a holey carbon Cu grid, allowing it to dry in a desiccator overnight.

X-ray Diffraction (XRD). XRD measurements were performed using a PANalytical instrument (Cu Kα, 1.5406 Å; scan rate 1°/3 min).

Phase Identification (Le Bail Fitting Analysis). Le Bail fitting has been performed with adjusting background correction, zero correction, lattice parameters and width parameters to achieve fine fitting of the experimental data.

---

* Part of this chapter is from ACS Nano **14**, 9456 (2020).

Pt Markers on SiN$_x$ Membrane. Pt markers were deposited *via* ion beam induced deposition (IBID) from a Pt precursor inside the focused ion beam (FIB)/SEM dual beam instrument with Ga$^+$ ion source operating at 30 keV [1].

Scanning X-ray Diffraction Microscopy (SXDM). XRD is one of the method to analyze structures nondestructively, where the small wavelength of X-rays provides an opportunity to determine structures with atomic precision. In addition, the high penetration depth of hard X-rays permitted for the analysis of comparatively thick samples without slicing. Recent advancement in the nanometer sized X-ray beam in the form of SDXM, offers a great possibility of examining the local composition or structure of the thick sample in small volumes sampled by the nano-focus beam and recording maps of structural parameters by scanning the sample. In the case of semiconductor specially core-shell nanowires, the spatial distribution of different elements and strains corresponding to unit cells have been analyzed with resolutions in the range of nanometer. Here, 15 keV X-ray with beam size of 100 nm has been used.
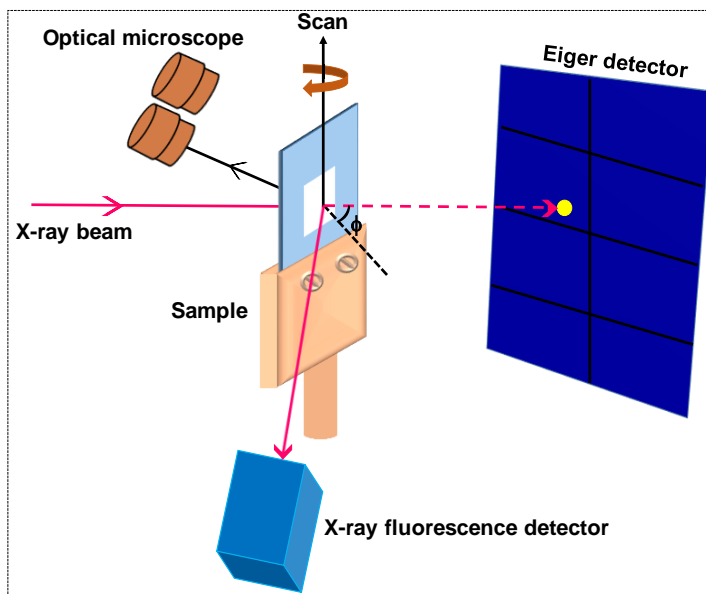
Figure II.2. SXDM experimental step up at the beamline.

The experiment was conducted at the nanoprobe end-station of the beamline P06 at PETRA III synchrotron radiation source (DESY, Germany). Two perpendicularly positioned nanofocusing refractive X-ray lenses (NFLs) etched in the Si wafers were used to focus the 15 keV X-ray beam on a sample [2]. An energy dispersive X-ray fluorescence detector (VORTEX EX) was placed at 90° with respect to the beam for the sample alignment and

location of the single Au microcrystal. An Eiger X 4M-detector (Dectris Ltd.) with a pixel size of 75×75 μm^2 was placed 148.1 mm (in **Chapter IV**)/101.2 mm (in **Chapter VI**) downstream from the sample for the X-ray diffraction. The size and shape of the nanofocused beam were determined using a ptychographic scan of a known test object; a pattern in a shape of a Siemens star etched in a tantalum film. This sample was scanned through the nanofocused X-ray beam over an area of 0.8×1.6 μm^2 (in **Chapter IV**)/1.0×2.0 μm^2 (in **Chapter VI**) in horizontal and vertical directions with a step size of 50 nm. The X-ray optics unit together with the laser interferometers for position control of the sample helped to track the sample position relative to the optics in scanning microscopy [3].

Atomic force microscopy (AFM). AFM experiments were carried out using multimode (Veeco, USA) Scanning Probe Microscope (multimode) in contact mode. Both amplitude and height information were recorded at a scan rate of 3.19 $\mu m/s$ and stored in a 512×512 pixel format. Images were processed using offline software.

Dektak Stylus. For film thickness measurements, a stylus profiler Dektak 6M (Veeco, USA) was used.

Thermogravimetric Analysis (TGA). TGA was carried out with a Mettler Toledo Star instrument (Weinheim, Germany) in the temperature range 25-450 °C under N_2 atmosphere and a heating rate of 5 °C/min.

Ar^+ Ion Sputtering. An Omicron ISE 10 ion gun with its controller have been used for the Ar^+ ion beam irradiation. The substrate holder was kept at 45° tilt facing towards the gun. Injection of Argon gas was done at a base pressure of 1×10^{-6} Torr and the working pressure was 5×10^{-5} Torr.

Keithley 4200. The resistive heater was characterized (by regular I-V) using Keithley 4200.

References

[1]   A. Stierle, T. F. Keller, H. Noei, V. Vonk, and R. Roehlsberger, *DESY NanoLab*, J. Large-Scale Res. Facil. JLSRF **2**, 1 (2016).

[2]   C. G. Schroer, P. Boye, J. M. Feldkamp, J. Patommel, D. Samberg, A. Schropp, A. Schwab, S. Stephan, G. Falkenberg, G. Wellenreuther, and N. Reimers, *Hard X-ray Nanoprobe at Beamline P06 at PETRA III*, Nucl. Instrum. Methods Phys. Res., Sect. A **616**, 93 (2010).

[3]   C. G. Schroer, M. Seyrich, M. Kahnt, S. Botta, R. Döhrmann, G. Falkenberg, J. Garrevoet, M. Lyubomirskiy, M. Scholz, A. Schropp, and F. Wittwer, *PtyNAMi:*

Ptychographic Nano-Analytical Microscope at PETRA III: Interferometrically Tracking Positions for 3D X-ray Scanning Microscopy Using a Ball-Lens Retroreflector, Proc. SPIE **10389**, 103890E (2017).

*   *   *

Maximization of non-Cubic Phases in Ambient Stable Au Microcrystallites

Summary

Properties of nanomaterials are dictated by their crystal structures and thus, stabilizing them in the form of their polymorphs can introduce a gallery of new properties. Herein, the study explores the possibility of stabilizing Au microcrystallites in maximum proportion of non-cubic lattices by tuning the reaction composition and kinetics. Thermolysis of the Au-organic precursor in the presence of Ag(I) and HCl at 250 °C results in body-centered orthorhombic (bco) and body-centered tetragonal (bct) lattices (altogether termed as bc(o,t)) with ~ 92% of its total volume. The presence of Ag(I) (a shape-directing agent) favors the formation of decahedron followed by the anisotropic growth leading to bipyramids. The inherent geometrical constraint in the decahedron induces strain which consequences in the stabilization of the bc(o,t) lattices. The formation of decahedron nucleus which finally dictates the growth of the bipyramid requires a lower reduction potential. Thus, by tuning the reaction pH (*i.e.*, addition of HCl) of the precursor composition, higher quantity of bipyramids and thereby maximization of the bc(o,t) lattices can be achieved.

III.1 Introduction

The physical and chemical properties exhibited by nanomaterials strongly depend on their internal crystal structure as well as morphology [1–3]. This is quite discernible in the case of metals. For example, inherent properties like plasmonic absorption can be morphology-dependent [4–6]. Au catalyst nanoparticles at the tips of Ge nanowires, for instance, exhibit different plasmonic features depending on the lattice type, hcp or fcc [7]. Ag nanorods grown in unconventional 4H phase exhibit Raman active modes which are otherwise inactive in the conventional fcc lattice [8].

Bulk Au crystallizes in fcc lattice and under extreme conditions, it can be stabilized in hcp (under high pressure) [9] and bcc (shock compression) [10,11] lattices. So far, very few literature report the ambient stable Au nanostructures away from conventional fcc lattice, for instance, 2H Au nanocrystallites [12,13]/nanosheets [14]/nanoplates [15,16]/nanorods [17,18]

/tadpole-shaped nanowires [19], 4H Au nanoribbons [20]/nanowires [21]/nanokites [22], multi-phased Au nanowires (2H, 4H, 6H and 8H) [23], bct Au nanocrystal [24] and Au microcrystals consisting non-cubic (bc(o,t)) lattices [25]. The different shapes and the polymorphs have been mostly synthesized by wet chemical processes, except the bct Au nanocrystal (under mechanical deformation) [24].

Most wet chemical syntheses are done in the liquid medium and the recent progress in liquid phase TEM allows to visualize and study single crystallite in great detail [26]. However, the intricacy involved with the TEM technique does not make it user friendly and thus, not very suitable for single crystallite microscopy studies on a routine basis. In solution-based synthesis, often the surface of the crystallites is coated by surfactant and thereby studying their properties and applications has become cumbersome, cost effective and involved in order to make the surfaces free. In contrast, the bc(o,t) crystallites have been prepared based on a solid-state synthetic route and are free from capping agents. The growth of the crystallite is easy to monitor at an individual crystallite level over the reaction period [25], similar to the growth of Au microplates (a solid-state reaction) monitored *via ex-situ* [27,28].

The Au microcrystallites hosting bc(o,t) lattices have been prepared earlier in this laboratory by thermolyzing the metal-organic precursor at 220 °C in air [25,29]. The as-synthesized crystallites consist of bipyramids, tetrahexahedral, hexagram and other shaped particles, while the bipyramids contribute to be the major (see **Figure III.1**a–e). The geometrical constraints induced by the penta-twinned geometry in the bipyramid induce stresses (within the elastic regime ($< 2\%$) as calculated theoretically) [25] which enhances with increasing crystal size. This would be contradictory to the commonly known nano size effect wherein bigger sizes exhibit lesser strain and hence tend to resist non-native lattices. Thus, the thermolysis temperature plays a crucial role in the stabilization of the bc(o,t) lattices as well as in the size of the crystallite. For example, thermolysis at lower temperatures (~ 150 °C) results in longer bipyramids (~ 8 µm) with a slow kinetics whereas at higher temperatures (~ 500 °C) small crystallites prevail due to fast kinetics [25,30]. The generated stresses can be accommodated by the slow kinetics and thereby, major contribution is from fcc. Again, fast kinetics at higher temperatures is capable to anneal the stresses and thereby the major product is yet again fcc. On the other hand, annealing at ~ 200 °C provides an optimized kinetics window, where the thermal annealing appears ineffectual while the growth is fast enough

thereby maintaining the strain in the form of non-fcc phases [25]. The bc(o,t) fraction in a collection of crystallites has been maximized as high as 85% of the total. The crystallites are stable under ambient and e-beam conditions. Although, the bc(o,t) phases experience irreversible and reversible phase transformations to fcc while annealing at ~ 700 °C and high pressure (~ 40 GPa), respectively. Therefore, the stability of the crystallites in the metastable phases is remarkable! Interestingly, the bc(o,t) phases exhibit different behavior in terms of catalytic property, which act as a better catalyst in a reduction reaction in comparison with fcc Au even when size is at the micro-scale [29].

III.2 Scope of the Investigation

The recipe already reported by the group provides maximum of non-cubic lattices (~ 85% mole fraction of the total) in a collection of crystallites. However, the recipe suffers from reproducibility, scalability and sensitivity to the working temperatures. The nucleation followed by the growth of the crystallites are solid-state reactions and thus, the interaction of the precursor with the substrate including the uniform dispersal of it decide the fate of the non-cubic mole fraction. Hence, most of the problems are encountered due to the wettability of the precursor on the surface of the substrate. Given these drawbacks, the chapter attempts to address some of the above mentioned points, for example, maximization of non-cubic lattices with high degree of reproducibility and scalability with tunable working temperatures.

III.3 Experimental Details

Chemicals. Hydrogen tetrachloroaurate-(III) hydrate ($HAuCl_4 \cdot 3H_2O$, min assay ~ 49%), tetraoctylammonium bromide (ToABr, 99%), and silver nitrate ($AgNO_3$, 99.9%) were bought from Spectrochem, India, and used without any purification. Aqueous ammonia (aq. NH_3, 25%), toluene (99.5%) and hydrochloric acid (35-38%) were purchased from SD Fine Chemicals, India. All reagents and solvents were used as received without further purification. Double-distilled water was used throughout this investigation.

Synthesis of AuAgToABr. Synthesis of Au microcrystallites was done by following previous literature [29]. Briefly 300 μL of 50 mM ToABr (in toluene) was added to 75 μL of $HAuCl_4$ (25 mM) and 25 μL of $AgNO_3$ (25 mM). The reaction mixture was kept for 40 min to facilitate the phase transfer of Ag(I) and Au(III) ions to the organic layer. The resultant organic layer is termed as AuAgToABr.

Thermal decomposition of AuAgToABr precursor at 220 °C fixed temperature (without any ramping) in the ambient resulted in Au microcrystallites. The as-prepared crystallites were washed with toluene followed by aq. ammonia to remove the unreacted precursors and any contaminations arising from Ag (such as AgBr) following a previous report from the group [25] as also shown schematically in **Figure III.1**a.

Synthesis of AuToABr. 300 μL of 50 mM ToABr (in toluene) was added to 100 μL of 25 mM $HAuCl_4$ and stirred for 5 min to facilitate the phase transfer of Au(III) ions to the organic layer. The organic layer develops a red color, and the organic layer is termed as AuToABr. Thermolysis of AuToABr at 250 °C resulted in Au microplates. The as-synthesized microplates were cleaned by toluene to remove the residual of the precursor.

Synthesis of AuAgToABr in presence of HCl. The reaction composition has been little modified and used throughout the thesis. Briefly, 300 μL of 50 mM ToABr, 75 μL of 25 mM $HAuCl_4$ and 30 μL of 25 mM $AgNO_3$ were added and left to stir for 5 min followed by addition of 100 μL of 35% (v/v) HCl to the mixture totaling the stir time to be 20 min. The resultant organic layer is named as AuAgToABr + HCl.

Addition of HCl was varied systematically by varying the (Au(III)+Ag(I))/HCl (v/v) ratio. Thermal decomposition of the AuAgToABr + HCl precursor at various temperatures was performed and resulted microcrystallites were washed similarly, as in before.

III.4 Results and Discussion

Au microcrystallites in bc(o,t) lattices were prepared by thermolyzing AuAgToABr precursor at ~ 220 °C, where the precursor is made by simultaneous phase transformation of aqueous Au(III) and Ag(I) ions into the organic toluene medium with the help of phase transferring agent, tetraoctylammonium bromide (ToABr). The as-synthesized crystallites were washed with toluene followed by aq. NH_3 to remove the unreacted precursor and the contaminations from Ag, respectively as shown in **Figure III.1**a. The bipyramids are ~ 3 μm in length and ~ 500 nm in width hosting high index facets indexable to {0kl} where the k, l ≥ 2. X-ray diffraction (XRD) pattern collected from the collection of crystallites exhibits a broad peak ~ 38.3° (see **Figure III.1**f) which can be assigned as the contributions arising from $(111)_C$, $(101)_O$, $(101)_T$ and $(011)_O$ while at ~ 44.5° in addition to $(002)_C$, a well separated peak assignable to $(002)_T$ and $(002)_O$ is identified (**Figure III.1**g). The area under the peaks have

been taken in consideration for the calculation of bc(o,t) lattices mole fractions, such as bco ~ 50% and bct ~ 35%.
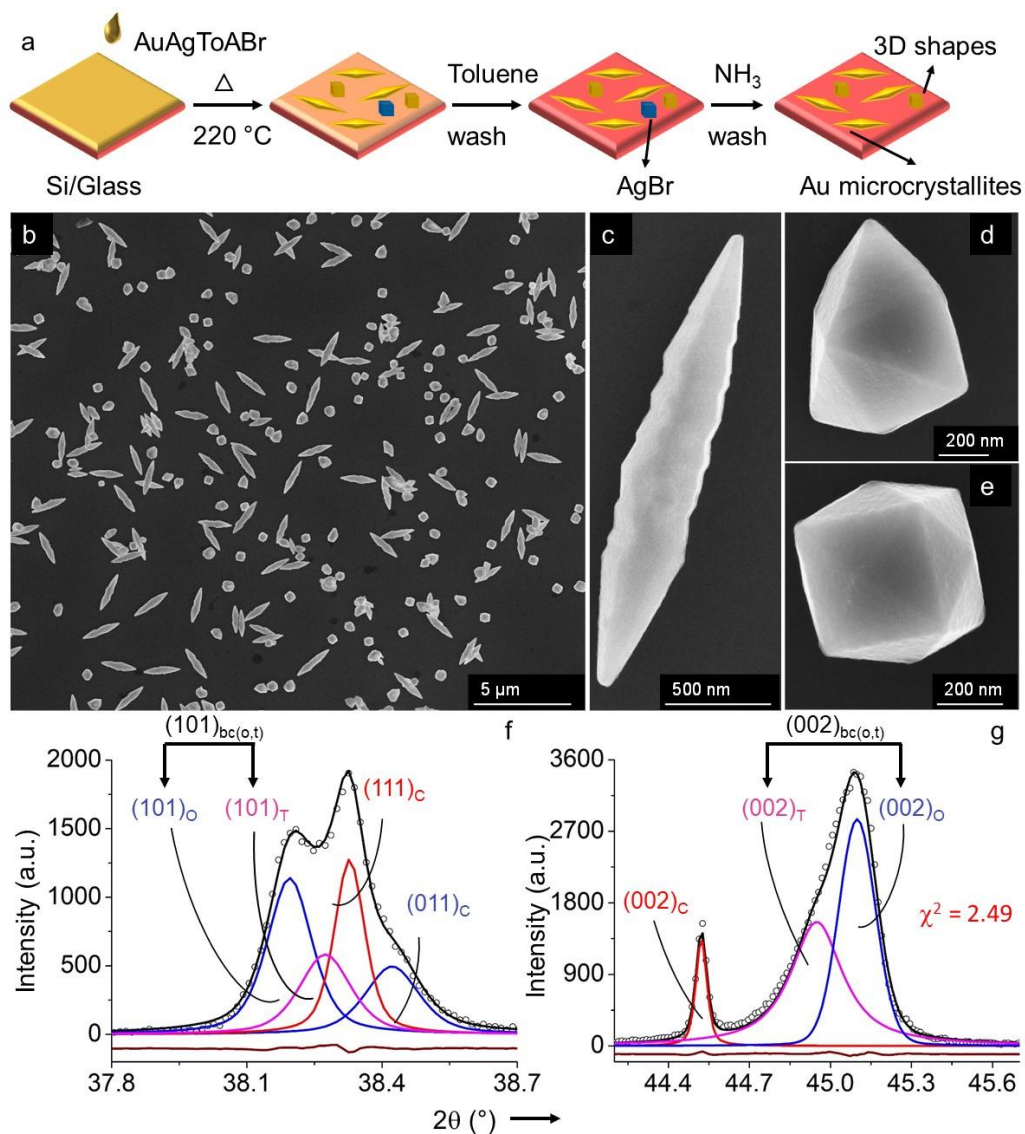
Figure III.1. (a) Schematic representation of the synthesis process where the Au(III) and Ag(I) ions are stabilized by ToABr in toluene (named as AuAgToABr). (b) Low magnified SEM image of the grown bc(o,t) Au microcrystallites. (c–e) High magnified SEM images of the Au bipyramid, hexagram and tetrahexahedral, respectively. (f–g) Le Bail fitting of the collected X-ray diffraction (XRD) pattern of pristine 85% bc(o,t) Au microcrystallites with space group of *Fm-3m* for fcc, *I4/mmm* for bct and *Immm* for bco. Black (circle), black (solid line), red, blue and pink color curves represent experimental, fitted, fcc (represented as C), bco (O) and bct (T) phases, respectively. Brown color curve corresponds to residual (experimental-calculated). The residual curve intensity has been shifted to -100 a.u. for better clarity. The χ^2 for combinations of fcc, bct and bco is 2.49.

Ag(I) ions are known to be a shape-directing agent and consequently, control the morphology of the crystallite. Surprisingly, the concentration of the Ag(I) ions also narrates the contribution of the lattices in the synthesized microcrystallite. For example, at an optimized Ag/Au ratio (0.34), the contribution of the non-cubic lattices can be maximized to as high as 85% of the total, whereas at lower and higher ratios, the mole fractions are much deviated from 85% [29]. Additionally, the thermolysis temperature dictates the existence of the bc(o,t) lattices, being optimum at ~ 220 °C [25], as discussed in section **III.1**. Micro-XRD data collected from a collection of crystallites confirm the presence of bc(o,t) lattices on bipyramids, tetrahexahedrals and hexagrams while the former contributes to be the major [29]. Therefore, maximization of the bc(o,t) lattices proportion tends to relate with the maximization of the bipyramids quantity.

In order to shade light upon the issues, a thorough literature survey was done. Few literature reports discuss the role of pH on the high throughput growth of Au penta-twinned bipyramids [31]. Accordingly, excess HCl (*i.e.*, M/HCl (v/v) is 0.105) was added to the AuAgToABr precursor during the phase transferring process and the resultant organic part (phase transferred) was thermolyzed at 250 °C. Surprisingly, the XRD pattern is no longer similar to the AuAgToABr decomposed pattern. Therefore for ready reference, XRD patterns which are collected from the thermolysis (at 250 °C) of different precursor compositions, such as AuToABr, AuAgToABr and AuAgToABr + excess HCl are shown in **Figure III.2**, where the resultant patterns are (111), (002) and (111) oriented, respectively. The increasing surface energy sequence for various facets of Au is as follows (111) < (001) < (110). Hence, the decomposition of the AuToABr precursor facilitates the highly favorable (111) [27], whereas, the presence of Ag(I), a shape-directing agent, favors the fate of the energetically expensive (001) facets, and thereby stabilizes the (002) facets in few µms long bipyramids, which is otherwise difficult to achieve [30]. Interestingly, addition of HCl provides a (111) oriented XRD pattern, very similar to the AuToABr decomposed pattern. Thus, the effect of Ag(I) is overruled by the addition of HCl while the orientation is altered from (002) to (111). The ratios of (111)/(002) for the different patterns are shown, which show that the addition of HCl enhances the (111) orientation with (111)/(002) ratio of ~ 210. The FWHM of the $(111)_f$ and $(002)_f$ peaks are 0.059° and 0.083° for AuAgToABr + excess HCl precursor in comparison to

0.041° and 0.051° for AuToABr, respectively. As a result, the addition of HCl increases disorder.
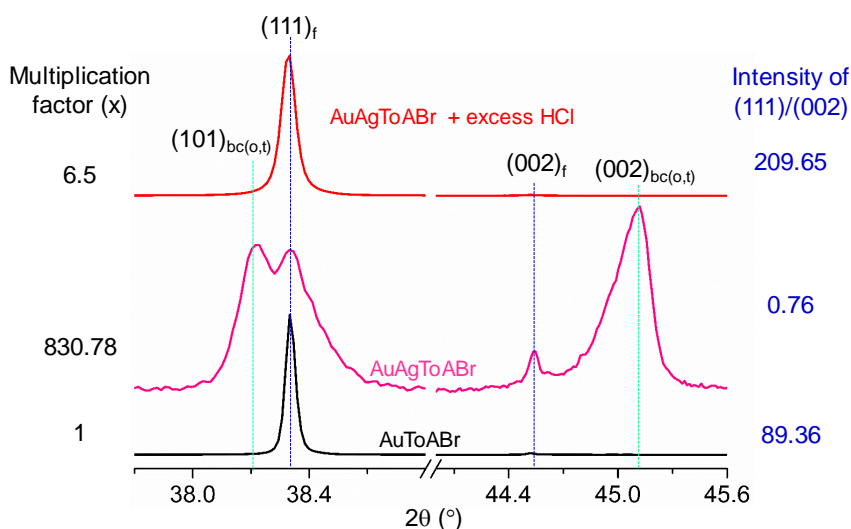
Figure III.2. XRD patterns of the Au microcrystallites prepared by thermolysis of different precursors at 250 °C such as AuToABr, AuAgToABr and AuAgToABr + excess HCl. The XRD patterns have been normalized with respect to $(111)_f$ intensity of the AuToABr by a multiplication factor (shown at the left). The ratios of $(111)/(002)$ intensities have been presented at the right. For bc(o,t), (002) intensity refers to the $(002)_{bc(o,t)}$ region. The $(111)/(002)$ ratio exhibiting a value much different from conventional Au reveals the alteration in the exposed facets, for example, the ratio being 89.36 indicates anisotropy (the exposed facets are (111)). f represents fcc.

In order to understand the (111) oriented XRD pattern of the HCl added precursor, the crystallites morphology was examined by scanning electron microscopy (SEM), as shown in **Figure III.3**. Thermolysis of AuToABr majorly generates micro-plates with small proportions of other shaped crystallites, while the thermolysis of the HCl-added AuAgToABr results in microplates and small crystallites, where the latter is mainly consisted of decahedrons. Thus, it may be noted that here, the primary contribution comes from the decahedrons and plates in contrast to the majorly observed plates in case of AuToABr. The decahedrons prepared by the addition of excess HCl are ~ few µms in size (see **Figure III.3**g–i) but interestingly, not in the form of bipyramids.

The energetics of various facets favor the (111) oriented decahedron morphology, however, the growth of (002) oriented bipyramids starting with decahedron nuclei is favored by addition of Ag(I) (see **Figure III.4**). Thus in presence of HCl (in excess quantity), the effect

of Ag(I) in stabilization of the {001} facets is blocked and thereby ~ 1: 1 ratio of plates and decahedrons is achieved in contrast to majorly bipyramids in AuAgToABr (derived from decahedrons). The growth of bipyramid from a decahedron nucleus in the presence of Ag(I) is longitudinally along the <110> direction and thereby maintains the width ~ half a μm (**Figure III.4**d). In contrast, the growth of the decahedrons is along <112> direction which eventually results in the μm sized decahedrons. This observation again emphasizes the role of the Ag(I) in the growth of bipyramids followed by the high index corrugated facets.
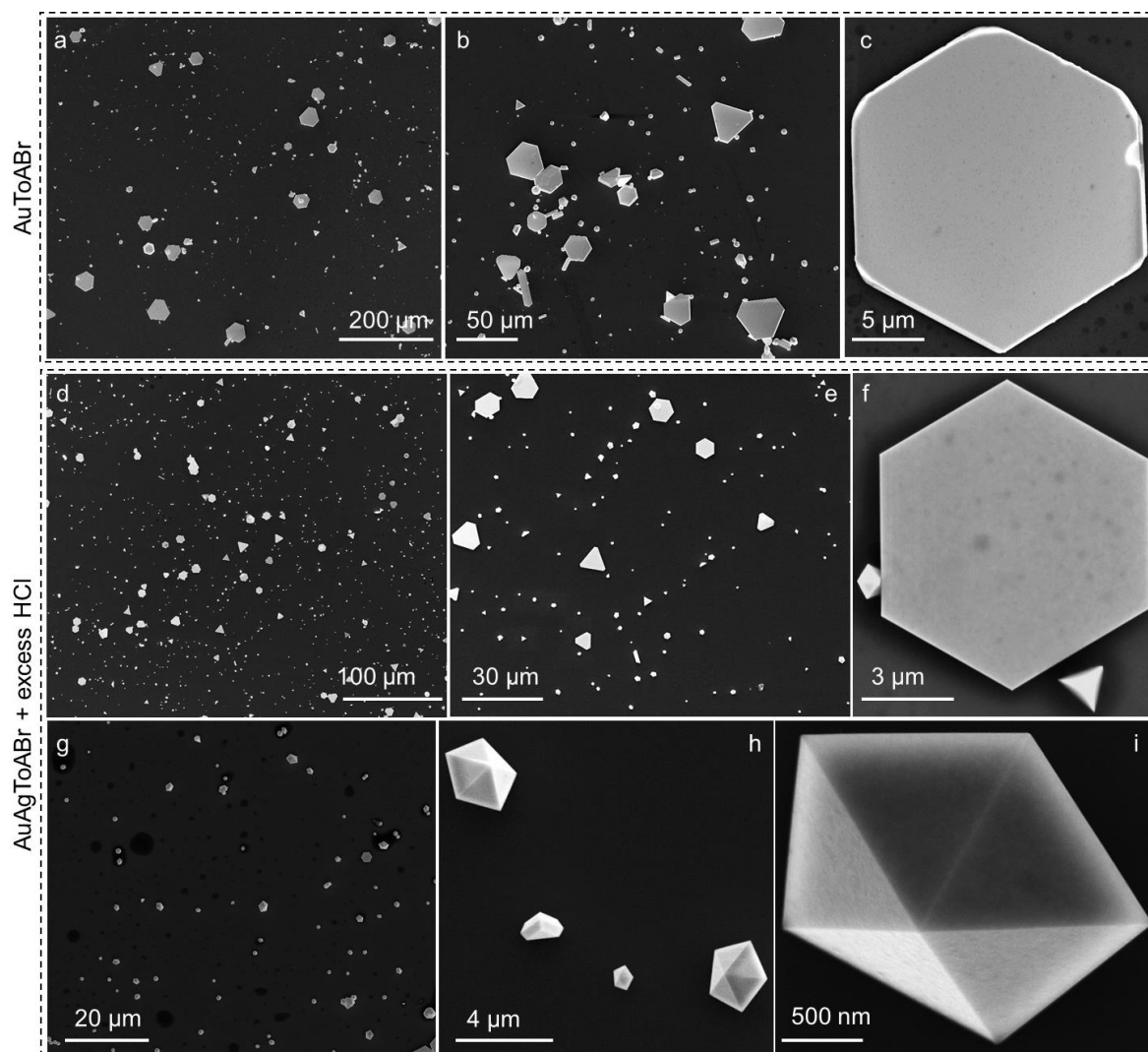
Figure III.3. SEM images of Au microcrystallites prepared by thermolyzing AuToABr (a−c) and AuAgToABr + excess HCl (d−i) at 250 °C. Thermolysis of AuToABr results in majorly Au microplates (mainly ~ 50 μm) while the latter precursor results in plates and decahedrons. In the AuAgToABr + excess HCl precursor, the decahedrons are ~ μm long. Thus, the addition of HCl shows the effect of Ag(I) and thermolysis of AuToABr.

Thus, a knowledge about the addition of HCl in the precursor is gained which can be implemented to tune the length and proportion of the bipyramids. The presence of Au plate and decahedron (see **Figure III.3**d–i) explains the enhanced (111)/(002) ratio which attributes to the presence of exposed 2 and 10 (111) facets, respectively. The occurrences of defects in the decahedrons in the form of twin boundaries cause the reduction in the total count of the XRD pattern (in **Figure III.2**) with overall broadening. These observations can be linked with the literature report discussing the effect of low pH resulting in decahedrons [31]. The addition of HCl results in enriching the proportion of plates and large decahedrons which can be understood considering the role of Cl⁻ in oxidative etching to dissolve the multiply-twinned structures [32] and favoring the formation of large (111) oriented plates [33]. Additionally, the literature reports demonstrate the superior role of HCl over NaCl/KCl in oxidative etching [34].
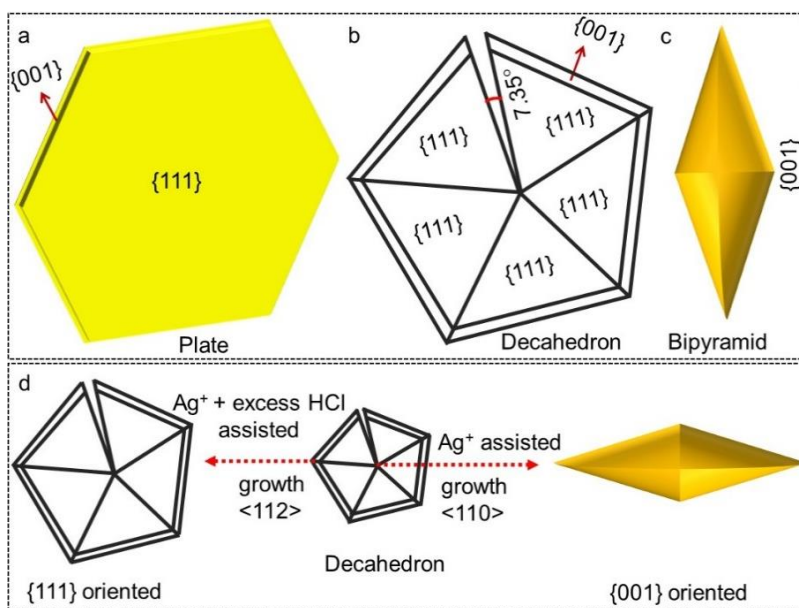
Figure III.4. (a–c) Schematic representation of the Au plate, decahedron and bipyramid exposing mainly {111} and {001} facets, *i.e.*, anisotropic morphologies. Thus, in **Figure III.2**, {111}/{001} ratio is very high for excess HCl-added precursor due to the presence of highly {111} oriented plates and decahedrons, where the latter consists of 10 {111} facets with {001} side facets which are very thin. In case of AuToABr, although the plates are major in contribution, however, the other shaped crystallites are also in good proportions exposing other facets. In case of bipyramids, the anisotropic 1-D morphology exhibits the {001} facets by the growth along {110} direction while retaining the 10 {111} facets only at the tips. Thus, the anisotropic morphology causes the suppression of the

{111}/{002} ratio. (d) Schematic representation of the growth of large decahedral/bipyramid from the decahedron nucleus. If, the growth is along the <110> direction *i.e.*, along the 5-fold apex, results in bipyramids whereas growth along the <112> direction *i.e.*, along the corners, results in large decahedra while exposing mainly the 10 {111} facets.
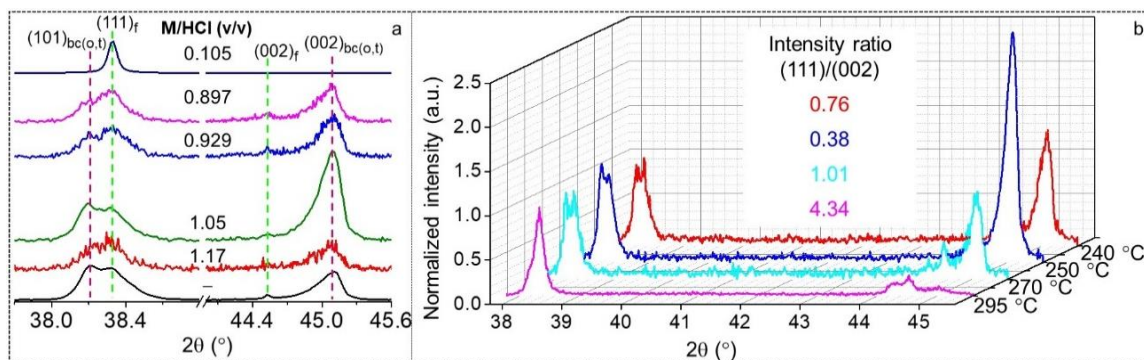
Figure III.5. (a) XRD patterns of the Au microcrystallites collected from thermolysis of various precursor compositions at 250 °C. (b) XRD patterns of the Au microcrystallites collected from thermolysis of the precursor with M/HCl (v/v) ratio of 1.05 at various thermolysis temperatures. The intensities have been normalized with respect to (111)$_f$. Thermolysis of the precursor at 250 °C results a XRD pattern with (111)/(002) ratio of 0.38, highlighting the highly (002) orientation. Note in clear contrast to the conventional fcc, the intensity in the region of (111)$_f$ is rather less compared to that at the (002) region. During optimization of the growth conditions the domination of the (002) region thus provides a hint for the emerging non-cubic lattices.

Hence, a controlled addition of HCl in the precursor composition is surveyed as shown in **Figure III.5**a. One of the main parameters for a higher bc(o,t) fraction is the wetting behavior of the precursor on the Si substrate, considering the synthesis of the crystallite is a solid-state reaction. Thus, systematic variation of the M/HCl (v/v) ratio in the precursor composition and followed by thermolysis at 250 °C result in the control of tuning the proportion of the bc(o,t) lattices *via* enhanced dispersion of the precursor in the substrate. For instance, at a ratio of ~ 1.05, the contribution from the bc(o,t) lattices is maximum (with Ag/Au (v/v) ~ 0.4 and M/ToABr (v/v) ~ 0.35). Therefore, the composition is locked and the temperature is varied systematically as shown in **Figure III.5**b. Thermolysis of the precursor at 250 °C results in a XRD pattern with (111)/(002) ratio of 0.38, while at higher or lower temperatures the patterns do not excel a lower (111)/(002) ratio and thus, the 250 °C temperature has been considered as ideal. The Le Bail fitting of the collected XRD pattern confirms the presence of fcc, bct and bco lattices with lattice parameters of

$a = b = c = 4.0810$ Å (for fcc); $a = b = 2.9062$ Å and $c = 4.0450$ Å (bct); $a = 2.9184$ Å, $b = 2.8931$ Å and $c = 4.0315$ Å (bco) similar to the previous report *i.e.*, 85% bc(o,t) [29] as shown in **Figure III.6**. In contrary to a conventional preparation, where the fcc Au exhibits a (111)/(002) ratio of > 1, however, here the ratio is 0.38. In a collection of preparation, among various shapes, bipyramids are the major along with the tetrahexahedral as shown in **Figures III.7–III.9**. However, the presence of hexagram and other irregular shaped particles has been suppressed in the total crystallites strength. The bipyramids comprise of corrugated surfaces indexable to {0kl} where k, l ≥ 2 and penta-twinned tips (see **Figure III.7**c). The bipyramids are ~ 3 μm in length and ~ 200-500 nm in width. The bc(o,t) proportions are quantified and found to be ~ 90-92% (see **Figure III.7**).
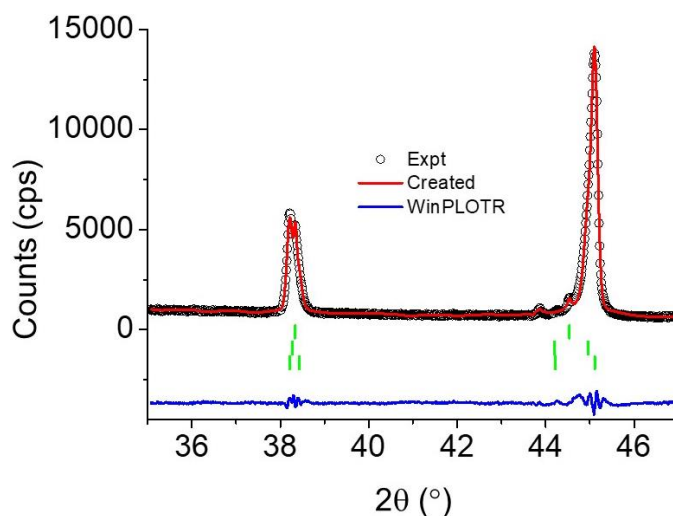
Figure III.6. Le Bail fitting of the XRD pattern (collected from the modified precursor composition and thermolysed at 250 °C) with a combination of fcc (space group *Fm-3m*), bct (*I4/mmm*) and bco (*Immm*) lattices. The black circle curve represents the experimental data, whereas the red is the fitted and their residual is shown in blue line. The Bragg positions have been shown by green vertical line.

Thus, the final reaction composition is slightly modified from the earlier report by the group and used throughout the thesis. Briefly, 300 μL of 50 mM ToABr, 75 μL of 25 mM $HAuCL_4$ and 30 μL of 25 mM $AgNO_3$ were added and left to stir for 5 min. In this concoction, 100 μL of 35% (v/v) HCl was added and again allowed to stir for 15 min. Finally, the phase transferred Au(III) and Ag(I) ions at the organic toluene medium were separated (termed as AuAgToABr + HCl) and used immediately. Thermolysis of AuAgToABr + HCl precursor at 250 °C in the ambient for 30 s outcomes in Au microcrystallites hosting non-cubic lattices with

maximum proportion ~ 92% of the total volume with large reproducibility (~ 90%) as shown in **Figure III.10**.
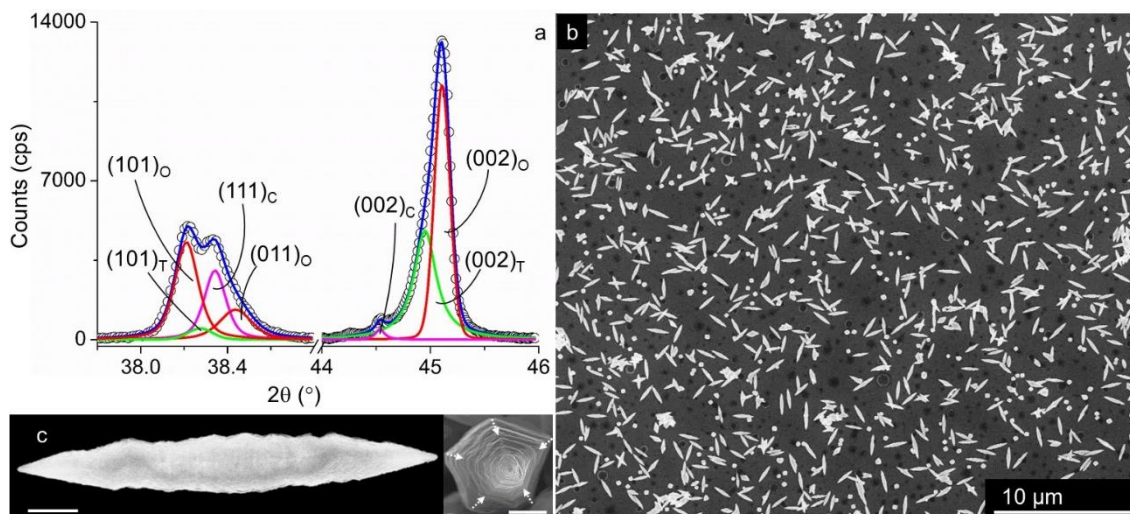
Figure III.7. Characterization of the crystallites prepared by the modified precursor at 250 °C. (a) XRD pattern of the crystallites exhibiting a (002) orientation. SEM images of (b) Au microcrystallites and (c) a bipyramid. In this synthetic process, bipyramid is a major product. Inset shows the magnified view of the tip in the tilted view. Arrows show the twin boundaries. Scale bar, 400 nm.

Addition of HCl increases the working temperature window from 220 °C to 250 °C with a small reaction completion time, 30 sec. This is in agreement with the literature reports which discuss the role of HCl-added precursor in slowing down the reaction kinetics [35]. Thus, the working temperature can be increased, while retaining the thermolysis kinetics in the similar order as observed at ~ 220 °C in the previously reported studies from the group [25]. Instead of $AgNO_3$ and HCl, addition of AgCl also leads to the growth of non-cubic lattices though the proportion does not exceed above ~ 80%. Therefore, further systematic addition of AgCl is not carried forward. Although the presence of Cl^- is crucial for the growth of bc(o,t) (since replacing the halide ions alters fraction of bc(o,t) lattices [25]), the concentration of H^+ *i.e.*, pH also plays a role.

In the literature reports, the effect of pH has been studied, importantly, a half unit change in pH refers to 10-fold increment in the reactant concentration [31]. It was reported, at low pH, spheroid shaped Au crystallite formed whereas at moderate pH Au bipyramids. Considering this point into account, at a moderate HCl addition, M/HCl (v/v) ~ 1.05, bipyramids proportion increases to ~ 72% (from 58%) as shown in **Figure III.9**. Whereas, at

M/HCl ~ 0.105, decahedra and plate form. The addition of excess HCl, *i.e.*, very low pH refers to the deformation from bipyramids. The ToABr stabilizes large sized Au microplates. Similar understanding can be taken into account for the stabilization of large sized decahedra, which at the beginning form at the assistance of Ag(I).
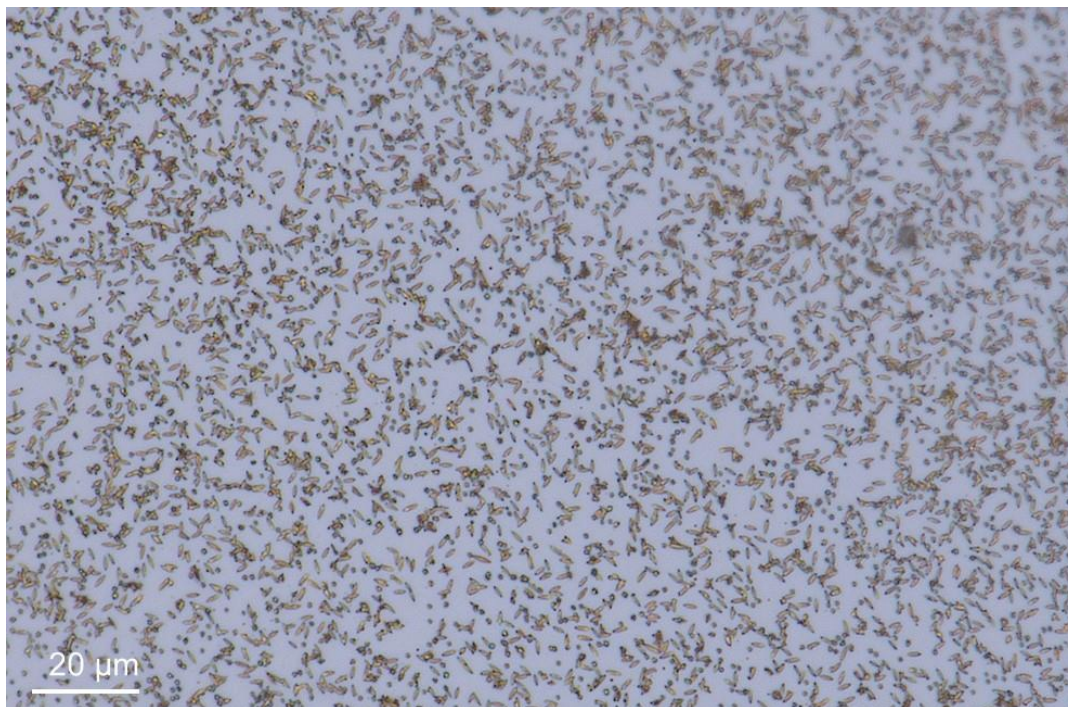
Figure III.8. Optical micrograph of the Au microcrystallites prepared using the modified precursor at 250 °C.
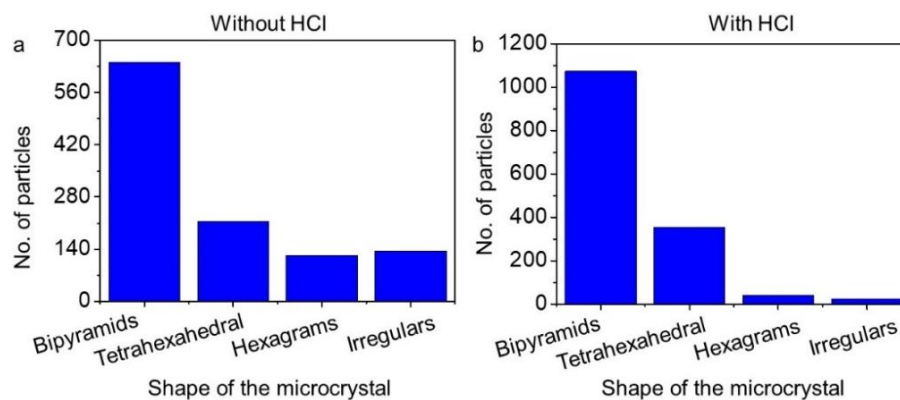
Figure III.9. Distribution of different shapes of crystallites obtained from varying the precursor compositions, (a) without and (b) with HCl.

The working size of the substrate can be increased from (5×5) mm^2 to (2×2) cm^2 while unaltering the precursor composition with bc(o,t) fraction of ~ 80%.
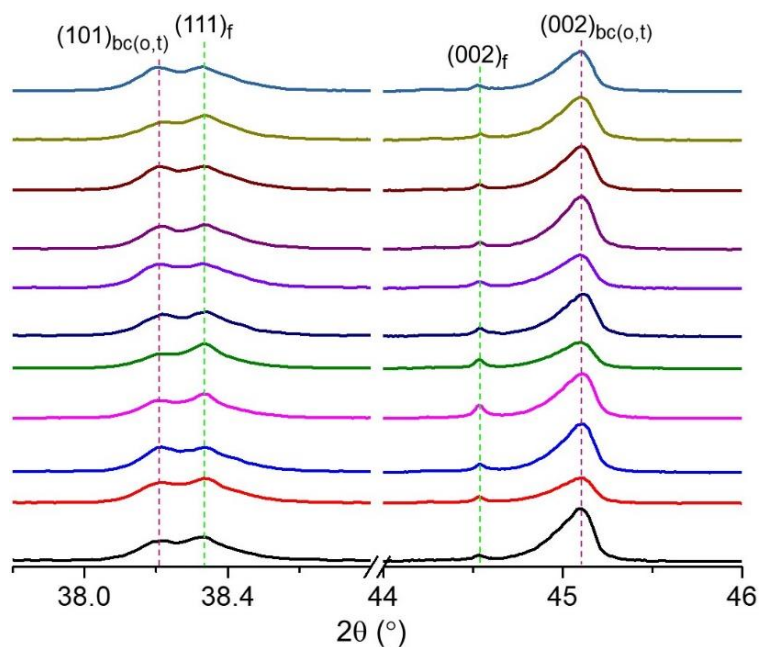
Figure III.10. XRD patterns of the Au microcrystallites prepared at 250 °C and the M/HCl (v/v) ratio of 1.05.

III.5 Conclusion

In summary, the precursor composition has been modified by introducing HCl during the preparation of reaction concoction. By adding HCl in excess (M/HCl (v/v) ~ 0.105), the growth of bipyramids can be hindered and instead, the growth of thermodynamically unfavorable large sized (~ few µms) decahedra is facilitated, as the growth direction changes from <011> to <112>. With HCl addition in moderation, M/HCl (v/v) ~ 1.05, the thermolysis led to higher population of the bipyramids and also a higher bc(o,t) mole fraction (~ 90-92%). This was quite reproducible. The interplay between HCl slowing down the reduction kinetics while the thermolysis temperature is being increased seem to play a key role in guiding the crystallite growth, an aspect which deserves a separate study.

References

[1]   H. Cheng, N. Yang, Q. Lu, Z. Zhang, and H. Zhang, *Syntheses and Properties of Metal Nanomaterials with Novel Crystal Phases*, Adv. Mater. **30**, 1707189 (2018).

[2]   Y. Chen, Z. Lai, X. Zhang, Z. Fan, Q. He, C. Tan, and H. Zhang, *Phase Engineering of Nanomaterials*, Nat. Rev. Chem. **4**, 243 (2020).

[3]   M. Zhao and Y. Xia, *Crystal-Phase and Surface-Structure Engineering of Ruthenium Nanocrystals*, Nat. Rev. Mater. **5**, 440 (2020).

[4]   K. G. Thomas, S. Barazzouk, B. I. Ipe, S. T. S. Joseph, and P. V. Kamat, *Uniaxial Plasmon Coupling through Longitudinal Self-Assembly of Gold Nanorods*, J. Phys. Chem. B **108**, 13066 (2004).

[5]   P. Pramod and K. G. Thomas, *Plasmon Coupling in Dimers of Au Nanorods*, Adv. Mater. **20**, 4300 (2008).

[6]   K. S. Krishna, C. S. S. Sandeep, R. Philip, and M. Eswaramoorthy, *Mixing Does the Magic: A Rapid Synthesis of High Surface Area Noble Metal Nanosponges Showing Broadband Nonlinear Optical Response*, ACS Nano **4**, 2681 (2010).

[7]   S. Peng, A. C. Meng, M. R. Braun, A. F. Marshall, and P. C. McIntyre, *Plasmons and Inter-Band Transitions of Hexagonal Close Packed Gold Nanoparticles*, Appl. Phys. Lett. **115**, 051107 (2019).

[8]   I. Chakraborty, S. N. Shirodkar, S. Gohil, U. V. Waghmare, and P. Ayyub, *A Stable, Quasi-2D Modification of Silver: Optical, Electronic, Vibrational and Mechanical Properties, and First Principles Calculations*, J. Phys. Condens. Matter **26**, 025402 (2014).

[9]   L. Dubrovinsky, N. Dubrovinskaia, W. A. Crichton, A. S. Mikhaylushkin, S. I. Simak, I. A. Abrikosov, J. S. De Almeida, R. Ahuja, W. Luo, and B. Johansson, *Noblest of All Metals Is Structurally Unstable at High Pressure*, Phys. Rev. Lett. **98**, 045503 (2007).

[10] S. M. Sharma, S. J. Turneaure, J. M. Winey, Y. Li, P. Rigg, A. Schuman, N. Sinclair, Y. Toyoda, X. Wang, N. Weir, J. Zhang, and Y. M. Gupta, *Structural Transformation and Melting in Gold Shock Compressed to 355 GPa*, Phys. Rev. Lett. **123**, 45702 (2019).

[11] R. Briggs, F. Coppari, M. G. Gorman, R. F. Smith, S. J. Tracy, A. L. Coleman, A. Fernandez-Pañella, M. Millot, J. H. Eggert, and D. E. Fratanduono, *Measurement of Body-Centered Cubic Gold and Melting under Shock Compression*, Phys. Rev. Lett. **123**, 45701 (2019).

[12] B. R. Jany, N. Gauquelin, T. Willhammar, M. Nikiel, K. H. W. Van Den Bos, A. Janas, K. Szajna, J. Verbeeck, S. Van Aert, G. Van Tendeloo, and F. Krok, *Controlled Growth of Hexagonal Gold Nanostructures during Thermally Induced Self-Assembling on Ge(001) Surface*, Sci. Rep. **7**, 42420 (2017).

[13] A. F. Marshall, I. A. Goldthorpe, H. Adhikari, M. Koto, Y.-C. Wang, L. Fu, E. Olsson, and P. C. McIntyre, *Hexagonal Close-Packed Structure of Au Nanocatalysts Solidified after Ge Nanowire Vapor-Liquid-Solid Growth*, Nano Lett. **10**, 3302 (2010).

[14] X. Huang, S. Li, Y. Huang, S. Wu, X. Zhou, S. Li, C. L. Gan, F. Boey, C. A. Mirkin, and H. Zhang, *Synthesis of Hexagonal Close-Packed Gold Nanostructures*, Nat. Commun. **2**, 292 (2011).

[15] D. Huo, Z. Cao, J. Li, M. Xie, J. Tao, and Y. Xia, *Seed-Mediated Growth of Au Nanospheres into Hexagonal Stars and the Emergence of a Hexagonal Close-Packed Phase*, Nano Lett. **19**, 3115 (2019).

[16] X. Huang, H. Li, S. Li, S. Wu, F. Boey, J. Ma, and H. Zhang, *Synthesis of Gold Square-like Plates from Ultrathin Gold Square Sheets: The Evolution of Structure Phase and*

Shape, Angew. Chem. Int. Ed. **50**, 12245 (2011).

[17]   S. Lee, C. Bae, J. Lee, S. Lee, S. H. Oh, J. Kim, G. S. Park, H. S. Jung, and H. Shin, *Fabrication of a Stable New Polymorph Gold Nanowire with Sixfold Rotational Symmetry*, Adv. Mater. **30**, 1706261 (2018).

[18]   Z. Fan, M. Bosman, Z. Huang, Y. Chen, C. Ling, L. Wu, Y. A. Akimov, R. Laskowski, B. Chen, P. Ercius, J. Zhang, X. Qi, M. H. Goh, Y. Ge, Z. Zhang, W. Niu, J. Wang, H. Zheng, and H. Zhang, *Heterophase fcc-2H-fcc Gold Nanorods*, Nat. Commun. **11**, 3293 (2020).

[19]   X. Huang, S. Li, S. Wu, Y. Huang, F. Boey, C. L. Gan, and H. Zhang, *Graphene Oxide-Templated Synthesis of Ultrathin or Tadpole-Shaped Au Nanowires with Alternating Hcp and Fcc Domains*, Adv. Mater. **24**, 979 (2012).

[20]   Z. Fan, M. Bosman, X. Huang, D. Huang, Y. Yu, K. P. Ong, Y. A. Akimov, L. Wu, B. Li, J. Wu, Y. Huang, Q. Liu, C. Eng Png, C. Lip Gan, P. Yang, and H. Zhang, *Stabilization of 4H Hexagonal Phase in Gold Nanoribbons*, Nat. Commun. **6**, 7684 (2015).

[21]   Q. Wang, Z. L. Zhao, C. Cai, H. Li, and M. Gu, *Ultra-Stable 4H-Gold Nanowires up to 800 °C in a Vacuum*, J. Mater. Chem. A **7**, 23812 (2019).

[22]   W. Niu, J. Liu, J. Huang, B. Chen, Q. He, A.-L. Wang, Q. Lu, Y. Chen, Q. Yun, J. Wang, C. Li, Y. Huang, Z. Lai, Z. Fan, X.-J. Wu, and H. Zhang, *Unusual 4H-Phase Twinned Noble Metal Nanokites*, Nat. Commun. **10**, 2881 (2019).

[23]   C. Wang, X. Li, L. Jin, P.-H. Lu, C. Dejoie, W. Zhu, Z. Wang, W. Bi, R. E. Dunin-Borkowski, K. Chen, and M. Jin, *Etching-Assisted Route to Heterophase Au Nanowires with Multiple Types of Active Surface Sites for Silane Oxidation*, Nano Lett. **19**, 6363 (2019).

[24]   H. Zheng, A. Cao, C. R. Weinberger, J. Y. Huang, K. Du, J. Wang, Y. Ma, Y. Xia, and S. X. Mao, *Discrete Plasticity in Sub-10-Nm-Sized Gold Crystals*, Nat. Commun. **1**, 144 (2010).

[25]   G. Mettela, M. Bhogra, U. V. Waghmare, and G. U. Kulkarni, *Ambient Stable Tetragonal and Orthorhombic Phases in Penta-Twinned Bipyramidal Au Microcrystals*, J. Am. Chem. Soc. **137**, 3024 (2015).

[26]   J. M. Yuk, J. Park, P. Ercius, K. Kim, D. J. Hellebusch, M. F. Crommie, J. Y. Lee, A. Zettl, and A. P. Alivisatos, *High-Resolution EM of Colloidal Nanocrystal Growth Using Graphene Liquid Cells*, Science **336**, 61 (2012).

[27]   B. Radha, M. Arif, R. Datta, T. K. Kundu, and G. U. Kulkarni, *Movable Au Microplates as Fluorescence Enhancing Substrates for Live Cells*, Nano Res. **3**, 738 (2010).

[28]   B. Radha and G. U. Kulkarni, *A Real Time Microscopy Study of the Growth of Giant Au Microplates*, Cryst. Growth Des. **11**, 320 (2011).

[29]   G. Mettela, N. Mammen, J. Joardar, S. Narasimhan, and G. U. Kulkarni, *Non-Fcc Rich Au Crystallites Exhibiting Unusual Catalytic Activity*, Nano Res. **10**, 2271 (2017).

[30] G. Mettela, R. Boya, D. Singh, G. V. P. Kumar, and G. U. Kulkarni, *Highly Tapered Pentagonal Bipyramidal Au Microcrystals with High Index Faceted Corrugation: Synthesis and Optical Properties*, Sci. Rep. **3**, 1 (2013).

[31] X. Zhang, R. Gallagher, D. He, and G. Chen, *PH Regulated Synthesis of Monodisperse Penta-Twinned Gold Nanoparticles with High Yield*, Chem. Mater. **32**, 5626 (2020).

[32] Y. Xia, Y. Xiong, B. Lim, and S. E. Skrabalak, *Shape-Controlled Synthesis of Metal Nanocrystals: Simple Chemistry Meets Complex Physics?*, Angew. Chem. Int. Ed. **48**, 60 (2009).

[33] L. Lv, X. Wu, Y. Yang, X. Han, R. Mezzenga, and C. Li, *Trans-Scale 2D Synthesis of Millimeter-Large Au Single Crystals via Silk Fibroin Templates*, ACS Sustain. Chem. Eng. **6**, 12419 (2018).

[34] R. Long, S. Zhou, B. J. Wiley, and Y. Xiong, *Oxidative Etching for Controlled Synthesis of Metal Nanocrystals: Atomic Addition and Subtraction*, Chem. Soc. Rev. **43**, 6288 (2014).

[35] J. H. Lee, K. J. Gibson, G. Chen, and Y. Weizmann, *Bipyramid-Templated Synthesis of Monodisperse Anisotropic Gold Nanocrystals*, Nat. Commun. **6**, 7571 (2015).

*   *   *

Unraveling the Spatial Distribution of Catalytic non-Cubic Au Phases in a Bipyramidal Microcrystallite by X-ray Diffraction Microscopy*

Summary

Tuning of crystal structures and shapes of sub-micrometer-sized noble metals have revealed fascinating catalytic, optical, electrical and magnetic properties that enable developments of environment friendly and durable nano-technological applications. Several attempts have been made to stabilize Au, knowing its extraordinary stability in its conventional fcc lattice, into different lattices particularly to develop Au-based catalysis for industry. Herein, the chapter discusses the results from scanning X-ray diffraction microscopy (SXDM) measurements on an ambient-stable penta-twinned bipyramidal Au microcrystallite (about 1.36 μm in length and 230 nm in diameter) stabilized in non-cubic lattice, exhibiting catalytic properties. With more than 82% of the crystal volume, the majority crystallite structure is identified as bco, while the remainder is the standard fcc. A careful analysis of the diffraction maps reveals that the tips are made up of fcc, while the body contains mainly bco with very high strain. The reported structural imaging technique of representative single crystallite will be useful to investigate the growth-mechanism of similar multiphase nano- and micrometer-sized crystals.

IV.1 Introduction

Noble metals stabilize in high symmetry structures, fcc or hcp phases, and it is quite uncommon to find metal crystals in non-native less-symmetric lattice types. However, as the crystal-size approaches nanometer length-scale, where the surface energy may dominate, the crystals of noble metal may be easily driven to unconventional lattice types [1–3]. There are many such examples like Ag nanorods [4–7], Au nanosheets [8,9], nanocrystals of Rh [10] and Ru [11], and with increasing crystallite size, the metals invariably assumes its native lattice. For example, Ag nanowires (~ 30 nm diameter) exhibiting 4H structure grow into longer and thicker wires exhibiting mainly the fcc lattice [3]. Under unusual circumstances depending on the nature of the nucleus, the growth may lead to unconventional lattices stabilizing even at μm sizes. For example, a decahedra shaped nucleus of Ag with 10 (111) facets arranged on

---

two penta-twinned tips grows along the <110> direction expanding its (010) facets to give rise to a few micrometers long Ag nanowire [12]. What is interesting is that the bct phase carried by the decahedra proliferates even in the nanowire, up to ~ 75% [13]. Another example comes from this laboratory [14,15], relating to Au decahedral nuclei which grow into bipyramidal microcrystallites hosting non-cubic phases up to 85%.

As is well-known, structure dictates property. Literature contains several reports on the properties of metals in foreign lattices while in the form of nanocrystallites, nanorods or wires. For example, fcc Ru nanoparticles (instead of conventional hcp) act as a superior catalyst in CO oxidation reaction [11]. While bulk Au is inactive, Au crystallites hosting non-cubic lattices are shown to serve as catalyst in a reduction reaction [15]. Ag film in 4H lattice appears golden-yellow in reflected light (instead of shiny-white) and is found to be less metallic than the fcc counterpart [7]. 4H Au nanoribbons possess lower bulk modulus than the fcc, indicating softer behavior to compression [16].

It has been of great interest in the literature to study the occurrence and distribution of unconventional lattice phases both in nanocrystals and wires using high-resolution transmission electron microscopy (HRTEM) as it allows the desired spatial resolution. For example, HRTEM has been effectively employed to monitor lattice deformation as well as phase transformation from fcc to bct in the case of Au nanocrystals (10 nm) [2]. The presence of alternating hcp and fcc phases in tadpole-shaped Au nanowires has been confirmed by HRTEM [17]. Similarly, a thin slice of as-grown Ag nanowire has shown the presence of bct in the core and fcc in the shell [12]. Although HRTEM and the associated techniques like electron tomography [18] and electron energy loss spectroscopy (EELS) [19] provide insightful data, measurements involving micrometer sized crystallites is challenging due to their limited probe depth. Slicing methods such as focused ion beam (FIB) can prove destructive [20] for these sensitive samples.

XRD on the other hand, is a nondestructive technique with high penetration depth (~ few μms) suitable for determining structures with atomic precision, provided the X-ray beam energy and size is tailored to suit the desired probe volume. Recent advancement in the nanometer sized synchrotron X-ray beam in the form of SXDM [21], offers a great possibility of examining the local composition as well as lattice structure of nano and microcrystallites.

Its ability has been well established in the case of core-shell semiconductor nanowires [22–24].

IV.2 Scope of the Investigation

The catalytic bc(o,t) Au microcrystallites are ~ half a µm thick and thus, not suitable to study by HRTEM (due to the low penetration depths of electrons). Further the well-celebrated sectioning technique *i.e.*, FIB may induce damage on the crystallite [20] and thus the current study focuses on a non-destructive technique (such as XRD) while retaining the high penetration depth into account. The present study unravels the contribution of the phases using SXDM measurements on an ambient stable micrometer-sized penta-twinned bipyramidal Au microcrystallite, where the high energy X-ray beam (*i.e.*, synchrotron source 15 keV) overcomes the depth issue while the spatial distribution can be achieved by tailoring the probe size in the nano regime (~ 100 nm) using SXDM technique [25].

IV.3 Experimental Details

Au Microcrystallites on SiN$_x$ Membrane. The as-prepared crystallites were dispersed in acetone and transferred onto the SiN$_x$ membrane (100 nm thick), NX5050C, X-ray window from Norcada Inc., Canada.

Scanning X-ray Diffraction Microscopy (SXDM). An Eiger X 4M-detector (Dectris Ltd.) with a pixel size of 75×75 µm^2 was placed 148.1 mm downstream from the sample for the XRD. This sample was scanned through the nanofocused X-ray beam over an area of 0.8×1.6 µm^2 in horizontal and vertical directions with a step size of 50 nm. A video demonstrating the experiment can be found at page no. 91.

Data Analysis. The diffraction data were extracted with the help of scripts written in MATLAB and Python. The distance between the crystal and the beam centers was calibrated by performing diffraction on LaB$_6$ powder as reference (at the beamline during the measurement). Then the θ value (for a diffraction spot) was calculated by following the formula (equation 1) using DPDAK software,

$$tan2\theta = \frac{x * 75 \text{ µm} * 0.001}{distance \ (mm)} \qquad (1)$$

where x= diameter of the circle passing through the diffraction spot (with respect to the beam center) and each pixel is 75 µm.

From the value of θ in equation (1), *d* or q was calculated by the equation (2),

$$q = \frac{2\pi}{d} = \frac{4\pi sin\theta}{\lambda} \qquad (2)$$

The line profiles were drawn using the DPDAK software by performing angular integration of the diffraction spots. Similarly, the angular spread has also been calculated using the DPDAK software.

The diffraction maps were obtained by the position sensitive pixel data. The experiment was performed with a chosen scan step (see section **IV.4.A**). Therefore, from each step, one could relate the diffraction nature of a tiny domain within the crystallite volume. Again, the scripts written in MATLAB and python help to extract the diffraction maps. XRF map was used to ensure the retention of the crystallite in the scanning window during the measurement.

Simulating Diffraction Pattern. The diffraction patterns were generated using the CrystalMaker software package.

Calculating bco Contribution. The integrated Intensity of the diffraction spots has been calculated using ImageJ software.

IV.4 Results and Discussion

The Au microcrystallites studied here are stabilized in bco and bct lattices, in short bc(o,t) [14]. The present study emphasizes on the bipyramidal microcrystallites with penta-twinned tips, exhibiting nanofacets ascribed to unusually high indices [14] (see **Figure IV.1**a,b and **Figure III.7**c in **Chapter III**). The bipyramids grow to a length of few µms with ~ half a µm diameter where the twin boundaries propagate from one tip to the other over the body of the crystal as indicated for illustration, by the white dotted line in **Figure IV.1**a. Each crystallite may host both the bco and bct lattices up to ~ 92% of its volume, the rest being the conventional fcc according to the Le Bail fitting of the XRD as shown in **Figure IV.1**c and **Figure III.7**a in **Chapter III**.

It is indeed surprising that Au, which is known to be robust retaining its fcc lattice against extreme thermodynamic conditions [26], could easily form lattices of lesser symmetries in a chemical synthesis [14,15]. The key to such synthesis is the decahedral nucleus which tend to develop high internal strain as it grows, leading to lesser symmetry lattices (see Supporting information, **Figure S14** of reference 14). The crystallites are stable at

ambient conditions as examined over the last five years and are also robust under moderate temperatures (< 400 °C) and pressures (< 15 GPa) [27]. In addition, the phases are found to be catalytically active in certain reactions unlike the bulk Au which is always inactive [15]. Thus, the bc(o,t) Au behaves quite differently from the conventional fcc phase. A study of the spatial distribution of these phases in the crystal volume is therefore worthwhile. In what follows, the study pertains a carefully chosen individual microcrystallite.
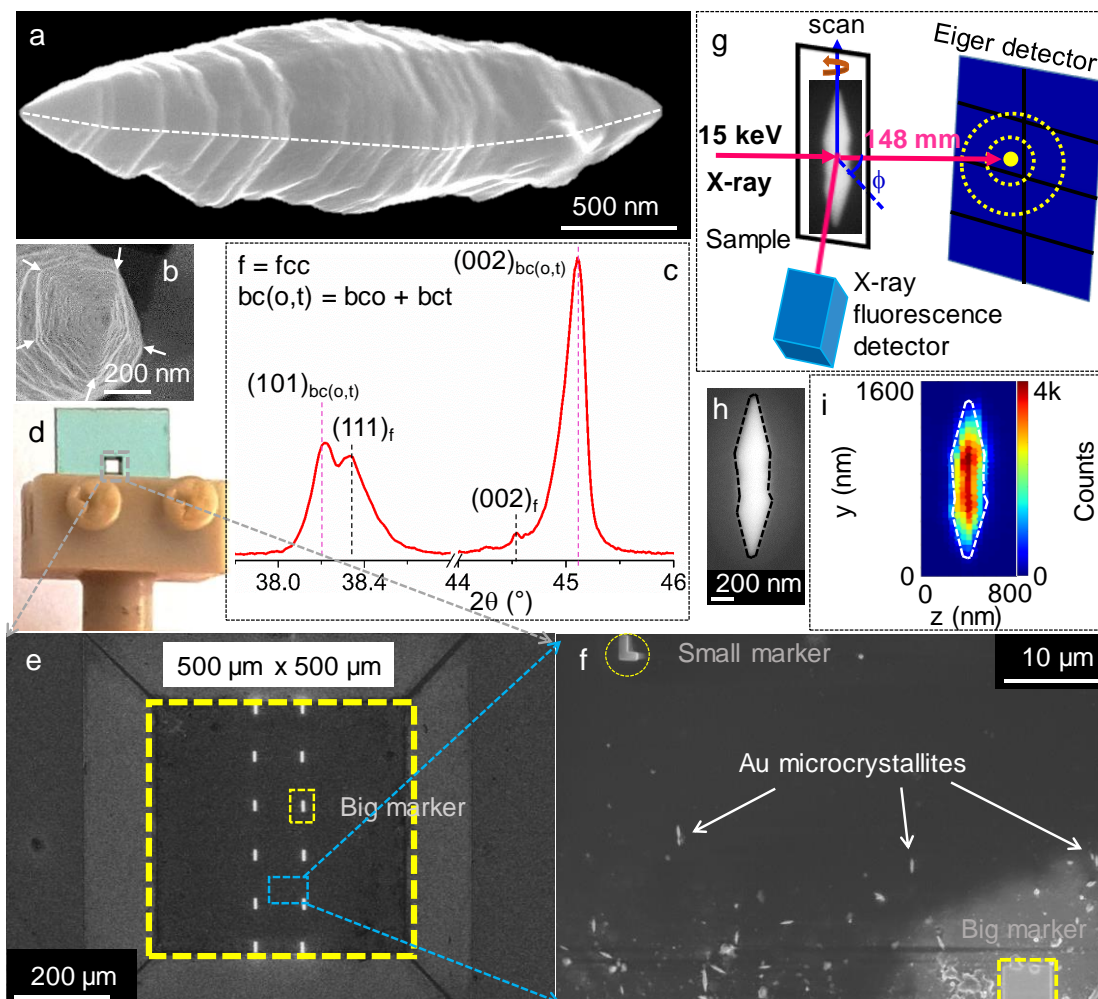
Figure IV.1. Preparation of crystallite for scanning X-ray diffraction microscopy (SXDM) experiment. (a,b) SEM image of a Au microcrystallite along with one of its penta-twinned tip, in the tilted view. A white dotted line is drawn in (a) connecting corners of pentagonal segments from one tip to the other along the body of the crystallite. The penta-twin tip in (b) is shown by white arrows. (c) XRD pattern of a collection of bc(o,t) Au microcrystallites. Also see **Figure III.7**a of **Chapter III**, for details. Surveying and marking a crystallite. (d) Photograph of a Si/SiN$_x$ nanochip mounted on the sample holder along with Au microcrystallites and Pt marker. (e) SEM image of the 100 nm thick SiN$_x$

membrane window with visible big Pt markers. (f) SEM image of the selected region of the membrane showing a small Pt marker along with Au microcrystallites spread out in the neighborhood. The tip of a big marker is seen at the bottom right of the image. The halo around it is due to spreading of the Pt deposition. (g) Schematic representation of the experimental setup. ϕ has been varied from 4° to -37° with an interval of -1°. (h,i) SEM and integrated X-ray fluorescence (XRF) images of the examined microcrystallite, respectively. The contour of the crystallite is shown in black and white dashed lines, respectively for better visibility. The fluorescence contribution was collected from the Au $L\alpha_1$ and $L\beta_2$ lines.
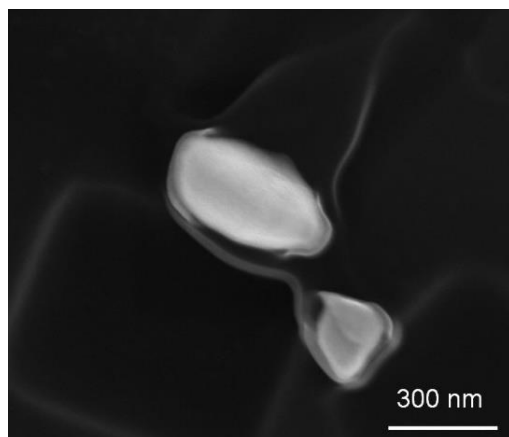
Figure IV.2. SEM image of Au slice obtained from the center of the Au bipyramid using FIB. The image shows the deformed morphology of the crystallite, not suitable for in-depth study of the pristine crystal structures.

Similar like the Ag nanowires in bct phase [28], an attempt to section the Au bipyramid from the middle of it was performed. Surprisingly, the crystallites start melting as shown in **Figure IV.2**. Probably, the portion of energy transferred from the Ga^+ ions to the Au surface is extremely high and thus the crystallites hosting metastable lattices undergo deformation. The focus of the present study being locating the ambient stable phases in the as-prepared crystallites, not suitable to proceed with this technique further.

IV.4.A Locating a Single Microcrystallite and Performing SXDM

The as-prepared Au crystallites are drop coated on a Si/SiN_x substrate hosting a thin (100 nm) SiN_x membrane in the middle (500 × 500 μm^2) for the beam to pass through (see **Figure IV.1**d–f). Survey scans were carried out using a dual beam FIB/SEM [29] to locate a region containing several microcrystallites. A hierarchical marker system was used consisting

of two sets of Pt markers deposited on the SiN_x membrane inside the FIB/SEM instrument (see **Figures IV.1**e,f and **IV.3**).
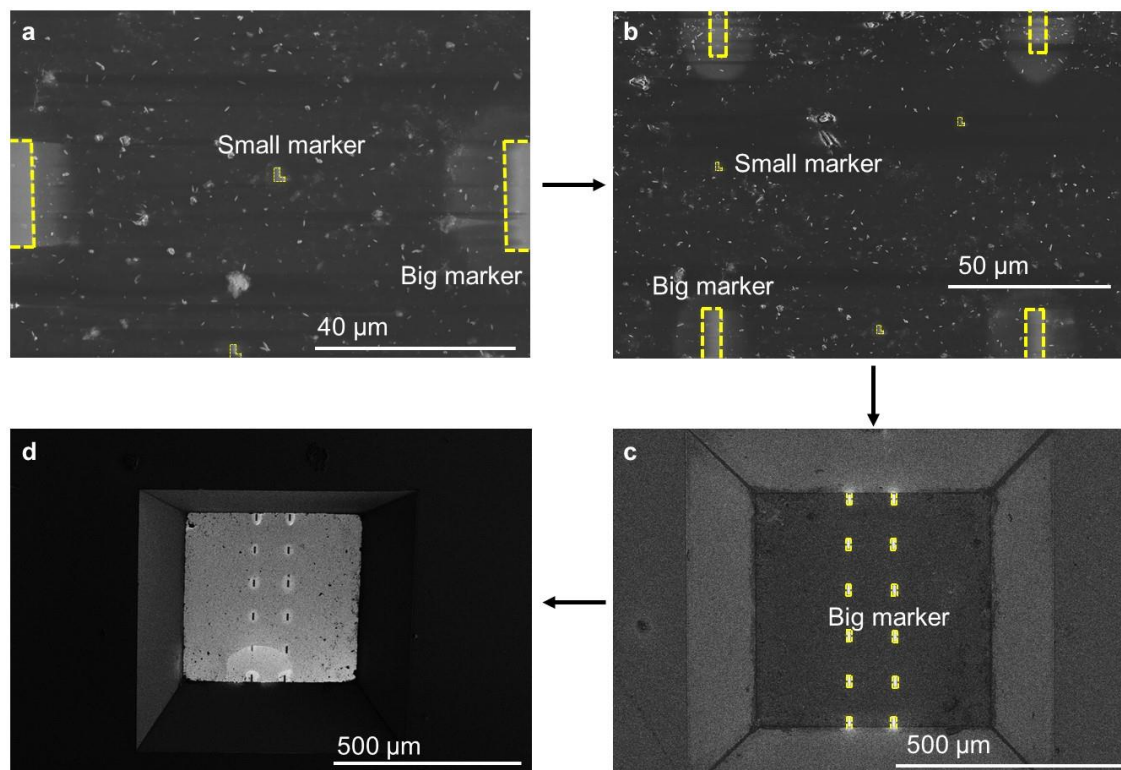
Figure IV.3. Pt markers. (a–d) SEM images of Pt markers on SiN_x nano-chip membrane viewed under different magnifications. The dashed lines represent the boundaries of the markers in (a–c). The markers consisted of i) rectangular shaped big markers ($20 \times 6 \ \mu m^2$ each, 12 in number) in the middle region along the vertical direction and ii) L shaped small markers ($3 \times 2 \ \mu m^2$, 18) in between the big markers (also see **Figure IV.1**d–f) at chosen places. The latter were decided based on the SEM scans over the region. The small markers were made adjacent to those crystallites which fell within the rectangular region of the big markers but oriented nearly parallel to the long side of the rectangle. The orientation of each small L marker was such that its long side remained parallel to that of the bigger rectangle (and therefore, parallel to the elongated crystal adjacent to it).

A coarse relocalization of the central region of the membrane and the rectangular shaped set of big markers at the focused X-ray beamline was achieved by using the optical beamline microscope with $100\times$ magnification that was set along the X-ray path (**Figure IV.4**). The fine alignment of the crystallite was made with fast X-ray fluorescence microscope (XFM) scans (see **Figure IV.1**g). The monochromatized synchrotron X-ray beam (15 keV) was scanned in steps (50 nm × 50 nm, 0.01 s) over the membrane to locate the smaller Pt markers

(using Pt Lα_1, 9.4 keV; and Lβ_4, 11.07 keV fluorescence lines) and to arrive at the chosen region, and the crystallite under study was located by monitoring Au Lα_1 (9.7 keV) and Lβ_2 (11.4 keV) intensities. The chosen crystallite, $\sim$ 1.36 µm in length, was thus positioned nearly parallel to the long side of the L marker. Finally, scanning the beam slowly (1 s/step) over the crystallite along z-y directions with mesh of 800×1600 nm^2 as shown in **Figure IV.5**, and fine-tuning the goniometer, the morphology of the bipyramid emerged clearly in the fluorescence map (see **Figure IV.1**h,i). Thus, the above scheme of markers as well as fine-tuning with the XFM scans enabled to settle with a crystallite whose long axis was almost vertical coinciding with the ϕ axis of the goniometer (y-axis). The chosen crystallite remained stable all through the measurements (see **Figure IV.6**).
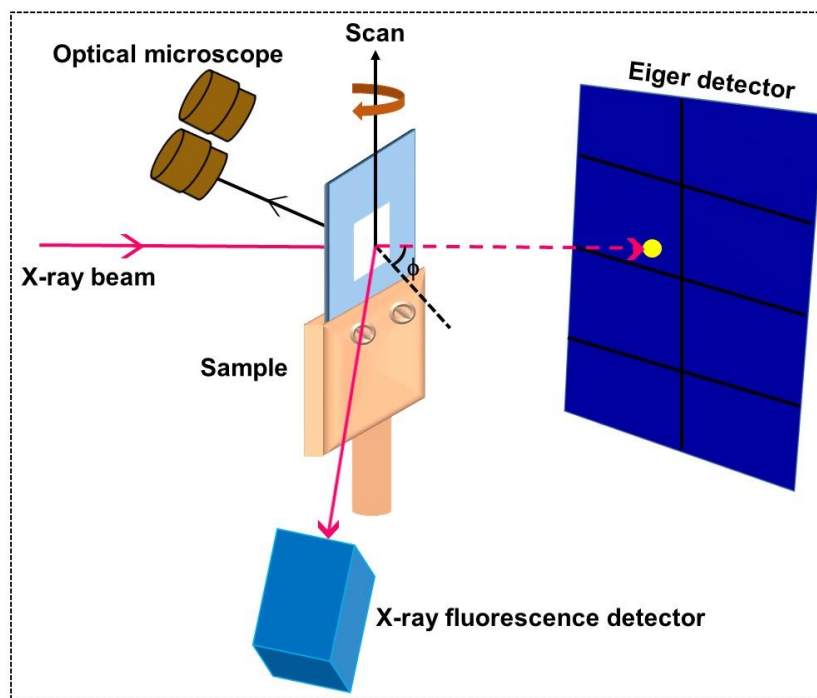
Figure IV.4. Locating the Pt markers. The optical microscope was set along the X-ray path and the big markers (rectangular shaped) were visible through the optical microscope (100× magnification). Thus, while locating the big markers, X-ray was turned off and after locating the markers, the optical microscope was moved away and X-ray was turned on. The L-shaped small markers were not visible with the optical microscope. Here, XRF microscope becomes handy on the goniometer stage in identifying these markers by monitoring the Pt Lα_1 and Lβ_4 lines intensity.

In order to avoid the spread of the deposited Pt on top of the targeted Au crystallite (chosen for diffraction), the big marker (required high dose) was deposited at least 40 µm away

(see **Figure IV.7**a). In addition, for precise position marking, a relatively small L shaped marker (with a lower dose) was deposited 15 µm away from the targeted crystallite. Prior to performing the SXDM measurements, the monochromatized X-ray beam was scanned in steps (50 nm × 50 nm, 0.01 s) over the membrane to locate the smaller Pt markers (L shaped), eventually which helped to located the examined crystallite as shown in **Figure IV.7**b.
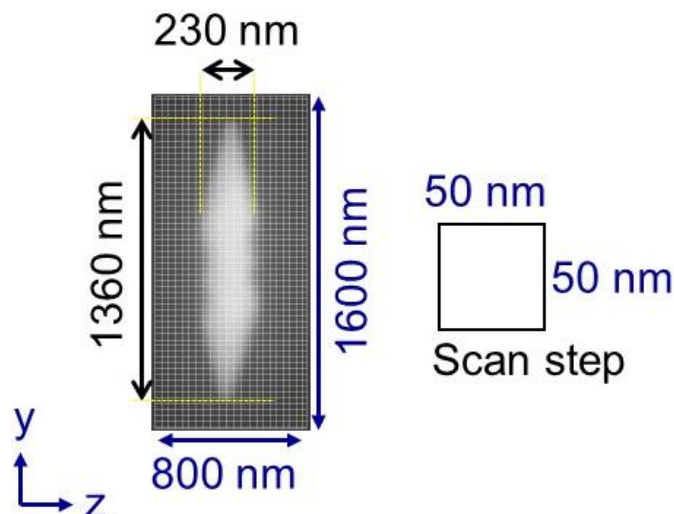
Figure IV.5. Defining the mesh scan. A representation of the mesh scan data collected over an 800 (z) × 1600 (y) nm^2 grid covering the chosen Au microcrystallite. The scan step is $50 × 50$ nm^2 and thus there were 16 columns the z direction and 32 rows along the y. The mesh parameters were chosen considering the beam diameter (100 nm), the crystallite size (~ 1.36 µm in length and ~ 230 nm wide in the middle, but ~ 100 nm at the tips) and the data acquisition time per frame (9.4 min).
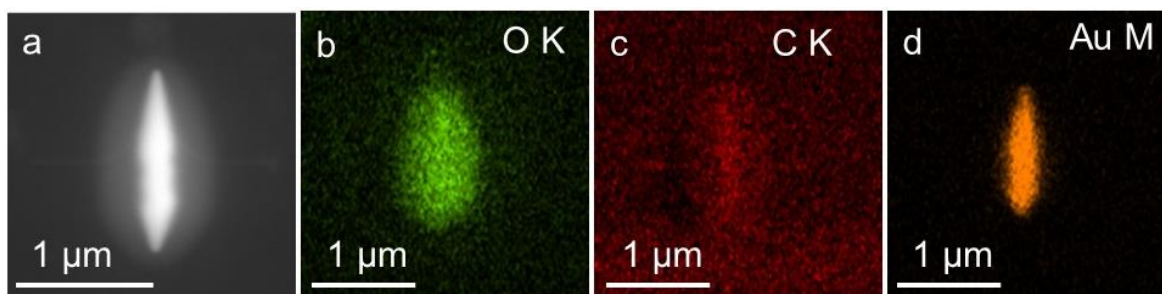
Figure IV.6. X-ray induced changes in Au crystallite. (a) SEM image of the Au crystallite collected after the diffraction experiments. The morphology of the crystallite remained similar, however, with an additional halo built up around it. (b−d) EDX mapping confirms the presence of carbon and oxygen in the halo region, which arise due to carbonaceous deposition under the high energy X-ray beam.
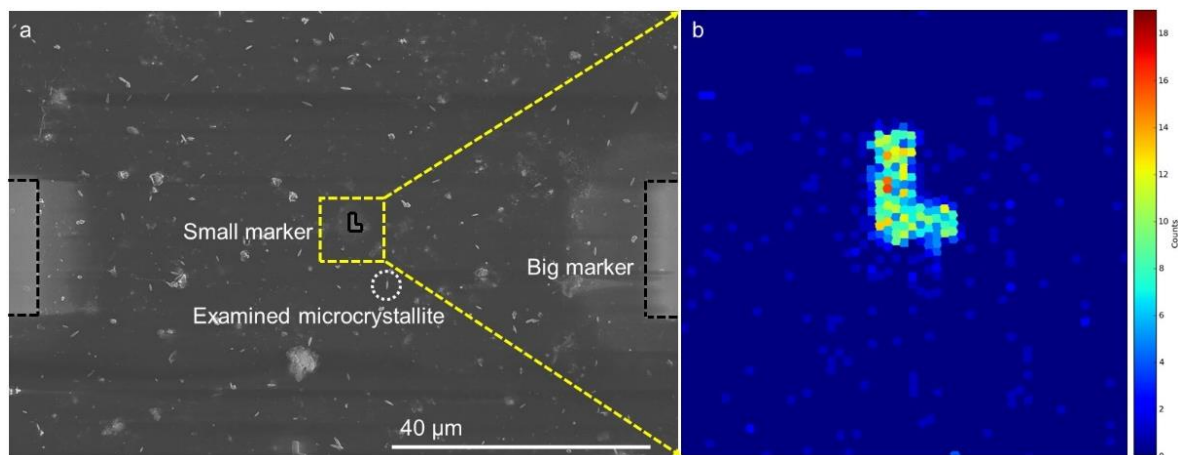
Figure IV.7. (a) SEM image of the Pt markers on SiN_x nano-chip membrane, where the black dashed lines represent the boundaries of the big markers ($20 \times 6 \ \mu m^2$ each) and the L shaped small marker ($3 \times 2 \ \mu m^2$) in between the big markers (also drawn the boundaries by black lines). (b) Integrated XRF image of Pt $L\alpha_1$ and $L\beta_4$ lines intensity.
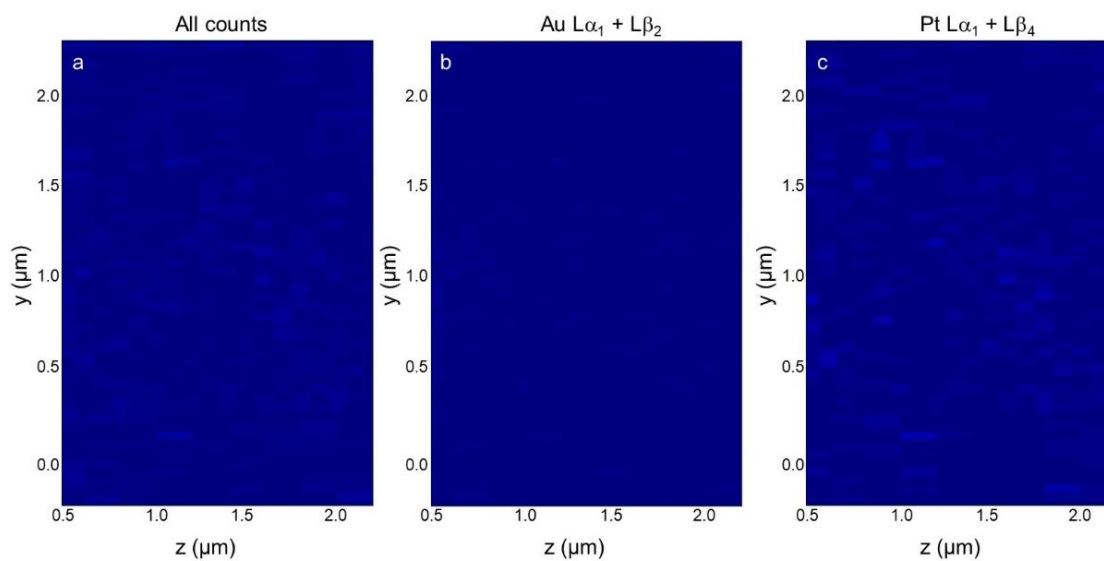
Figure IV.8. (a–c) Integrated XRF maps of all counts, Au and Pt fluorescence lines, respectively. Refer the color chart in **Figure IV.7**b.

X-ray fluorescence mapping was performed in the region surrounding the targeted Au crystallite for the Pt signal. During such a scan, the Au crystallite was left just outside of the scanning window to avoid the interference of the Au fluorescence signal with that of Pt. Herein, the mapping data from one such scanning window has been shown (**Figure IV.8**), where no trace of the crystallite could be seen. Indeed, the collected XRF signals show absence

of any fluorescence intensity from Pt (also of Au), ruling out possible general spreading of the Pt precursor.

φ Rotation (°) →		4	3	2	1	0	-1	-2	-3	-4	-5	-6	-7	-8	-9	-10	-11	-12	-13	-14	-15	-16
Drift correction (nm)	z	29	60	28	123	73	145	74	89	93	4	40	31	4	0	131	43	35	39	4	17	29
	y	27	21	0	210	167	48	100	156	135	81	48	5	5	0	140	32	16	0	0	119	146

φ Rotation (°) →		-17	-18	-19	-20	-21	-22	-23	-24	-25	-26	-27	-28	-29	-30	-31	-32	-33	-34	-35	-36	-37
Drift correction (nm)	z	0	115	86	42	39	72	2	24	48	44	2	21	125	51	21	17	51	34	66	29	29
	y	81	167	16	11	16	27	16	54	135	75	140	0	32	32	98	0	102	97	21	43	167
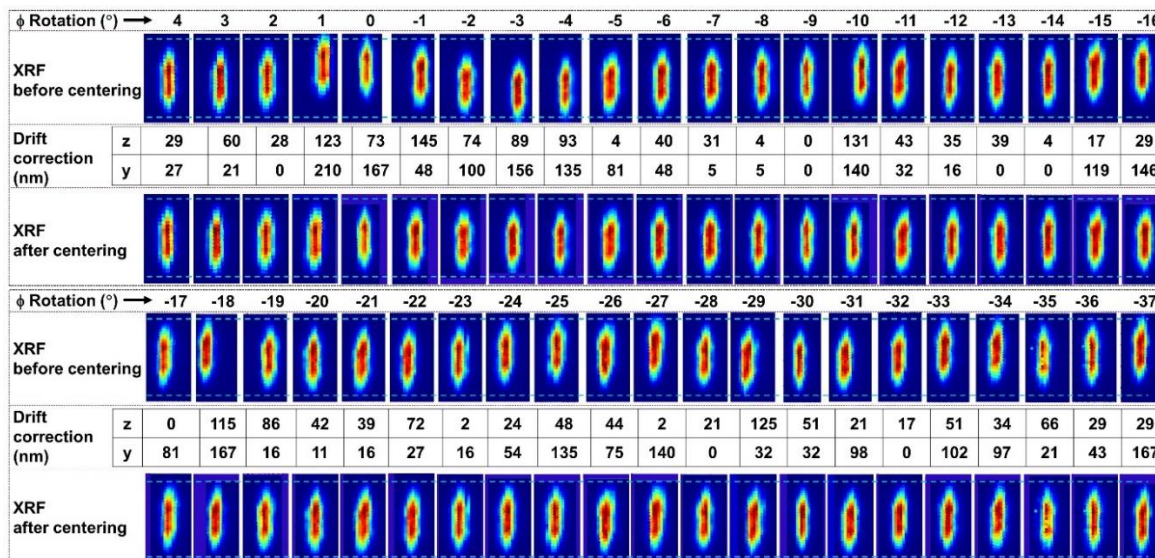
Figure IV.9. XRF maps and crystal centering corrections. XRF microscopy complements the SXDM measurements as it permits monitoring and thereby ensuring the position and orientation of the crystallite during diffraction data collection. In the given experimental set up, using the known coordinates of the pixel illuminated by the nanofocused X-ray beam, one may uniquely map the diffraction intensity measured from the Eiger detector onto the scan mesh and thus arrive at the diffraction maps. Here, diffraction maps pertaining to nanoregions provide extremely important insights when it comes to twinned crystals such as the one dealt here. During φ rotation, the crystallite undergoes small drifts along the z and y directions and the corrections are derived off-line based on the XRF images. Thus obtained corrections were then applied on the diffraction maps to present the same in the coming figures. The cyan dotted lines are drawn to guide the eye.
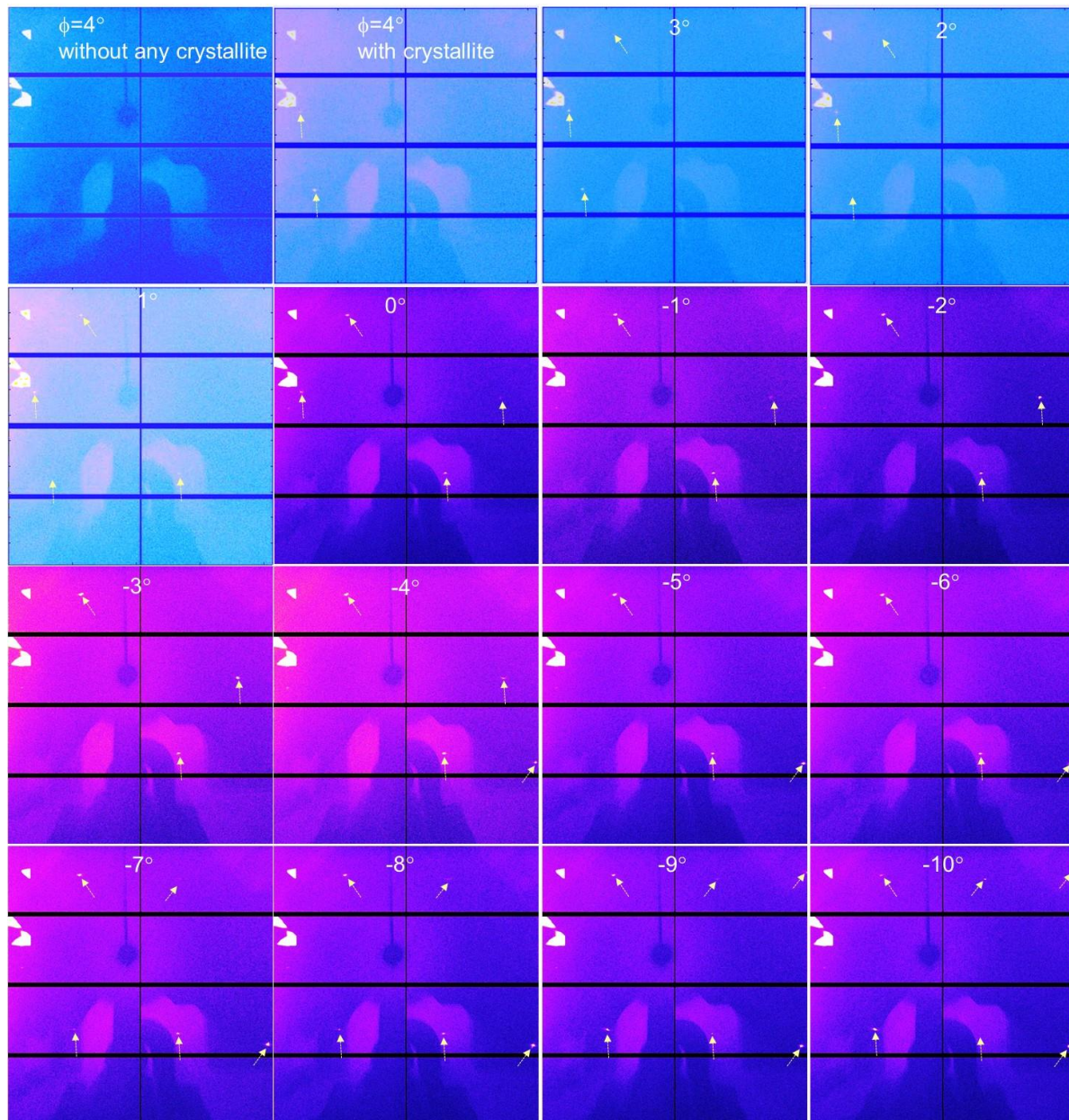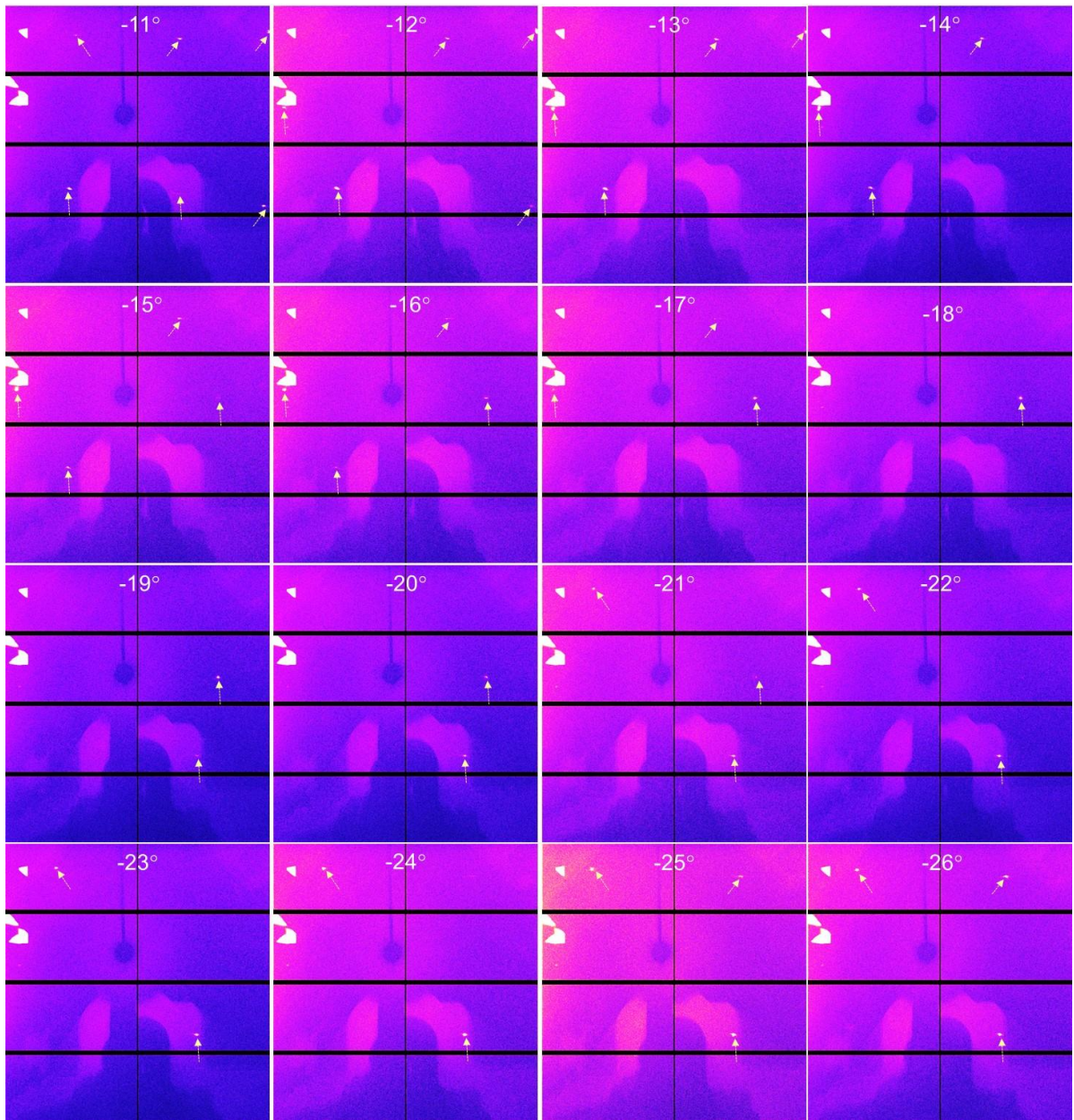
Continued…

Continued…
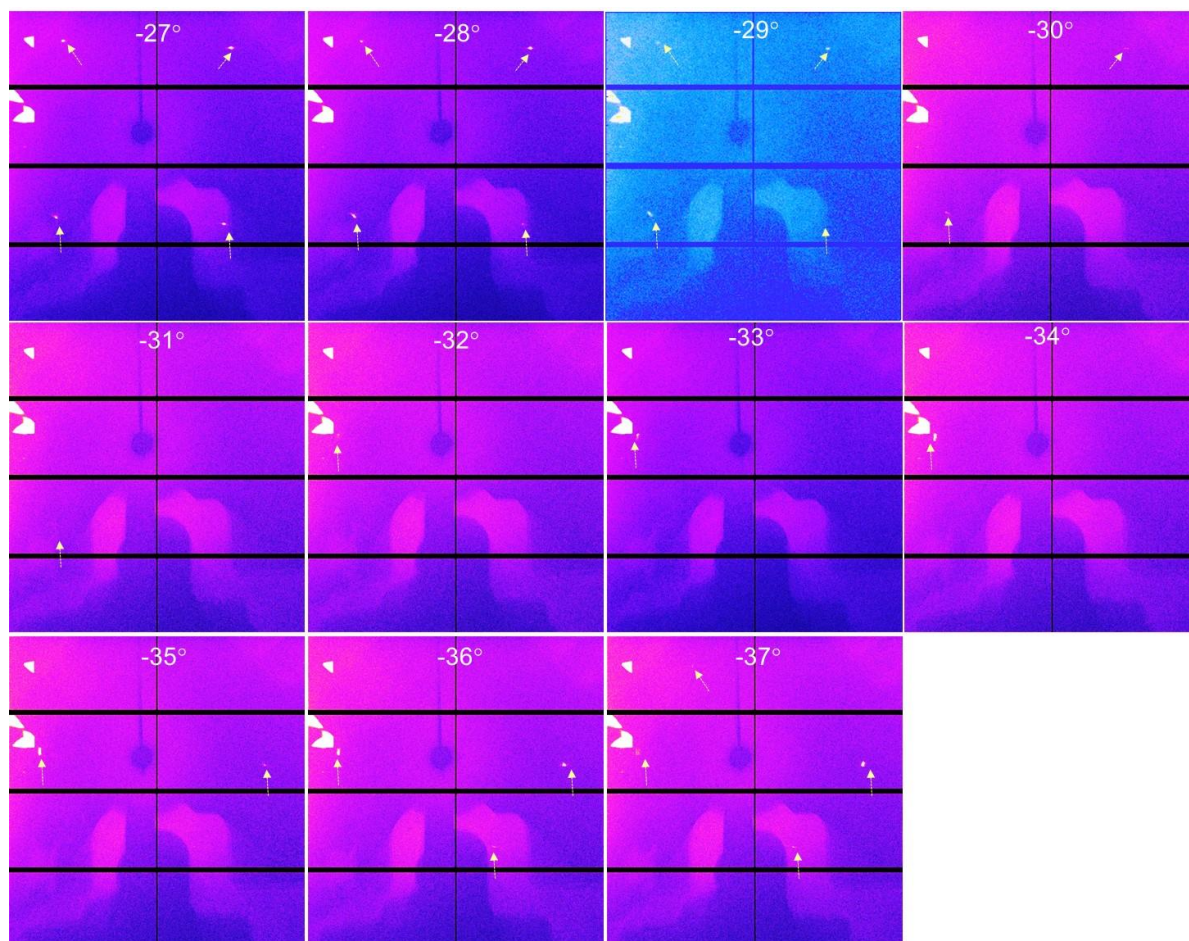
Figure IV.10. Representation of diffraction data for individual ϕ scans. Diffraction data collected using the mesh scan at different ϕ values, 4° to -37° in steps of -1° on an 8-segment Eiger 4M detector. The diffraction spots are marked by the yellow arrows to guide the eye. The illuminated regions other than the arrow markings arise from the background scattering and beam leakage (see details in **Figure IV.11**). Note, no diffraction spots were to be found at the bottom two segments at all ϕ values used.

The diffraction data was collected over the scan mesh using an Eiger 4M detector placed 148.1 mm away from the crystal center (see **Figure IV.1**g). The crystallite was rotated along the ϕ axis from 4° to -37° with -1° interval. The fluorescence and diffraction data sets were collected simultaneously with an acquisition time of 9.4 min per scan (see **Figures IV.9** and **IV.10**). As shown in **Figure IV.11**, the diffraction data integrated over the total ϕ rotation shows in all, 14 spots in different detector segments (also see **Figure IV.12**). The diffraction spots have been marked, a-n, in accordance to their sequence of appearance (also see **Figures IV.10** and **IV.13**) and alongside are their magnified views (see **Figure IV.12**). The individual

as well as integrated intensities are spread out, an aspect covered in detail below (also see **Figures IV.12** and **IV.13**).
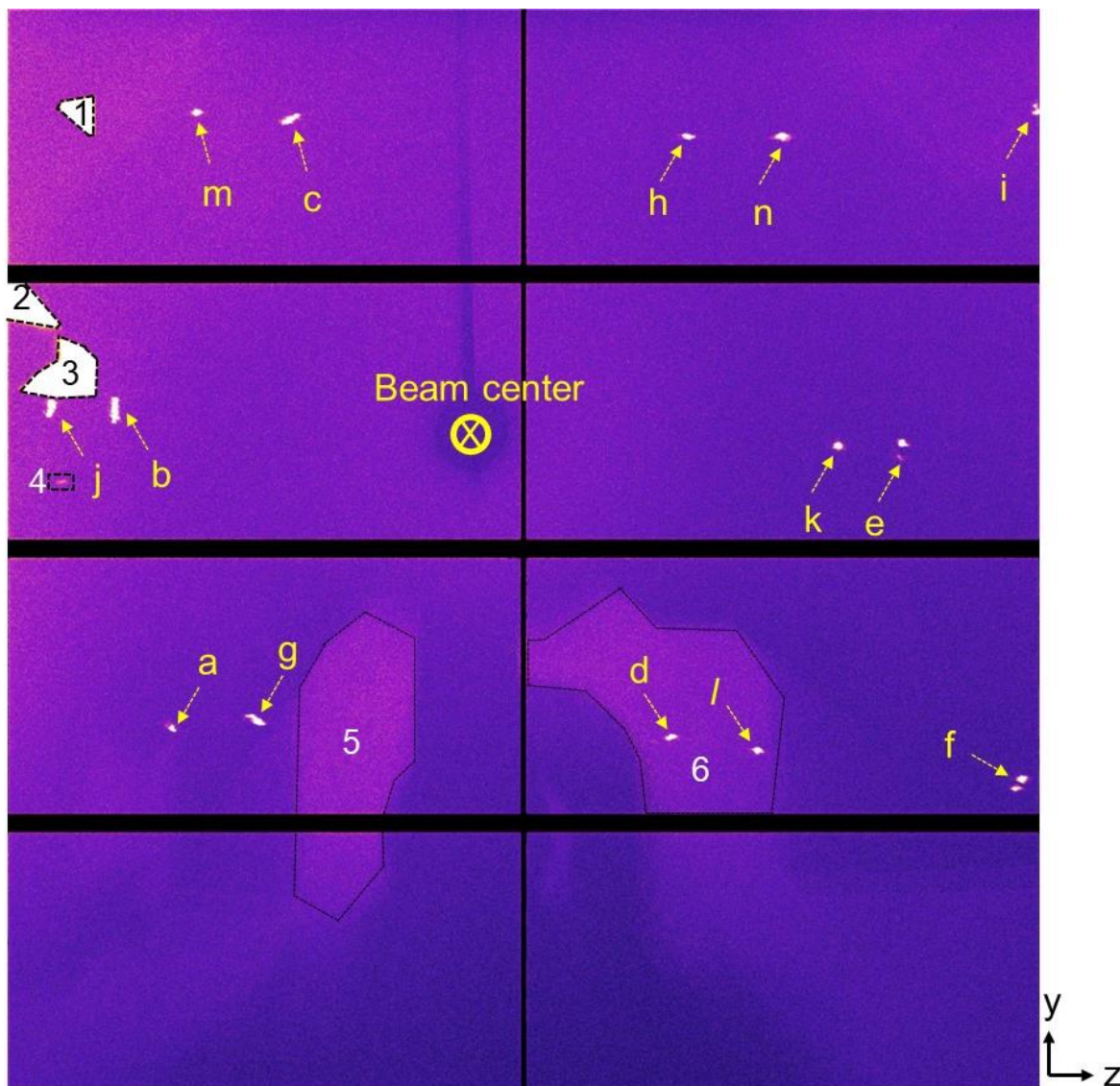
Figure IV.11. Integrated diffraction spots. Integrated diffraction data for ϕ spanning over 4° to -37° collected using an 8-segment Eiger 4M detector. This detector contains 2167 (y) × 2070 (z) pixels (where 1 pixel = 75 µm) and provides horizontal and vertical ranges of q, 39.09 nm^{-1} and 44.054 nm^{-1}, respectively. The regions enclosed with black dashes, numbered 1 to 6 are due to the background scattering and beam leakage. The diffraction spots are marked by the yellow arrows to guide the eye. Instead of circular spots, a spread in the intensity is seen in varying shapes for all observed reflections, clearly originating from the presence of multitude of lattices. While the radial spread (along the radii drawn from the beam centre) provides the range of q values (different unit cells), the spread along other directions stands for varying orientations of the different unit cells (*vide infra*).
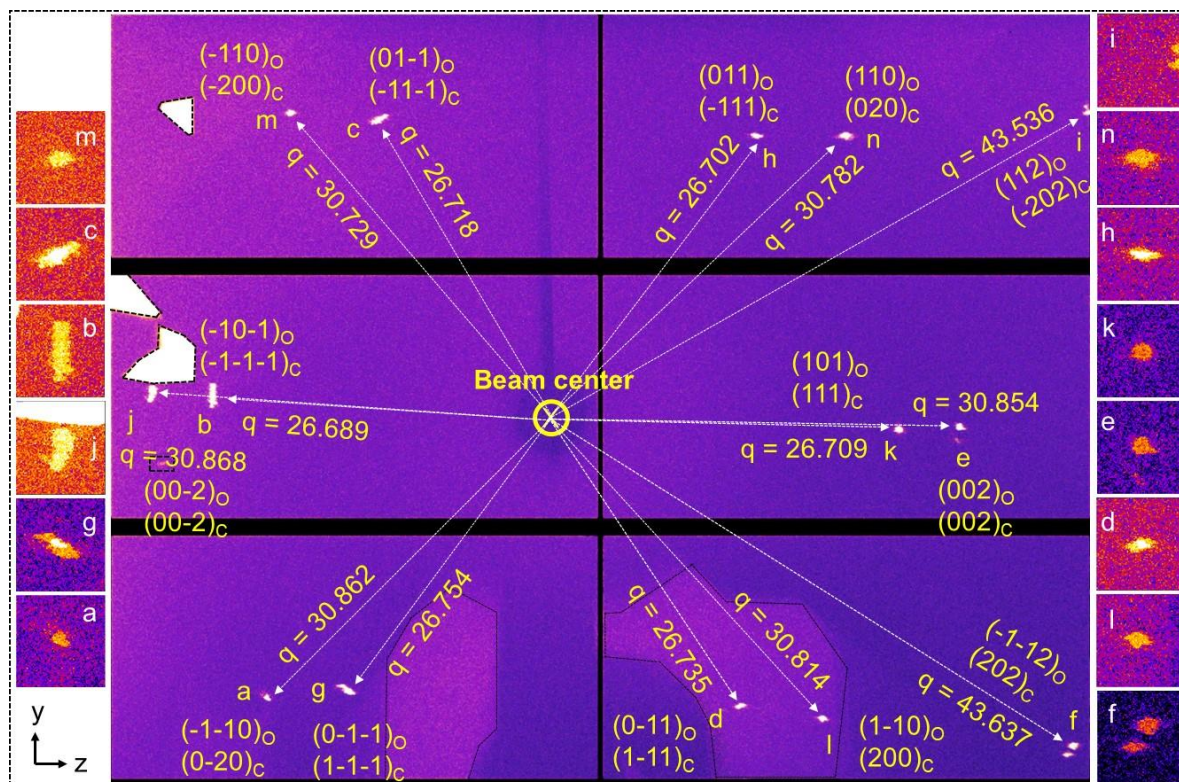
Figure IV.12. Indexing the collected diffraction spots on the detector. The integrated diffraction data as collected using an Eiger 4 M detector is shown. The wide dark lines demarcate the segments of the detector. The spots, a-n, have been named based on the sequence of their appearance during data collection (see **Figures IV.10** and **IV.13**). As the bottom two segments did not host any diffraction spots, they are removed in the figure (see **Figure IV.11** for full view). Henceforth, only the top six segments are referred to in the discussion. The spots have been indexed where O and C refer to bco and fcc unit cells, respectively. Mean q values are denoted in nm^{-1}. Diffraction spots from each segment shown magnified with pixel windows $86(z) \times 90(y)$ in rectangular boxes placed alongside, illustrate the widespread of the intensity, which is addressed under **Figure IV.14**.

IV.4.B Identifying the Unit Cells and the Relative Orientations

The q values were estimated from the centroids of the line profiles (**Table IV.1**) within the permissible resolution of ± 0.04 nm^{-1} of the detector. Considering the horizontal line on the detector plane, four spots, b, e, j, and k are present (see **Figure IV.12**). Reflections e and j possessing similar q values 30.854 and 30.868 nm^{-1} respectively, appear on either side of the beam center as though they are symmetry reflections. The occurrence of such symmetry reflections within a limited crystal rotation (-42°) is intriguing and will be dealt with later. Continuing with the q values as estimated from the centroids of the line profiles, (b,k), (c,d),

(g,h), (l,m), (a,n) and (f,i) are similarly pairs of symmetry reflections as shown in **Figure IV.12**. Interestingly, the (c,h,d,g) and (m,n,l,a) seem to form the corners of two rectangles as shown in **Figure IV.14**a, where the acute angles extended by the diagonals are 68.40° and 87.35°, respectively. These values may be compared with those exhibited by fcc{hhh} and fcc{h00} reflections, 70.50° and 90°, respectively; the deviations arising from the intensity spread of the spots, are obvious.

Each spot exhibits spread along both radial and circumferential directions (**Table IV.2**), highlighting the presence of multiple lattices (see **Figure IV.15** for details). Considering the rectangles to be arising as due to symmetry, the (m,n,l,a) can be considered as symmetry reflections and similarly, (c,h,d,g). Thus, the mean q of the symmetry related spots has been taken and calculate the spread with respect to the mean q as shown in **Table IV.2**. The differences in the radial spread are much higher than the instrumental accuracy (± 0.04 nm^{-1}), implying that they may arise from different lattices. The circumferential spreads are even higher, which can be linked to misorientations of diffracting domains or simply, mosaicity. The mean q values obtained from the symmetry considerations, were used for indexing, after comparing with the q values from the high resolution XRD data obtained earlier [27] (**Tables IV.3** and **IV.4**).

Given the spread of the spots, each spot can have possible assignments as listed in **Table IV.4**. Now referring to the rectangle comprised of (m,n,l,a) spots, the mean q value can be assigned to fcc{002} (see **Tables IV.3** and **IV.4**), the error being -0.019 nm^{-1}. Considering the asymmetry in the diffraction spots and the line profiles (see **Figures IV.12**, **IV.13** and **Table IV.1**), the spots are not solely arising from a standard fcc cell; instead, the bidirectional asymmetric spots emphasize the presence of multiple lattices. Thus, the other possibilities of assigning the spots are bco{110} or bct{110}, the errors being -0.227 and -0.243 nm^{-1}. Accordingly, the angles extended by pairs of spots fall in the ranges, $\sim$ 88.35-96.70° (see **Figure IV.14**a) and 83.50-91.20°, respectively, which can be assigned to bco{110} because in others (bct{110} and fcc{002}), the angle required is 90°, forming a perfect square. Following this assignment, one may argue that the *c*-axis of the bco cell (termed *c″*) lies along the horizontal line, while the *b*-axis (*b″*) is placed vertically (see **Figure IV.14**b and **IV.16**), along the crystal axis, such that *c″* > *a″* and *b″*.
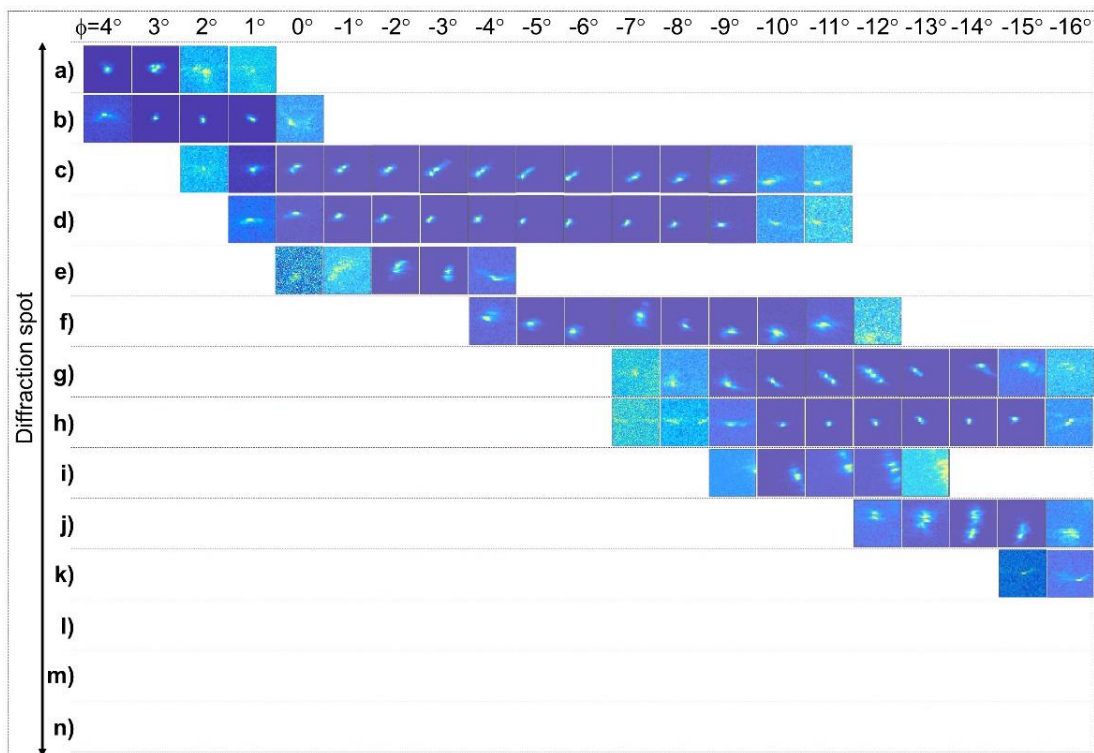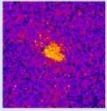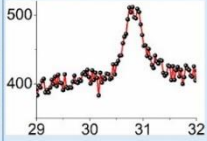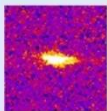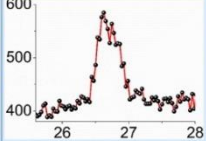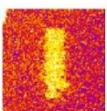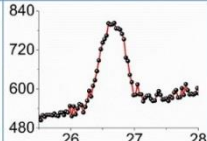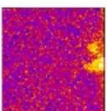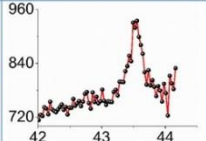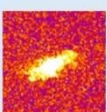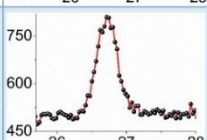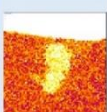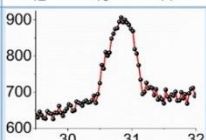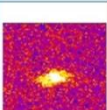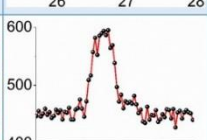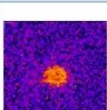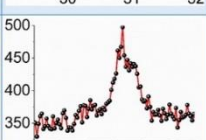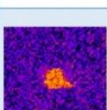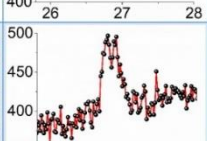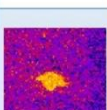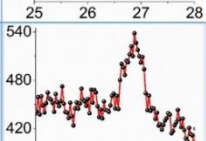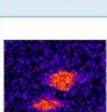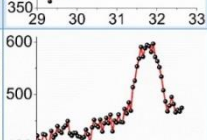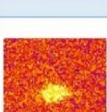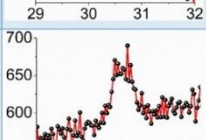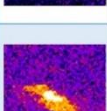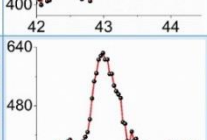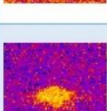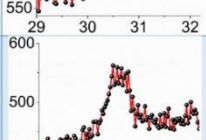
Continued…
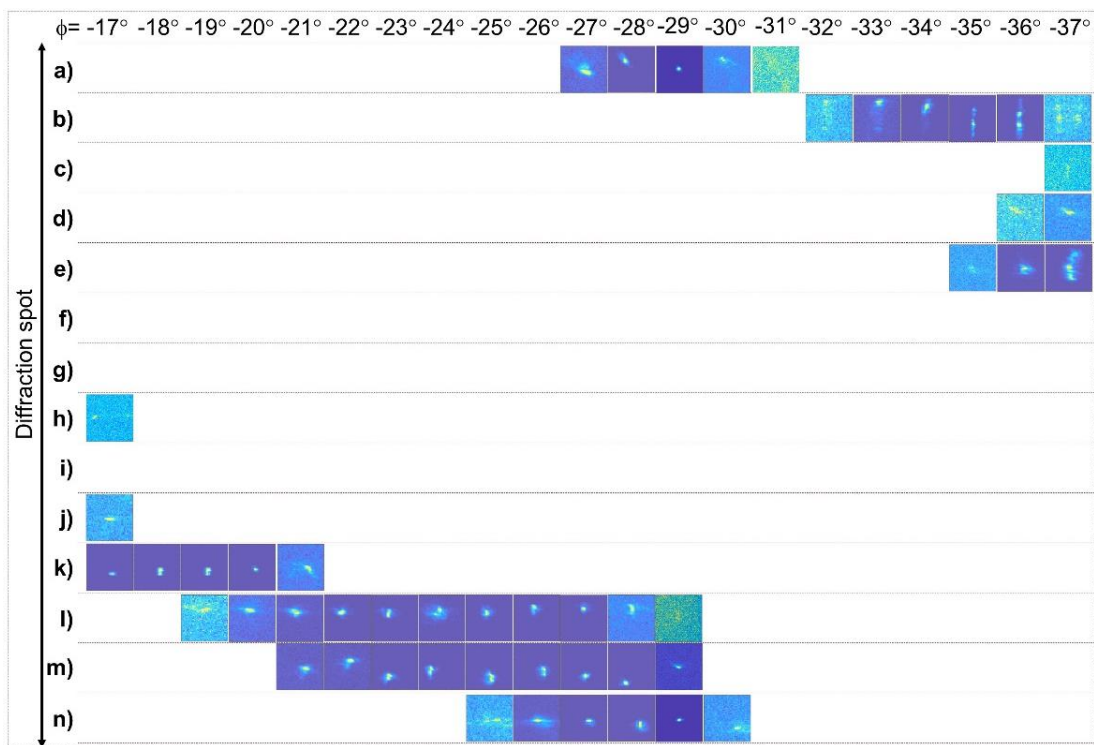
Figure IV.13. Individual diffraction spots extracted and collated. Zoomed-in views of the individual spots showing intensity spread for different ϕ rotations. The spots are named a to n based on the

sequence of their appearance. Neither the dimension of the box nor the q ranges are held fixed; the viewgraphs are only meant for detailed examination of the uneven intensity spread.

Table IV.1. Quantifying q values. The q values were calculated from the centroids of the line profiles, drawn over the diffraction spots within the permissible resolution accuracy of ±0.04 nm^{-1} of the detector. The line profiles are asymmetric, indicating the presence of strain or multiple lattices.

Label	Diffraction spot	Line profile, intensity (a.u.) *vs.* q (nm^{-1})	q (nm^{-1})	Label	Diffraction spot	Line profile, intensity (a.u.) *vs.* q (nm^{-1})	q (nm^{-1})
a			30.862	h			26.702
b			26.689	i			43.536
c			26.718	j			30.868
d			26.735	k			26.709
e			30.854	l			30.814
f			43.637	m			30.729
g			26.754	n			30.782

Using this construction, the diffraction spots of both fcc and bco were generated by simulation, considering 360° rotation along the crystal axis (see **Figures IV.14**c and **IV.17**). Within the maximum coverable range of the detector (see **Figure IV.11**), the generated reflections are assignable to {111}, {002}, and {202} of fcc and {101}, {011}, {110}, {002}, and {112} of bco as shown schematically in **Figures IV.14**c and **IV.17**. As expected, the pairs of spots from fcc and bco appear in close proximity, and overall, these patterns appear similar

to the experimentally obtained pattern. Thus, the spot, m for instance, is concurrently assignable to fcc(-200) and bco(-110). In other words, both fcc and bco are simultaneously present within the widely spread integrated intensities of the experimental spots (see **Figure IV.12** and **Table IV.1**), which is even visible at a single ϕ frame (**Figure IV.13**). Thus, one may consider all 14 spots to arise from a combination of fcc and bco in spite of higher errors in some cases. Previous literature [14,27] has shown the coexistence of bct and bco phases along with fcc, however, for the sake of simplicity as well as generality, here, only bco has been considered along with fcc.
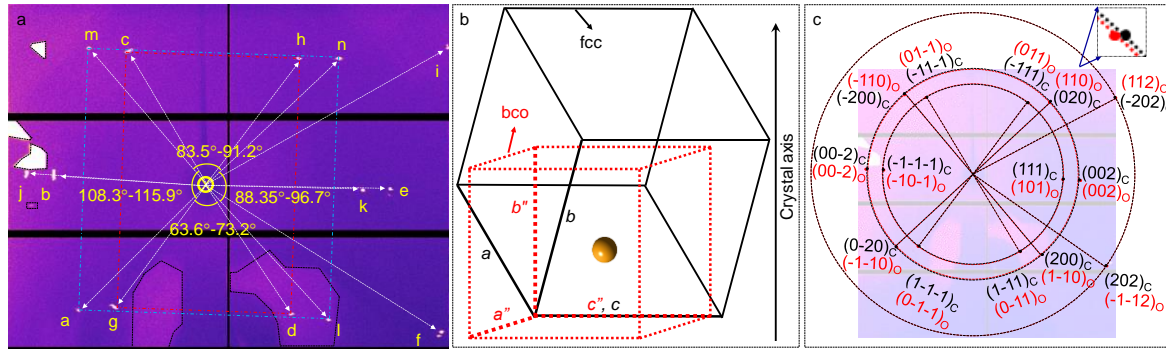
Figure IV.14. Identifying symmetry related reflections and visualizing the unit cells. (a) Rectangles connecting the symmetry related spots, (c,h,d, and g, red) and (m,n,l, and a, blue). (b) The orientation of the unit cells, *i.e.*, bco and fcc in the crystallite. *a*, *b*, and *c* are the fcc axes. Similarly, *a″*, *b″*, and *c″* are the axes for bco, respectively (shown in **Figure IV.16**). The schematic is not to scale. The bco *b″*-axis is parallel to both the crystal growth direction and the goniometer y-axis. Both *c*-axes, *c* and *c″*, coincide and lie in the horizontal plane. The two unit cells are rotated by 45° along the c-axes, and the lattice parameters follow the sequence, *c″* > *a″* and *b″*. (c) Simulated diffraction patterns from the two unit cells with 360° ϕ rotation, overlaid (see **Figure IV.17** for more details). The eight segments of the detector are shown in the background for reference. Inset, reflection $(110)_O/(020)_C$ has been magnified by eight times and shown.

To gain further insight, one may consider the radial and circumferential spreads in greater detail by enclosing the spreads from the symmetry related reflections between two co-centric circles such that the inner one possesses the lowest q_{min} as the radius and the outer one, highest q_{max}. For convenience, this exercise was begun with (c,h,d,g) spots with radii of 27.097 nm^{-1} (as q_{max}) and 26.363 nm^{-1} (q_{min}) as tabulated in **Table IV.2** (also see the **Figures IV.18**a,c and **IV.19** for detailed analysis). The circle in the middle refers to the standard fcc Au ($a = b = c = 4.0810$ Å) with $q_{fcc}\{111\} = 26.677$ nm^{-1}. Thus, the two circles drawn at q_{min}

and q_{max} can be considered as contributions from $bco_{max}\{011\}$ and $bco_{min}\{011\}$, respectively, which will be made use later for the calculation of cell parameters.
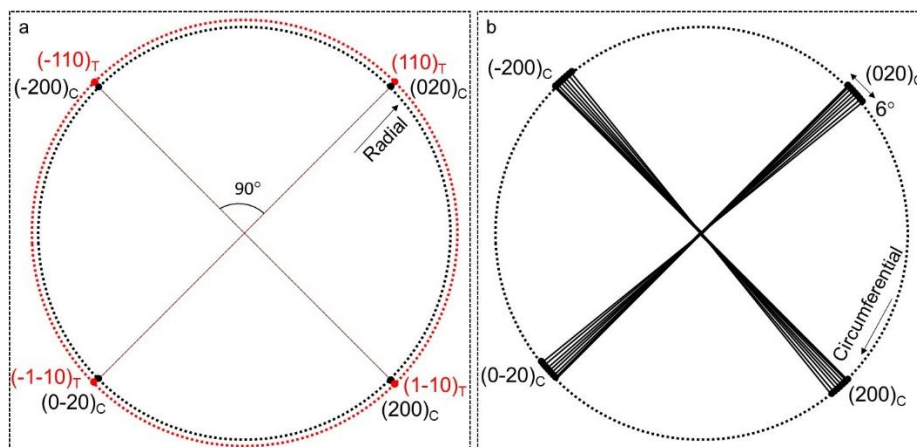
Figure IV.15. Variation of diffraction spots. The fcc{002} reflections along with different spreads. (a) Radial distribution of the spots define variation in lattice parameters. For example, introducing another set of reflections, bct{110}, which also has four-fold symmetry similar to fcc{002}, will not alter the inter-angle extended among the reflections (90°). However, the spots will have a radial spread. Here, the lattice parameters of bct (termed as T) $a = b <$ fcc (C) lattice parameters. (b) Spread of a spot along the circumferential direction defines by the multiple differently oriented domains. Here, the inter-reflections angle will have spread instead of prefect 90°. Thus, bidirectional spreads of a spot imply deviation from fcc lattice.

Table IV.2. Measuring the spread of the diffraction spots. The diffraction spots, at both individual ϕ rotations (see **Figure IV.13**) and the integrated counterparts (see **Figure IV.11**) exhibit highly asymmetric intensity spreads both radially and circumferentially. Indeed, the intensity spread covers reflections from both lattices (bco and fcc) for each spot. The drawn line profiles over the diffraction spots also reveal the associated asymmetry (see **Table IV.1**). In the table given below, for each spot with assigned (hkl) values from the two lattices, the q_{min} and q_{max} values extracted after examining the intensity spread at every ϕ over the entire range, is given along with the mean, the lowest and the highest q values considering the symmetry related reflections. Similarly, the maximum intensity spread observed circumferentially was also calculated and averaged over the symmetry related reflections. The differences in the radial spread are much higher than the instrumental resolution (± 0.04 nm^{-1}). The circumferential spreads are even higher. The circumferential spread can be assigned as mosaicity, a measure of imperfection in the crystal, which can arise due to the presence of misoriented domains with similar lattice parameters or oriented domains with different lattice parameters.

Integrated diffraction Spot	q_{min} (nm^{-1})	q_{max} (nm^{-1})	q_{mean} (nm^{-1})	Lowest q_{min} (nm^{-1})	Highest q_{max} (nm^{-1})	Radial spread (nm^{-1})	Circumferential spread (°)	Average circumferential spread (°)	ϕ range (°)	bco and fcc reflections (Subscript O and C, respectively)
Spot a	30.327	31.502				1.175	4.20		-27 to -31 and 4 to 1	$(-1-10)_O/(0-20)_C$
Spot m	30.327	31.155	30.823	30.327	31.502	0.828	4.15	3.11	-21 to -29	$(-110)_O/(-200)_C$
Spot n	30.327	31.344				1.017	2.40		-25 to -30	$(110)_O/(020)_C$
Spot l	30.391	31.218				0.827	1.70		-19 to -29	$(1-10)_O/(200)_C$
Spot b	26.262	27.379	26.820	26.262	27.379	1.117	4.25	2.7	4 to 0 and -32 to -37	$(-10-1)_O/(-1-1-1)_C$
Spot k	26.262	27.379				1.117	1.15		-15 to -21	$(101)_O/(111)_C$
Spot c	26.363	27.097				0.734	3.70		2 to -11 and -37	$(01-1)_O/(-11-1)_C$
Spot h	26.363	27.081	26.717	26.363	27.097	0.718	2.10	3.12	-7 to -17	$(011)_O/(-111)_C$
Spot d	26.379	27.031				0.652	2.80		1 to -11 and -36 to -37	$(0-11)_O/(1-11)_C$
Spot g	26.413	27.014				0.601	3.90		-7 to -16	$(0-1-1)_O/(1-1-1)_C$
Spot e	30.487	31.502	30.891	30.231	31.502	1.015	3.55	3.17	0 to -4 and -35 to -37	$(002)_O/(002)_C$
Spot j	30.231	31.344				1.113	2.80		-12 to -17	$(00-2)_O/(00-2)_C$
Spot f	43.281	43.997	43.621	43.281	43.997	0.716	2.45	2.05	-4 to -12	$(-1-12)_O/(202)_C$
Spot i	43.281	43.926				0.645	1.65		-9 to -13	$(112)_O/(-202)_C$

Table IV.3. The corresponding (hkl) and q values from the previous reports [27] for fcc, bct and bco lattices, respectively. The lattice parameters of fcc, $a = b = c = 4.0810$ Å; bct, $a = b = 2.9069$Å, $c = 4.0430$ Å and bco, $a = 2.9178$Å, $b = 2.8930$, $c = 4.0314$ Å, respectively.

fcc		bct		bco	
(hkl)	q (nm⁻¹)	(hkl)	q (nm⁻¹)	(hkl)	q (nm⁻¹)
(111)	26.677	(101)	26.632	(101)	26.593
(200)	30.804	(110)	30.580	(011)	26.742
(220)	43.564	(002)	31.094	(110)	30.596
		(200)	43.246	(002)	31.183
		(112)	43.611	(200)	43.085
				(020)	43.454
				(112)	43.687
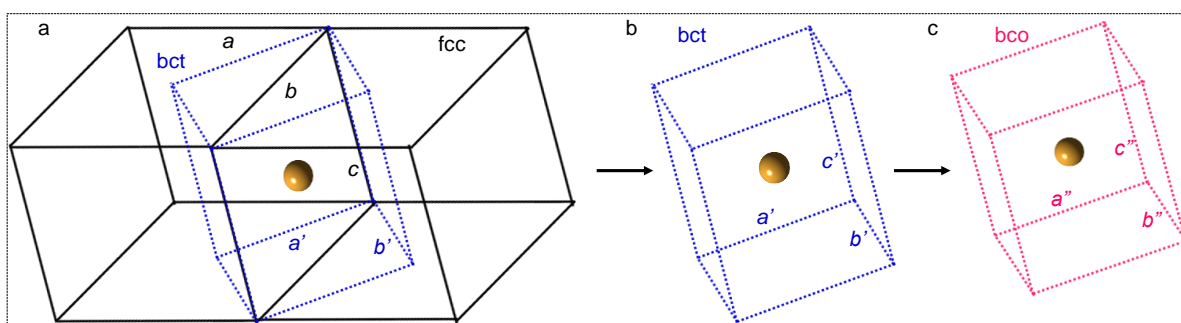
Figure IV.16. Generation of bco from a fcc unit cell. (a) A bct unit cell is borne out of two face-shared fcc unit cells by connecting the face diagonals such that $a' = b' = a/\sqrt{2}$ and $c' = c$, i.e., $c'/a' = 1.414$. (b) Equal expansions along the a and b axes and compression along the c-axis result in the experimentally observed bct unit cell [14]. (c) Similarly, an unequal expansion along the a and b axes results in a bco unit cell, where $c'' > a''$ and b'' i.e., c''/a'' and $c''/b'' \neq 1.414$. Schematic, not to scale.

Table IV.4. Assigning diffraction spots. Experimental error involved in assigning the mean q of the symmetry related reflections. From the q values, indexing of the spots is not straightforward, as the q values are assignable to multiple reflections within the accuracy of the detector resolution. The final assignments (shown in bold) are based on the q values and angles between the reflections as detailed in **Table IV.2** and **Figure IV.14**. Each experimental value is shown against possible assignments along with the associated error.

Integrated diffraction spots	mean q (nm⁻¹)	Experimental error involved (nm⁻¹)	Possible (hkl)	Previously reported q (nm⁻¹)	Angle between the extended reflections (°)			Angle between the reflections (°)		Remarks
					Spots under consideration	Min	Max	Lowest min	Highest max	
a, m, n, l	30.823	**-0.019**	**fcc{002}**	**30.804**	a,m	88.35	96.70	88.35	96.70	Among the possible (hkl), fcc{002} and bct{110} will generate four reflections, which can be considered as the corners of a perfect square with an inter-reflections angle of 90°. Considering the experimental angles (specifically the distribution), the rectangle can only be generated from bco{110}, whereas the angle extended by bct{002} and bco{002} reflections are 180°.
		-0.227	**bco{110}**	**30.596**	n,l	90.40	94.50			
		-0.243	bct{110}	30.580	m,n	83.50	90.05	83.50	91.20	
		+0.271	bct{002}	31.094						
		+0.360	bco{002}	31.183	l,a	85.30	91.20			
b, k	26.820	-0.078	bco{011}	26.742	b,k	178.50	183.90	178.50	183.90	Angle between any mirror reflections will be always 180° and the deviation from a perfect 180° defines presence of multiple domains.
		-0.143	**fcc(111)**	**26.677**						
		-0.188	bct{101}	26.632						
		-0.227	**bco{101}**	**26.593**						
c, h, d, g	26.717	**+0.025**	**bco{011}**	**26.742**	c,h	63.60	69.40	63.60	73.20	The angle extended between the reflections are 70.5° and 109.5° for fcc{111}. Any deviation in the angle can be ascribed to other possibilities.
		-0.040	**fcc(111)**	**26.677**	d,g	66.50	73.20			
		-0.085	bct{101}	26.632	h,d	109.10	114.00	108.30	115.90	
		-0.124	bco{101}	26.593	g,c	108.30	115.90			
e, j	30.891	**-0.087**	**fcc{002}**	**30.804**	e,j	177.45	183.80	177.45	183.80	Angle between any mirror reflections will be always 180° and the deviation from a perfect 180° defines presence of multiple domains.
		+0.203	bct{002}	31.094						
		+0.292	**bco{002}**	**31.183**						
		-0.295	bco{110}	30.596						
		-0.311	bct{110}	30.580						
f, i	43.621	-0.010	bct{112}	43.611	f,i	60.65	64.75	60.65	64.75	Angle extended between the fcc{220} reflections are 60°. Any deviation can be ascribed to bct{112} and bco{112}. The angle extended by bco{020} and bco{200} are 180°, whereas the extended angles are 90° and 180° for bct{200}.
		-0.057	**fcc{220}**	**43.564**						
		+0.066	**bco{112}**	**43.687**						
		-0.167	bco{020}	43.454						
		-0.375	bct{200}	43.246						
		-0.536	bco{200}	43.085						

Figure IV.17. Simulating the diffractions spots from the assumed orientations of the bco and fcc unit cells. The diffraction spots were generated using CrystalMaker software package taking the lattice parameters of fcc to be $a = b = c = 4.081$ Å and those of bco, $a = 2.9178$, $b = 2.8930$ and $c = 4.0314$ Å. Going by the detector dimensions, the simulation is restricted to q radius of 44.054 nm^{-1}. Here, the x, y and z axes are equivalent to a, b and c axes, respectively. (a–e) Screenshots of the bco unit cell while rotating ($\phi = 360°$) along the goniometer y-axis. The bco y-axis coincides with the goniometer y-axis and thus, with the ϕ rotation, the bco unit cell rotates along the y-axis in the xz plane. (f–i) Screenshots of the fcc unit cell (already rotated 45° with respect to z-axis, see **Figure IV.14**b) while rotating ($\phi = 360°$) along the goniometer y-axis. Since the z-axes of both bco and fcc unit cells coincide while being horizontal (see **Figure IV.14**b), a rotation of 360° along the goniometer y-axis rotate the bco in the xz plane, whereas for fcc, all three axes rotate. The pink and yellow spheres represent the atoms of the fcc and bco unit cells, respectively. (j,k) The simulated diffraction spots with indexing shown. The O and C represent bco and fcc lattices, respectively. (l) The overlaid simulated diffraction patterns from

the two unit cells (as shown in **Figure IV.14**c) has been magnified by 8 times and presented. The diffraction spots of the two unit cells are closely placed with small changes in the *d*-spacings as well as the angles between the reflections, seen experimentally as intensity spread.

IV.4.C Locating the Different Phases in the Crystallite Volume
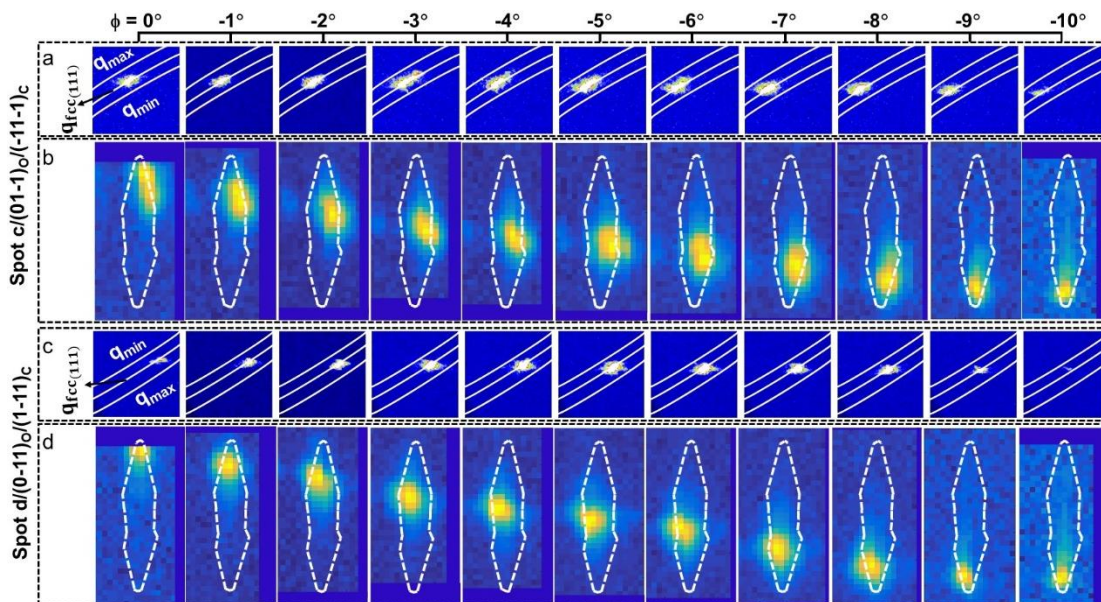
Figure IV.18. Diffraction spots, c and d, and the corresponding diffraction maps. (a,c) Growth and decay of mirror reflections, c and d, for varying ϕ values (4° to -37°), pixel windows (80 × 80). The ϕ values are shown in the top row. The spots are shown enclosed between q_{min} and q_{max} circles (white) obtained by considering the intensity spread of the spot in various frames (for detailed calculation see **Table IV.2**), including those of the symmetry related ones (see **Figure IV.19**) with the circle corresponding to the q value of fcc(111) passing in between. The latter was calculated from the standard fcc Au lattice parameters. The c and d spots appear intense in the ϕ range -2° to -8°. (b,d) Diffraction maps in the real space for different ϕ rotations (4° to -37°). The contour of the crystallite as seen in the XRF image in **Figure IV.1**i is shown as white dashed line to visualize the relative position of the diffracting region. Note, c and d appear from longitudinally opposite halves of the crystallite. Some of the ϕ frames have not been displayed, which contain weak features (see **Figures IV.13** and **IV.21**). From the diffraction maps, the spatial distribution of the planes was elucidated after correlating with the known coordinates of the pixel illuminated by the nanofocused X-ray beam.

Considering the spot c at $\phi = 0°$, which appears on the q_{fcc} arc with radial spread toward both q_{min} and q_{max} (see **Figure 19**a), implies the presence of a combination of fcc and bco lattices. With increasing ϕ from 0° to -2°, the intensity spreading was observed toward the q_{max} arc (nearly touching the q_{max} arc), and the scenario continues until -8° and finally traces

backward toward q_{fcc}, on further increasing ϕ. Thus, from the aforementioned radial spread, one may consider the -2° to -8° region to be rich in bco lattices. The spot also exhibits a circumferential spread ($\sim 2.40°$) at $\phi = 0°$, which accounts for the inherent misorientations, which together with the radial spread indicates the presence of a range of bco unit cells. The centroid of the spot moves circumferentially $\sim 3.70°$ starting from $\phi = 0°$ to $\phi = -10°$, further highlighting the presence of mosaicity. This also may account for the unusual corrugated morphology seen in the SEM image of a tilted crystallite in **Figure IV.1**a.
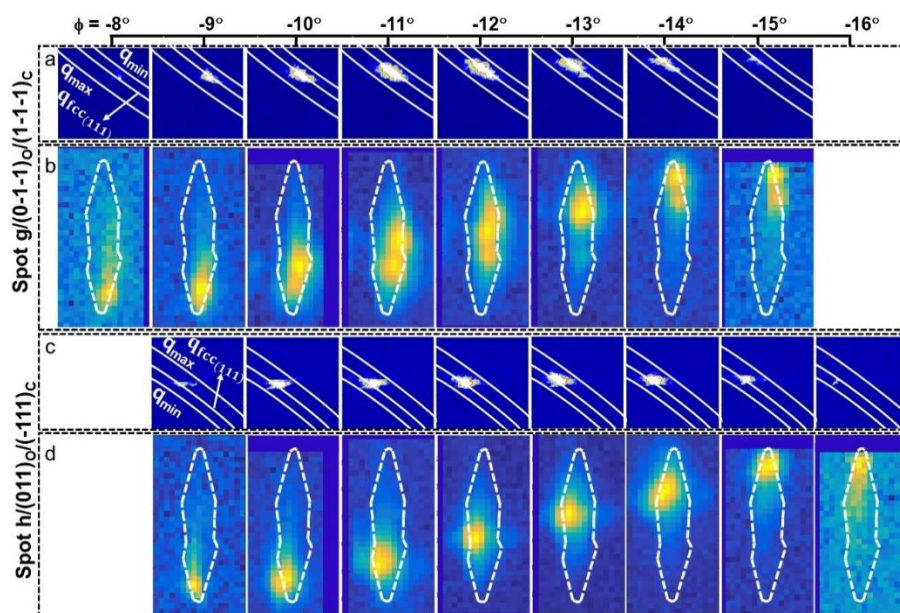
Figure IV.19. Diffraction spots, g and h, and the corresponding diffraction maps. (a,c) Growth and decay of mirror reflections, g and h, for varying ϕ values (4° to -37°) and (b,d) the corresponding diffraction maps. While reflections c and d are dealt with in **Figure IV.18**, the remaining symmetry related reflections namely, g and h, are presented in this figure. The diffraction spots, g and h also exhibit high radial as well as circumferential spreads (also see **Table IV.2**). Among the four, overall circumferential spread is maximum in case of g ($\sim 3.9°$) and the corresponding diffraction maps are also widely spread, particularly along the crystal y-axis implying higher mosaicity. Likewise, the diffracting volumes in both cases (g and h) move from bottom tip of the crystallite to the top (opposite to c and d cases); in g case, from the right side (like c) and in h, from the left (like d). Further, the g spot has contributions primarily from different orientations of crystallites while the h spot from the presence of different lattices.
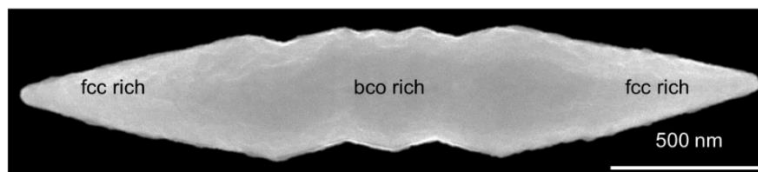
Figure IV.20. Distribution of fcc and bco lattices in the crystallite. SEM image of a Au crystallite shown along with the contribution of the phases.
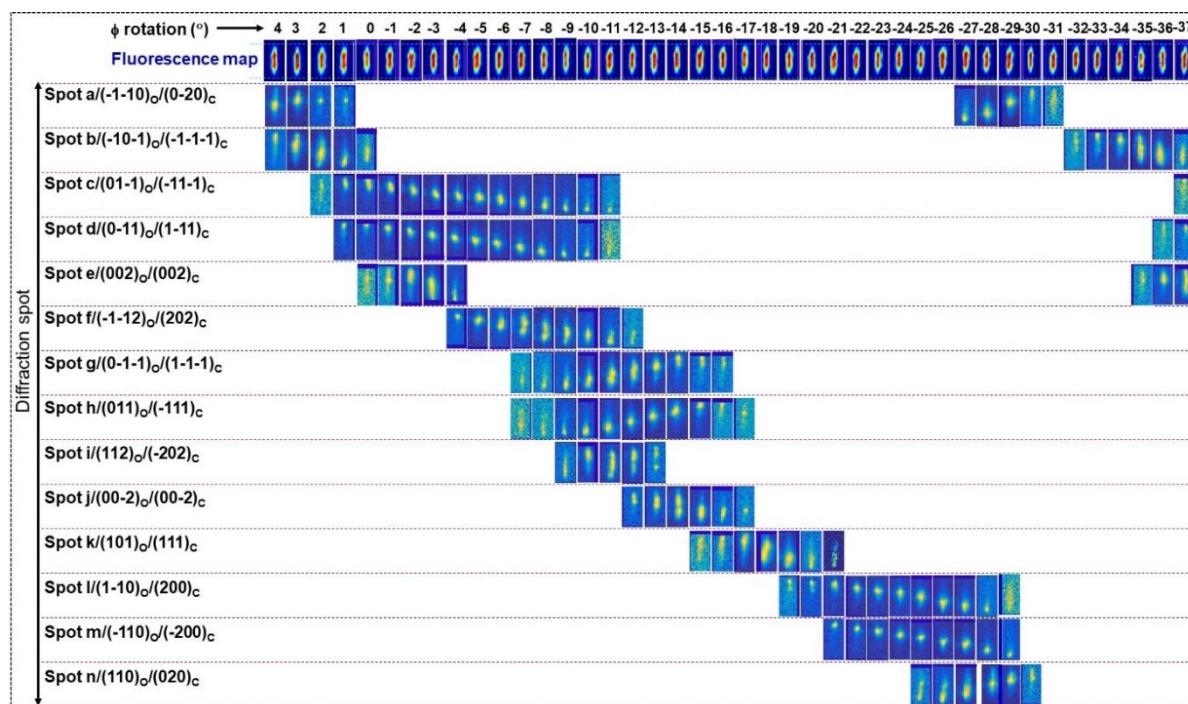
Figure IV.21. Summed up diffraction maps for total ϕ rotation. A collection of all diffraction maps (drift corrected) obtained over different ϕ (4° to -37°) rotations.

The diffraction maps may be invoked to explain the persistence of a spot in a wide range, *i.e.*, to unravel the nature of tiny diffracting volume being probed by the nano-beam. For example for spot c at $\phi = 0°$, the corresponding diffraction volume appears nearly at the top tip and with a rotation of 11°, it moves downward to nearly reach the bottom tip crossing the crystallite body (**Figure IV.18**b). Thus, it appears that the crystallite is made of domains representing systematically rotated diffraction volumes, the total rotation from the top tip to the bottom being 11° (the total rotation is 14° considering frames before 0° and after -10° which contain only weak features). In the range of $\phi = -2°$ to -8°, the diffraction volume is mainly concentrated at the central part of the crystallite, which is also rich in bco lattices (see **Figure IV.20**).

d	Domains under consideration		Angle extended by the domains (°)
	1	3	69
	2	4	78
	3	5	73
	4	1	72
	5	2	68
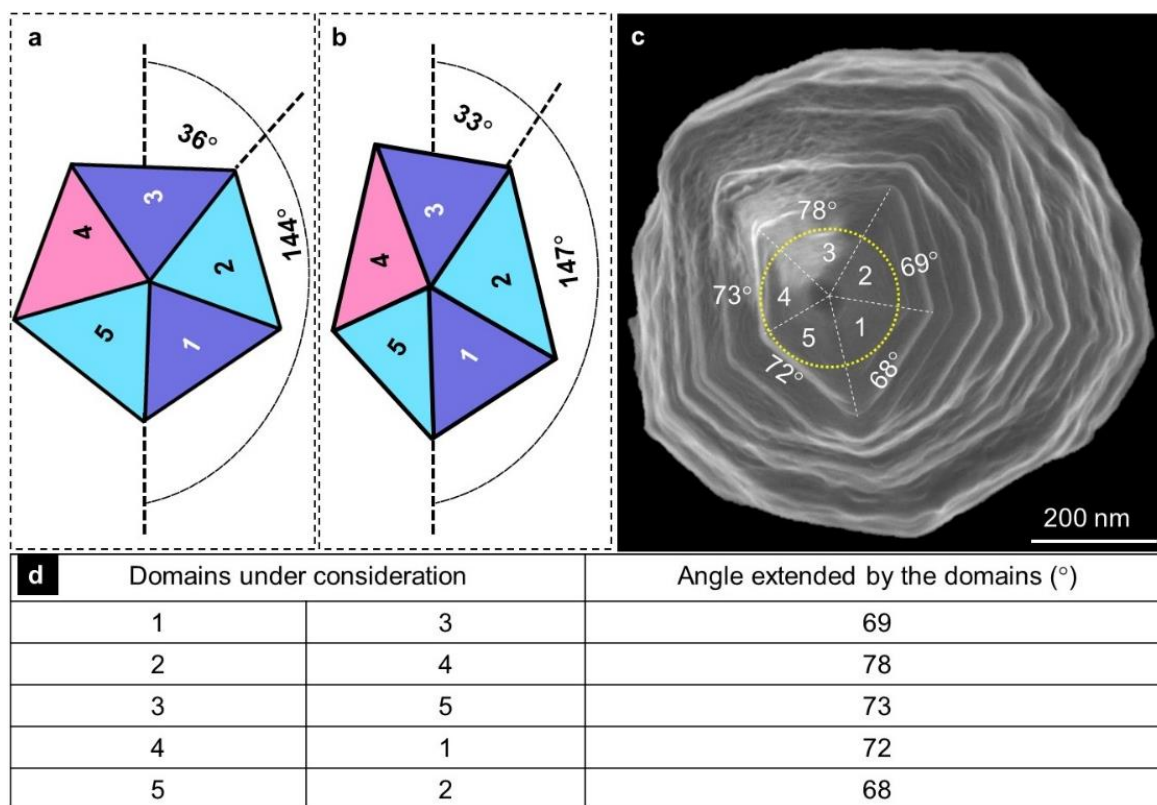
Figure IV.22. The Penta-twinned tip. (a) A penta-twinned geometry introduces reappearance of reflections with a crystal rotation of 36°. The dashed line along the (5,1) boundary is taken as reference. The angle extended by a twin domain is 72° and therefore, it requires (180°- 2×72°) rotation (36°) to make it parallel to the initial position. (b) An example of a nearly penta-twinned geometry of the microcrystallite introducing reappearance of reflections with a rotation of 33°. As the angles are not exactly 36° as required for the perfect 5-fold symmetry, the angles at which the reappearance of reflections takes place are also distributed. Similar observations have been reported in the literature by Canbek *et al.* for example, for Au bipyramidal nanocrystals [30]. (c) The example chosen refers to the SEM image of the tip of the crystallite where the angles and twinned boundaries (white dashed lines) are marked. (d) Angles extended by the twin boundaries as seen from the SEM image are tabulated. This concept is applicable to the entire crystallite.

The reappearance of the spot c at $\phi = -37°$ relates to the crystallite geometry (see **Figure IV.21**). For a perfect penta-twinned geometry, a 36° rotation along the crystal axis leaves the crystal equivalent to 180° rotated position (see **Figure IV.22**a). This observation corroborates with the SEM image of the tip (see the **Figure IV.22**b,c). Thus, experimentally, the repeat angles can vary from 29° to 43° as tabulated in **Table IV.5**.

Table IV.5. Analyzing the repeat angle. From the SEM image (**Figure IV.22**c), the angles of rotation required for the reappearance of reflections have been calculated as below. Note, the angles are distributed within ±7° of the ideal angle, 36°, while the total is 180°.

Adjacent domains under consideration	Total angle extended by adjacent domains (°)	The minimum required angle of rotation (°)
1 and 4	(69 + 78) = 147	(180 - 147) = 33
2 and 5	(78 + 73) = 151	(180 - 151) = 29
3 and 1	(73 + 72) =145	(180 - 145) = 35
4 and 2	(72 + 68) =140	(180 - 140) = 40
5 and 3	(68 + 69) = 137	(180 - 137) = 43
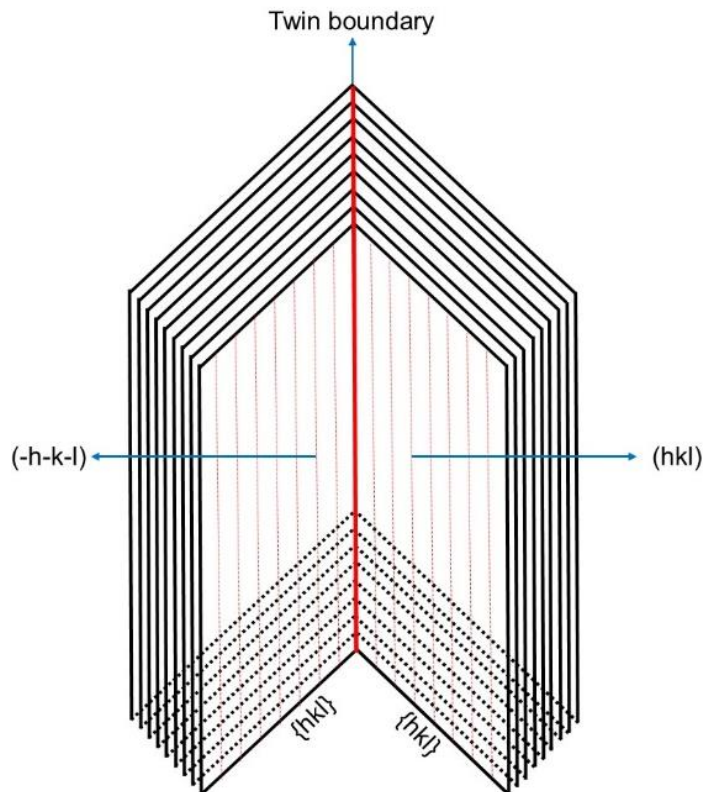
Figure IV.23. Adjacent twins producing mirror reflections. As a twin boundary serves as a mirror, a reflection, (hkl), arising from one of the twin domains at a specific crystal rotation, is accompanied by its symmetry related reflection, (-h-k-l), from the other twin. Previously, Wang *et al.* have shown an illustration of a twin boundary producing mirror related reflections [31].
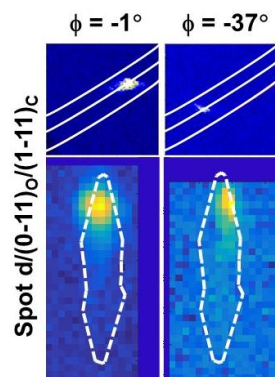
Figure IV.24. Reappearance of diffraction spot, d. The spot d appears in the ϕ range 1° to -11° and reappears as a twin related reflection starting from ϕ = -36° (the higher angle limit falls outside of the data range collected). In the panels above, the spot d as observed at ϕ = -1° is shown along with its twin related reappearance as observed at ϕ = -37° with implicit difference of 36° related to twin relation. In the panels below are shown the diffraction map in relation to the crystal geometry. Note, the diffraction volumes are symmetry related.
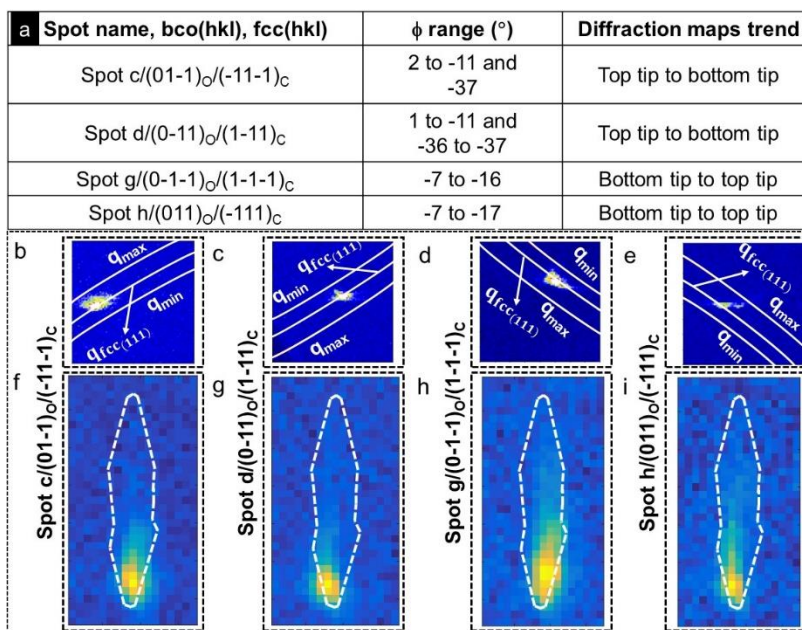
Figure IV.25. Crystal rotation ranges for the diffraction spots, c, d, g, and h. (a) The crystal rotation ranges for the four spots are shown. As seen in (a), the ranges for c and d spots are quite similar and similar is the case for g and h. As the spots being symmetry related form the corners of a rectangle (see **Figure IV.14**a), their co-occurrence in a narrow window of crystal rotation is noteworthy. Indeed, all four were present at ϕ = -9°! This need not be surprising as the different spots originate from different domains, yet symmetry related. Interestingly, the diffracting volumes corresponding to c and d spots appear from top tip at ϕ ~ 2° and move gradually downward to the bottom tip (ϕ = -11°) but from

opposite sides of the crystallite. The trend is opposite with respect to spots g and h. Both diffraction volumes appear from the bottom tip and move upward while being on the opposite sides. It may be noted that the difference in the onset of the two pairs of spots (~ 10°) relates to the twist along the length of the crystallite. (b–e) At ϕ = -9°, the symmetry related diffraction spots, c, d, g, and h are co-present. All four spots appear over the $q_{fcc_{(111)}}$ arc however with varying spreads. (f–i) The diffraction maps corresponding to the symmetry related reflections appear from the bottom tip however with different diffracting volumes corresponding to four different domains.

Table IV.6. Reappearance of reflections. The diffraction spots (see **Figures IV.10** and **IV.13**) reappear after certain degrees of crystal rotation for the microcrystallite employed in the diffraction measurements (different from the one used in SEM imaging and shown in **Figure IV.22**c). Note, the angles are distributed within ±4° of the ideal angle, 36°, which means that the crystallite chosen for diffraction was more closer to being perfect penta-twinning. Out of 14 spots observed, only five reappeared within the range of crystal rotation used in the experiment (4° to -37°). Among the five reflections (tabulated below), the angle 38° comes from spots b and d, *i.e.*, both arise from the same domain. Now, considering the four domains contributing towards the repeat appearance of spots a, b, c, and e, the total repeat angle is 147° and thus, the another angle of rotation will be (5×36°-147°) = 33°.

Diffraction spot	Angle of rotation (°)
a	33
b	38
c	40
d	38
e	36

Similar to the spot c, d also has the first ϕ range from 0° to -10° with reappearance from -36° as in **Figures IV.18**c and **IV.21** (further range was not collected). The spot is seen with much lower radial and circumferential spreads as of c (**Table IV.2**). The spots, c and d, are the mirror related reflections but occur in similar ϕ ranges as the corresponding diffraction volumes belong to different domains of the crystallite; c mainly from the right half, and d, left

half of the twin boundary (**Figures IV.18**b,d and **IV.23**). This explains why the intensity spreads do not match exactly as also their ϕ ranges, 14° and 13°, respectively. The spot d reappears at -36° from the right-hand side of the crystallite after an interval of 38° in contrast to original volume, which was from the left-hand side (see **Figures IV.22**b and **IV.24** for more details), highlighting the internal angle between two twin boundaries (5,1 and 2,3) is (180-38)° = 142° (see **Table IV.6**).

Like the c and d pair, the spots, g and h, are symmetry related with similar q spreads (see **Table IV.2** and **Figure IV.19**), with the difference that the corresponding diffraction volumes move from the bottom tip to the top of the crystallite with ϕ rotation, g from the right side and h from the left. Interestingly, all four spots are co-present in a narrow range of ϕ (~ -9°) as shown in **Figure IV.25**, and so are their diffracting volumes from near the bottom tip, however, from neighboring domains.

A similarly treatment was followed for (b,k), (m,n,l,a), (e,j), and (f,i) sets of symmetry related spots after estimating the corresponding (q_{min}, q_{max}) sets of values as tabulated in **Table IV.2**. From the $(hkl)_O$ assignments from **Figure IV.12**, bco_{max} and bco_{min} lattice parameters were arrived at, a_{min} = 2.8005 Å, b_{min} = 2.8435 Å, c_{min} = 4.0089 Å, and a_{max} = 2.9396 Å, b_{max} = 2.9226 Å, c_{max} = 4.1223 Å, respectively, as tabulated in **Table IV.7** (see details calculation below). Thus, one may consider the presence of fcc, bco_{min} and bco_{max} lattices in the given crystallite as shown in **Figure IV.26**, although the latter two represent the two extremes, while in reality, a range of bco lattices may be present in the crystallite. The volume corresponding to bco_{min}, bco_{max} and fcc are 31.9237, 35.4158, and 33.9836 $Å^3$ (per two atoms), respectively. The bco_{min} cell possesses 6.06% less volume compared to that of fcc, while the bco_{max} cell 4.21% more volume.

Table IV.7. Calculating bco lattice parameters. Table shows the lattice parameters of the bco_{min} and bco_{max} unit cells calculated using the q_{max} and q_{min} values.

	Experimentally obtained *d*-spacings					Calculated lattice parameters		
	d_{101} (Å)	d_{011} (Å)	d_{110} (Å)	d_{002} (Å)	d_{112} (Å)	*a* (Å)	*b* (Å)	*c* (Å)
q_{max}	2.2958	2.3197	1.9953	1.9953	1.4286	2.8005	2.8435	4.0089
q_{min}	2.3934	2.3842	2.0726	2.0792	1.4523	2.9396	2.9226	4.1223

Calculation of bco lattice parameters:

$$\frac{1}{d_{hkl}^2} = \frac{h^2}{a^2} + \frac{k^2}{b^2} + \frac{l^2}{c^2} \qquad (3)$$

$$\frac{1}{d_{101}^2} = \frac{1}{a^2} + \frac{1}{c^2} \qquad (4)$$

$$\frac{1}{d_{011}^2} = \frac{1}{b^2} + \frac{1}{c^2} \qquad (5)$$

$$\frac{1}{d_{110}^2} = \frac{1}{a^2} + \frac{1}{b^2} \qquad (6)$$

By subtracting (3) from (2),

$$\frac{1}{d_{101}^2} - \frac{1}{d_{011}^2} = \frac{1}{a^2} - \frac{1}{b^2} \qquad (7)$$

By adding (4) and (5),

$$\frac{1}{d_{110}^2} + \frac{1}{d_{101}^2} - \frac{1}{d_{011}^2} = \frac{2}{a^2} \qquad (8)$$

Taking q_{max} value from **Table IV.7**, $d_{101} = 2.2958$, $d_{011} = 2.3197$ and $d_{110} = 1.9953$ Å

Inserting the d_{101}, d_{011} and d_{110} values (from q_{max}) in equation (8),

$$\frac{1}{(2.2958)^2} - \frac{1}{(2.3197)^2} + \frac{1}{(1.9953)^2} = \frac{2}{a^2}$$

$$\frac{2}{a^2} = 0.2550$$

$$a^2 = 7.8431$$

$$a_{min} = 2.8005 \text{ Å}$$

Inserting the value of a in equation (4),

$$c_{min} = 4.0089 \text{ Å}$$

Inserting the value of a in equation (6),

$$b_{min} = 2.8435 \text{ Å}$$

Therefore, the lattice parameters of bco$_{min}$ are a_{min} = 2.8005, b_{min} = 2.8435, c_{min} = 4.0089 Å as shown in **Table IV.7**.

Similarly, from the q$_{min}$ in **Table IV.7**, d_{101} = 2.3934, d_{011} = 2.3842 and d_{110} = 2.0726 Å

Inserting the d_{101}, d_{011} and d_{110} values (from q$_{min}$) in equation (8),

$$\frac{1}{(2.3934)^2} - \frac{1}{(2.3842)^2} + \frac{1}{(2.0726)^2} = \frac{2}{a^2}$$

$$\frac{2}{a^2} = 0.2314$$

$$a^2 = 8.6414$$

$$a_{max} = 2.9396 \text{ Å}$$

Inserting the value of a in equation (4),

$$c_{max} = 4.1223 \text{ Å}$$

Inserting the value of a in equation (6)

$$b_{max} = 2.9226 \text{ Å}$$

Therefore, the lattice parameters of bco$_{max}$ are a_{max} = 2.9396, b_{max} = 2.9226, c_{max} = 4.1223 Å as shown in **Table IV.7**.
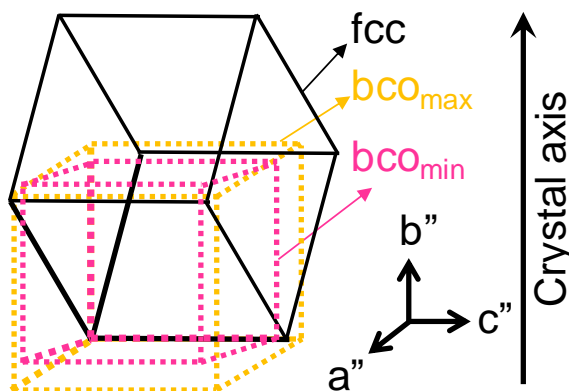
Figure IV.26. Presence of various unit cells. A representation of fcc, bco$_{min}$ and bco$_{max}$ unit cells in the crystallite. The bco$_{min}$ and bco$_{max}$ unit cells have been shown in magenta and orange colors, respectively.

Specific mention should be made of the spot b occurring along the horizontal line assignable to bco(-10-1)/fcc(-1-1-1) planes, which are parallel to the crystal axis (see **Figures IV.2**1 and **IV.2**7). It is therefore not surprising that the spot b occurs in a narrow range of

ϕ (4° to 0° and -32° to -37°). In the diffraction map (**Figure IV.27**b), the corresponding volume appears to switch sides from left to right halfway through, a scenario which repeats itself from ϕ (-32° to -37°) as shown in **Figure IV.27**b. This is understandable due to the presence of twist along the crystallite longitudinal direction. With this spot, the circumferential spread is high even in a single frame ($\sim 4.10°$ at $\phi = -35°$) as shown in **Figure IV.28**a, and the diffraction volume is also spread out considerably longitudinally, indicating that the corresponding domains are misoriented along the crystal axis (see **Figure IV.28**b,c). Interestingly, the repeat diffraction spots elucidate the coexistence of bco_{min} and bco_{max} lattices (as shown in **Figure IV.27**a). The mirror related spot k, bco(101)/fcc(111) appears much later, beyond ϕ of -15° and continues for another 6° (see **Figures IV.13** and **IV.21**). From the large radial spread (~ 1.117 nm^{-1}), it is clear that the spot has contributions from various lattices, bco_{min} to bco_{max} including fcc, while circumferential spread of 1.15° indicates that the corresponding domains are relatively less misoriented compared to those associated with the spot b (see **Figure IV.27**c,d and **Table IV.2**).
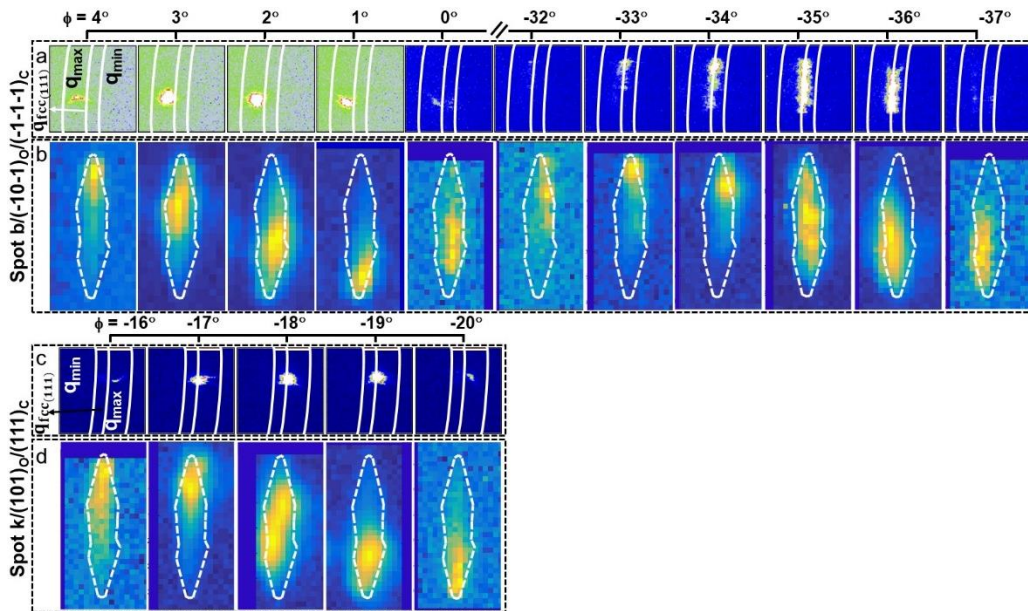
Figure IV.27. Diffraction spots, b and k, and the corresponding diffraction maps. (a,c) Growth and decay of horizontal mirror reflections, b and k, for varying ϕ values (4° to -37°) and (b,d) the corresponding diffraction maps, similar to **Figure IV.18**. The wide spread spots have been covered by the ranges of absolute q_{min} and q_{max} circles (for detailed calculation see **Table IV.2**). The diffraction spot, b appears at $\phi = 4°$ to 0° and reappears at ϕ range of -32° to -37°. The position of the spot is quite different in both the ϕ ranges. At the 1st ϕ range, the spot is towards the q_{max}, while in the latter range,

the spot is towards the q_{min}. In addition to the radial spread, the spots exhibit different circumferential spreads. For example, the circumferential spread at $\phi = 3°$ and -35° are ~ 1.95° and 4.1°, respectively accounting for the anisotropic distribution of lattices. The diffraction maps corresponding to those ϕ show different distribution of diffracting volumes, again emphasizing upon different domains contributing towards the repeat appearance of the spot. The ϕ spreads for both the spots b and k are ~ 6°. Spots b, k contribute to longitudinal direction planes in the crystallite volume.
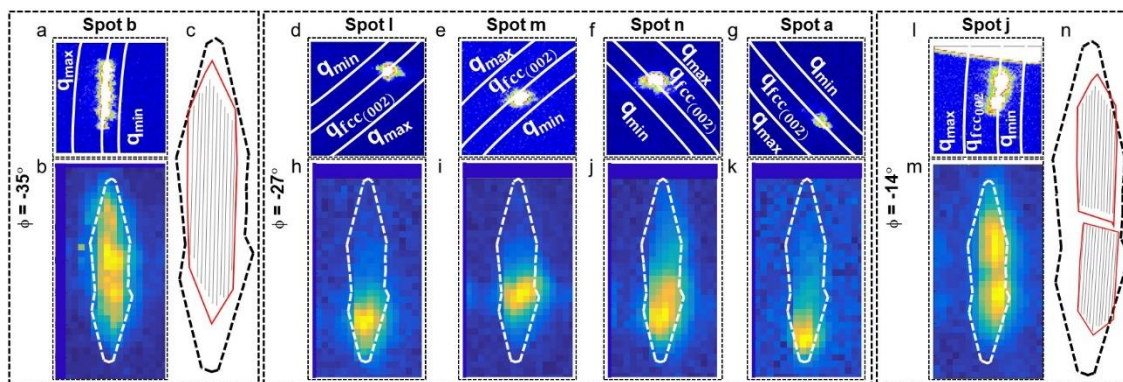
Figure IV.28. Correlating the additional features of the diffraction spots and the corresponding diffraction maps. (a,b) The widespread spot b at $\phi = -35°$ and the contributing diffracting volume containing $(-10-1)_O/(-1-1-1)_C$ along the longitudinal direction as in schematic (c). (d−g) Simultaneous appearance of symmetry related diffraction spots (m,n,l,a) at $\phi = -27°$ and (h−k) the corresponding diffracting volumes of the crystallite, as depicted in the diffraction maps. (l,m) The widespread spot j at $\phi = -14°$ and the contributing diffracting volume containing $(00-2)_O/(00-2)_C$ along the longitudinal direction as in schematic (n).

The (m,n,l,a) set of spots assigned to bco{110}/fcc{200}behave similar to the set (c,h,d,g), the difference is that in the former domains from the central part of the crystallite participate (not the right or the left, for more details see **Figures IV.21**, **IV.29** and **IV.30**). The concurrent appearance of the symmetry related diffraction spots (m,n,l,a) at $\phi = -27°$ made to study in detail the variations in the radial as well circumferential spreads for the family of reflections (**Figure IV.28**d−g). The spreads are non-uniform and so are their diffracting volumes, representing varied strain across the crystallite volume (**Figure IV.28**h−k), which goes well with the literature of Au decahedra [32]. The radial spread being relatively high for spots m and n, the corresponding diffraction volume, namely the body of the crystallite, seems to host larger strain compared to the tips (see spreads from spots l and a in **Figure IV.28**d−k).

Figure IV.29. Diffraction spots, l and m, and the corresponding diffraction maps. (a,c) Growth and decay of mirror reflections, l and m, for varying ϕ values (4° to -37°) and (b,d) the corresponding diffraction maps, similar to **Figure IV.18**. The wide spread spots have been covered by the ranges of absolute q_{min} and q_{max} circles (for detailed calculation see **Table IV.2**). The arcs of the circles (white line) along with the $q_{fcc_{(002)}}$ arc in between have been drawn over the spots. The q_{fcc} has been calculated from the standard fcc Au lattice parameters. The diffraction maps corresponding to spots c and d appear from two halves of the crystallite, whereas the l and m appear from the middle part of the crystallite. The diffracting volume is quite small compared to the spots c and d, although the trend is similar from top tip to the bottom. Although, the diffracting volume is small, the diffraction spots have very high radial spread.

Similar to (b,k), the other pair of reflections (e,j) occurring in the horizontal line are assignable to bco{002}/fcc{002} as shown in **Figure IV.31.** The curvy nature of the intensity spread stands for the simultaneous presence of multiple lattices although slightly different from each other. The diffraction maps for spot j ($\phi = -14°$) clearly show top and bottom halves of the crystallite (**Figure IV.28**l–n), illustrating the planes are along the growth direction and linked to the observed morphology in the SEM (**Figure IV.1**a). The other two reflections (f,i) can be assigned to bco{112}/fcc{202} (see **Figure IV.32**). The integrated diffraction spots have been used to quantify the bco and fcc lattices in the crystallite volume, where the former being $\sim 82\%$ as shown in **Figure IV.33**.
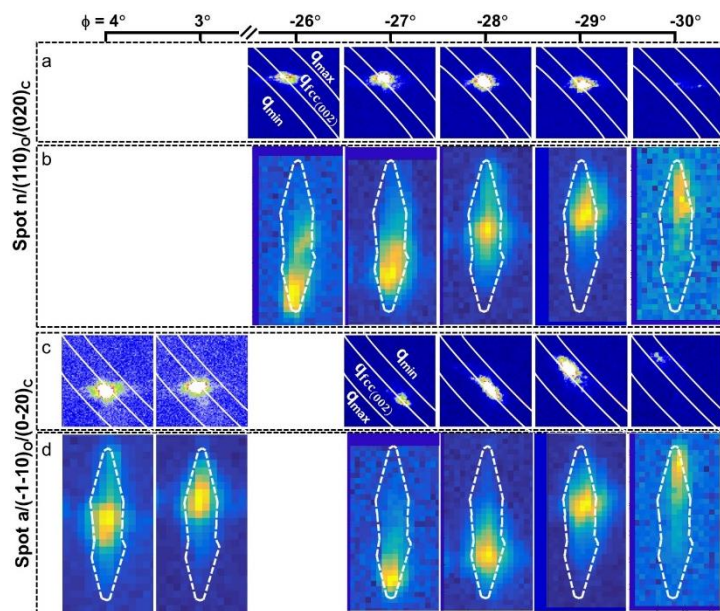
Figure IV.30. Diffraction spots, n and a, and the corresponding diffraction maps. (a,c) Growth and decay of mirror reflections, n and a, for varying ϕ values (4° to -37°) and (b,d) the corresponding diffraction maps, similar to **Figure IV.29**. The diffraction spots l, m, n, and a are family of reflections and simultaneously appear at ϕ = -27° (see details in **Figure IV.28**d–k). Interestingly, the l, m appear with a trend of top tip to the bottom while the n, a appear from bottom to the top. The appearance of all symmetry reflections without rotating the crystal for 360° is achieved due to symmetry.
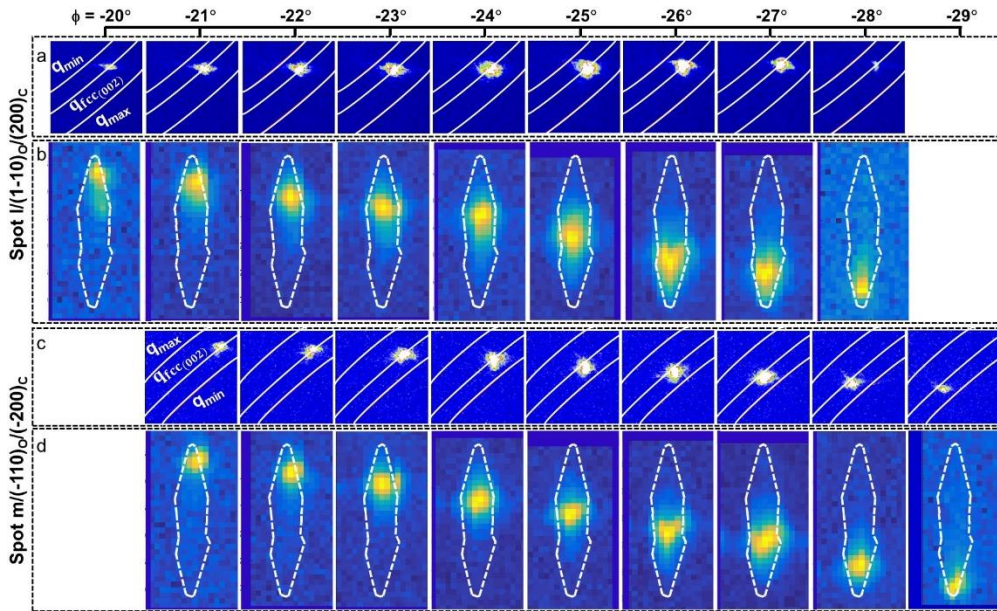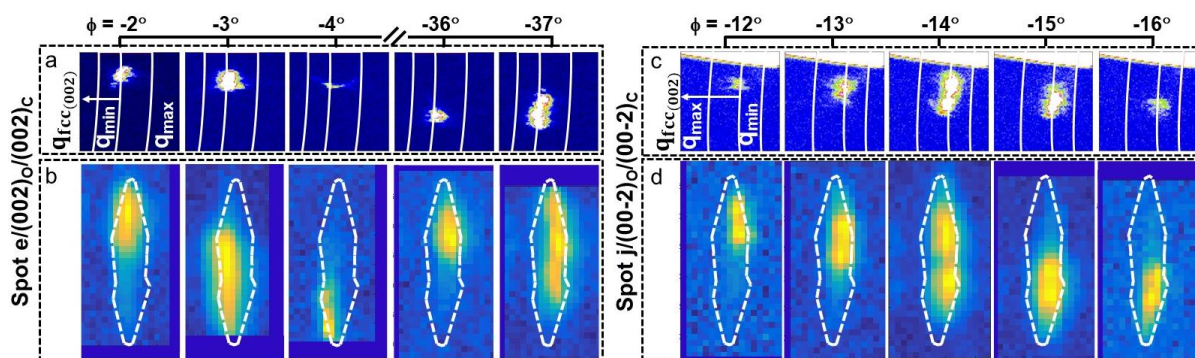

Figure IV.31. Diffraction spots, e and j, and the corresponding diffraction maps. (a,c) Growth and decay of mirror reflections, e and j, for varying ϕ values (4° to -37°) and (b,d) the corresponding diffraction maps, similar to **Figure IV.18**. The wide spread spots have been covered by the ranges of absolute q_{min} and q_{max} circles (for detailed calculation see **Table IV.2**). The diffraction spots e, j contribute to longitudinal direction planes in the crystallite volume.
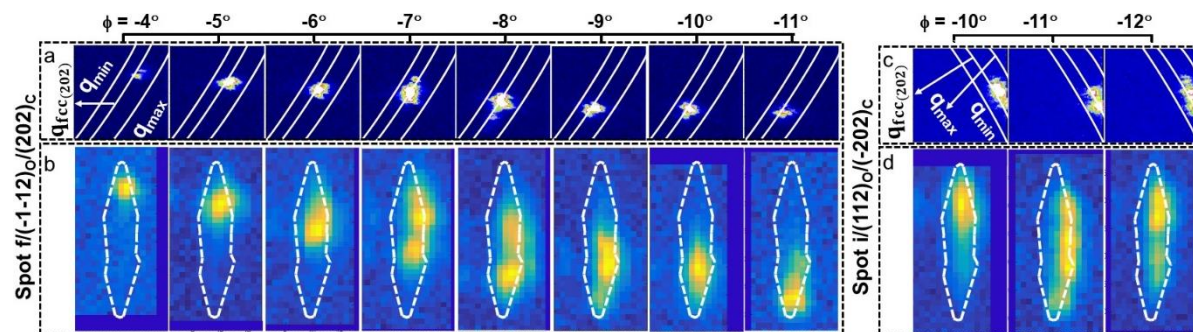
Figure IV.32. Diffraction spots, f and i, and the corresponding diffraction maps. (a,c) Growth and decay of symmetry related reflections, f and i, for varying ϕ values (4° to -37°) and (b,d) the corresponding diffraction maps, similar to **Figure IV.18**. The wide spread spots have been covered by the ranges of absolute q_{min} and q_{max} circles (for detailed calculation see **Table IV.2**). The arcs of the circles (white line) along with the $q_{fcc_{(202)}}$ arc in between have been drawn over the spots. The q_{fcc} has been calculated from the standard fcc Au lattice parameters.

The above results corroborate with the crystal morphology seen from the SEM images (**Figure IV.1**a,b) as also with TEM and powder XRD data from the earlier studies [14,27]. The crystal under study possesses a bipyramidal geometry with penta-twinned tips. This may very well explain the observations made during synthesis and optimization that the occurrence of bc(o,t) phases is limited to a narrow temperature window which may have led to accumulation of internal stress as the decahedral nuclei grow and eventual deviation from the cubic lattice [14,33]. Previous studies using TEM have shown the presence of lattice expansion in Au decahedra to the extent of ~ 5% [34,35] in its fcc lattice. The reminiscence of the 5-fold symmetry seen at the tips prevails along the body of the crystallite, although the latter is made up of mainly bco lattices due to increased strain. The study allows to both visualize and characterize the possible ranges of the bco unit cells between bco_{min} and bco_{max} in the crystallite volume as shown in **Figure IV.26**.

Surprisingly, the study has shown the co-presence of compression (6.06% for bco_{min}) and expansion (4.21% for bco_{max}) of the bco unit cells, in comparison to fcc. Several electron microscopy studies regarding the growth mechanism of the bipyramid starting with decahedra nanoparticle show growth along fcc $\langle 110 \rangle$ direction [18,36,37]. The primary difficulty to understand the growth mechanism through these electron microscopy studies was due to the presence of penta-twinned geometry and inhomogeneity among the five segments and lack of data from the bulk of the crystallites as TEM could be done only from edges and tips of

microcrystallites unless crystallites are very small [14,15]. Here, the bco unit cell borne out of distortion in the fcc cell is situated at an angle of 45°, which dictates the crystal growth direction (⟨010⟩ and ⟨110⟩ for bco and fcc, respectively) as shown in **Figure IV.14**b. Therefore, the SXDM data is in coherence with the previously observed growth direction of fcc bipyramid [33,36,37].
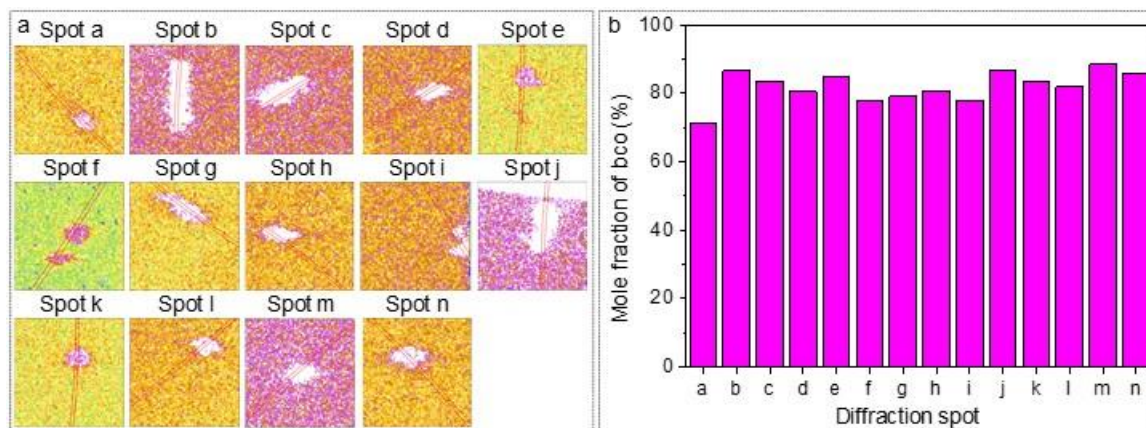
Figure IV.33. Calculation of bco contribution. (a) Contribution of fcc lattice has been calculated by drawing two co-centric circles with radii of q_{fcc} ±0.04 nm^{-1} over the integrated diffraction spots. The red lines represent the arcs. Thus, the integrated intensity of the pixels in between the two arcs represents fcc contribution, whereas the rest of the intensity, that of bco. (b) bco mole fraction values as estimated using different diffraction spots. The bco contribution has been underestimated since the background makes it difficult to consider weaker part of the intensity spread.

The five domains of the crystallite contain a range of the bco unit cells, which is understandable from the varied intensity spreads of the symmetry related reflections for both radial and circumferential directions, as seen for example, for the (c,h,d,g) spots in **Figure IV.25**. The fact that the spread varies within a given family of reflections highlights the variations in their geometrical origins as well as anisotropy in the crystallite. In all, it appears that there are two sets of mirror related domains, for example, c,d and g,h, one propagating from the top tip while the other propagating from the bottom. Considering the strain inherent to the crystal [32], it is indeed surprising that the four distinct diffracting regions follow symmetry as though arising from a single domain, as seen from the varied ranges of inter-reflection angles extended in between the pairs, m,n and l,a are ∼ 83.50°-91.20°, and 88.35°-96.70°, respectively. Relating the diffraction spots with the corresponding diffraction maps, it was realized that the crystallite exhibits an inherent twist of ∼ 6° from the top tip to

the bottom (**Figures IV.27** and **IV.31**). The central part of the crystallite appears to be dominated by bco lattices as the spreads, particularly the circumferential spreads, are higher (see **Figure IV.22**). Therefore, the crystallite volume was considered to consist of three regions, the strained body and less strained tips (shown in **Figure IV.20**). Similarly, these insights may provide useful information with regard to exuberant catalytic activity exhibited by the crystallites [15]. One may also design experiments to study catalysis at the single crystallite level.

Unraveling the exact spatial distribution differentiation of the bct and bco lattices is difficult to achieve and especially, considering the presence of ranges of lattice parameters. The route to the generation of the bco is *via* the bct (exactly, fcc to bct to bco) and therefore, the growth directions will be same in both cases. Additionally, bct is a subset of bco (where $a = b$) and therefore, will exhibit similar reflections. Hence, it may be considered that the central part of the crystallite is enriched with bc(o,t) lattices. The presence of large strains and defects arisen from morphology (twist and twin boundaries) may contribute for the lower intensity in powder XRD pattern, when compared to the fcc Au pattern (refer **Chapter III**).

IV.5 Conclusions

In summary, this diffraction microscopy study brings out the nature of the diffracting regions within a penta-twinned bipyramidal Au crystallite of length $\sim$ 1.36 μm and central diameter, $\sim$ 230 nm, hosting non-cubic (bco) phases. The collected diffraction spots appeared rather broad (circumferential spread or mosaicity, $\sim$ 2.91°). The radial spread associated with each spot is on an average 0.876 nm^{-1}, signifying the presence of a range of bco cells compressed and expanded with respect to the fcc. Both types of spreads may relate to the inherent strain in the crystal. Within the -42° crystal rotation employed, in all, 14 spots appeared forming five symmetry sets, each set assignable to both fcc and bco reflections. The sets are thus assigned to bco{011}/fcc{111}, bco{101}/fcc{111}, bco{110}/fcc{002}, bco{002}/fcc{002}, and bco{112}/fcc{202}. The occurrence of the symmetry related reflections within a narrow range of crystal rotation relates to the penta-twinned crystal geometry. TEM literatures narrate the growth of the fcc bipyramids to be in the ⟨110⟩ direction. Interestingly, the presented SXDM results here reconfirm the growth direction of the crystallites to be fcc ⟨110⟩, and given the crystal geometry, this is closely related to bco ⟨010⟩.

Successfully, the fcc and bco phases have been mapped within the volume of the chosen crystallite based on diffraction microscopy. Accordingly, the bco phase seems to form the body of the crystallite while the fcc resides in the tips. The two halves of the bipyramid lattices are found to be twisted as evidenced by the drifting of the diffracting volume along the crystal length by $\sim 6°$. An in-depth understanding of the distribution of bco and fcc in the central part and the tips demand further studies.

References

[1] J. Diao, K. Gall, and M. L. Dunn, *Surface-Stress-Induced Phase Transformation in Metal Nanowires*, Nat. Mater. **2**, 656 (2003).

[2] H. Zheng, A. Cao, C. R. Weinberger, J. Y. Huang, K. Du, J. Wang, Y. Ma, Y. Xia, and S. X. Mao, *Discrete Plasticity in Sub-10-nm-Sized Gold Crystals*, Nat. Commun. **1**, 144 (2010).

[3] X. Liu, J. Luo, and J. Zhu, *Size Effect on the Crystal Structure of Silver Nanowires*, Nano Lett. **6**, 408 (2006).

[4] A. Singh and A. Ghosh, *Stabilizing High-Energy Crystal Structure in Silver Nanowires with Underpotential Electrochemistry*, J. Phys. Chem. C **112**, 3460 (2008).

[5] I. Chakraborty, D. Carvalho, S. N. Shirodkar, S. Lahiri, S. Bhattacharyya, R. Banerjee, U. Waghmare, and P. Ayyub, *Novel Hexagonal Polytypes of Silver: Growth, Characterization and First-Principles Calculations*, J. Phys. Condens. Matter **23**, 325401 (2011).

[6] I. Chakraborty, S. N. Shirodkar, S. Gohil, U. V. Waghmare, and P. Ayyub, *The Nature of the Structural Phase Transition from the Hexagonal (4H) Phase to the Cubic (3C) Phase of Silver*, J. Phys. Condens. Matter **26**, 115405 (2014).

[7] I. Chakraborty, S. N. Shirodkar, S. Gohil, U. V. Waghmare, and P. Ayyub, *A Stable, Quasi-2D Modification of Silver: Optical, Electronic, Vibrational and Mechanical Properties, and First Principles Calculations*, J. Phys. Condens. Matter **26**, 025402 (2014).

[8] X. Huang, S. Li, Y. Huang, S. Wu, X. Zhou, S. Li, C. L. Gan, F. Boey, C. A. Mirkin, and H. Zhang, *Synthesis of Hexagonal Close-Packed Gold Nanostructures*, Nat. Commun. **2**, 292 (2011).

[9] Z. Fan, M. Bosman, X. Huang, D. Huang, Y. Yu, K. P. Ong, Y. A. Akimov, L. Wu, B. Li, J. Wu, Y. Huang, Q. Liu, C. Eng Png, C. Lip Gan, P. Yang, and H. Zhang, *Stabilization of 4H Hexagonal Phase in Gold Nanoribbons*, Nat. Commun. **6**, 7684 (2015).

[10] J. L. Huang, Z. Li, H. H. Duan, Z. Y. Cheng, Y. D. Li, J. Zhu, and R. Yu, *Formation of Hexagonal-Close Packed (hcp) Rhodium as a Size Effect*, J. Am. Chem. Soc. **139**, 575 (2017).

[11] K. Kusada, H. Kobayashi, T. Yamamoto, S. Matsumura, N. Sumi, K. Sato, K. Nagaoka, Y. Kubota, and H. Kitagawa, *Discovery of Face-Centered-Cubic Ruthenium Nanoparticles: Facile Size-Controlled Synthesis Using the Chemical Reduction Method*, J. Am. Chem. Soc. **135**, 5493 (2013).

[12] Y. Sun, Y. Ren, Y. Liu, J. Wen, J. S. Okasinski, and D. J. Miller, *Ambient Stable Tetragonal Phase in Silver Nanostructures*, Nat. Commun. **3**, 971 (2012).

[13] Z. Li, J. S. Okasinski, J. D. Almer, Y. Ren, X. Zuo, and Y. Sun, *Quantitative Determination of Fragmentation Kinetics and Thermodynamics of Colloidal Silver Nanowires by in Situ High-Energy Synchrotron X-ray Diffraction*, Nanoscale **6**, 365 (2014).

[14] G. Mettela, M. Bhogra, U. V. Waghmare, and G. U. Kulkarni, *Ambient Stable Tetragonal and Orthorhombic Phases in Penta-Twinned Bipyramidal Au Microcrystals*, J. Am. Chem. Soc. **137**, 3024 (2015).

[15] G. Mettela, N. Mammen, J. Joardar, S. Narasimhan, and G. U. Kulkarni, *Non-fcc Rich Au Crystallites Exhibiting Unusual Catalytic Activity*, Nano Res. **10**, 2271 (2017).

[16] Q. Li, W. Niu, X. Liu, Y. Chen, X. Wu, X. Wen, Z. Wang, H. Zhang, and Z. Quan, *Pressure-Induced Phase Engineering of Gold Nanostructures*, J. Am. Chem. Soc. **140**, 15783 (2018).

[17] X. Huang, S. Li, S. Wu, Y. Huang, F. Boey, C. L. Gan, and H. Zhang, *Graphene Oxide-Templated Synthesis of Ultrathin or Tadpole-Shaped Au Nanowires with Alternating hcp and fcc Domains*, Adv. Mater. **24**, 979 (2012).

[18] A. Sánchez-Iglesias, N. Winckelmans, T. Altantzis, S. Bals, M. Grzelczak, and L. M. Liz-Marzán, *High-Yield Seeded Growth of Monodisperse Pentatwinned Gold Nanoparticles through Thermally Induced Seed Twinning*, J. Am. Chem. Soc. **139**, 107 (2017).

[19] R. Arenal, L. Henrard, L. Roiban, O. Ersen, J. Burgin, and M. Treguer-Delapierre, *Local Plasmonic Studies on Individual Core–Shell Gold–Silver and Pure Gold Nano-Bipyramids*, J. Phys. Chem. C **118**, 25643 (2014).

[20] F. Hofmann, R. J. Harder, W. Liu, Y. Liu, I. K. Robinson, and Y. Zayachuk, *Glancing-Incidence Focussed Ion Beam Milling: A Coherent X-ray Diffraction Study of 3D Nano-Scale Lattice Strains and Crystal Defects*, Acta Mater. **154**, 113 (2018).

[21] P. Thibault, M. Dierolf, A. Menzel, O. Bunk, C. David, and F. Pfeiffer, *High-Resolution Scanning X-ray Diffraction Microscopy*, Science **321**, 379 (2008).

[22] T. Stankevič, E. Hilner, F. Seiboth, R. Ciechonski, G. Vescovi, O. Kryliouk, U. Johansson, L. Samuelson, G. Wellenreuther, G. Falkenberg, R. Feidenhans'l, and A. Mikkelsen, *Fast Strain Mapping of Nanowire Light-Emitting Diodes Using Nanofocused X-ray Beams*, ACS Nano **9**, 6978 (2015).

[23] T. Stankevič, D. Dzhigaev, Z. Bi, M. Rose, A. Shabalin, J. Reinhardt, A. Mikkelsen, L. Samuelson, G. Falkenberg, I. A. Vartanyants, and R. Feidenhans'l, *Strain Mapping in an InGaN/GaN Nanowire Using a Nano-Focused X-ray Beam*, Appl. Phys. Lett. **107**,

103101 (2015).

[24] T. Stankevič, D. Dzhigaev, Z. Bi, M. Rose, A. Shabalin, J. Reinhardt, A. Mikkelsen, L. Samuelson, G. Falkenberg, I. A. Vartanyants, and R. Feidenhans'l, *Nanofocused X-ray Beams Applied for Mapping Strain in Core-Shell Nanowires*, Proc. SPIE **9592**, 95920D (2015).

[25] C. G. Schroer, P. Boye, J. M. Feldkamp, J. Patommel, D. Samberg, A. Schropp, A. Schwab, S. Stephan, G. Falkenberg, G. Wellenreuther, and N. Reimers, *Hard X-ray Nanoprobe at Beamline P06 at PETRA III*, Nucl. Instrum. Methods Phys. Res., Sect. A **616**, 93 (2010).

[26] L. Dubrovinsky, N. Dubrovinskaia, W. A. Crichton, A. S. Mikhaylushkin, S. I. Simak, I. A. Abrikosov, J. S. De Almeida, R. Ahuja, W. Luo, and B. Johansson, *Noblest of All Metals Is Structurally Unstable at High Pressure*, Phys. Rev. Lett. **98**, 45503 (2007).

[27] G. Mettela, Y. A. Sorb, A. Shukla, C. Bellin, V. Svitlyk, M. Mezouar, C. Narayana, and G. U. Kulkarni, *Extraordinarily Stable Noncubic Structures of Au: A High-Pressure and -Temperature Study*, Chem. Mater. **29**, 1485 (2017).

[28] Y. Sun, Y. Ren, Y. Liu, J. Wen, J. S. Okasinski, and D. J. Miller, *Ambient-Stable Tetragonal Phase in Silver Nanostructures*, Nat. Commun. **3**, 971 (2012).

[29] A. Stierle, T. F. Keller, H. Noei, V. Vonk, and R. Roehlsberger, *DESY NanoLab*, J. Large-Scale Res. Facil. JLSRF **2**, 1 (2016).

[30] Z. C. Canbek, R. Cortes-Huerto, F. Testard, O. Spalla, S. Moldovan, O. Ersen, A. Wisnet, G. Wang, J. Goniakowski, C. Noguera, and N. Menguy, *Twinned Gold Nanoparticles under Growth: Bipyramids Shape Controlled by Environment*, Cryst. Growth Des. **15**, 3637 (2015).

[31] Z. L. Wang, M. B. Mohamed, S. Link, and M. A. El-Sayed, *Crystallographic Facets and Shapes of Gold Nanorods of Different Aspect Ratios*, Surf. Sci. **440**, L809 (1999).

[32] C. L. Johnson, E. Snoeck, M. Ezcurdia, B. Rodríguez-González, I. Pastoriza-Santos, L. M. Liz-Marzán, and M. J. Htch, *Effects of Elastic Anisotropy on Strain Distributions in Decahedral Gold Nanoparticles*, Nat. Mater. **7**, 120 (2008).

[33] G. Mettela, R. Boya, D. Singh, G. V. P. Kumar, and G. U. Kulkarni, *Highly Tapered Pentagonal Bipyramidal Au Microcrystals with High Index Faceted Corrugation: Synthesis and Optical Properties*, Sci. Rep. **3**, 1793 (2013).

[34] M. J. Walsh, K. Yoshida, A. Kuwabara, M. L. Pay, P. L. Gai, and E. D. Boyes, *On the Structural Origin of the Catalytic Properties of Inherently Strained Ultrasmall Decahedral Gold Nanoparticles*, Nano Lett. **12**, 2027 (2012).

[35] B. Goris, J. De Beenhouwer, A. De Backer, D. Zanaga, K. J. Batenburg, A. Sánchez-Iglesias, L. M. Liz-Marzán, S. Van Aert, S. Bals, J. Sijbers, and G. Van Tendeloo, *Measuring Lattice Strain in Three Dimensions through Electron Microscopy*, Nano Lett. **15**, 6996 (2015).

[36] M. Liu and P. Guyot-Sionnest, *Mechanism of Silver(I)-Assisted Growth of Gold*

Nanorods and Bipyramids, J. Phys. Chem. B **109**, 22192 (2005).

[37]   G. Zhou, Y. Yang, S. Han, W. Chen, Y. Fu, C. Zou, L. Zhang, and S. Huang, *Growth of Nanobipyramid by Using Large Sized Au Decahedra as Seeds*, ACS Appl. Mater. Interfaces **5**, 13340 (2013).
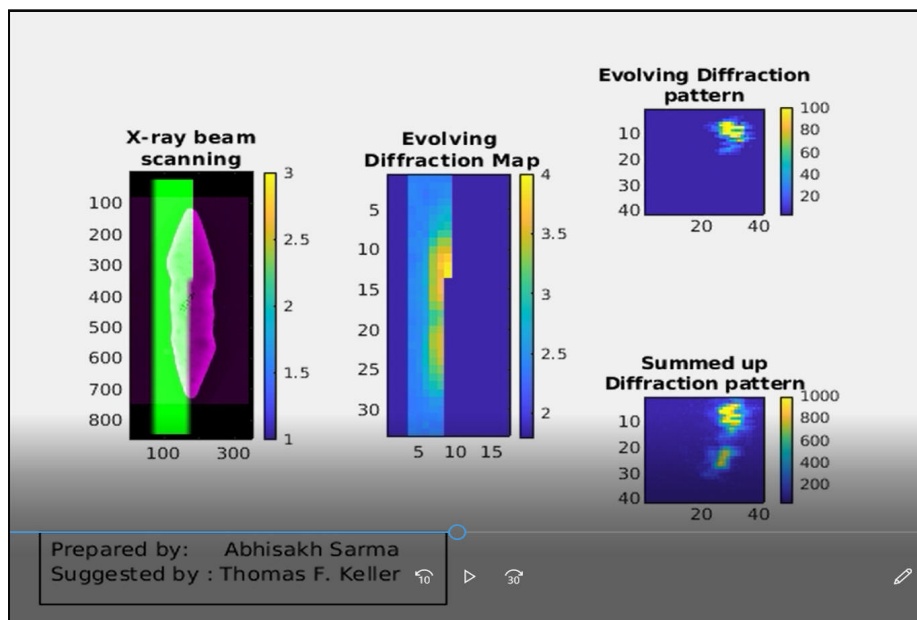
Video. A bc(o,t) Au bipyramid is scanned with X-ray nanobeam and the diffracting volume evolves at the diffraction map. The diffraction spot corresponding to the diffraction map is also shown.

*   *   *

Unusually Persistent Body-Centered Tetragonal (bct) Phase of Au Microcrystallites Induced by Ar$^+$ Ion Irradiation[*]

Summary

Properties of materials are dictated by their intrinsic crystal structures and thus, interesting to stabilize them in different lattices. Au conventionally crystallizes in fcc lattice and robust to occur in other lattice forms even at application of extreme pressure or under shock compression. Herein, non-cubic Au microcrystallites have been subjected to Ar$^+$ ion irradiation (operated at a nominal beam energy ~ 1.2-5 keV), where the probe is known to use in cleaning the surfaces in ultra-high vacuum studies on a routine basis. The ion irradiation acts as a perturbant and introduces another new phase, bct. Time of exposure, beam energy *etc*., act as strain engineer and stabilize ranges of bcts through uniaxial expansion, however being distinctly different from each other. Interestingly, these phases exhibit an expansion of volume, upto ~ 0.98% and are the routes to cause phase transformation to fcc. These phases are stable at ambient condition and impose extreme difficulty in phase transformation even during thermal annealing.

V.1 Introduction

A metal in an unconventional lattice is metastable and can be reverted back to its native stable lattice subjecting to perturbations such as temperature, pressure or charged particle beam exposure [1]. With nanoscale materials in contrast, multitude of crystal phases is possible and the transformation to a stable phase is rather common. As-prepared Ag nanowires for example, are stabilized in a bct structure [2] and transform back to fcc upon thermal annealing [3]. Au crystallized in hcp structure in the form of nanosheets (2H) [4], and ribbons (4H) [5], gets destabilized upon reacting with thiols to form the stable fcc structure [6]. The transformation could also be brought about by exposing to e-beam while carrying out microscopy studies [7]. For example, 4H hexagonal Ag nanowires transform to fcc Ag upon exposure to e-beam [8]. Another example relates to bc(o,t) Au microcrystallites from the laboratory which contain mixed phases [9] and are extraordinarily stable, indeed for years. The crystals begin to transform to fcc only beyond 500 °C [10] and under high pressure (up to 40 GPa), interestingly, the phases showed mere reversible transformation.

Ion beam irradiation has been employed to bring about phase transformation in nanoscale metals, from commonly occurring stable phases to unconventional lattices and vice versa. Indeed, since the last few decades, there has been tremendous activity in this field employing laboratory ion sources as well as particle accelerators on thin films and particulates [11]. Relevant to the present work are examples involving common metals and low energy beams addressing transformation from metastable phases to native phases. In one such example, a focused Ar^+ ion beam with energy ~ few keV has been used for magnetic patterning on a nonmagnetic fcc Fe film to locally transform the lattice to the stable ferromagnetic body-centered cubic (bcc) [12–14]. Thin film of Ni grown on W(100) exhibits a metastable bcc lattice which upon exposure of Ar^+ beam, transforms to a more stable hcp phase but not to the conventional fcc [15]. Co stabilized into metastable fcc lattice phase transforms back to stable hcp by swift heavy ion irradiation in both nanoparticles and thin films [16].

V.2 Scope of the Investigation

A study of the effect of ion beam exposure on the structure and morphology of bc(o,t) Au microcrystallites has hitherto not been carried out. In contrast to thermal annealing and pressure induced transformations, the influence of an energetic ion beam can be quite different as individual ions can penetrate surface layers and impart energy on the crystal lattice at cellular level. A neutral external perturbant such as Ar^+ ion irradiation may throw light on the stability of the lattices in the crystallite. It would be interesting to understand the stress relaxation processes that take place in the lattice upon ion impingement. Another important aspect would be reversible or irreversible nature of the process. Such studies not only provide insight into relative stabilities of the metastable phases but also, though uncommonly, indicate possible presence of new phases during transformation to the native phase.

V.3 Experimental Details

Ion beam irradiation. An Omicron ISE 10 ion gun with its controller have been used for the ion beam irradiation. The substrate holder was kept at 45° tilt facing towards the gun. Injection of Argon gas was done at a base pressure of 1 x 10^{-6} Torr and the working pressure was 5 x 10^{-5} Torr. The beam diameter was 5 mm. Beam energy and beam current have been varied systematically during the experiment.

V.4 Results and Discussion
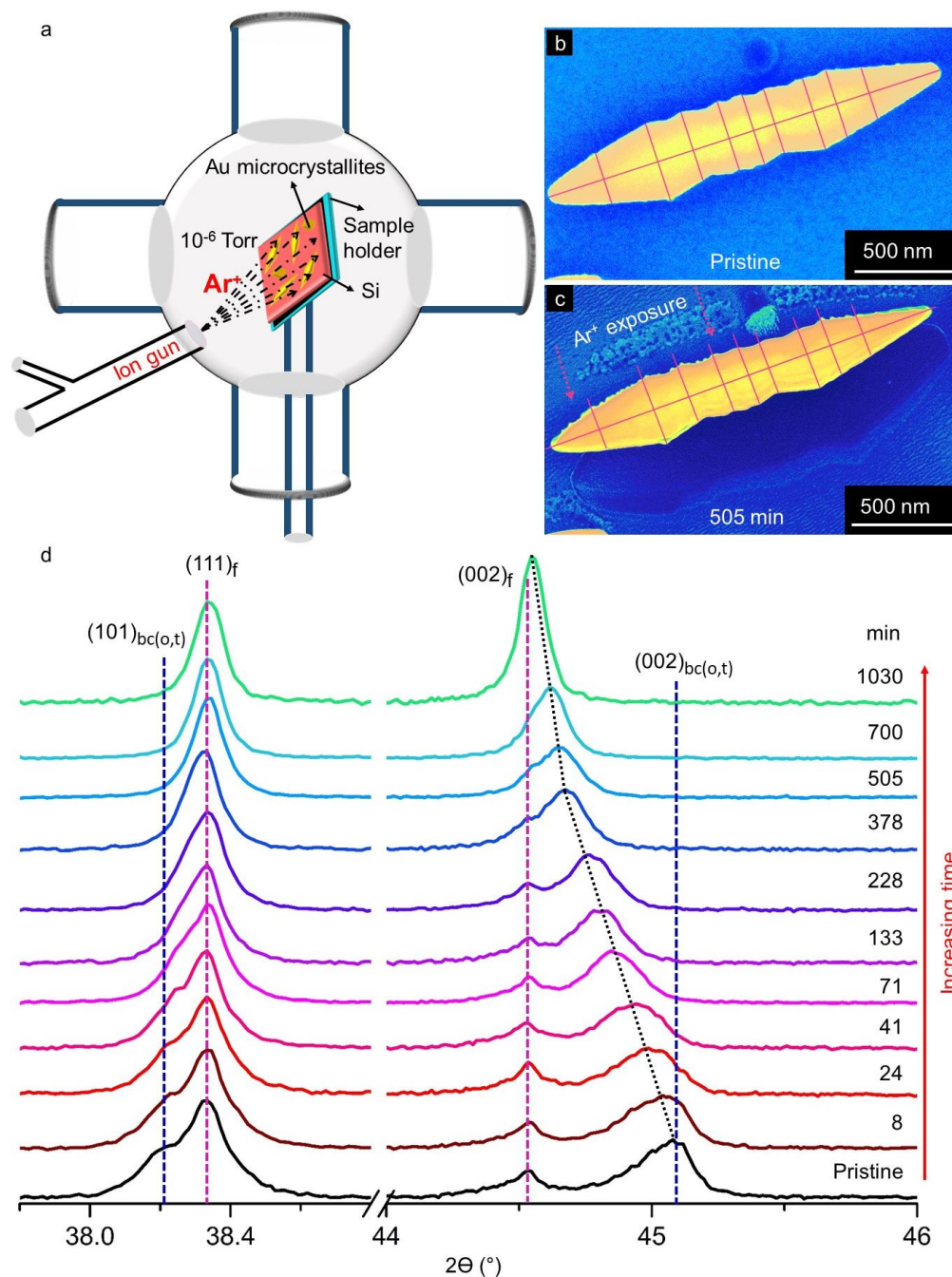
Figure V.1. (a) Schematic representation of the ion beam system. (b) SEM image of the pristine bc(o,t) Au microcrystallite. (c) SEM image of the Au bipyramid after Ar^+ beam exposure for 505 min at 1.2 keV with emission current of 10 mA. (d) XRD patterns collected after Ar^+ bombardment at 1.2 keV energy with emission current of 10 mA with variation of time. f and bc(o,t) represent fcc and bc(o,t), respectively. The magenta lines show the length and at different positions width of the bipyramid. The magenta arrow shows the direction of Ar^+ exposure. The black dotted line shows the new shifted peak.

The present study involves exposure of the bc(o,t) crystallites to energetic Ar^+ beam (see **Figure V.1**a) and monitoring possible lattice transformation in them. Upon exposure to Ar^+ beam (1.2 keV and 10 mA) for 505 min, no significant changes were seen in the morphology of the bipyramidal crystallite (see **Figures V.1**b,c and **V.2**) but an overall thinning along the beam direction (shown by magenta lines) amounting to ~ 17% reduction in size was observed. This is expected as Ar^+ etches away surface atoms much the same way when used for cleaning of surfaces in vacuum, which can be clearly seen by the arrow shaped hillocks formed at the surfaces (in **Figure V.3**). Indeed, the unshadowed region of Si seen as a step below the crystallite (**Figures V.1**c and **V.2**) stands as a signature for Ar^+ induced surface etching. The changes in the XRD pattern were carefully monitored with increasing the time of exposure to the beam (**Figure V.1**d). Interestingly, the exposure of Ar^+ brings about major changes in the XRD pattern; the $(101)_{bc(o,t)}$ shoulder gradually diminished in intensity while the peak $(002)_{bc(o,t)}$ shifted concomitantly to lower 2θ. After 1030 min of exposure, the $(101)_{bc(o,t)}$ shoulder nearly vanished and the peak in the region of $(002)_{bc(o,t)}$ appears to have shifted close to $(002)_f$ while becoming noticeably narrower (see **Figure V.1**d).
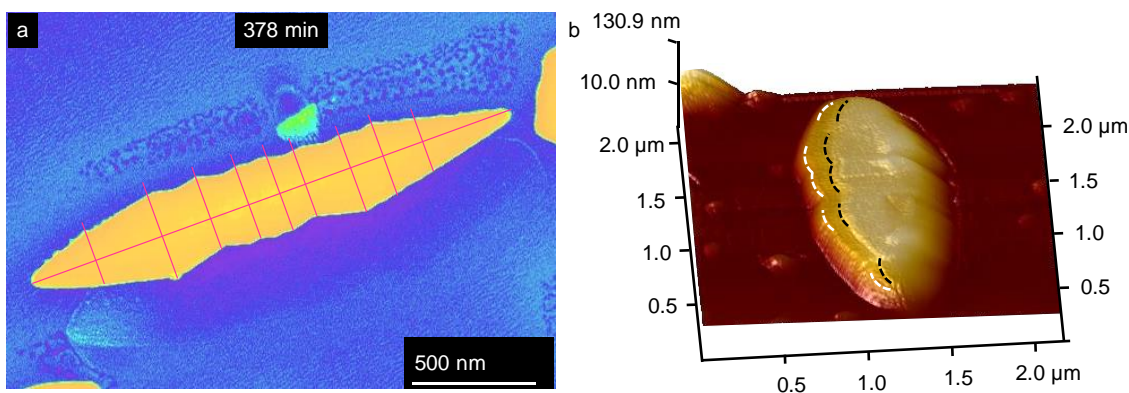
Figure V.2. (a) SEM image of Au bipyramid after 378 min of Ar^+ beam exposure at 1.2 keV with emission current of 10 mA. The platform feature around the Au microcrystallite is seen emerging due to etching of Si all regions around the microcrystallite. (b) AFM image of Au bipyramid after Ar^+ bombardment for 45 min at 5 keV energy with emission current of 10 mA. The black and white lines show the boundary of the bipyramid and extra platform, respectively. The black and white lines are drawn as guide to the eye. The magenta lines show the length and at different positions width of the bipyramid.
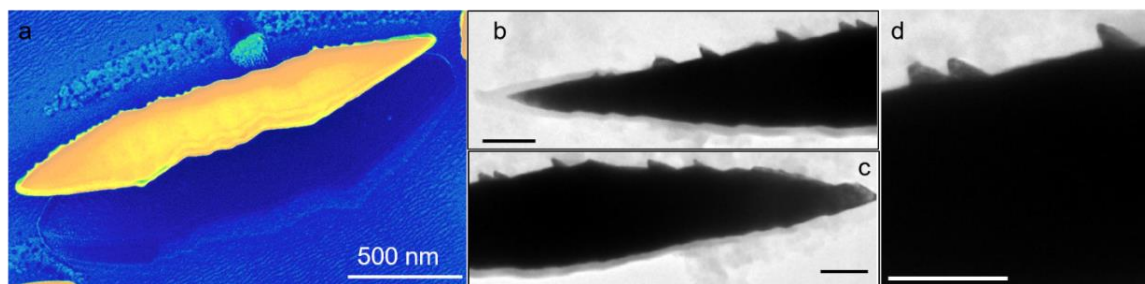
Figure V.3. (a) SEM and (b–d) TEM images of Au microcrystallites viewed at different magnifications. Scale bar, 200 nm. Arrow-shaped hillocks form at one side of the crystallite, *i.e.*, unidirectional which can be linked with the direction of the ion irradiation.

V.4.A Stabilizing Ranges of New bct Phases

Given the major changes in the XRD pattern, it is clear that the set of space groups used previously to fit bc(o,t) phases (see **Chapter III**) need to be revisited. From **Figure V.1**d, after ~ 71 min of beam exposure, the intensity in the original position of $(002)_{bc(o,t)}$ (see blue dashed line) diminished almost entirely with the intensity maximum shifting closer to $(002)_f$. When a combination of fcc + bct + bco space groups was tried (as done for the pristine bc(o,t), see **Figure III.6** in **Chapter III**), it resulted in a bad fit with $\chi^2 = 16.1$ (**Figure V.4**a). It appeared that bco was not required as the fit produced a large negative residual around the $(002)_O$ position ($2\theta \sim 45°$). Then the Le Bail fitting was attempted with the combination of fcc + bct, which improved the fitting but only marginally ($\chi^2 = 13.8$) as shown in **Figure V.4**b. After several such trials, it was realized that it is important to introduce an extra bct phase (termed here as bct-I). Thus, fcc + bct + bct-I produced the best fit with $\chi^2 = 1.51$ (see **Figure V.4**c). The bct-I is distinctly different having lattice parameters of $a = b = 2.9013 \pm 0.0005$ Å and $c = 4.0551 \pm 0.0003$ Å which may be compared to bct lattice parameters, $a = b = 2.9062$ Å and $c = 4.0450$ Å, the space group in both cases being *I4/mmm*. For the sake of illustration, the XRD patterns obtained after 71 and 505 min exposure, respectively were presented in **Figure V.5**a along with that of the pristine. The 71 min XRD pattern shows that the $(002)_T$ deconvoluted peak which had a prominent intensity to begin with (under the shoulder, see **Figure V.5**a) carried much less intensity. Here, the major contribution comes from the new $(002)_{T-I}$ peak. Thus is the evidence of co-presence of two bct phases during the transformation. With higher beam exposure (505 min), the intensity in the region of $(002)_{T-I}$ also diminished when the profile fitting could be done with a combination of fcc and only one bct. However,

the latter consisted of a cell ($a = b = 2.9012 \pm 0.0003$ Å and $c = 4.0697 \pm 0.0002$ Å) much different from the bcts encountered earlier. It is as though new bcts (clubbed under bct-I, for simplicity) are borne with continual changes in the lattice parameters (also see **Figures V.1**d **and V.6**). Corresponding changes are seen in the $(101)_{bc(o,t)}$ as well. Le Bail fitting of the data for other exposures are shown in **Figure V.6**. Interestingly, the peaks assignable to bct-I phases are also observed in the higher 2θ region as shown in **Figure V.7**.
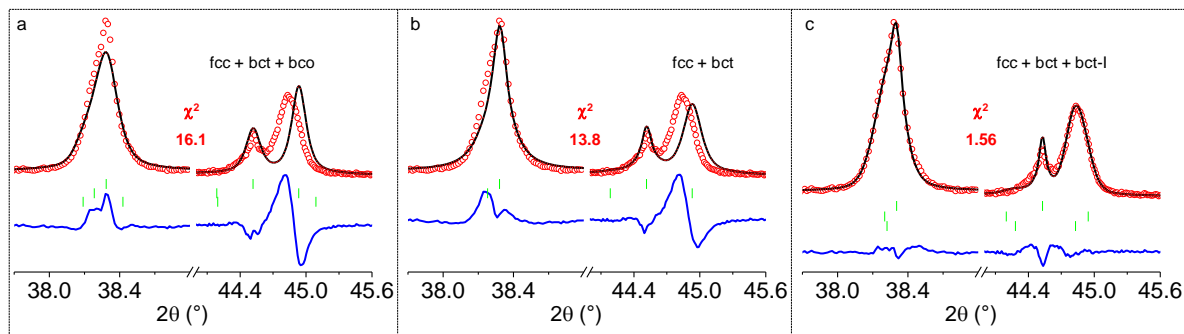
Figure V.4. (a–c) Le Bail fitting of the collected XRD pattern after Ar+ beam exposure of 71 min (at 1.2 keV and 10 mA) with combinations of fcc, bct, bco and body-centered tetragonal-I (bct-I). In all the cases, space group *Fm-3m* for fcc, *I4/mmm* for bct, *I4/mmm* for bct-I and *Immm* for bco. Red (circle), black and blue color curves represent experimental, fitted and residual (experimental-calculated), respectively and green vertical lines represent Bragg peak positions. The χ^2 for various combinations of fcc, bct, bco and bct-I are shown in the middle.

The changes in the lattice parameters of the different bc(o,t) phases are depicted in **Figure V.5**b,c. The cell parameters of bco remain almost unchanged as long as the phase lasted (~ 41 min) (see **Figure V.5**b) and similar was the situation with the bct phase till ~ 338 min (**Figure V.5**c). On the other hand, for the case of bct-I, a parameter nearly remained constant (~ 2.9015 Å) while the c parameter gradually increased starting from 4.0561 Å (at 41 min) to 4.0768 Å (1030 min). Thus, the c parameter follows a continuous increment reaching towards the fcc (4.081 Å) over the time frame however being distinctly different as shown in **Figure V.5**c. Thus, a unidirectional expansion (along the c-direction) was acting over the pristine lattices, which also illustrate the gradual increment in c/a of bct-I in **Figure V.8**, from 1.3975 to 1.4051. The final c/a approaches that of fcc in the tetragonal setting (1.4142), but remains distinctly lower even after 1030 min of exposure. The persistence of bct-I is remarkable. The mole fraction of the phases quantified from the area under the curves (see **Figure V.6**), which exhibits a decrement in the bco (at ~ 71 min) proportion as shown in **Figure V.5**d, while an

increment in bct till ~ 41 min followed by a monotonous decrement and finally vanishes by 378 min. Interestingly, the bct-I appears at 41 min and eventually contains the maximum proportion (~ 0.40) and retains till ~ 700 min (see **Figure V.5**d,e). Further, exposure (~ 1030 min) drastically reduces down the mole fraction of bc(o,t) to ~ 0.16 in the form of bct-I under the beam conditions used while feeding the total proportion into fcc. The reduction in mole fraction in the extended period of time frame (~ 1030 min) can be linked with the overall reduction in the mass of the crystallites due to sputtering and redeposition of fcc particulates.
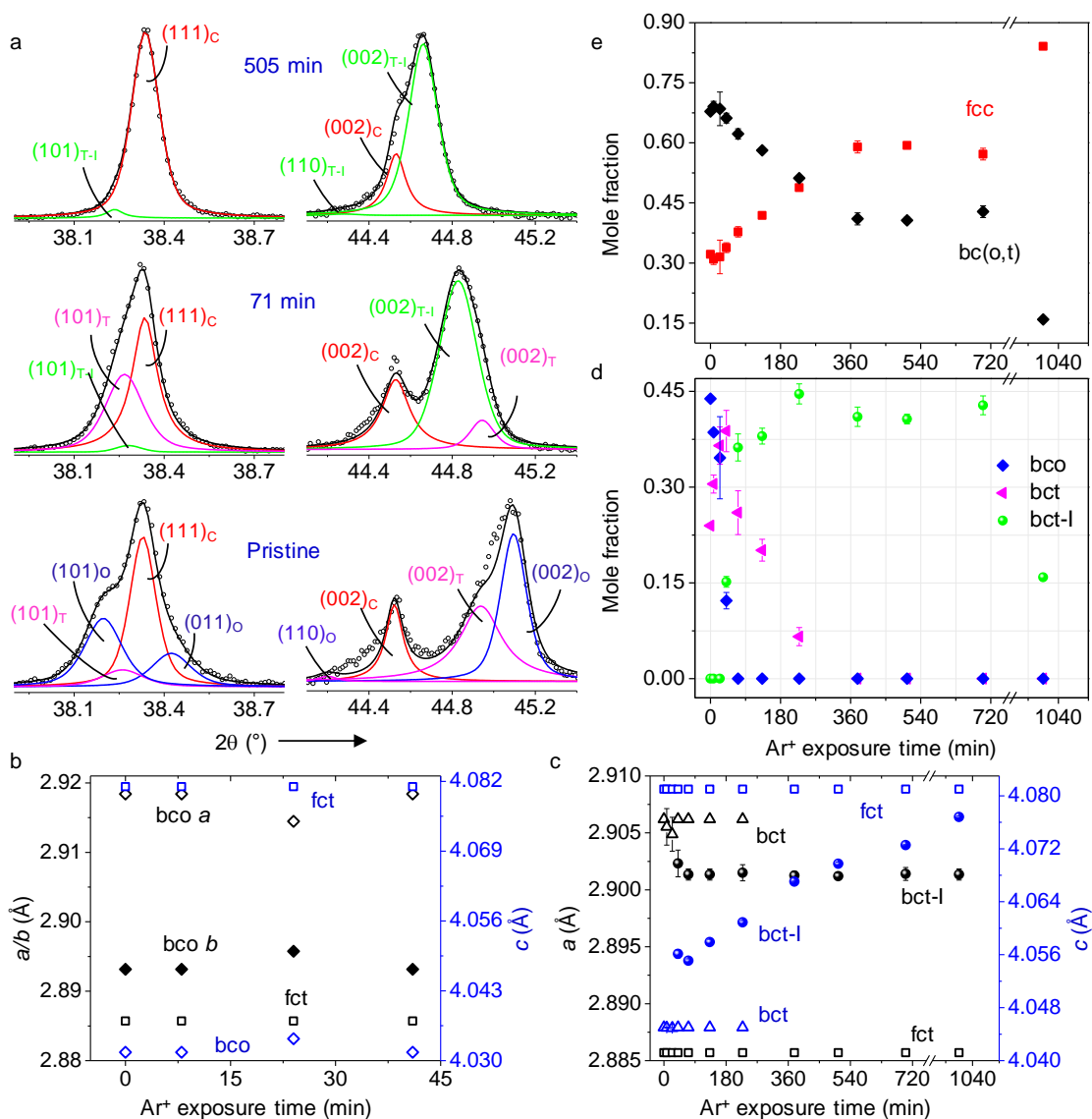
Figure V.5. (a) Profile fitting of the collected XRD patterns for pristine, after Ar$^+$ bombardment for 71 and 505 min, respectively. Black circle represents experimental result. Red, blue, magenta and green color curves represents fcc (represented as C), bco (O), bct (T) and bct-I (T-I) phases, respectively and

their sum is shown in black curve. Graphical representation of time dependent variation in a/b and c parameters for (b) bco, face-centered tetragonal (fct) and (c) bct, fct and bct-I phases. (d) Variation of mole fraction with Ar$^+$ beam exposure time for bco, bct and bct-I phases. (e) Variation of mole fraction of fcc and bc(o,t) phases with Ar$^+$ beam exposure time.
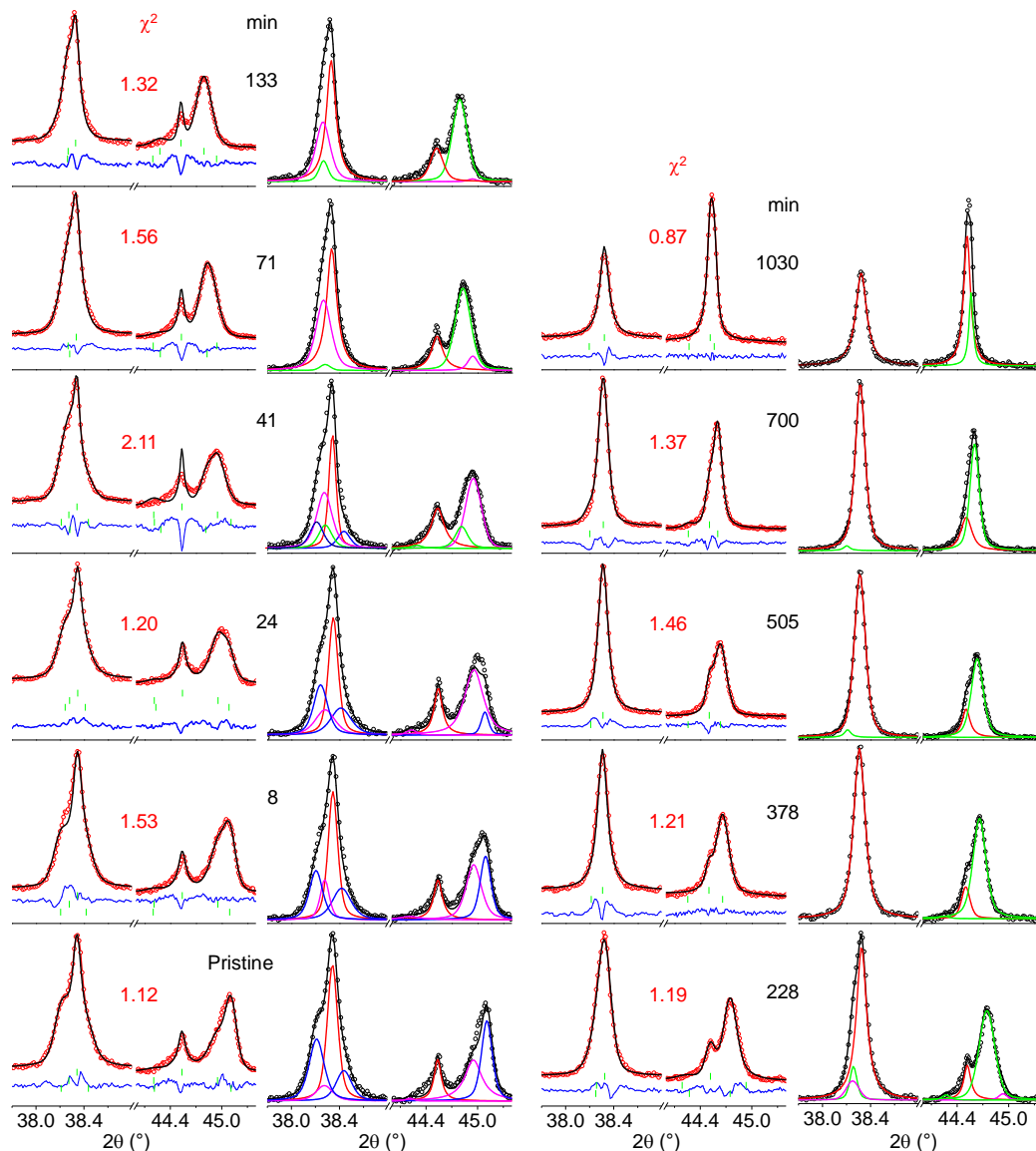
Figure V.6. Le Bail fitting of the collected XRD patterns for different Ar$^+$ beam exposure time (at 1.2 keV, 10 mA). Fitting XRD patterns with combinations of fcc, bct, bco and bct-I. In all the cases space group *Fm-3m* for fcc, *I4/mmm* for bct, *I4/mmm* for bct-I and Immm for bco. Red (circle), black and blue color curves represent experimental, fitted and residual (experimental-calculated), respectively and green vertical lines represents Bragg peak positions. Multi curve fitting corresponding to each time Ar$^+$ beam exposure has been performed. Black (circle), black, red, blue, pink and green

color curves represents experimental, fitted, fcc, bco, bct and bct-I phases, respectively. The χ^2 for various combinations of fcc, bct, bco and bct-I are shown in the middle of the figures.
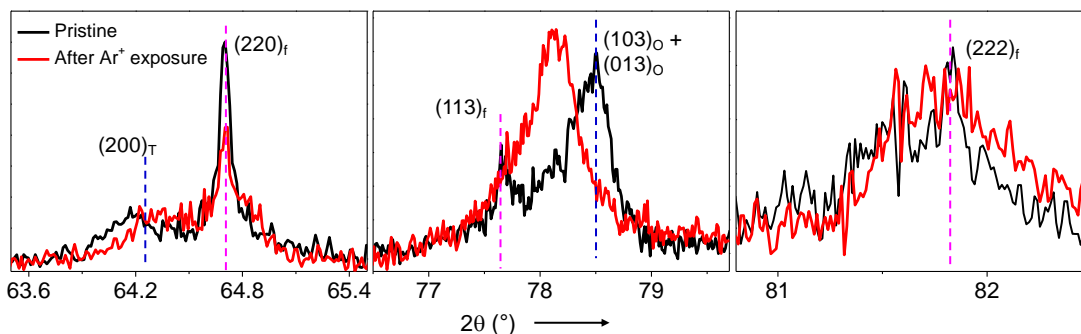
Figure V.7. Effect of Ar^+ bombardment on XRD pattern of bc(o,t) Au microcrystallites for higher index planes, such as (220), (113) and (222), respectively.
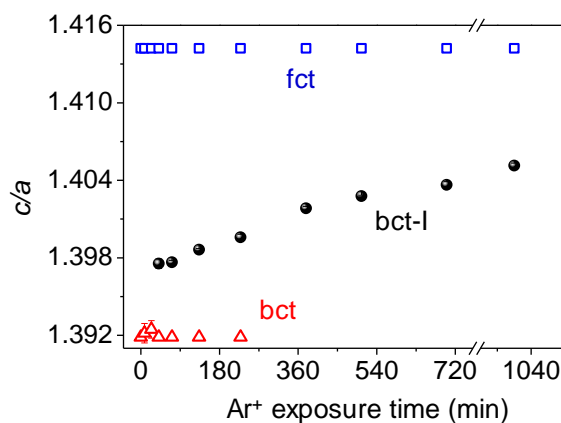
Figure V.8. Graphical representation of time dependent variation in *c/a* ratio for bct-I phase.
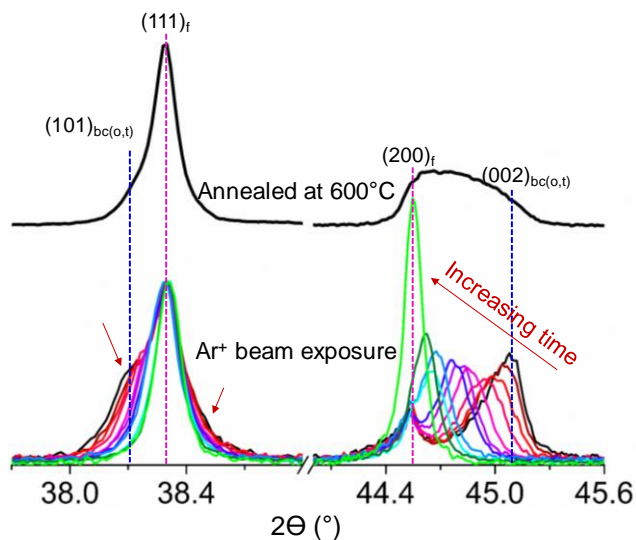
Figure V.9. Comparison of the XRD patterns of Au crystallites exposed with Ar^+ (at 1.2 keV) and annealed at 600 °C (~ 100 min), respectively. The $(002)_{bc(o,t)}$ peak broadens during annealing in contrast

to the significant narrowing on prolonged ion-exposure ~ 1030 min (see details under **Figure V.1**d). The red arrows indicate the direction of peak position shift with increasing exposure time. The patterns have been normalized with respect to $(111)_f$.
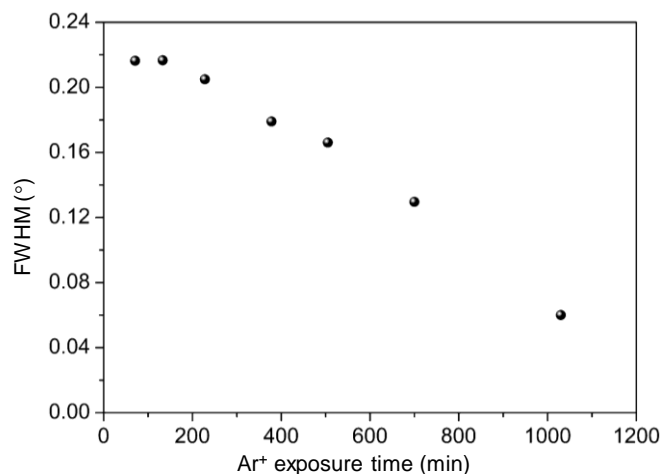
Figure V.10. Variation of the FWHM of the $(002)_{bc(o,t)}$ peak with Ar⁺ exposure time at 1.2 keV. With increment in the exposure time, the FWHM reduces.
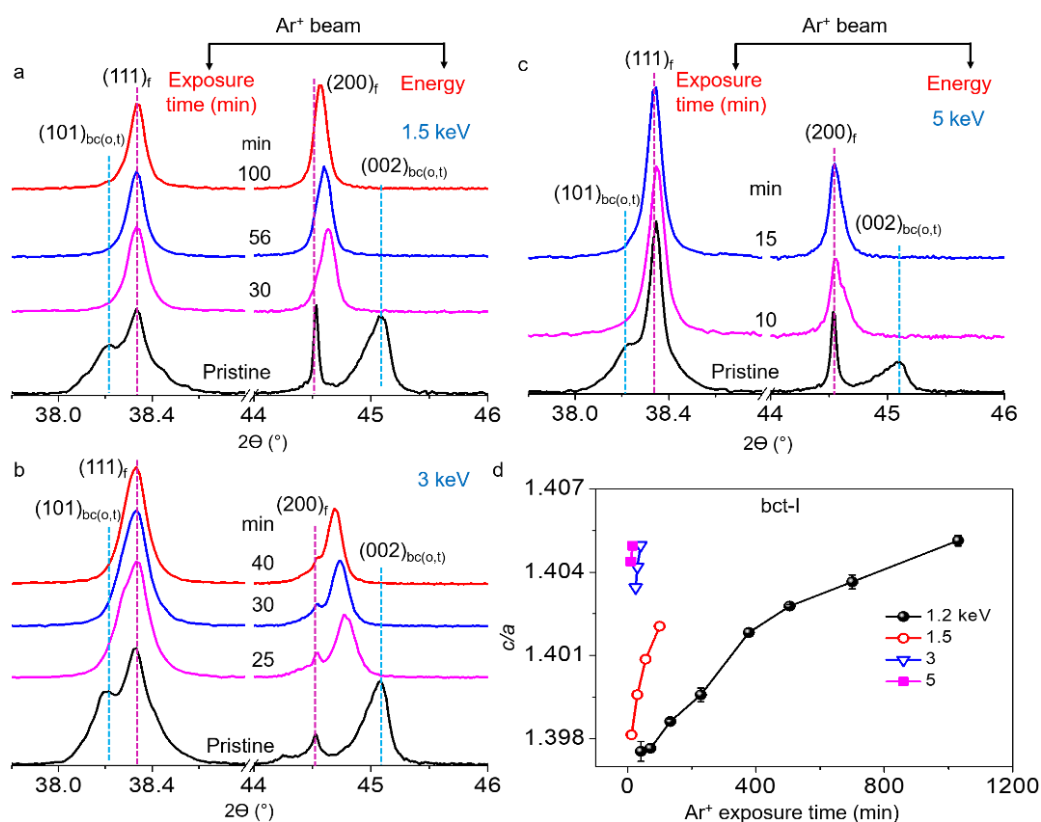
Figure V.11. (a–c) Energy dependent Ar⁺ bombardment on bc(o,t) Au microcrystallites at emission current of 10 mA with energy of 1.5, 3 and 5 keV, respectively. (d) Graphical representation of time

dependent *c/a* ratios for bct-I phase for different beam energies. The lines are drawn as guide to the eye.

In order to understand the effects arising due to Ar$^+$ exposure, the time dependent XRD patterns (from **Figure V.1**d) are presented along with 600 °C annealed pattern (for 100 min) in **Figure V.9**. Surprisingly, the annealing induced pattern (the (002)$_{bc(o,t)}$ region) expresses as an envelope to the Ar$^+$ exposed patterns, elucidating simultaneous presence of series of bct-I along with the pristine bc(o,t). Thus, the broad pattern explains the introduction of disorder by thermal annealing. In contrast to annealing, the Ar$^+$ irradiated patterns exhibit time respective decreasing FWHM of the (002)$_{bc(o,t)}$ peak (**Figure V.10**) and thus, decreasing disorder/randomization with enhanced crystallinity by forming well-controlled phases. Although the final outcome is fcc, the governing principle differs in both annealing and Ar$^+$ ion irradiation processes.
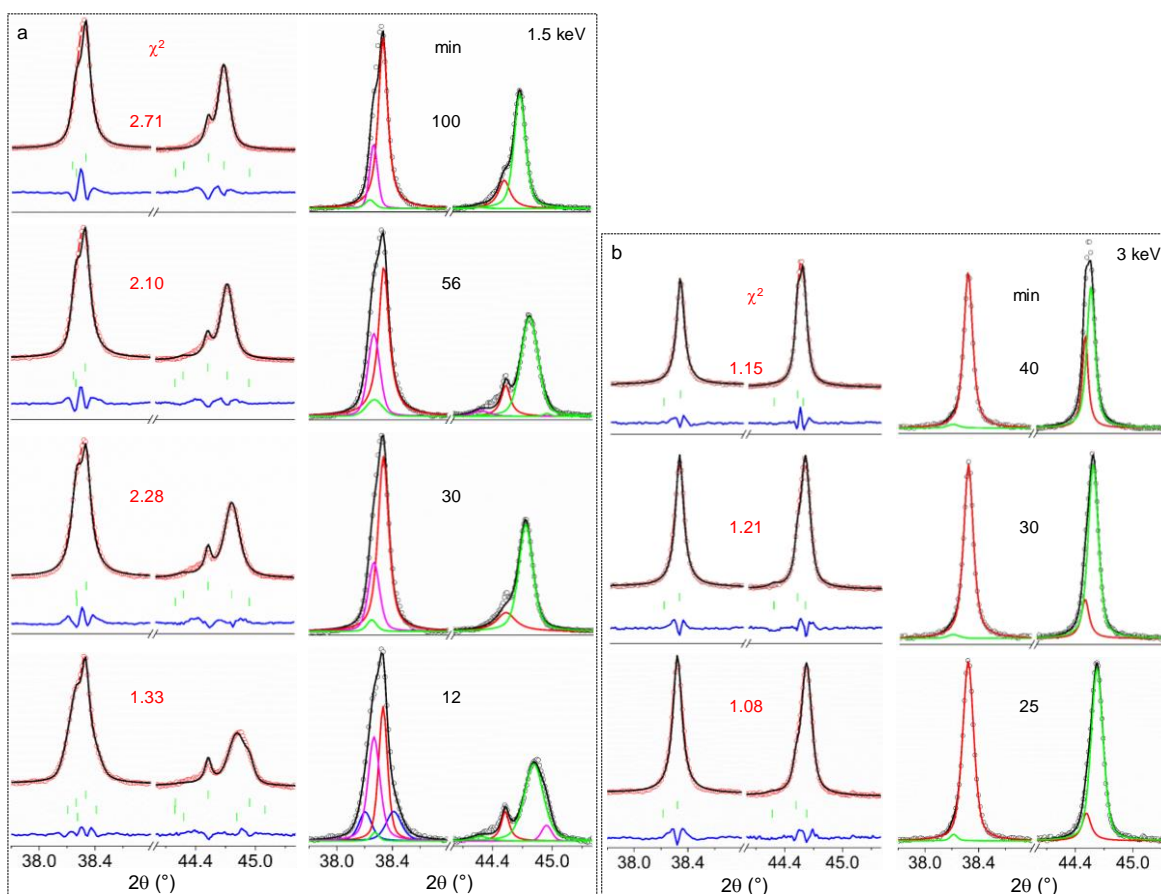
Figure V.12. Le Bail fitting of the collected XRD patterns for different Ar$^+$ beam exposure time at (a) 1.5 and (b) 3 keV energies with 10 mA emission current (similar to **Figure V.6**).
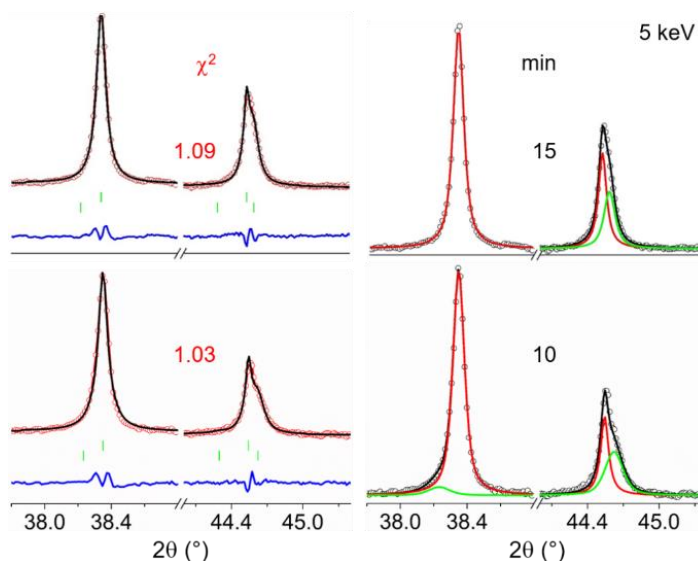
Figure V.13. Le Bail fitting of the collected XRD patterns for different Ar⁺ beam exposure time at 5 keV energy and 10 mA emission current (similar to **Figure V.6**).
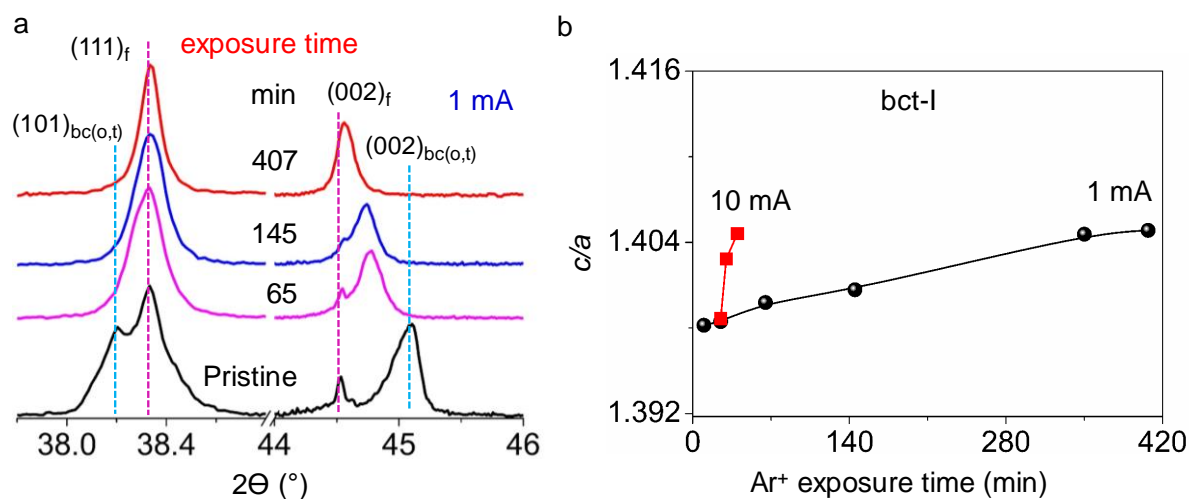
Figure V.14. (a) Exposure of Ar⁺ on bc(o,t) Au microcrystallites with bombardment energy of 3 keV and emission current of 1 mA. (b) Variation in lattice parameters (c/a) of bct-I phase with time for emission current of 1 and 10 mA, respectively.
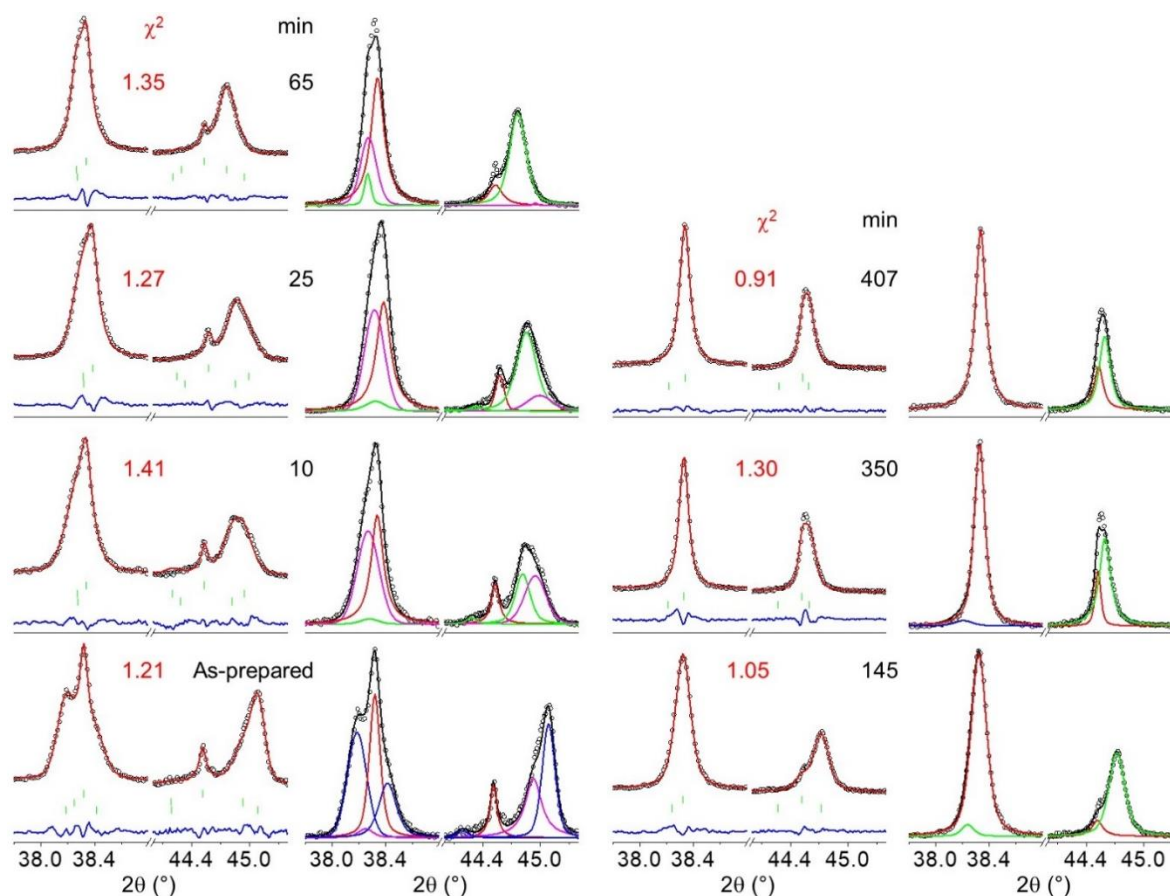
Figure V.15. Le Bail fitting of the collected XRD patterns for different Ar^+ beam exposure time at 3 keV bombardment energy and 1 mA emission current (similar to **Figure V.6**).

Energy dependent exposure has been carried out with emission current of 10 mA as shown in **Figure V.11**. The $(002)_{bc(o,t)}$ peak shifts close to $(002)_f$ after 100 min of exposure at 1.5 keV bombardment energy (see **Figures V.11**a **and V.12**a). Similarly at higher beam energies, 3 and 5 keV, the $(002)_{bc(o,t)}$ peak almost merges with the $(002)_f$ peak after relatively shorter times, 40 and 15 min, respectively (see **Figures V.11**b,c, **V.12**b and **V.13**). Variation of lattice parameter (*c/a*) of the bct-I phases with time has been plotted for different flux values (see **Figure V.11**d). At 1.2 keV, it required a long exposure of 1030 min to make the *c/a* reach its maximum value of 1.4051 whereas at 1.5 keV, it took much shorter time to reach saturation (*c/a* ~ 1.4021). Similarly, with higher energies (3 and 5 keV), the maximum values (*c/a* ~ 1.4050) can be achieved in 40 and 15 min, respectively. The similar changes can be introduced by the alternation of beam current (1 mA) as shown in **Figures V.14** and **V.15**. Thus, increasing flux (at 10 mA emission current in **Figure V.11**d) or emission current (at 3

keV bombardment energy in **Figure V.14**b) leads to faster achievement of higher *c/a* and thereby faster phase transformation (from bc(o,t) to fcc). The deviation in the XRD peak positions with respect to unstrained fcc Au, even at longer irradiation time (~ 1030 min in **Figure V.1**d), highlights the presence of large cumulative strains in the core of the microcrystallites. This is quite evident from the ED pattern collected from a tip of a crystalliteat an intermediate time interval (300 min) of the Ar⁺ exposure (at 3 keV, 1 mA) as shown in **Figure V.16** along the [001] direction that the pattern exhibits falling out of (002) and (220) spots from their respective circles, denoting deviation in *d*-spacing ~ 1% from unstrained fcc. Further, the ED pattern collected from the edge of the crystallite along the [011] direction highlights asymmetric spots and so their imperfect Gaussian line profiles, implying the presence of non-cubic lattices even at the prolonged exposure. Longer exposure to energetic beam may cause visible changes in the morphology of the bipyramidal crystallite as shown in **Figure V.17**.
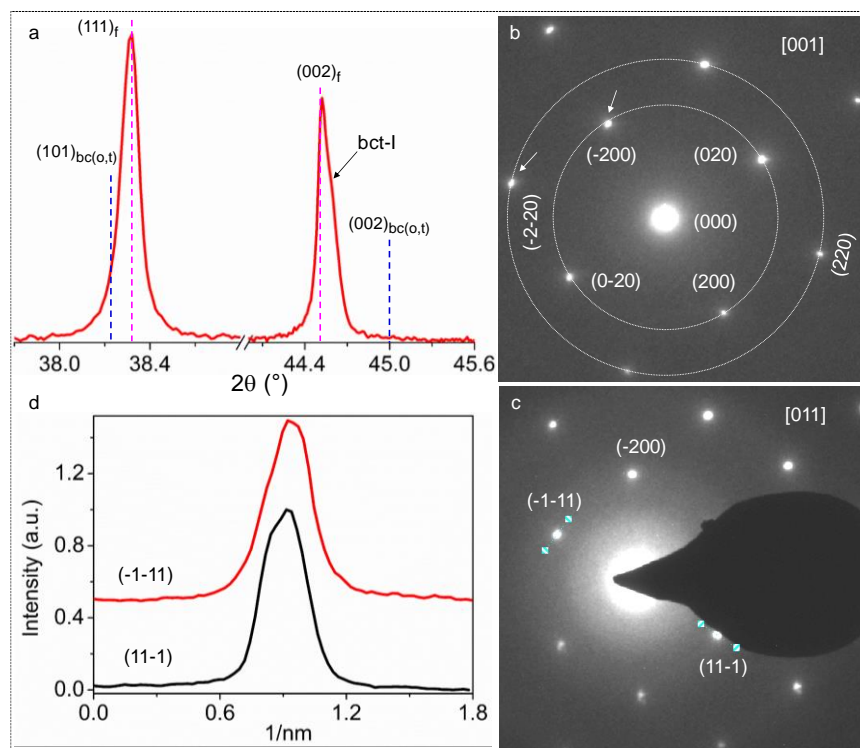
Figure V.16. (a) XRD pattern of Au microcrystallites after 300 min of Ar⁺ exposure at 3 keV, 1 mA. (b,c) ED pattern collected from the tip and edge of a Au bipyramid (from a collection of crystallites examined in (a) along [001] and [011] directions, respectively. The *d*-spacings corresponding to (200) and (-200) spots are 1.99 and 1.97 Å, respectively indicating ~ 1% deviation in (b). (d) Intensity profiles

drawn over the (11-1) and (-1-11) spots in (c). The magnified view of the spots is shown in the right panel, deviating from perfect circle and thus, the broadened line profiles.
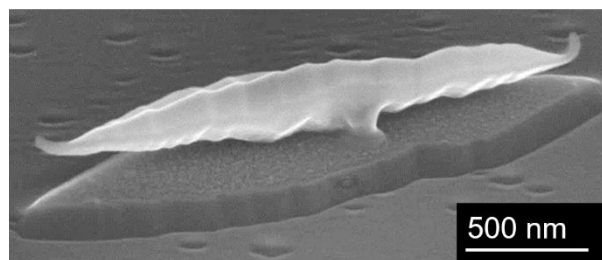
Figure V.17. SEM image of Au microcrystallite after Ar$^+$ bombardment (for 45 min at 5 keV energy and emission current of 10 mA). Sputtering effect induces the thinning down of the crystallites tips, whereas shadowing effect leads to the formation of the grooves in the Si (opposite to the beam direction).

V.4.B Stability of the bct-I Phases
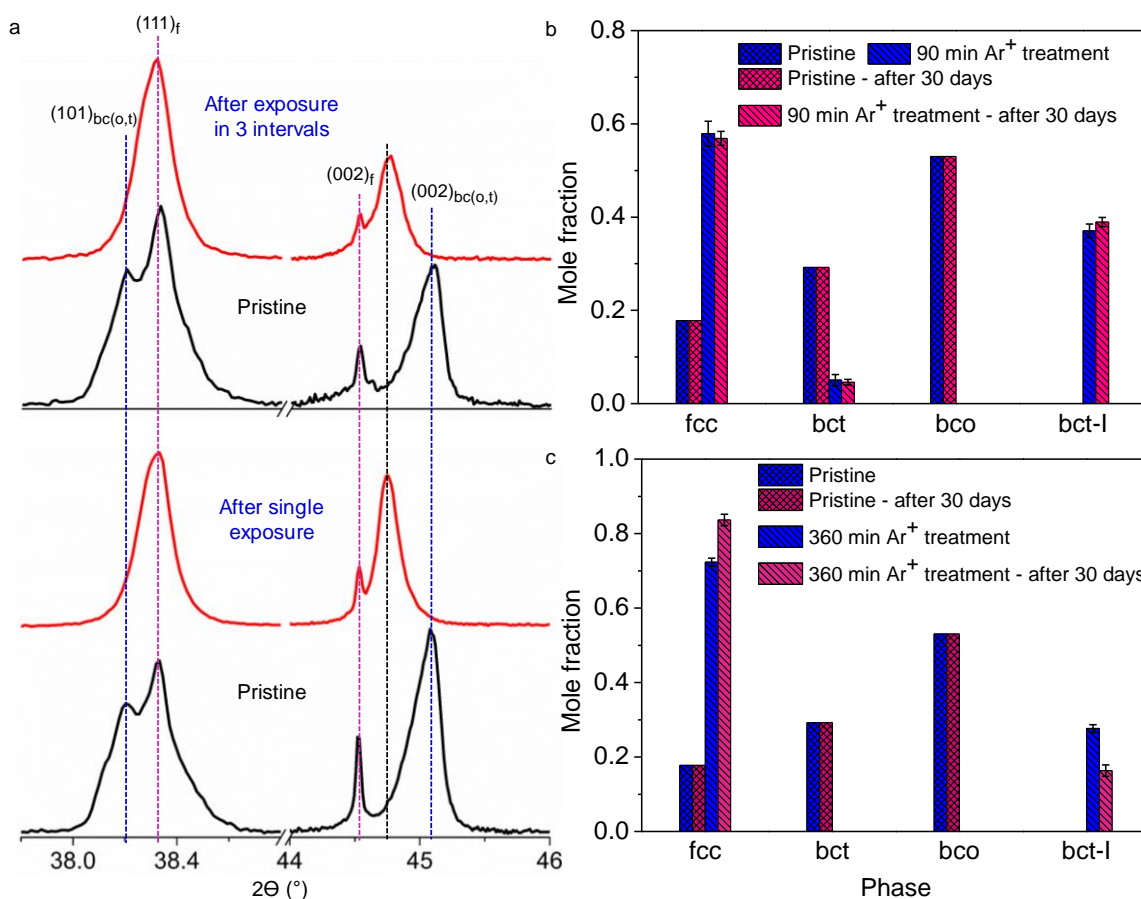
Figure V.18. (a) Ar$^+$ bombardment in single and three intervals processes on bc(o,t) Au microcrystallites with 3 keV bombardment energy and 1 mA emission current for total 65 min. The black dotted line shows the shifted peak position. Variation of mole fraction of different phases with

time for (b) 90 min and (c) 360 min Ar⁺ treated (at 3 keV energy and 1 mA emission current) Au microcrystallites along with pristine bc(o,t) for 30 days interval.

Interestingly from the above observations, it appears that the extent of perturbation induced by the Ar⁺ exposure decides the nature of the bct-I lattice; more the exposure, closer is the *c/a* of the bct-I phase to fcc. The disturbances need not to be introduced in one stretch, as shown in **Figure V.18**a; a single exposure of 65 min to Ar⁺ beam (3 keV, 1 mA) brings in similar transformations as do three successive exposures of totaling 65 min. The latter times, separated by ~ 8 h time, mostly arise from vacuum transfer of the sample and XRD measurements. In short, both single and successive (intermittent steps are shown in **Figure V.19**) exposures led to the diminishing of the $(002)_{bc(o,t)}$ peak and the appearance of a new peak at $2\theta \sim 44.76°$ and $44.77°$ respectively (see black dotted line in **Figure V.18**a). This experiment clearly shows that the strain added by exposing to Ar⁺ beam is additive and the transformation caused is irreversible. Besides, all intermittent bct-I phases are equally stable and the proportions of the phases are similar even after 30 days as shown in **Figure V.18**b,c.

Although the crystallites are stable under e-beam exposure during TEM measurements (at 200 keV) [17], they undergo phase transformation upon Ar⁺ exposure (5 keV). This can be understood by the energy transfer on the Au surfaces caused by e-/Ar⁺-beam being 2.2 eV and 2.8 keV, respectively (see the detailed calculation below). Having very small mass, the electron does not affect the ~ half a µm thick crystallites. In contrast, the higher mass of Ar⁺ leads to higher energy transfer and thereby, it acts as strong perturbant.

$$E_2 = \frac{4E_1M_1M_2}{(M_1 + M_2)^2} \qquad (1)$$

$$E_2 = \frac{4 \times 200 \times 9.1 \times 10^{-31} \times 3.27 \times 10^{-25}}{(9.1 \times 10^{-31} + 3.27 \times 10^{-25})^2} \text{ keV}$$

$$E_2 = 2.2 \text{ eV}$$

where M_1 and M_2 are the masses of an electron and Au atom, respectively and E_1 and E_2 are the energies of the exposed e-beam and the transferred energy to Au surface, respectively.

Similarly, $E_2 = 2.8$ keV for the Ar⁺ ion, where the M_1 and E_1 are 6.633×10^{-26} kg and 5 keV, respectively.

The change in volume of the bct-I has been presented in **Figure V.20** along with bco, bct and fcc. Surprisingly with exposure time, the volume (per two atoms) of the bct-I cell expands to the extent of ~ 0.98% (at 1030 min) and continues to be stable at ambient condition; this is in contradiction to the commonly known phase transformation (*i.e.*, reduction in volume). Shifts in XRD-peaks towards larger *d*-values as well as the atypical volume increase has been explained by understanding the role of electronic excitations in Au atoms of the microcrystallites. Electrons at higher temperatures (of the order of 10^3 K) in the core of microcrystallites as a response to ion-irradiation process tune the elastic strains primarily along [001] of bc(o,t) phases. The changes involve coupling of electrons with the softest longitudinal acoustic branch of Au, and formation of pseudo-gap in the density of electronic states of metastable bct configurations.
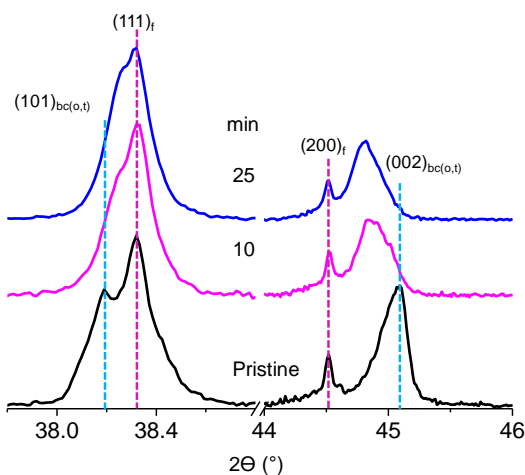
Figure V.19. XRD patterns of the intermediate steps for three intervals Ar⁺ exposure process at 3 kV energy and 1 mA emission current.

Au crystallites (with an intermediate bct-I phase) have been subjected to thermal annealing at 500 °C and the post annealing (for 18 h) introduces a shift in the $(002)_{T-I}$ peak (see **Figure V.21**), specially towards the lower 2θ side, from 44.742° to 44.663° with a reduction in FWHM (from 0.198° to 0.167°). This observation is in clear contrast with the observation drawn in **Figure V.9**, annealing of pristine bc(o,t) crystallites. One would expect the outcome as regeneration of pristine bc(o,t) pattern/phase transformation to fcc/simultaneous appearance of ranges of bcts (like the known effect in annealing in **Figure V.9**), however, neither of the proposed transformations occurred. The annealed pattern resembles the Ar⁺ exposed pattern (505 min in **Figure V.1**d with FWHM of 0.166°), hinting a follower to the latter, however in

a slow pace (*i.e.*, 18 h at 500 °C ≅ ~ 270 min at 1.2 keV and 10 mA). Thus, the well-known thermal annealing can also be used as a probe to stabilize the individual bct-I alike to the Ar⁺ exposure, however with a pretreatment of the latter. The intensity of the peaks, enhanced during the post annealing, implies improvement in the crystallinity (see **Figure V.21**). This was previously not monitored (in case of Ar⁺ exposure) due to the sputtering induced loss of masses.
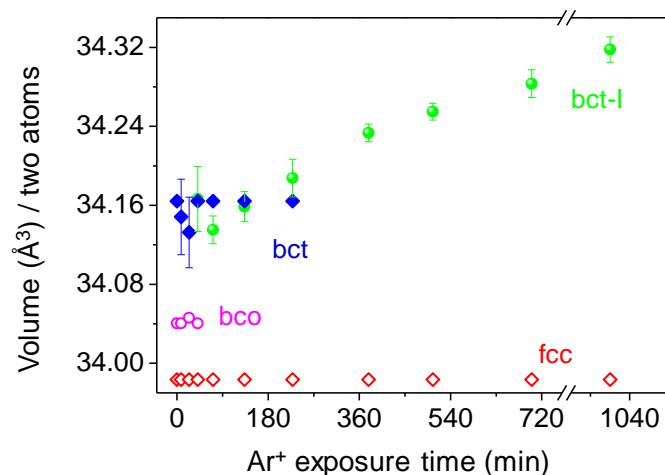
Figure V.20. Changes in volume of fcc, bco and bct and bct-I lattices with Ar⁺ exposure time (at 1.2 keV and 10 mA).
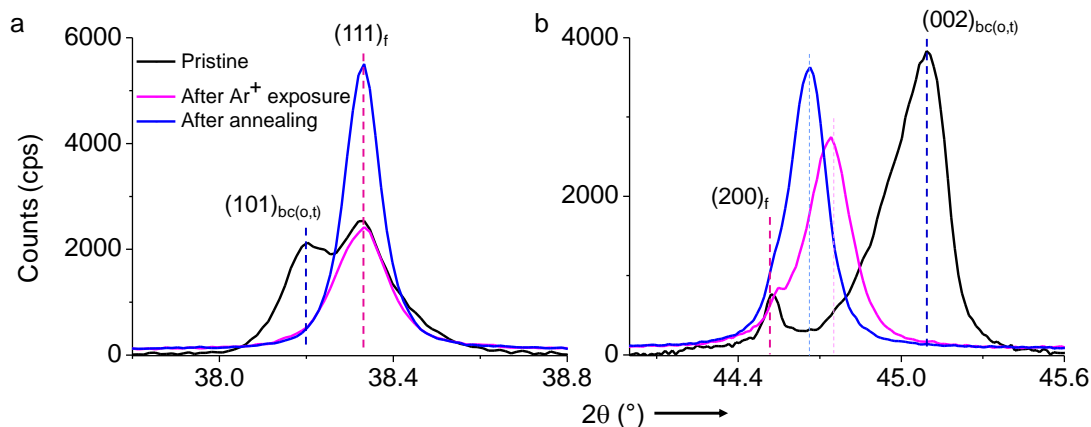
Figure V.21. Thermal stability of the bct-I. (a,b) XRD patterns of the Ar⁺ exposed and followed by annealing at 500 °C (for 18 h) along with the pristine.

V.5 Conclusions

In summary, the effect of low keV Ar⁺ ion irradiation on the metastable bc(o,t) phases has been studied. The ion irradiation facilitates the generation of a range of new metastable bct phases *via* expansion along the *c*-direction. The ion beam induced transformation is additive

in nature; removal of ion irradiation after certain exposure time arrests the new metastable phase generated during that time period and keeps it indefinitely stable till exposed again. This enabled careful *ex-situ* monitoring of the generated phases. With increased exposure, the *c*-direction approaches that of fcc. The transformation involving an increment in volume (~ 0.98%) along the [001] direction, caused by this process enhances the crystallinity more effectively than the thermal annealing.

References

[1]   H. Cheng, N. Yang, Q. Lu, Z. Zhang, and H. Zhang, *Syntheses and Properties of Metal Nanomaterials with Novel Crystal Phases*, Adv. Mater. **30**, 1707189 (2018).

[2]   Y. Sun, Y. Ren, Y. Liu, J. Wen, J. S. Okasinski, and D. J. Miller, *Ambient Stable Tetragonal Phase in Silver Nanostructures*, Nat. Commun. **3**, 971 (2012).

[3]   Z. Li, J. S. Okasinski, J. D. Almer, Y. Ren, X. Zuo, and Y. Sun, *Quantitative Determination of Fragmentation Kinetics and Thermodynamics of Colloidal Silver Nanowires by in Situ High-Energy Synchrotron X-ray Diffraction*, Nanoscale **6**, 365 (2014).

[4]   X. Huang, S. Li, Y. Huang, S. Wu, X. Zhou, S. Li, C. L. Gan, F. Boey, C. A. Mirkin, and H. Zhang, *Synthesis of Hexagonal Close-Packed Gold Nanostructures*, Nat. Commun. **2**, 292 (2011).

[5]   Z. Fan, M. Bosman, X. Huang, D. Huang, Y. Yu, K. P. Ong, Y. A. Akimov, L. Wu, B. Li, J. Wu, Y. Huang, Q. Liu, C. Eng Png, C. Lip Gan, P. Yang, and H. Zhang, *Stabilization of 4H Hexagonal Phase in Gold Nanoribbons*, Nat. Commun. **6**, 7684 (2015).

[6]   Z. Fan, X. Huang, Y. Han, M. Bosman, Q. Wang, Y. Zhu, Q. Liu, B. Li, Z. Zeng, J. Wu, W. Shi, S. Li, C. L. Gan, and H. Zhang, *Surface Modification-Induced Phase Transformation of Hexagonal Close-Packed Gold Square Sheets*, Nat. Commun. **6**, 6571 (2015).

[7]   X. Huang, S. Li, Y. Huang, S. Wu, X. Zhou, S. Li, C. L. Gan, F. Boey, C. A. Mirkin, and H. Zhang, *Synthesis of Hexagonal Close-Packed Gold Nanostructures*, Nat. Commun. **2**, 292 (2011).

[8]   C. Liang, K. Terabe, T. Hasegawa, and M. Aono, *Formation of Metastable Silver Nanowires of Hexagonal Structure and Their Structural Transformation under Electron Beam Irradiation*, Jpn. J. Appl. Phys. **45**, 6046 (2006).

[9]   G. Mettela, M. Bhogra, U. V. Waghmare, and G. U. Kulkarni, *Ambient Stable Tetragonal and Orthorhombic Phases in Penta-Twinned Bipyramidal Au Microcrystals*, J. Am. Chem. Soc. **137**, 3024 (2015).

[10] G. Mettela, Y. A. Sorb, A. Shukla, C. Bellin, V. Svitlyk, M. Mezouar, C. Narayana, and G. U. Kulkarni, *Extraordinarily Stable Noncubic Structures of Au: A High-Pressure and*

-Temperature Study, Chem. Mater. **29**, 1485 (2017).

[11] A. V. Krasheninnikov and K. Nordlund, *Ion and Electron Irradiation-Induced Effects in Nanostructured Materials*, J. Appl. Phys. **107**, 071301 (2010).

[12] W. Rupp, A. Biedermann, B. Kamenik, R. Ritter, C. Klein, E. Platzgummer, M. Schmid, and P. Varga, *Ion-Beam Induced fcc-bcc Transition in Ultrathin Fe Films for Ferromagnetic Patterning*, Appl. Phys. Lett. **93**, 063102 (2008).

[13] S. Shah Zaman, H. Oßmer, J. Jonner, Z. Novotný, A. Buchsbaum, M. Schmid, and P. Varga, *Ion-Beam-Induced Magnetic Transformation of CO-Stabilized fcc Fe Films on Cu(100)*, Phys. Rev. B **82**, 235401 (2010).

[14] J. Gloss, S. Shah Zaman, J. Jonner, Z. Novotny, M. Schmid, P. Varga, and M. Urbánek, *Ion-Beam-Induced Magnetic and Structural Phase Transformation of Ni-Stabilized Face-Centered-Cubic Fe Films on Cu(100)*, Appl. Phys. Lett. **103**, 262405 (2013).

[15] C. Gopalakrishnan, S. Ramaswamy, K. R. Ganesh, and K. Jeganathan, *Influence of Low Energy Ar-Ion Bombardment on Monolayer Ni/W(1 0 0)*, Phys. E **56**, 337 (2014).

[16] D. J. Sprouster, R. Giulian, C. S. Schnohr, L. L. Araujo, P. Kluth, A. P. Byrne, G. J. Foran, B. Johannessen, and M. C. Ridgway, *fcc-hcp Phase Transformation in Co Nanoparticles Induced by Swift Heavy-Ion Irradiation*, Phys. Rev. B **80**, (2009).

[17] G. Mettela, N. Mammen, J. Joardar, S. Narasimhan, and G. U. Kulkarni, *Non-fcc Rich Au Crystallites Exhibiting Unusual Catalytic Activity*, Nano Res. **10**, 2271 (2017).

*   *   *

Real-Time Monitoring of the Thermal Annealing Induced Phase Transformation of a non-Cubic Au Bipyramid to fcc by Scanning X-ray Diffraction Microscopy[*]

Summary

Au bipyramids hosting non-cubic lattices exhibit extraordinary stability at ambient condition and under applied high-temperature and -pressure. The phases undergo conversion to fcc during annealing at 700 °C, due to the unlocking of the geometrically induced stresses, which is otherwise very difficult to achieve. The spatial distribution of the phases in the crystallite volume reveals the fcc capped non-cubic lattices. The two halves of the bipyramid are twisted by ∼ 6° along the length with ∼ ±5% strain. Thus, the monitoring of the phase transformation from non-cubic to fcc lattice *via* the mapping of the geometrical location of the various phases will be interesting. Herein, using SXDM, *in-situ* annealing of the non-cubic Au crystallite was performed (on 1.49 μm long and 295 nm wide Au bipyramid), which reveals the untwisting of the domains assisted by the supplied large kinetic energy.

VI.1 Introduction

Stabilization of Au in unconventional lattice structures has been a subject of matter since few decades. There have been a few reports on the phase transformation to hcp and bcc lattice structures, under high pressure [1] and under high shock compression [2,3], respectively. However at ambient condition, non-fcc lattice structures in bulk Au are yet not known. So far, few reports have led the path by stabilizing Au in non-cubic lattices in the nanoscale, *e.g.*, 2H and 4H phases of Au square sheets [4], nanoribbons [5], nanokites [6], nanorods [7,8] and nanowires [9–12] and nanostars [13]. Au nanocrystals in bct phase have been reported under mechanical deformation [14]. From the group, Au microcrystallites have been stabilized in the form of bc(o,t) [15] and these crystallites act as an excellent catalyst [16].

Among the many known physical perturbants responsible to cause phase transformation, the widely used ones are temperature, pressure and e-/ion-beam. The temperature and pressure induced phase transformation to fcc has been seen in 4H Au

---

nanoribbons [17]/nanowires [9], and e-beam induced transition, in the case of 2H Au square sheets [4]. The bc(o,t) Au crystallites which are stable indefinitely under the ambient are also stable under e-beam application (200 keV) [16]. A previous report shows the thermal stability of the bc(o,t) Au at ~ 400 °C, while an irreversible phase transformation at ~ 700 °C was observed by *ex-situ* SEM and laboratory XRD (at the microscale) [18]. During the phase transformation to fcc, the crystallites undergo deformation in the morphology due to the diffusion of the mobile atoms. Besides, the crystallites display a reversible phase transformation under the applied pressure ~ 40 GPa.

Stabilization of the bc(o,t) lattices in the microcrystallites is mainly favored by the geometrical constraints induced by the penta-twinned bipyramidal morphology. Under the proper growth kinetics, the unlocking of stresses is controlled by the stabilization of the bc(o,t) lattices. Theoretical calculation reveals, the stresses are within the elastic regime (~ 2%) [15]. Under high temperature treatment, the metastable phases convert back to stable fcc which is linked with the relaxation of strains. The relaxation of strains is higher at higher temperatures [18].

VI.2 Scope of the Investigation

Recent SXDM study of a bc(o,t) Au crystallite has revealed the presence of large strain (~ ±5%) and strain anisotropy among the domains (see section **IV.4.C** in **Chapter IV**). These phases are kinetically arrested in the crystallite volume, and thus annealing at high temperature tends to release the stresses by stabilizing the thermodynamically stable fcc lattice. Considering the presence of twist and anisotropic strains in large extend in the entire crystallite body parts, the relaxation of strain is also expected to be non-uniform. Thus, monitoring of the phase transformation *via in-situ* annealing with spatial resolution should bring out interesting observations.

VI.3 Experimental Details

Au microcrystallites on SiN$_x$ nanochip with in-built heater. The as-synthesized crystallites were dispersed in acetone and drop casted onto the single-tilt nanochip membrane (SiN$_x$) with in-built heater from Wildfire nanochip (DENS solutions for Thermo Fisher Scientific (FEI) microscopes, P.T.H.SS.1).

Fabrication of the device.

1. Customizing the substrate holder. The substrate holder was designed and manually cut in such a way that the nanochip fits well in the holder and at the same time, the four contact pads are reachable for making contacts as well as remained unhampered during SXDM measurement. At the bottom of the holder, a PCB board is attached for the electrical contacts.

2. Making the contacts: The Au microcrystallites loaded membrane was used for making contacts. From the pre-furbished four contact pads, four thin (~ 40 µm) Cu wires were used to establish the connections between the four contact pads of the Wildfire nanochip and the PCB board. Ag-epoxy (cured at 120 °C in the air for an hour) was used for making contacts using Cu wire with the contact pads of the Wildfire chip and Sn-Pb solder for making contacts with the four pads of the PCB board. Afterward, four thick (~ 100 µm) insulated Cu wires were soldered with the four contact pads of the PCB. These four connecting wires were used for connecting with the required instrument module (Keithley 4200-SCS semiconductor Characterization System and DENS-E-03-00 Digi-heater control box) according to the use.

3. Measuring the resistance: After completion of two rounds of making contacts from the contact pad to the PCB board and from the PCB board to the power supply controller, the device was studied using a Keithley 4200-SCS Semiconductor Characterization System in the 4-probe measurement configuration. The 4-probe measurement shows the resistance of the heater as ~ 200 Ω.

Interfacing the heater with the software for the *in-situ* control. The calibrated heater was connected with the temperature controller procured from DENS solutions. The controller is pre-programmed to monitor the temperature of the heater while remaining outside of the hutch. The calibrated temperature *vs.* resistance data (obtained from the manufacturer) was used at the time of experiment.

VI.4 Results and Discussion

In order to study the *in-situ* strain relaxation at the nanoscale at high temperatures (~ 800 °C) while keeping the sophisticated experimental set up unaltered (as discussed in **Chapter II**), a MEMS-based resistive heater is used, where the heating at the metallic coil is very local (almost no heating at a far distance ~ 35 µm). The heat is generated due to the Joule heating of the conducting metals while passing current (see **Figure VI.1**).
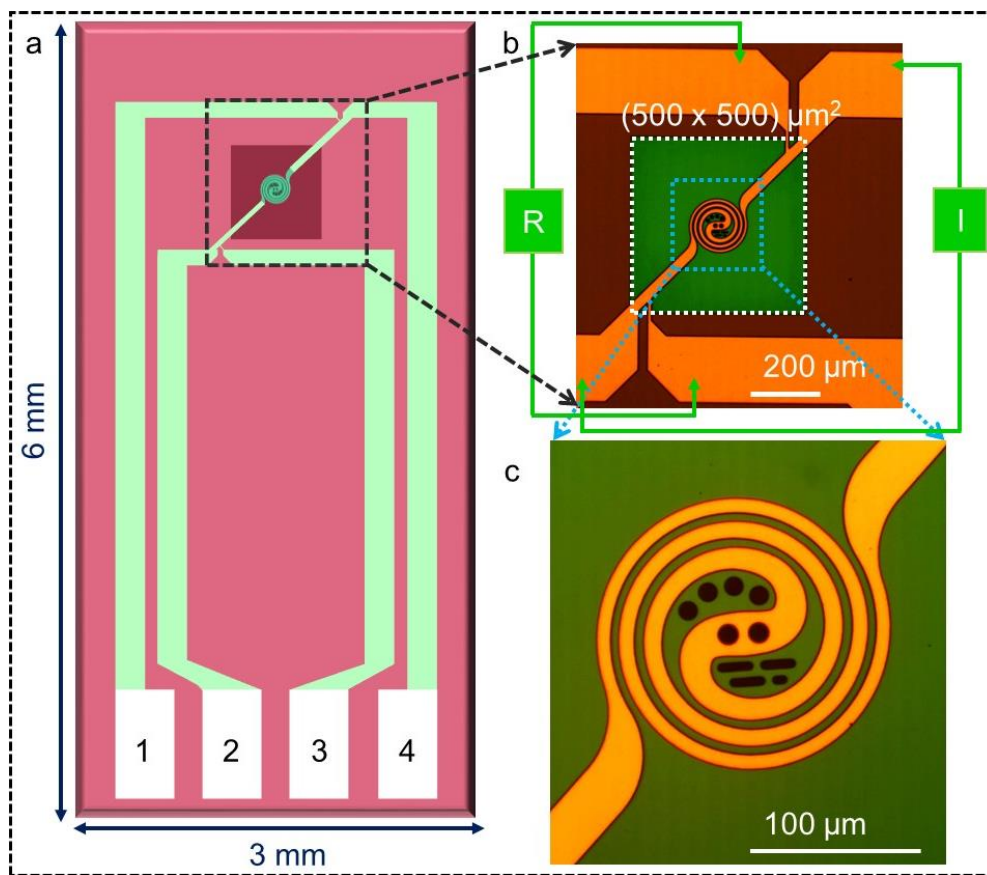
Figure VI.1. Nanochip with in-built heater. (a) Schematic representation of the as-procured nanochip with in-built heater in it. The four contact pads are shown in white color. (b) Optical image of the heater along with connections required for the 4-probe measurement. The nanochip consists of a (500×500) μm^2 SiN$_x$ membrane area (in green) within which a resistive heater (orange) is present. The contact pads (2,4) and (1,3) (as shown in (a)), used for applying current (I) and measuring resistance (R), respectively during the heating experiment. (c) Optical image of the heater, where the orange and greenish colors present the metallic coil and SiN$_x$ membrane, respectively. At the central region of the heater, few circular and rod-shaped holes are present, which are made of ultrathin SiN$_x$ membrane ($\sim$ 10 nm thick).

The as-prepared bc(o,t) crystallites were drop casted on a Si/SiN$_x$ membrane based heater hosting a thin SiN$_x$ membrane at the middle (500 μm $\times$ 500 μm) as shown in **Figure VI.2**a–c for the beam to pass through. An in-built metallic coil ($\sim$ 173 μm in diameter) placed within the membrane was used for local heating (upto 800 °C, with the precision of 95%). The heater consists of 6 circular and 4 rod shaped holes made of thin SiN$_x$ membrane ($\sim$ 10 nm) as shown in **Figure VI.2**c. The almost vertically aligned crystallites placed in the membrane of

the nanochip were located using a dual beam FIB/SEM while the crystallites on top of the metallic coil or outside the coil were not considered due to the hindrance caused in the X-ray beam passage and the caused temperature gradient, respectively. The heater along with the different shaped holes in it act as markers and are visible by the optical microscope ($100\times$ magnification at the beamline) and thereby are easily locatable. In contrast, the small-sized crystallites ($\sim$ 1.5-3 µm in length) are not locatable by the optical microscope. Thus, Pt markers (4 in number) were fabricated with the size of 10×5 µm^2 at the proximity of the vertically aligned crystallites ($\sim$ 20 µm away) in the nanochip (see **Figure VI.2**d). The Pt markers helped to locate the crystallites with ease by XRF maps.
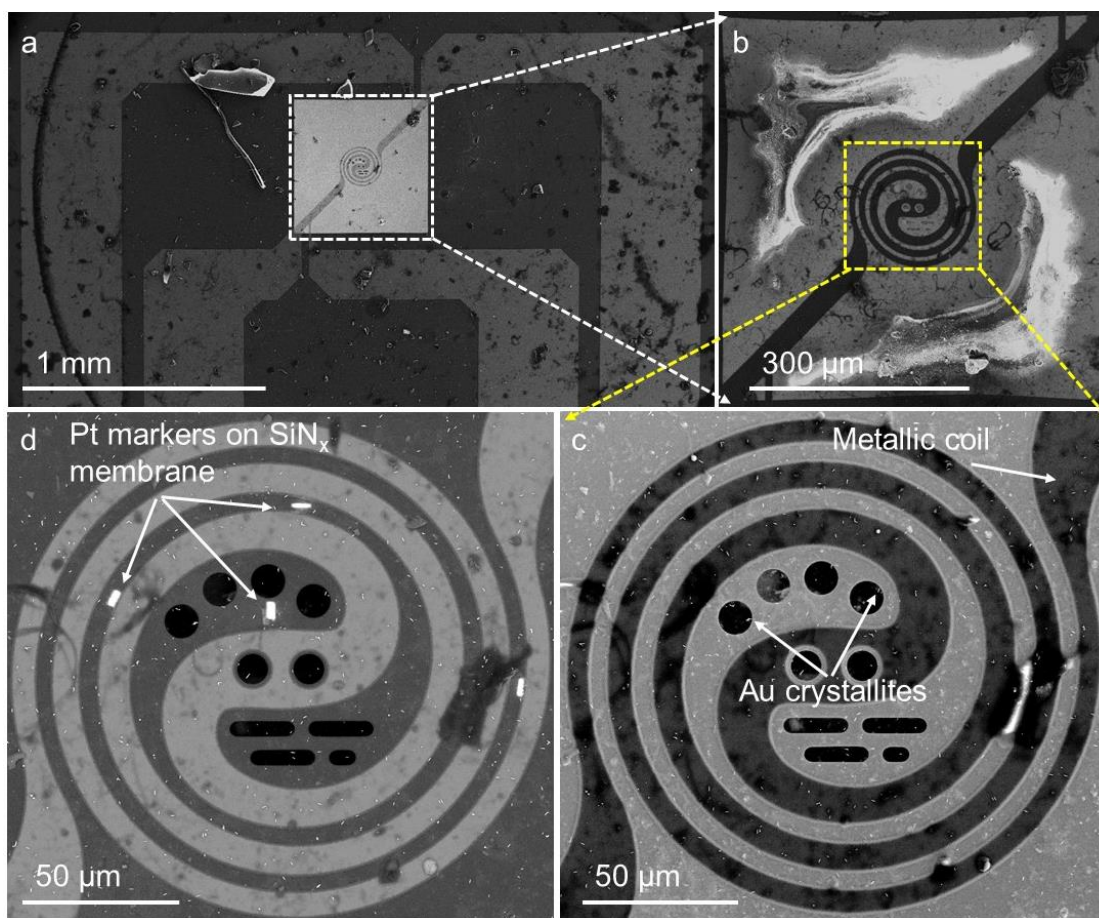
Figure VI.2. (a–c) SEM images of Au crystallites loaded nanochip at different magnifications displaying the SiN$_x$ membrane, heater and the crystallites. The microcrystallites were drop casted on the heater region of the membrane as shown in **Figure VI.1**. (d) SEM image of the nanochip in (c) with Pt markers in it. The metallic coil and holes are easily locatable by optical microscope ($100\times$ magnification at the beamline). Thus, only small sized four Pt markers ($\sim 10 \times 5$ µm^2) near the vertically

oriented crystallites were fabricated on the SiN_x membrane (in the greenish region in **Figure VI.1**c). These markers were located using XRF signals of Pt $L\alpha_1$ and $L\beta_4$ lines intensity as discussed later.
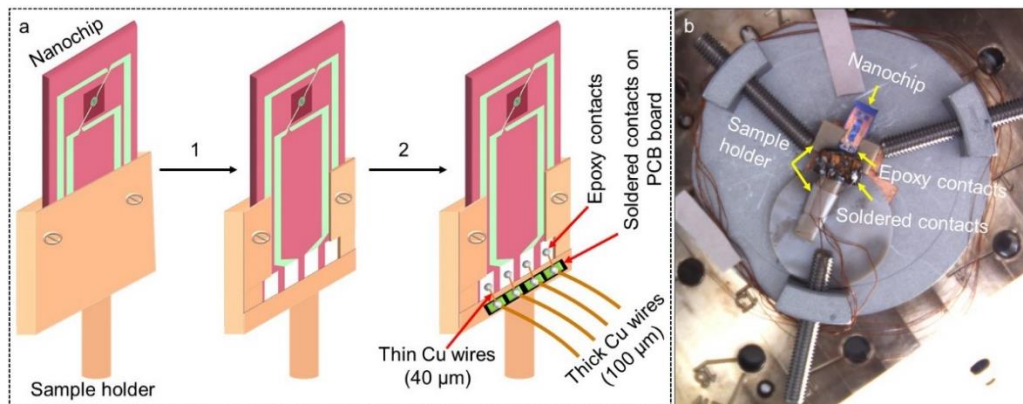
Figure VI.3. (a) Schematic representation of the customized sample holder preparation (1) and creating contacts on the nanochip (2) to connect with the power supply controller. (b) Photograph of the nanochip mounted on the sample holder collected while imaging inside SEM (during the post annealing data collection process).
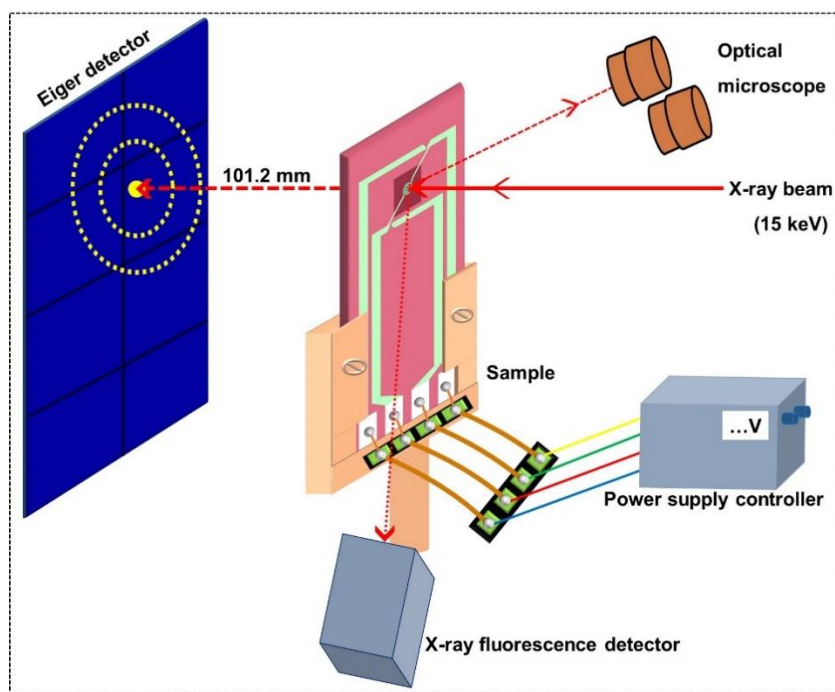
Figure VI.4. Schematic representation of the experimental setup. 15 keV X-ray with 100 nm diameter beam was scanned with a step of $\sim 50 \times 50$ nm^2. The optical microscope was set along the X-ray path and used to locate the bigger holes and the heater coil in the membrane. Further, the optical microscope was removed and X-ray was turned on and used to locate the rectangle-shaped small Pt markers using the XRF microscopy.

The nanochip was mounted in the customized holder and manually made connections as shown in **Figure VI.3** (also see section **VI.3**). The temperature could be fine-tuned and accurately set through the computer controlled calibrated software (from outside the hutch).

Prior to the diffraction experiment, fast raster scan was performed with the 15 keV X-rays (0.826825 Å wavelength and 100 nm beam) in 50×50 nm^2 steps (0.05 s/step) to locate the Pt markers by monitoring Pt Lα_1 (9.4 keV) and Lβ_4 (11.07 keV) fluorescence lines (see **Figures VI.4** and **VI.5**). Later, the crystallite placed vertically near to the marker was located using Au Lα_1 (9.7 keV) and Lβ_2 (11.4 keV) lines. The chosen crystallite thus became nearly parallel to the goniometer axis (y) as shown in **Figure VI.6**a–c. The selected crystallite, ~ 1.49 μm in length, was scanned with the beam slowly (for 14.35 min) with mesh of (2000×1000) nm^2 along y-z directions as shown in **Figure VI.7**. The morphology of the crystallite emerged in the fluorescence map as shown in **Figures VI.6**d and **VI.8**.
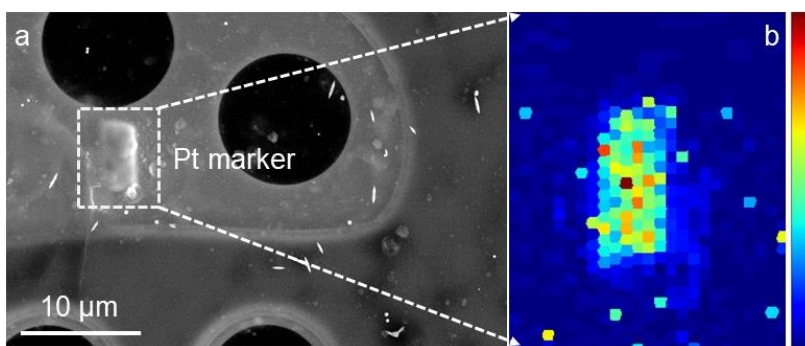
Figure VI.5. Pt marker. (a) SEM image of the Pt marker on SiN$_x$ nano-chip membrane (10×5 μm^2 in size). (b) Integrated XRF image of Pt Lα_1 and Lβ_4 lines.

The morphology of the crystallite was monitored through the XRF map during the entire experiment ensuring the presence of the crystallite within the scanning window. The temperature of the heater coil was elevated by applying voltage (by following the relation obtained from the manufacturer). The required temperature of the heater (such as 180 °C) was achieved within 2 min of applying voltage. After attaining the temperature, the voltage was applied continuously for 10 min which resulted in continuous heating at 180 °C for 10 min. Then, the voltage was gradually brought down (in ~ 5 min) until the temperature reached 20 °C. The SXDM data was recorded from the crystallite at 20 °C. Similarly, other temperatures (*i.e.*, 300, 400, 600, 700 and 800 °C) were achieved by following the above mentioned process though only by varying voltage while retaining the rest of it similar.

The annealing induced deformation in the morphology has already been shown in a previous report [18]. After annealing, the shape of the e-beam deposited Pt marker also evolves due to the removal of the residual organic contaminants and enhancement in the metallicity. The adjacent proximity of the Pt marker displays small Pt particulates which were present due to the spread of the precursor. This observation can be linked with the smaller region of the spread of the precursor, thereby not affecting the examined crystallite.
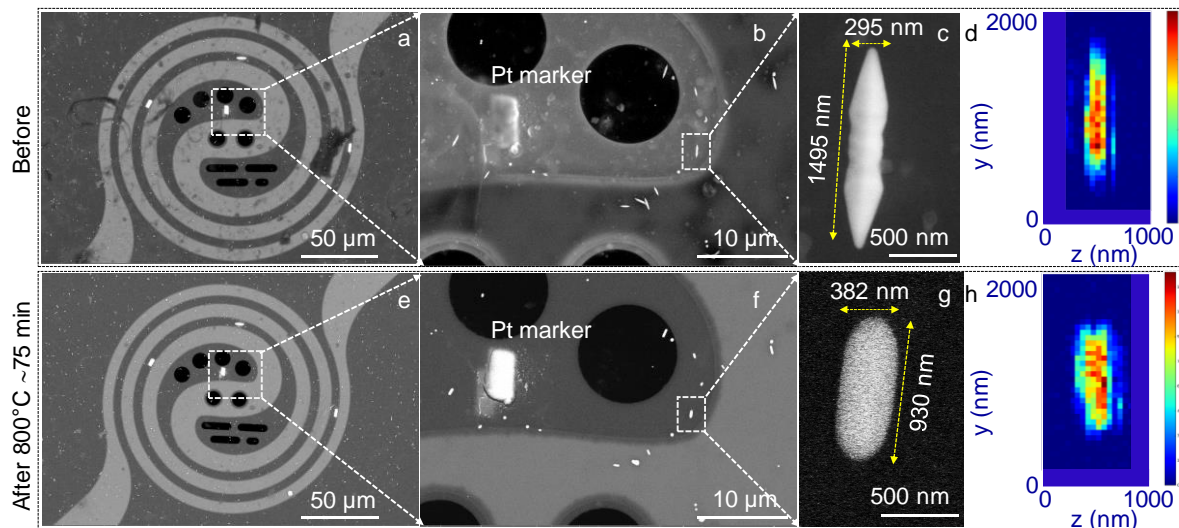
Figure VI.6. Monitoring the Au microcrystallite on the SiN_x membrane before and after the annealing experiment. (a) SEM image of the pre-deposited Pt markers (white rectangles, $\sim 10 \times 5 \ \mu m^2$) on the SiN_x membrane along with the Au microcrystallites. (b,c) The magnified SEM images of the studied region of the membrane and the crystallite. The chosen crystallite was nearly parallel to the Pt marker and thus, nearly vertically aligned in the experimental setup. The halo around the Pt marker is due to the spread of the organometallic complex during the deposition. (d) The XRF map of the examined crystallite emerges the morphology of the crystallite using the Au $L\alpha_1$ and $L\beta_2$ lines intensity. (e−g) SEM images of the same heater, Pt marker and the crystallite as in above panel after the annealing experiment at 800 °C. Note, the morphology of the crystallite has changed during the annealing process (see c and g). (h) The XRF map of the crystallite at the post-annealing at 800 °C depicts deformation in the morphology.

In order to confirm the completion of the *in-situ* local heating, the crystallite was imaged during the post-experiment process by SEM, where the Pt markers exhibit very bright contrast unlike to the as-prepared ones as shown in **Figure VI.6**e. Additionally, the shape of the markers emerged clearly (in **Figure VI.6**f) which can be understood due to the enhancement in metallicity arisen from the decomposition of residual carbon in the Pt

organometallic precursor (the composition of precursor is Pt:C = 70:30) during heating. Moreover, surrounding of the Pt marker in **Figure VI.6**f exhibits bright, contrasted particulates composed of Pt which appeared due to the spreading of the precursor during the preparation of the marker. The SEM image of the examined crystallite exhibits a deformed shape (dumbbell alike) which can be seen by the demolishing of the sharp tips and high index facets while spreading the width uniformly throughout the length as shown in **Figure VI.6**g,h. In contrast to the pre-annealed crystallite in **Figure VI.6**d (1495 nm in length and 295 nm in width), the crystallite features are ~ 930 nm in length and 382 nm in width, *i.e.*, reduction in the area by ~ 9%. The surrounding crystallites also undergo similar changes in the morphology (see **Figure VI.6**b,f) and thereby confirm the deformation is rather induced by thermal heating, not by the used high energy X-ray. This rounding of the crystallite has been observed previously by the group *via ex-situ* heating experiment (at 700 °C) [18]. Thus, the rounding of the bipyramid confirms the heating generated by high temperatures. The overall modification in the morphology occurred mainly at the un-coordinated sharp tips and high-index facets was caused due to the diffusion of the mobile atoms under the huge source of kinetic energy [18]. Interestingly, the crystallites at the immediate outside of the heater coil display rounded feature (see **Figure VI.9**), whereas at ~ 35 µm away from the edge of the heater coil exhibits bipyramidal morphology *i.e.*, retention of the shape. Therefore, a large temperature gradient was observed within 35 µm distance far from the heating coil, which reveals the local heating at the coil (see **Figure VI.9**).

The diffraction data was collected over the scan mesh using an Eiger 4 M detector placed at 101.2 mm away from the crystal center (see **Figure VI.4**). The pristine crystallite was rotated along the crystal axis until few spots concurrently satisfy the diffraction condition and appear in the detector screen. The appropriate conditions were locked and used throughout the entire experiment. The fluorescence and diffraction data sets were collected simultaneously with an acquisition time of 14.35 min per scan (see **Figure VI.7**). At 20 °C, the diffraction data collected from the pristine crystallite shows in all, 6 bright spots in different detector segments (**Figures VI.10** and **VI.11**). Herein, the study has been restricted only to the first 4 spots which are marked as a to d in **Figure VI.11**. The integrated intensities are spread out (see **Table VI.1**).
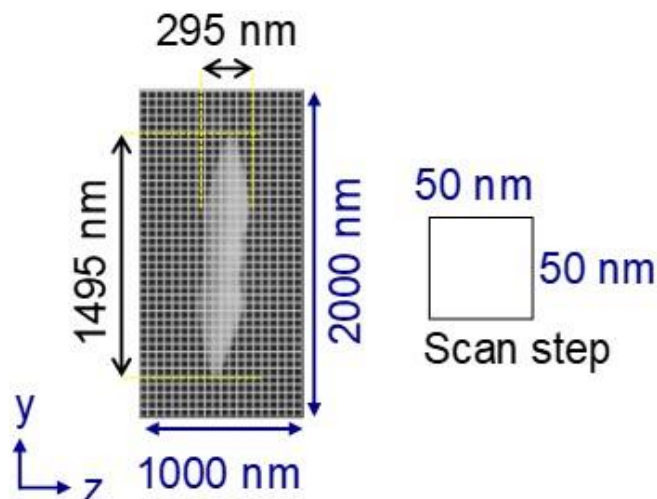
Figure VI.7. Defining the mesh scan. A representation of the mesh scan data collected over a 2000 (y) × 1000 (z) nm^2 grid covering the chosen Au microcrystallite. The scanned step is 50 × 50 nm^2 and thus there were 40 rows along the y direction and 20 along the z. The mesh parameters were chosen considering the beam diameter (100 nm), the crystallite size (~ 1.49 μm in length and ~ 295 nm wide in the middle, but ~ 100 nm at the tips) and the data acquisition time per frame (14.35 min).
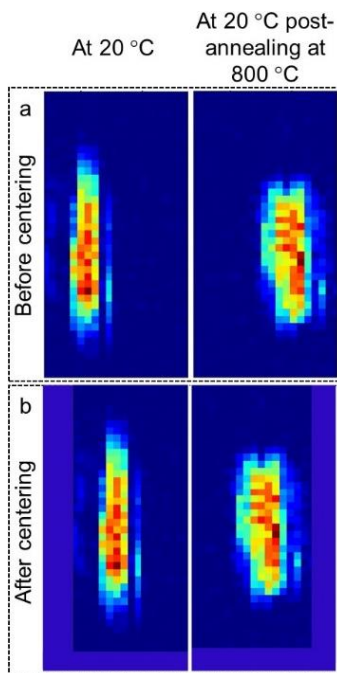
Figure VI.8. Similar like to **Figure IV.9** in **Chapter IV**, XRF maps undergo drift which have been corrected by centering the crystallite.
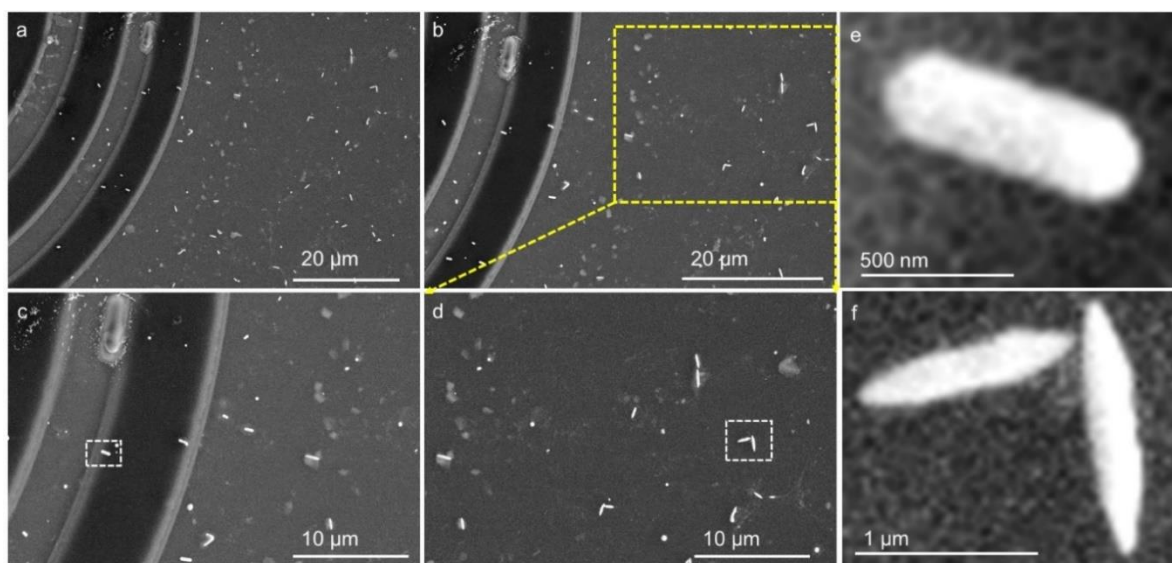
Figure VI.9. (a–d) SEM images of the heating coil and crystallites inside the coil at different magnifications are shown. The magnified views of the crystallites marked in (c,d) are shown in (e,f), respectively. SEM images of Au crystallites (e) inside the heating coil and (f) ~ 35 μm away from the edge of the coil, exhibiting two different morphologies. From the SEM images, the heating appears to be local, since the morphologies of the crystallites are nearly intact in (f), indicating a high temperature gradient.

The q values were estimated from the centroids of the line profiles (**Table VI.1**) within the permissible resolution of ± 0.04 nm^{-1} of the detector. The a, b and d reflections exhibit q of 30.994, 30.998 and 30.850 nm^{-1}, respectively and seem to appear from a family of reflections. Occurrence of such symmetry reflections without a crystal rotation is intriguing. Interestingly, the three spots seem to form three corners of a rectangle as shown in **Figure VI.11**, where the angles extended by the diagonals are 83.35-89.90° and 90.20-94.95°, respectively. These values may be compared with those exhibited by fcc{h00} reflections. The reflections with similar q ranges were observed in another SXDM study of bc(o,t) Au crystallite as reported in **Figure IV.14**a, **Chapter IV**. Besides, the angular spreads are also in the similar range. Hence, the similar discussions related to **Chapter IV** can be invoked here, *i.e.*, the penta-twinned geometry allows to satisfy the symmetry reflections at a particular ϕ and the reflections can be simultaneously assigned as $\{110\}_O/\{200\}_C$. Notably, the growth directions of the different phases are bco<010> and fcc<110> as shown in **Figure VI.12** (for more details visit section **IV.4.B** in **Chapter IV**).

In the horizontal line on the detector plane, the spot c (see **Figure VI.11**), possessing q value of 43.567 nm^{-1}, is present which can be assigned as $\{200\}_O/\{220\}_C$. It may be noted that this spot was out of the detector coverage in the previous SXDM study (see **Figure IV.10** in **Chapter IV**) and thus, was not observed. Here, spot c exhibits large radial spread (~ 2.497 nm^{-1}).
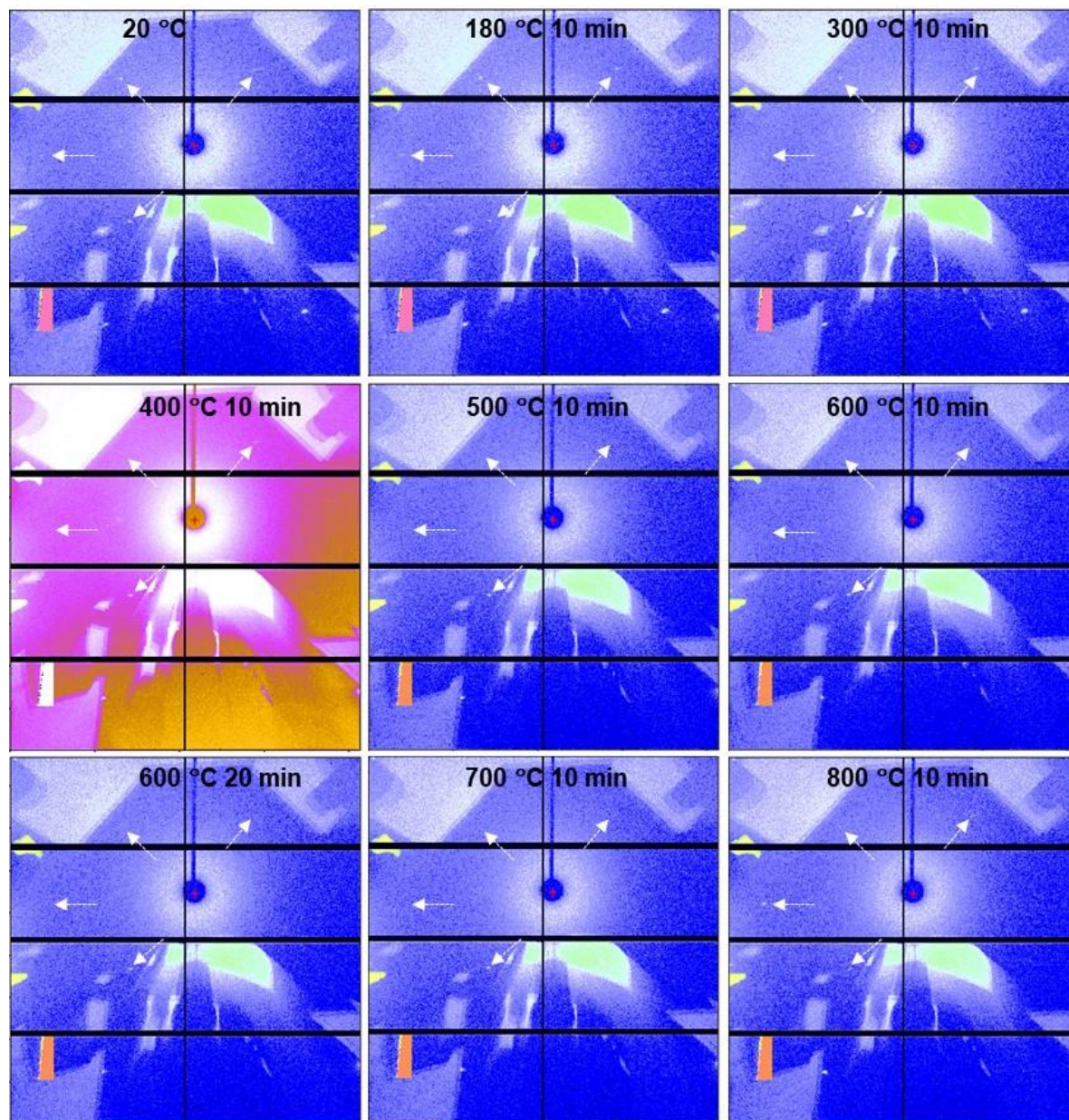
Figure VI.10. Integrated diffraction data as collected for the thermally treated crystallite using an Eiger 4M detector at 20 °C.
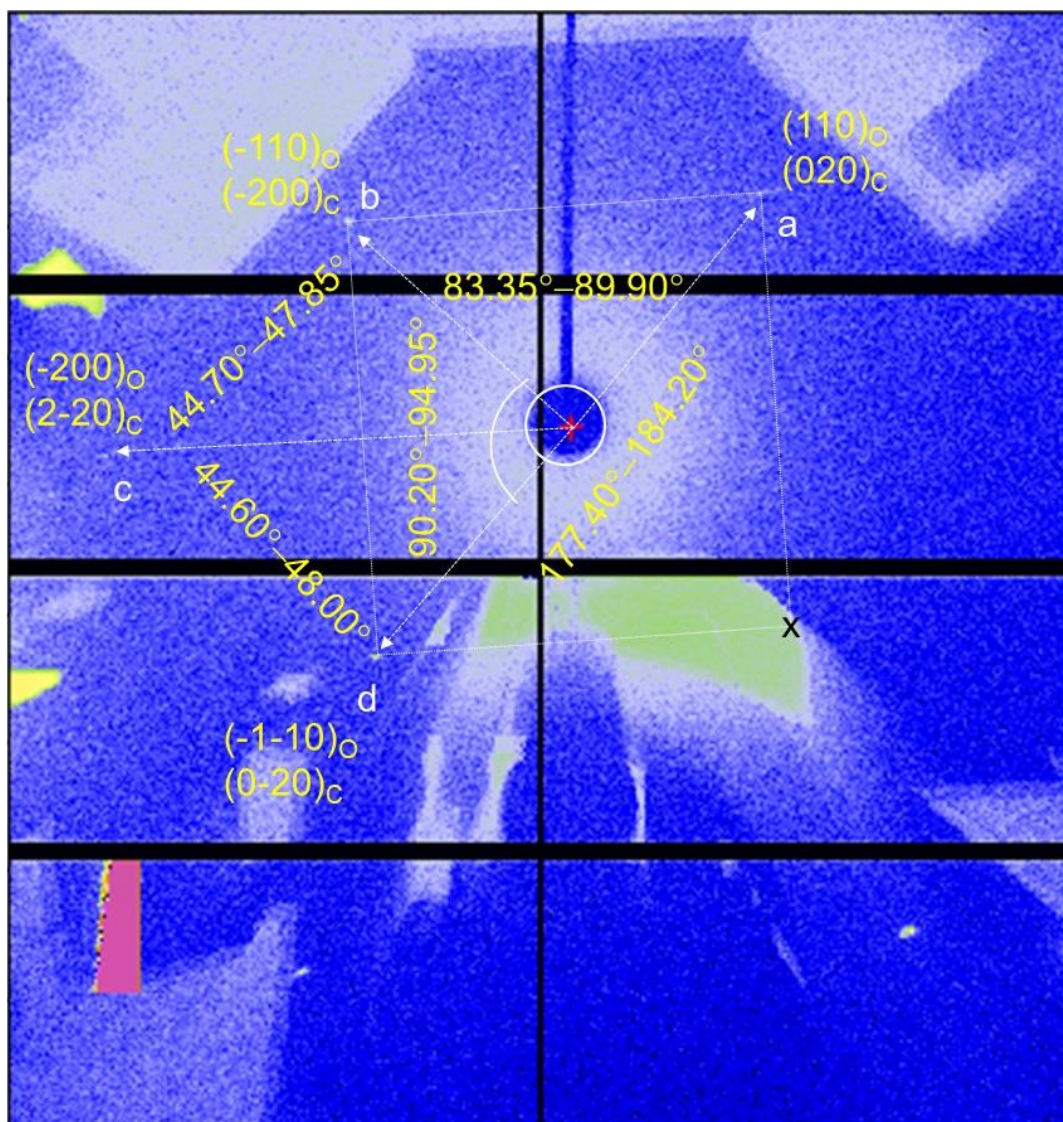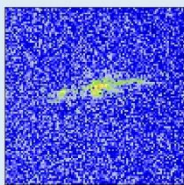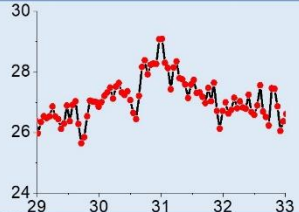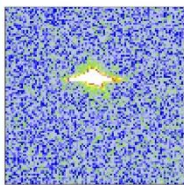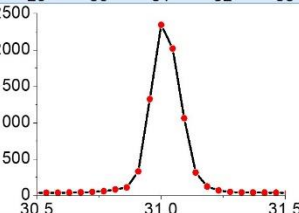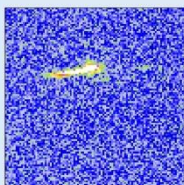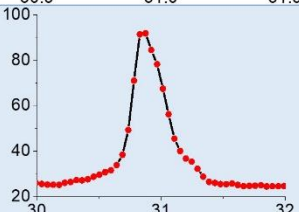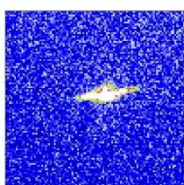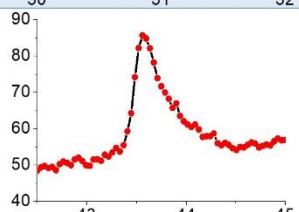
Figure VI.11. Integrated diffraction data as collected from the pristine crystallite using an Eiger 4M detector at 20 °C. Although many spots appear at the detector, the analysis has been restricted only to the four spots, labelled as a to d. The spots have been indexed considering the orientation of the unit cells in **Figures IV.12** and **IV.14**b in **Chapter IV**. Mean q values are denoted in nm^{-1}. Identifying symmetry related reflections and visualizing the unit cells. A white rectangle is drawn to connect the symmetry related spots (a,b,d and an imaginary spot, x).

Using the CrystalMaker software package, the diffraction spots were simulated by rotating both the bco and fcc unit cells along the crystal axis for 360°. The generated patterns were overlaid, as displayed in **Figure VI.12**b (similar to **Figures IV.14**c and **IV.17**j,k in **Chapter IV**). Here, the simulation was restricted to the q radius of 45.5 nm^{-1}.

Table VI.1. Quantifying q values. The q values were quantified from the centroids of the line profiles, drawn over the diffraction spots within the permissible resolution accuracy of $\pm$ 0.04 nm^{-1} of the detector. The line profiles are asymmetric, indicating the presence of strain or multiple lattices. The zoomed-in views of the diffraction spots with (100×100) pixels exhibiting the wide spread along radial and circumferential directions.

In order to correlate the simultaneous presence of symmetry reflections, the diffraction maps were invoked in **Figure VI.13**. Interestingly, the geometrical locations of the diffracting volumes are different, such as nearly bottom tip contributes to spot a, central part for spot b and top tip for spot d. Hence, the different domains contribute to the symmetry reflections due to the presence of penta-twinned geometry. Specifically, the appearance of mirror reflections from the top and bottom tips of the crystallite (spots a and d) highlights the contributions from different domains among the five. The circumferential spreads are also relatively large as observed in the other study (sections **IV.4.B and IV.4.C** in **Chapter IV**).
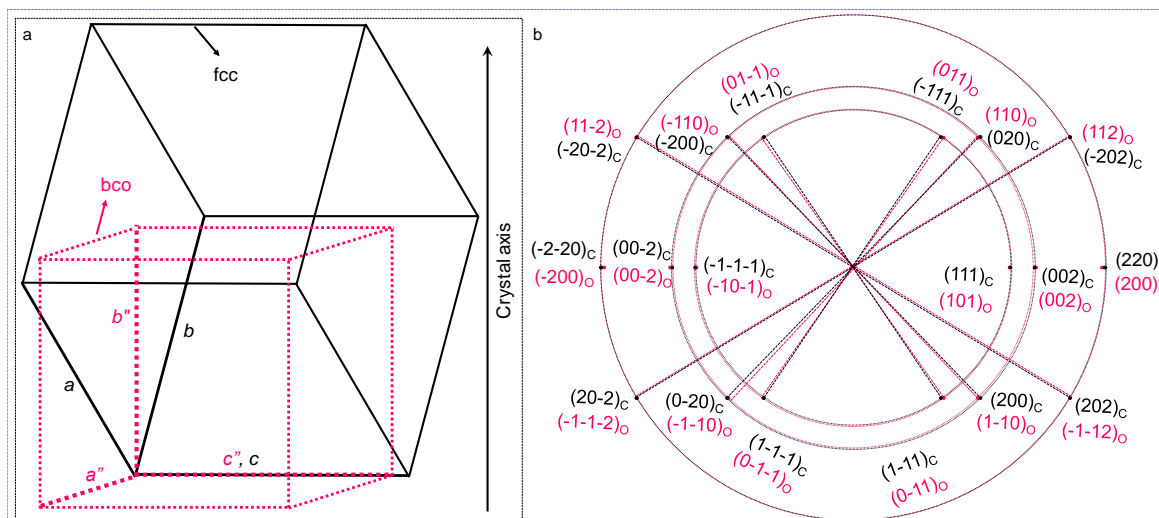
Figure VI.12. Visualizing the unit cells and simulating the corresponding reflections. (a) The orientation of the unit cells, *i.e.*, bco and fcc in the crystallite. *a*, *b* and *c* are the fcc axes. Similarly, *a''*, *b''* and *c''* are the axes for bco. The schematic is not to scale. The bco *b''*-axis is parallel to both the crystal growth direction and the goniometer y-axis. Both *c*-axes, *c* and *c''*, coincide and lie in the horizontal plane. The two unit cells are rotated by 45° along the *c*-axes, and the lattice parameters follow the sequence, *c''* > *a''* and *b''*. (b) Simulated diffraction pattern from the two unit cells with 360° ϕ rotation, overlaid.

Spot c appears from the bottom tip of the crystallite (see **Figure VI.14**). It may be understood that the spots, a and c appear from the similar place. Hence, the appearance of $\{110\}_O/\{200\}_C$ and $\{200\}_O/\{220\}_C$ symmetry reflections reconfirms the growth directions as bco<010> and fcc<110> with a large strain within. Importantly, the observations can be generalized and are applicable for the collection of crystallites prepared in the similar manner.

The diffraction data collected from the 180 °C heated crystallite exhibits nearly unaltered spread (except spot d) and the corresponding diffracting volumes (see **Figures VI.10, VI.13 and VI.14**). Further increasing the temperature to 300 °C, the diffraction data introduces significant changes in the spots (see **Table VI.2** and **Figures VI.13**, **VI.14**). Specifically to spot d, the spreads are ~ 1.774 nm^{-1} (radial) and 3.6° (circumferential). The effects are even visible in the diffraction maps (See **Figures VI.13**c,e,g and **VI.14**c), such as enhancement in the diffracting volume for all the spots. These enhancements are general observations, not specific to a plane. Further increasing the temperature to 400 °C, the diffraction data exhibits a much broader spot where the spreads for spot a (radial−3.065 nm^{-1} and circumferential−6°),

spot b (2.972 nm^{-1}, 4°), spot c (2.972 nm^{-1}, 0.7°) and spot d (1.499 nm^{-1}, 3.3°) are large and non-uniform (see **Table VI.2**).
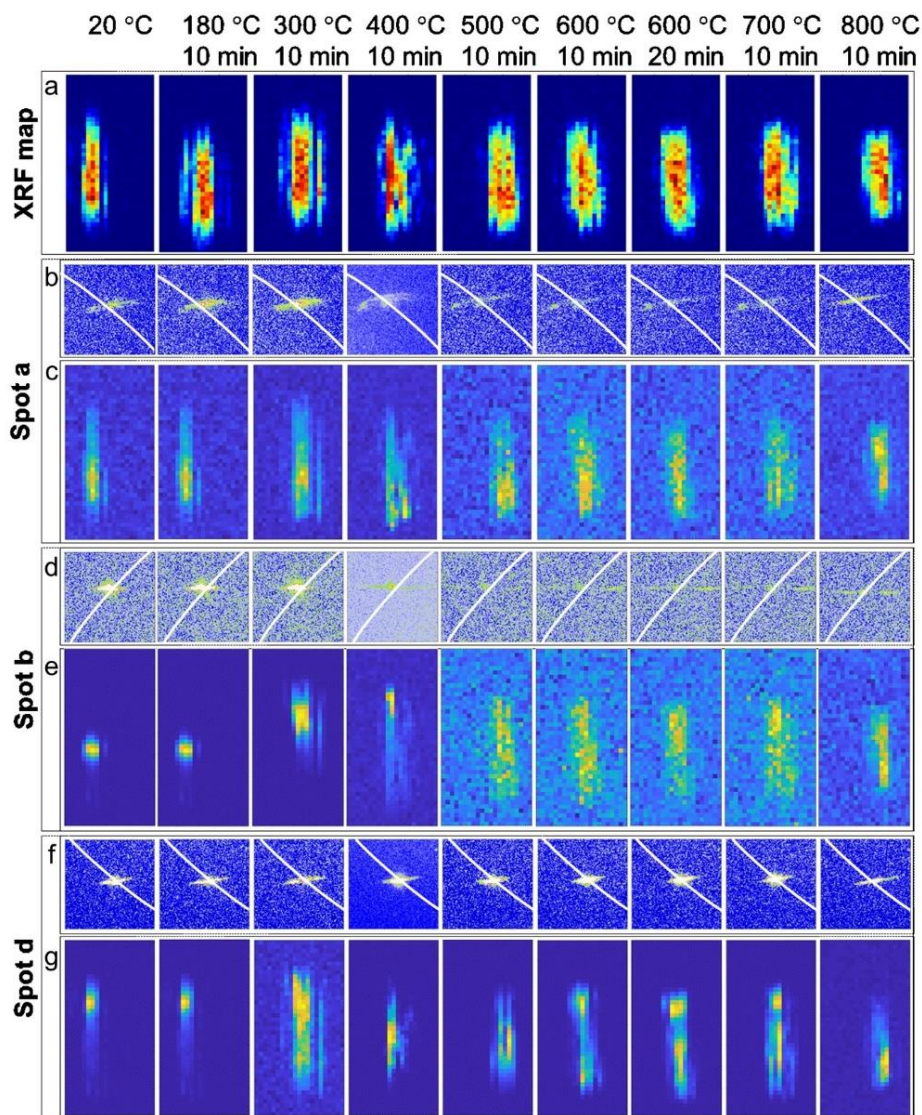
Figure VI.13. Temperature dependent (a) XRF maps, (b,d,f) diffraction spots a,b and d and (c,e,g) the corresponding diffraction maps, respectively. Pixel windows (100 × 100) in (b,d,f). The temperature and time details are shown in the top row. The spots are encompassed with one circle (white) corresponding to the q value of fcc (200) passing in between. The latter was calculated from the standard fcc Au lattice parameters (30.804 nm^{-1}).
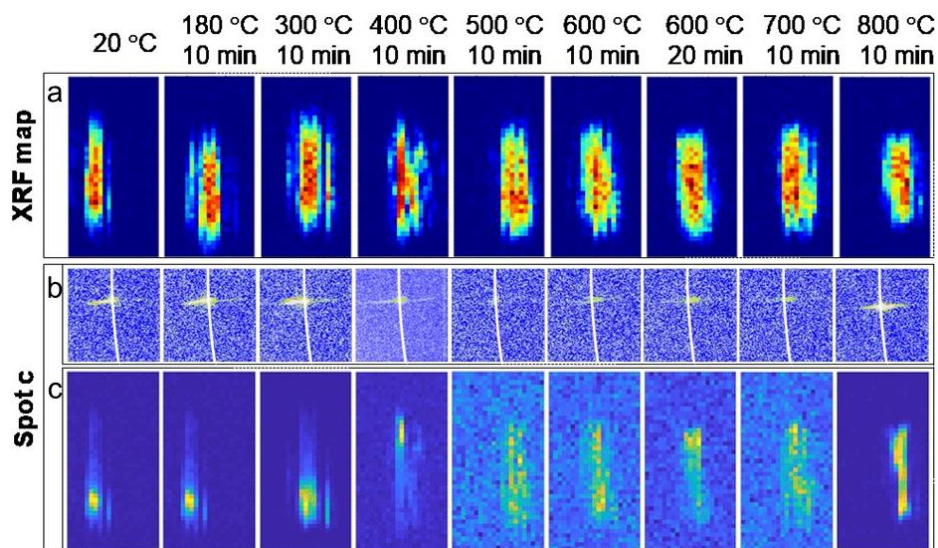
Figure VI.14. Temperature dependent (a) XRF maps, (b) diffraction spot c and (c) the corresponding diffraction map. Pixel windows (100×100) in (b). The temperature and time details are shown in the top row. The spots are encompassed with one circle (white) corresponding to the q value of fcc (200) passing in between. The latter was calculated from the standard fcc Au lattice parameters (43.564 nm^{-1}).

Table VI.2. Measuring the spread of the diffraction spots. The diffraction spots, at both pre-annealed and post-annealed (see **Figures VI.13**b,d,f and **VI.14**b) exhibit highly asymmetric intensity spreads both radially and circumferentially. Indeed, the intensity spread covers reflections from both lattices (bco and fcc) for each spot. The drawn line profiles over the diffraction spots also reveal the associated asymmetry (see **Table VI.1**). In the table given below, for each spot with assigned (hkl) values from the two lattices, the q_{min} and q_{max} values extracted after examining the intensity spread at every ϕ over the entire range. Similarly, the maximum intensity spread observed circumferentially was also calculated and averaged over the symmetry related reflections. The differences in the radial spread are much higher than the instrumental resolution ($\pm$ 0.04 nm^{-1}). The circumferential spreads are even higher. The circumferential spread can be assigned as mosaicity, a measure of imperfection in the crystal, which can arise due to the presence of misoriented domains with similar lattice parameters or oriented domains with different lattice parameters.

Diffraction spot	Temperature (°C)	Time (min)	q_{min} (nm^{-1})	q_{max} (nm^{-1})	Radial spread (nm^{-1})	Circumferential spread (°)
Spot a	20	10	30.421	31.627	1.206	2.25
	180	10	30.421	31.650	1.229	2.5
	300	10	30.491	31.604	1.113	2.15

Thermal Annealing Induced Phase Transformation

Diffraction spot	Temperature (°C)	Time (min)	q_{min} (nm^{-1})	q_{max} (nm^{-1})	Radial spread (nm^{-1})	Circumferential spread (°)
	400	10	29.339	32.404	3.065	6
	500	10	30.794	32.222	1.4278	2.6
	600	10	29.387	32.222	2.835	5.6
	600	20	29.387	32.085	2.698	5.3
	700	10	28.650	31.258	2.608	3.8
	800	10	29.528	31.810	2.282	4.4
Spot b	20	10	29.741	31.948	2.207	4.3
	180	10	29.670	31.879	2.209	4.3
	300	10	29.906	31.856	1.950	3.8
	400	10	29.434	31.856	2.422	4
	500	10	29.528	32.176	2.648	4.6
	600	10	29.481	32.222	2.741	5.1
	600	20	29.481	32.222	2.741	5.1
	700	10	29.576	31.603	2.027	4
	800	10	30.047	31.741	1.694	3.1
Spot c	20	10	42.141	44.638	2.497	0.9
	180	10	42.141	44.638	2.497	0.8
	300	10	42.141	44.638	2.497	0.9
	400	10	42.180	45.152	2.972	0.7
	500	10	43.291	43.857	0.566	0.8
	600	10	43.063	43.857	0.794	0.8
	600	20	43.063	43.857	0.794	0.5
	700	10	43.025	44.308	1.280	0.6
	800	10	42.334	44.453	2.119	1
Spot d	20	10	30.187	31.535	1.348	2.5
	180	10	30.112	31.719	1.607	3.2
	300	10	29.990	31.764	1.774	3.6
	400	10	29.990	31.489	1.499	3.3
	500	10	30.164	31.489	1.325	2.9
	600	10	30.094	31.534	1.440	2.7

Diffraction spot	Temperature (°C)	Time (min)	q_{min} (nm^{-1})	q_{max} (nm^{-1})	Radial spread (nm^{-1})	Circumferential spread (°)
	600	20	30.094	31.442	1.348	2.7
	700	10	30.141	31.419	1.278	2.4
	800	10	29.765	31.581	1.816	3.65

The large spreads can be explained by comparing with the powder pattern collected from a collection of annealed crystallites as reported by the laboratory [18] and **Figures VI.13**b,d,f and **VI.14**b. The pattern collected from the annealed crystallites (*via ex-situ*) exhibits broad (002) reflection as shown in **Figure VI.15** (at 2θ ~ 44.5°) starting from ~ 400 °C and prominent at 500 °C and beyond [18]. During annealing at 400 °C, a new phase (bct-I) introduces with an increase in volume of the unit cell [18]. The similar observations can be correlated with the *in-situ* annealing effect (see **Figures VI.13** and **VI.14**).
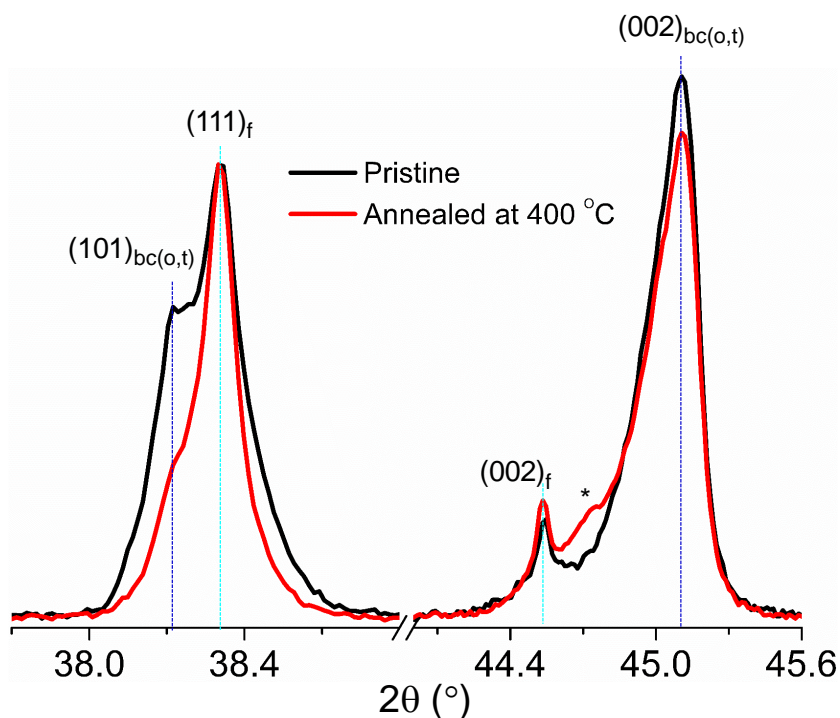
Figure VI.15. XRD pattern of bc(o,t) Au crystallites annealed at 400 °C for 30 min along with the pristine pattern. * denotes the peak newly formed during thermal annealing, which was absent in the pristine pattern. f represents fcc.

Further, the temperature is elevated in steps to 500 °C, 600 °C, 700 °C and finally to 800 °C and the corresponding collected diffraction data represent large radial spreads towards

q_{max} and q_{min}, hinting the presence of compressive as well as tensile strains. This observation is interesting! With increasing annealing temperature, the circumferential spreads also become quite higher, which together with the radial spread refer to the disorder/randomization. The enhancement in the radial spread signifies distribution of lattice parameters which is intriguing when compared with a conventional bc(o,t) to fcc phase transformation where change in volume is prevalent. The XRF maps of the crystallite exhibit the deformation in the morphology, a dumbbell like feature which can be correlated with the SEM image collected during the post-experiment, as shown in **Figure VI.6**g. Thus, the changes in the powder pattern observed previously by the group [18] should also be seen in this case.
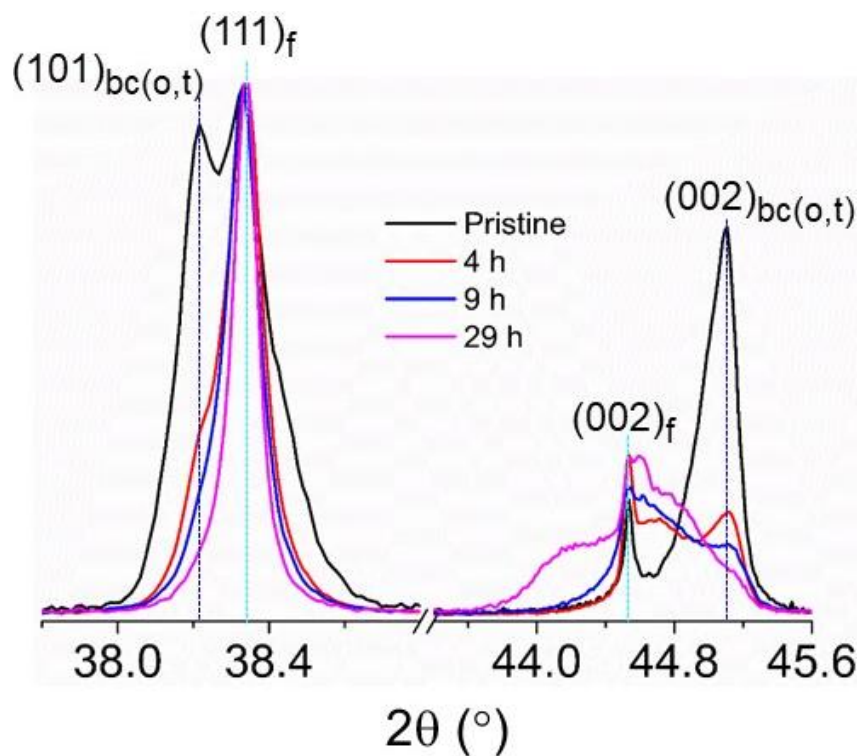
Figure VI.16. XRD patterns of bc(o,t) Au crystallites annealed at 707 °C for different time intervals are presented along with the pristine pattern.

The powder diffraction pattern collected from a collection of crystallites annealed at 707 °C exhibits a broad pattern specifically at (002) regions as was discussed in detail at **Figure V.9** and shown in **Figure VI.16**. The occurrences of series of bct-I phases in addition to the pristine phases (bc(o,t) and fcc) can be linked with the wide spread spot. Annealing induced phase transformation is neither a complete transformation nor a direct conversion. However, the continuous formation of phases and their gradual changes in the intensity distributions are

the observations reflected in the *in-situ* annealing. The formation of bct/bco can be understood by the deviation in *c/a* and *c/b* (from perfect 1.414). The revert back process to fcc can also be understood in a similar manner, for example, alteration in the lattice parameters in a systematic way to achieve the perfect 1.414. In this process, the ranges of *c/a* can be accommodated which project as the spread.
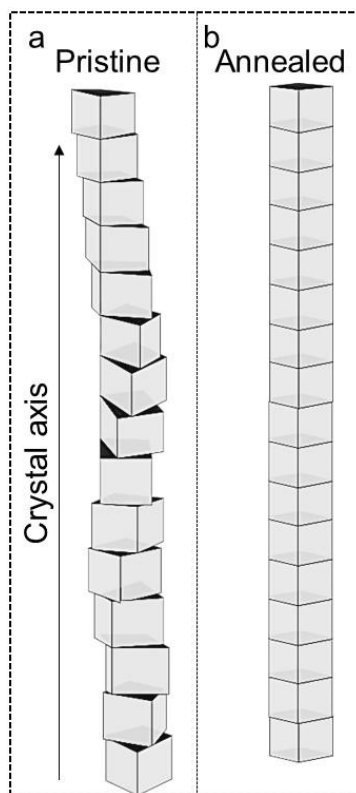
Figure VI.17. Schematic representation of the presence of (a) twisted and (b) untwisted domains in the crystallite. Annealing induced untying of the twist along the same direction with respect to the crystal axis allows to the enhancement of the diffracting volume.

An observation drawn from the diffraction maps of the spots implies that the diffracting volume satisfying Bragg's condition has increased irrespective of the spot. SXDM study on a pristine bc(o,t) crystallite revealed the presence of ~ 6° twist along the length (see **Figures IV.27** and **IV.31** in **Chapter IV**) which hinders to satisfy the diffraction condition throughout the length. Therefore, the emerging diffraction volume can be linked with the reduction in twist along the crystal axis which simultaneously favors to most of the crystallite length. This is in coherence with the annealing induced enhancement in crystallinity which arises due to the growth of bigger grains and deformation in the morphology [18].

With annealing, a reduction in the inherent twist occurs by unfolding it, importantly, in a coherent manner such that the grains mend in the same orientation (see **Figure VI.17**). The unfolded grains favor diffraction condition concurrently, leading to increase in the diffracting volume. In order to understand the change in the spot, line profiles were drawn along the radial direction for spots c and d in **Figure VI.18** (for few temperatures). The profiles exhibit the stark changes starting from 300 °C and with further increase in temperature, the disorder is expressed as increased line broadening and in the form of multiple peaks. The diffraction maps corresponding to spots, a and c must be originating from the similar diffracting region (for 800 °C), and hence from the same domain.
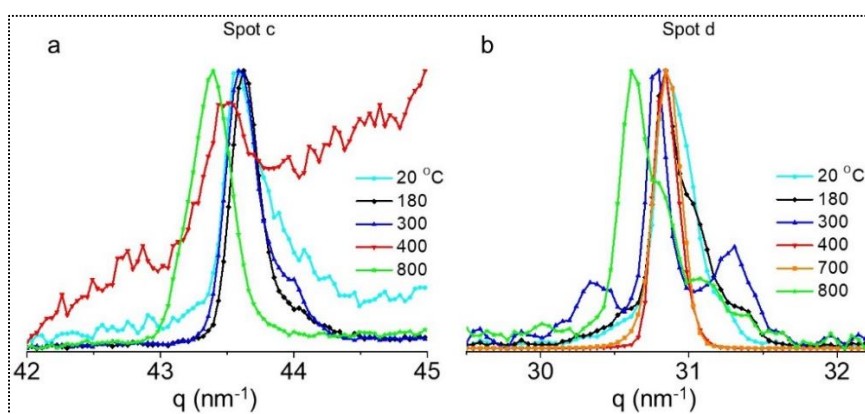
Figure VI.18. (a,b) Line profiles of the diffraction spots c and d, respectively drawn along the radial direction for various temperatures. The intensities have been normalized.

The above results may be contrasted with a study on Ag nanowires [19]. Annealing induced phase transformation has been observed in penta-twinned Ag nanowires hosting bct lattice. During annealing, the nanowires undergo splitting due to the large difference in the activation energy with the bulk [19]. In this study, however, the activation energy differences are rather small according to a result from the laboratory [18], and therefore, the twist-assisted morphological tuning may play a major role in retaining the morphology intact, without undergoing split up.

VI.5 Conclusions

In summary, the study reconfirms the presence of penta-twinned geometry in the bc(o,t) Au bipyramid with the bco<010> and fcc<110> growth directions. Thus, the observations can be generalized for a collection of bc(o,t) crystallites. The study also reconfirms the presence of large strain and thereby addresses the strain relaxation process through the growth of

diffracting volume. The inherent twist among the diffracting domains undergoes untwisting during annealing and interestingly, in the same direction such that the diffraction volume increases. At the end of the annealing experiment, the co-presence of large compressive and tensile strains reveals the strain relaxation process towards fcc, through alteration in the *c/a* ratio. Additionally, the study allows to visualize the rotation of domains and reduction in twists along the crystal axis, which are otherwise difficult to visualize and further understand.

References

[1]   L. Dubrovinsky, N. Dubrovinskaia, W. A. Crichton, A. S. Mikhaylushkin, S. I. Simak, I. A. Abrikosov, J. S. De Almeida, R. Ahuja, W. Luo, and B. Johansson, *Noblest of All Metals Is Structurally Unstable at High Pressure*, Phys. Rev. Lett. **98**, 45503 (2007).

[2]   S. M. Sharma, S. J. Turneaure, J. M. Winey, Y. Li, P. Rigg, A. Schuman, N. Sinclair, Y. Toyoda, X. Wang, N. Weir, J. Zhang, and Y. M. Gupta, *Structural Transformation and Melting in Gold Shock Compressed to 355 GPa*, Phys. Rev. Lett. **123**, 45702 (2019).

[3]   R. Briggs, F. Coppari, M. G. Gorman, R. F. Smith, S. J. Tracy, A. L. Coleman, A. Fernandez-Pañella, M. Millot, J. H. Eggert, and D. E. Fratanduono, *Measurement of Body-Centered Cubic Gold and Melting under Shock Compression*, Phys. Rev. Lett. **123**, 45701 (2019).

[4]   X. Huang, S. Li, Y. Huang, S. Wu, X. Zhou, S. Li, C. L. Gan, F. Boey, C. A. Mirkin, and H. Zhang, *Synthesis of Hexagonal Close-Packed Gold Nanostructures*, Nat. Commun. **2**, 292 (2011).

[5]   Z. Fan, M. Bosman, X. Huang, D. Huang, Y. Yu, K. P. Ong, Y. A. Akimov, L. Wu, B. Li, J. Wu, Y. Huang, Q. Liu, C. Eng Png, C. Lip Gan, P. Yang, and H. Zhang, *Stabilization of 4H Hexagonal Phase in Gold Nanoribbons*, Nat. Commun. **6**, 7684 (2015).

[6]   W. Niu, J. Liu, J. Huang, B. Chen, Q. He, A.-L. Wang, Q. Lu, Y. Chen, Q. Yun, J. Wang, C. Li, Y. Huang, Z. Lai, Z. Fan, X.-J. Wu, and H. Zhang, *Unusual 4H-Phase Twinned Noble Metal Nanokites*, Nat. Commun. **10**, 2881 (2019).

[7]   Y. Chen, Z. Fan, Z. Luo, X. Liu, Z. Lai, B. Li, Y. Zong, L. Gu, and H. Zhang, *High-Yield Synthesis of Crystal-Phase-Heterostructured 4H/fcc Au@Pd Core–Shell Nanorods for Electrocatalytic Ethanol Oxidation*, Adv. Mater. **29**, 1 (2017).

[8]   S. Lee, C. Bae, J. Lee, S. Lee, S. H. Oh, J. Kim, G. S. Park, H. S. Jung, and H. Shin, *Fabrication of a Stable New Polymorph Gold Nanowire with Sixfold Rotational Symmetry*, Adv. Mater. **30**, 1706261 (2018).

[9]   Q. Wang, Z. L. Zhao, C. Cai, H. Li, and M. Gu, *Ultra-Stable 4H-Gold Nanowires up to 800 °C in a Vacuum*, J. Mater. Chem. A **7**, 23812 (2019).

[10]   Q. Lu, A. L. Wang, Y. Gong, W. Hao, H. Cheng, J. Chen, B. Li, N. Yang, W. Niu, J. Wang, Y. Yu, X. Zhang, Y. Chen, Z. Fan, X. J. Wu, J. Chen, J. Luo, S. Li, L. Gu, and

H. Zhang, *Crystal Phase-Based Epitaxial Growth of Hybrid Noble Metal Nanostructures on 4H/fcc Au Nanowires*, Nat. Chem. **10**, 456 (2018).

[11] X. Huang, S. Li, S. Wu, Y. Huang, F. Boey, C. L. Gan, and H. Zhang, *Graphene Oxide-Templated Synthesis of Ultrathin or Tadpole-Shaped Au Nanowires with Alternating hcp and fcc Domains*, Adv. Mater. **24**, 979 (2012).

[12] C. Wang, X. Li, L. Jin, P. H. Lu, C. Dejoie, W. Zhu, Z. Wang, W. Bi, R. E. Dunin-Borkowski, K. Chen, and M. Jin, *Etching-Assisted Route to Heterophase Au Nanowires with Multiple Types of Active Surface Sites for Silane Oxidation*, Nano Lett. **19**, 6363 (2019).

[13] D. Huo, Z. Cao, J. Li, M. Xie, J. Tao, and Y. Xia, *Seed-Mediated Growth of Au Nanospheres into Hexagonal Stars and the Emergence of a Hexagonal Close-Packed Phase*, Nano Lett. **19**, 3115 (2019).

[14] H. Zheng, A. Cao, C. R. Weinberger, J. Y. Huang, K. Du, J. Wang, Y. Ma, Y. Xia, and S. X. Mao, *Discrete Plasticity in Sub-10-nm-Sized Gold Crystals*, Nat. Commun. **1**, 144 (2010).

[15] G. Mettela, M. Bhogra, U. V. Waghmare, and G. U. Kulkarni, *Ambient Stable Tetragonal and Orthorhombic Phases in Penta-Twinned Bipyramidal Au Microcrystals*, J. Am. Chem. Soc. **137**, 3024 (2015).

[16] G. Mettela, N. Mammen, J. Joardar, S. Narasimhan, and G. U. Kulkarni, *Non-fcc Rich Au Crystallites Exhibiting Unusual Catalytic Activity*, Nano Res. **10**, 2271 (2017).

[17] P. Li, Y. Han, X. Zhou, Z. Fan, S. Xu, K. Cao, F. Meng, L. Gao, J. Song, H. Zhang, and Y. Lu, *Thermal Effect and Rayleigh Instability of Ultrathin 4H Hexagonal Gold Nanoribbons*, Matter **2**, 658 (2020).

[18] G. Mettela, Y. A. Sorb, A. Shukla, C. Bellin, V. Svitlyk, M. Mezouar, C. Narayana, and G. U. Kulkarni, *Extraordinarily Stable Noncubic Structures of Au: A High-Pressure and -Temperature Study*, Chem. Mater. **29**, 1485 (2017).

[19] Z. Li, J. S. Okasinski, J. D. Almer, Y. Ren, X. Zuo, and Y. Sun, *Quantitative Determination of Fragmentation Kinetics and Thermodynamics of Colloidal Silver Nanowires by in Situ High-Energy Synchrotron X-ray Diffraction*, Nanoscale **6**, 365 (2014).

*   *   *

Adsorbent Induced Phase Transformation of Ambient Stable non-Cubic Lattices in Au Microcrystallite[*]

Summary

Modulating crystal structures of noble metals can provide a library of new properties, such as optical, electrical, catalytic and so on. Surprisingly, most of the lattice conversions occur at very high temperature and pressure. Recently, Au microcrystallites have been stabilized in bco and bct lattices *via* chemical route which exhibit exuberant catalytic performance. The non-cubic lattices reveal very robust stability features at high pressure (~ 40 GPa) and temperature (< 700 °C). Herein, the work pertains to the interaction of various adsorbents with the bc(o,t) crystallites, the enhancement in crystallinity, the irreversible phase transformation to thermodynamically stable fcc lattice induced by surfactants at moderate temperatures (such as at ~ 200 °C) with $(002)_{non-cubic} \rightarrow (111)_{fcc}/(002)_{fcc}$ orientation. The conversion is governed by the binding strength of the adsorbent and polarity of the medium. The extent of transformation can be fine-tuned at any instance by simply controlling the reaction kinetics or by adding a synergistic or blocking agent. The presence of strong oxidizing agent, Au(III)/tetraoctylammonium bromide is capable of dissolving the µm sized crystallites while displaying crystal structure dependent reactivity, higher at the bc(o,t) lattices than the fcc.

VII.1 Introduction

Surfactant induced morphology-controlled synthesis of crystallites (specifically, anisotropic nanostructures) and further tailoring of their crystal structures have attracted immense interest due to their wide applications in optical, catalytic, electrical and SERS [1,2]. The surfactants are commonly known for suppressing the surface energy of the nanoparticles, thereby stabilizing the energetically expensive facets while accompanying in the growth process, which may also facilitate the stabilization of anisotropic morphology/unconventional lattices. For example, Au nanorods [3–7] and 1D metallic nanowires [8,9] were successfully synthesized by using CTAB and oleylamine as surfactant/template, respectively. Additionally, stabilization of hcp phase in the form of square sheets [10], nanoribbons [11], nanowires [12]

---

and nanorods [13] was achieved by tuning the surfactants, *i.e.*, oleylamine/dodecylamine. The same surfactant, oleylamine promotes the stabilization of 1D metallic fcc Au nanowires [14] and unconventional 2H and 4H phases in Au nanosheets/nanowires/nanoribbons, where the latter demand additional controlling parameters, such as polarity and kinetics.

Stability and reactivity of nanostructures are mainly defined by the surface energies of the planes where the surface energy takes over the system energy and accordingly, the surfaces follow different kinds of reconstructions such as herringbone reconstruction, displacive reconstruction, missing row reconstruction *etc*. Interestingly, many reports discuss the effect of surfactants/capping agents on controlling the morphology of the as-synthesized crystallites in the post-synthetic process. Among the many commonly known adsorbents, the widely used ones are thiols, amines and phosphines. Preferential adherence of surfactants on a specific facet can release the local stress which may lead to reconstruction. For example, thiols are known for lifting up the herringbone reconstruction on Au(111) [15–20]. A change in faceting from (111) to (100) in Pt nanoparticles induced by H_2S is another example [21]. Similarly, tuning of the morphology was achieved in Au nanorods/nanoparticles by facet selective etching using $CuCl_2$, $FeCl_3$, ToABr [22], oxidizing agents [23,24] and CTAB [25–30] to nanowires/nano-particulates in the post-synthetic process. Further, surfactants can act as perturbants to cause phase transformation at the post-synthetic process as well. Examples include alteration in ZnS [31] and CdSe [32] crystallinity *via* interaction with capping agents, reversible switching of the crystallinity in Pd nanoparticle by exchanging the surface capping agent [33] and hcp (2H/4H) to fcc irreversible phase transformation in Au nanostructures [11,34] by exchanging surface capping agents. Thus, the switching in crystallinity in the post-treatment process is mainly governed by the binding strength of the adsorbents with the nanoparticles surface.

Besides the adsorbents, the crystal structure itself dictates most of its interesting properties [1,35]. For example, bulk Ag in fcc lattice appears shiny white, while in unconventional 4H lattice it is golden yellow and also less metallic than the fcc form [36]; fcc Ru is a much better catalyst than hcp form [37]. Therefore, tuning the crystal structure indirectly relates to its properties. Au conventionally crystallizes in fcc lattice and is highly robust and resistant to change to other lattices even at the application of extremely high pressure (240 GPa) [38] or under shock compression [39,40]. Chemically, Au has been

stabilized in the hcp phase as nanostars [41], square sheets [10], nanoribbons [11], nanowires [42–44], kites [45] and in bc(o,t) phases as microcrystallites [46,47].

Interaction between bc(o,t) Au microcrystallites and the well-known adsorbents/reducing agents (such as hexadecanethiol, Na_2S, cationic quaternary ammonium surfactants and metal-tetraoctylammonium bromide) in the post-synthetic process is explored. Hexadecanethiol reduces the mosaicity in the bipyramids (presence of mosaicity is discussed in **Chapter IV**), Na_2S induces phase transformation to fcc with reversal of the preferred orientation from (002) to (111), quaternary ammonium surfactants revert back the crystallites to fcc with (002) orientation in finely controlled manner by the presence of synergistic or blocking agents.

VII.2 Scope of the Investigation

The bc(o,t) Au crystallites exhibit extraordinary stability under different applied physical perturbations, however similar studies under chemical perturbations are unknown. The stability in chemical environments can be very different, considering the preferential adherence of the chemicals on various facets. This may lead to modifications in the preferential orientation/overall morphology possibly followed by the formation of metastable crystal structures. Thus, a study on the chemical stability of the crystallites (such as hexadecanethiol, Na_2S, cationic quaternary ammonium surfactants and metal-tetraoctylammonium bromide) will be worthwhile which would help in defining the chemical window for the bc(o,t) lattices for real applications. Additionally, the study should unveil the interaction selectivity on the various facets/crystal structures.

VII.3 Experimental Details

Chemicals. Ammonium bromide (NH_4Br, > 99.0%), tetraethylammonium hydroxide ($N(C_2H_5)_4OH$) (35 wt% solution), tetrapropylammonium hydroxide ($N(C_3H_7)_4OH$) (1.0 M solution in water), tetrakis(decyl)ammonium bromide ($N(C_{10}H_{21})_4Br$, ≥ 99.0%) were purchased from Aldrich company. Tetrahexadecylammonium bromide ($N(C_{16}H_{33})_4Br$, ≥ 98.0%), palladium (II) chloride, 99% ($PdCl_2$), chloroplatinic acid hexahydrate ($H_2PtCl_6.6H_2O$, abt. 40% Pt) and hexadecanethiol (~ 95%) were procured from Sigma-Aldrich. Ethanol, sodium sulphide flakes ($Na_2S.xH_2O$, 55.0-60.0%) and tetra-n-butylammonium bromide ($N(C_4H_9)_4Br$, 98%) were purchased from S-D Fine Chemicals, India. Copper(II)

chloride dehydrate ($CuCl_2.2H_2O$, 98%) was procured from Qualigens fine chemicals. All reagents and solvents were used as received without further purification. Double-distilled water was used throughout this investigation.

Synthesis of Au microcrystallites in fcc lattice. The fcc microcrystallites were prepared following a previous literature [48]. Briefly, thermolysis of AuAgToABr at 135 °C results in fcc Au microcrystallites. The prepared crystallites were washed with toluene followed by aq. NH_3 to remove the unreacted precursors and any contaminations arising from Ag.

Treatment with hexadecanethiol. The crystallites were treated with 60 µL of 50 mM hexadecanethiol solution in ethanol at various temperatures. The treated crystallites were cleaned by ethanol and dried under N_2.

Treatment with Na_2S. 50 mM Na_2S solution in water was prepared and used for treatment. The crystallites were treated with 60 µL of Na_2S solution at various temperatures.

Treatment with quaternary ammonium salts. The as-synthesized crystallites were treated with 30 µL of $NR_4^+X^-$ solution (50 mM) at 220 °C for 7 min, where the NH_4Br, $N(C_2H_5)_4OH$, $N(C_3H_7)_4OH$, $N(C_4H_9)_4Br$ solutions were made by dissolving in water and $N(C_8N_{17})_4Br$, $N(C_{10}H_{21})_4Br$, $N(C_{16}H_{33})_4Br$ in toluene. The treated crystallites were cleaned by water/toluene and dried under N_2.

Treatment with PtToABr. 50 µL of aqueous H_2PtCl_6 solution (25 mM) and 150 µL ToABr (50 mM) were added and shaken well forming the PtToABr precursor at the organic medium. 30 µL of PtToABr was drop coated over the as-synthesized Au microcrystallites on Si substrate and thermolysis of the PtToABr was allowed at 220 °C for 7 min. Later, the unreacted precursor was washed with toluene.

Treatment with PdToABr. 17.5 mg $PdCl_2$ was dissolved in 3.94 mL HCl (50 mM) and the $PdCl_4^{2-}$ stock solution was prepared. 50 µL of $PdCl_4^{2-}$ and 150 µL of ToABr (50 mM) were mixed and 30 µL of the phase transferred toluene solution (PdToABr) was used for the treatment. The next steps are similar to PtToABr.

Treatment with AgToABr. 50 µL of aqueous $AgNO_3$ solution (25 mM) and 10 µL of HCl (11.35 M) were mixed and stirred vigorously resulting in AgCl. With the AgCl solution, 150 µL of ToABr (50 mM) were mixed and 30 µL of the phase transferred toluene solution (AgToABr) was used for the treatment. The next steps are similar to PtToABr.

Treatment with CuToABr. 100 µL of aqueous $CuCl_2$ solution (25 mM) and 10 µL HCl (11.35 M) were mixed and stirred vigorously resulting in $CuCl_4^{2-}$ stock solution. 50 µL of $CuCl_4^{2-}$ and 150 µL of ToABr (50 mM) were mixed and 30 µL of the phase transferred toluene solution (CuToABr) was used for the treatment The next steps are similar to PtToABr.

Treatment with AuToABr at 220 °C. Aqueous $HAuCl_4$ solution (25 mM) and ToABr solution in toluene (50 mM) were mixed in 1:3 ratio and phase transferred the formed AuToABr in the organic medium. 30 µL of AuToABr was drop coated over the as-synthesized Au microcrystallites on Si substrate and thermolysis of the AuToABr was allowed at 220 °C for 7 min. Later, the unreacted precursor was washed with toluene.

Treatment with AuToABr at 150 °C. Aqueous $HAuCl_4$ solution (10 mM) and ToABr solution in toluene (50 mM) were mixed in 1:1 ratio and phase transferred the formed AuToABr in the organic medium. 20 µL of AuToABr was drop coated over the as-synthesized Au microcrystallites on Si substrate and thermolysis of the AuToABr was allowed at 150 °C for different time periods. Later, the unreacted precursor was washed with toluene.

VII.4 Results and Discussion

VII.4.A Treatment with Hexadecanethiol

Interaction between Au and thiols has been a subject of great interest since decades, dealing mainly with the role of chemisorbed thiols (in the form of self-assembled monolayer, SAM) in the reconstruction of the flat and cleaned Au(111) surfaces [16,49,50]. Although the detailed understanding of these reconstructions is quite controversial, it is generally believed that the thiol molecule binds to the adatom and leads to surface reconstruction [18,20]. Interestingly, the presence of unsatisfied coordination on the surface in the forms of kinks, steps, edges particularly on high index facets increases the thiol reactivity and results in a more facile reconstruction in comparison to that on flat surfaces [51]. A few reports discuss the role of adsorbent on the substrate in inducing metastable to stable crystal structure transformation which is otherwise conventionally achievable only at elevated temperatures under high pressure [52] or e-beam exposure [10]. For example, treatment of thiols to the 2H/4H Au nanostructures results in fcc phase at ambient condition [11,34]. A study on the interaction between robust non-cubic Au microcrystallites and hexadecanethiol will be interesting, considering the former is in the form of metastable lattices.
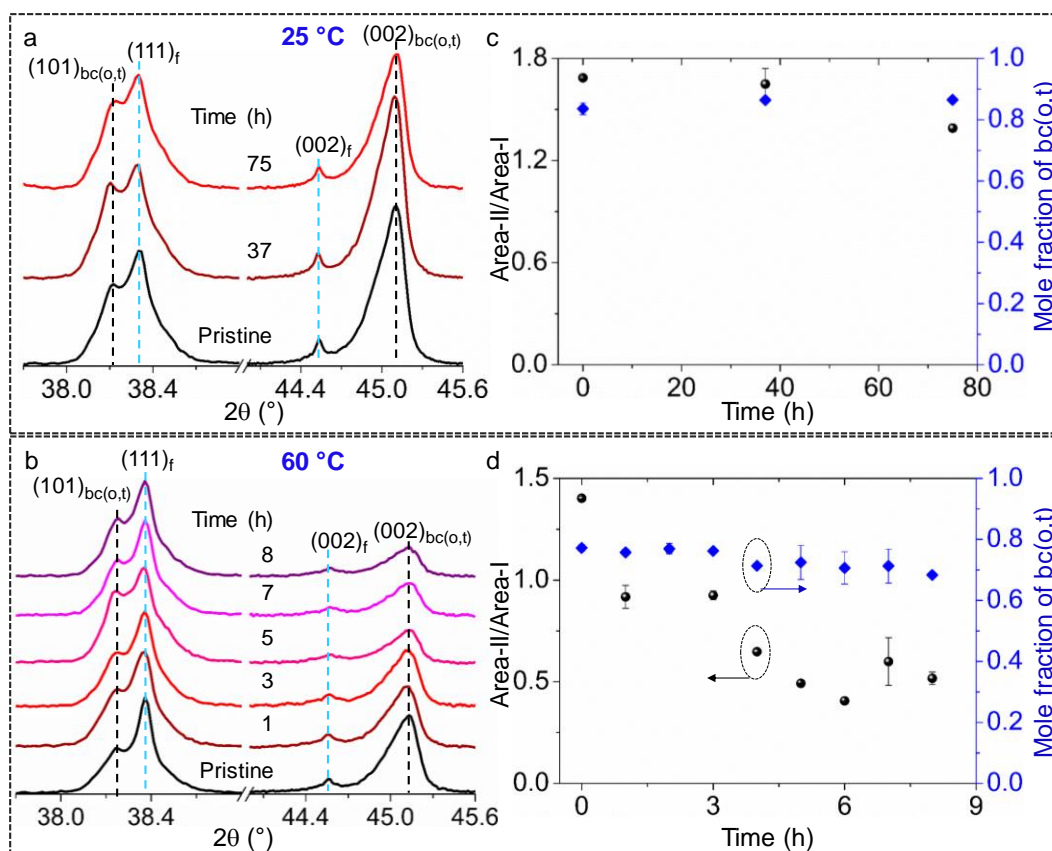
Figure VII.1. (a,b) Time dependent changes in XRD pattern collected upon hexadecanethiol treatment at 25 and 60 °C, respectively. The intensities have been normalized with respect to fcc(111). f represents fcc. (c,d) Changes in XRD (area-II/area-I) ratio and mole fraction of bc(o,t) with treatment time at 25 and 60 °C, respectively.

The crystallites were treated with a toluene solution of hexadecanethiol at 25 °C and the time dependent changes were monitored by XRD as shown in **Figure VII.1**a. The XRD patterns seemed to be unaltered even after 75 h, and therefore, the treatment temperature was elevated to 60 °C. Surprisingly post 8 h treatment, the XRD pattern contained an altogether different intensity distribution among the peaks, especially at the $(002)_{bc(o,t)}$ region when compared with the pristine (see **Figure VII.1**b). This is typical of an activated adsorption process. The reaction temperature was further increased to 90 °C, where the changes in the XRD pattern became explicit as shown in **Figure VII.2**a. Upon 2 h of treatment, the normalized intensity of the $(101)_{bc(o,t)}$ peak increases and the $(002)_{bc(o,t)}$ decreases when compared with the pristine (all patterns are normalized with respect to $(111)_f$). Interestingly after 9 h of treatment, most of the $(002)_{bc(o,t)}$ peak normalized intensity drops down while the

$(101)_{bc(o,t)}$ region gains. Profile fitting of the 9 h treated XRD pattern confirms the retention of similar lattice parameters as in the pristine (see **Figure VII.2**b,c). Upon further increasing the time of treatment to 13 h, small changes in the intensity of $(101)_{bc(o,t)}$ region are observed. Thus, the detected changes are quantified in the form of ratios, area-II/area-I (see **Figure VII.1**b,d) for different times of treatment and presented along with the variation in the bc(o,t) mole fraction. With the treatment time, the ratio nearly follows an exponential decay while the mole fraction of bc(o,t) (calculated from the $2\theta \sim 44\text{-}45°$ region) exhibits a small increment as shown in **Figure VII.2**d (for 90 °C). The monotonous decrement of ratio (in the area) with time continued till 9 h and beyond that the ratio remained nearly constant, which can be explained by the observed plateau beyond 9 h. The absolute area under the curve has been taken into consideration (in **Figure VII.3)**, where a monotonous increment in the overall pattern with the treatment time exemplifies the enhancement in crystallinity till 9 h and beyond that no significant changes were observed. Within the reaction time-frame, the enhancement in the area mainly counts for area-I with nearly unaltered area-II. Thus, the enhancement in crystallinity corresponding to the area-I comprises of $(111)_f$ and $(101)_{bc(o,t)}$ facets.

Similar changes were observed at 60 °C but at a lesser extent (**Figure VII.1**d), whereas at 25 °C, the effect was much less (see **Figure VII.1**b). The reaction temperature was not increased further due to the instability of hexadecanethiol at elevated temperature (> 100 °C). Once the crystallite is subjected to hexadecanethiol treatment, it continues to undergo changes in the crystallinity even under ambient conditions, albeit at a very slow pace. This observation was borne out from examining some old samples. The crystallites treated at 60 °C (cleaned and stored at ambient) were reexamined after 3 years. Surprisingly, the XRD pattern as shown in **Figure VII.4**a, exhibits nearly similar features like the 90 °C treated pattern (post 13 h in **Figure VII.2**a). Although the crystallites were cleaned by ethanol during the post-treatment of hexadecanethiol, the as-formed SAM retained causing kinetically driven changes in the XRD pattern. The effect of hexadecanethiol was also observed in the prolonged period, hinting the effect to be irreversible. Thus, the enhancement in the intensity is a kinetically controlled process, and the modification in XRD was upto the saturation level (*i.e.*, maximum achievable) as shown in **Figure VII.2**a. SEM image of the crystallites exhibits distinguishable contrast at the tips and at the central body (see **Figure VII.4**b), which can be related with the presence of hexadecanethiol molecules at the latter portion. SAED pattern collected from the edge of the

3 year old bipyramid exhibits asymmetric line profile, confirming the presence of non-cubic lattices.
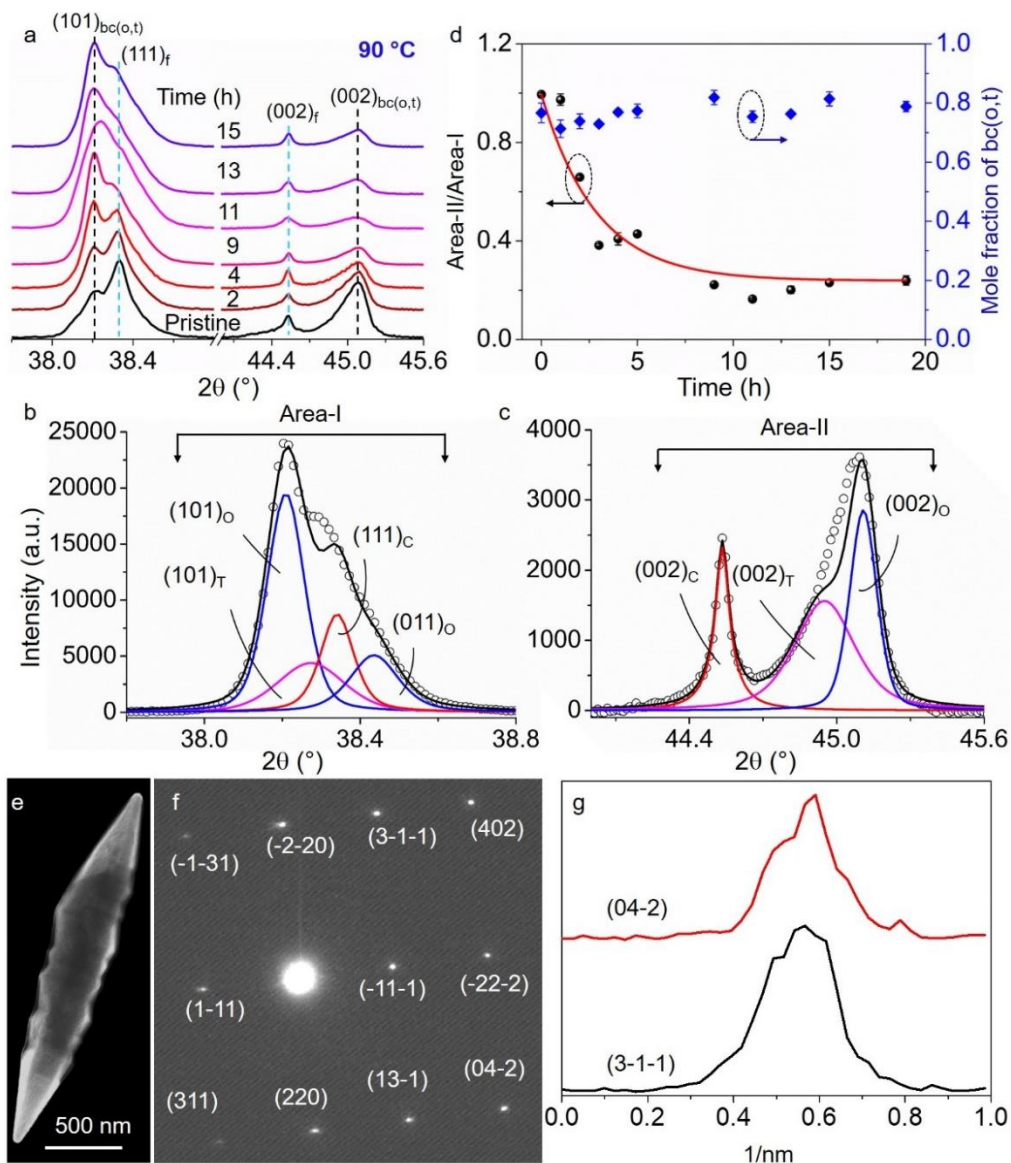
Figure VII.2. (a) Time dependent changes in bc(o,t) Au XRD pattern after treatment with hexadecanethiol at 90 °C. The intensities have been normalized with respect to fcc(002) peak. (b,c) Le Bail fitting of the XRD pattern obtained after 9 h of treatment. The XRD features are grouped into two regions marked as area-I and area-II. (d) Changes in ratio of XRD area-II/area-I and mole fraction of bc(o,t) with treatment time. (e) SEM image of a hexadecanethiol treated Au bipyramid examined after 3 years. (f) SAED pattern collected from the edge of the 3 year old Au bipyramid along the zone axis [1-1-2]. (g) Line profiles drawn over the (3-1-1) and (04-2) spots.
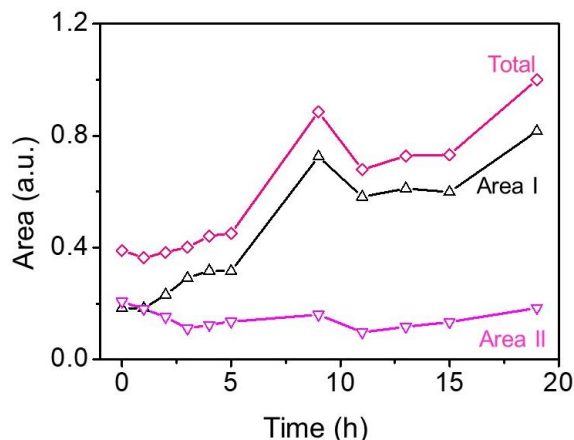
Figure VII.3. Time dependent changes in the area of the XRD pattern of the hexadecanethiol treated (at 90 °C) crystallite.
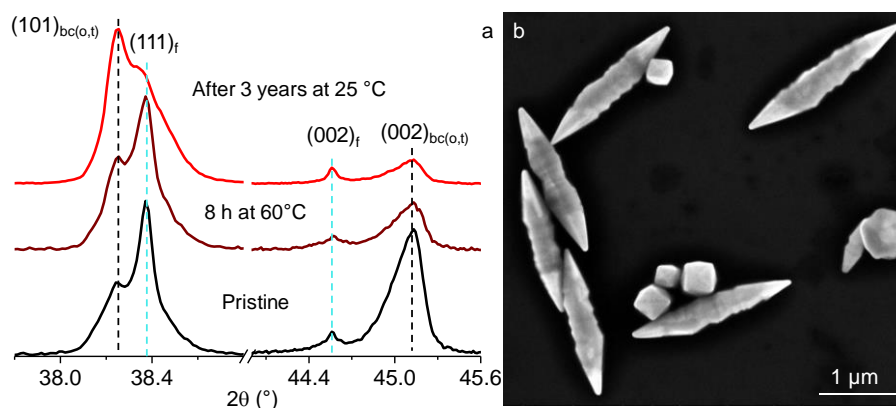
Figure VII.4. (a) Time dependent changes in the XRD patterns of the hexadecanethiol treated (at 60 °C) Au microcrystallites as in **Figure VII.1**b along with 3 years later data (kept at ambient). (b) SEM image of same crystallites examined after 3 years.

Observations drawn during the collection of SAED pattern are as follows, (1) the pristine bipyramids put forth an extreme difficulty in aligning the zone axis over the μm length, due to the presence of penta-twin boundaries and large misorientations associated with the inherent twist and mosaicity (as discussed in **Chapter IV**); (2) the scenario appears to be different in case of the thiol treated crystallites, which are able to satisfy zone axis over the length. From the SEM images, the residual contributions of the hexadecanethiol are clearly visible in the middle part of the bipyramid (in terms of image contrast). The strain and mosaicity associated with the bc(o,t) lattices are higher at the central part, rather than the fcc rich tips of the bipyramid as discussed in **Chapter IV**. Hence, the central part enriched with high index facets undergoes the reconstruction induced by hexadecanethiol, which is in

agreement with the literature discussing the enhanced activity of thiols at kinks, defects, steps and high-index facets [51,53]. The observations drawn from SAED, XRD and SEM images can be linked together and correlated with the presence of misoriented domains in the pristine crystallite as described in **Chapter IV**. These misorientations are reduced upon the treatment of hexadecanethiol. In other words, the enhancement in crystallinity is achieved by stitching the misoriented grains. This observation is in clear contrast with the observations in terms of 2H and 4H Au square sheets and nanoribbons which undergo phase transformation to fcc upon exchanging the surface capping agents by thiols [11,54], and therefore the bc(o,t) lattices exhibit superior stability.

Table VII.1. Surface energy of various Au surfaces.

Surfaces	Surface Energy (eV/Å^2)
fcc{111}	0.04
fcc{001}	0.09
bct{101}	0.17
bct{001}	0.25

Table VII.2. Binding energy of hexadecanethiol on various Au surfaces.

Surfaces	binding Energy (eV)
fcc{001}	-0.83
fcc{111}	-0.93
bct{001}	-0.97
bct{101}	-1.31

The enhancement in the counts from $(111)_f$ and $(101)_{bc(o,t)}$ regions upon hexadecanethiol treatment can be linked with the enhanced crystallinity favoring the $(111)_f$ and $(101)_{bc(o,t)}$ intensities. DFT calculations have revealed an increasing surface energy trend for various facets as $(001)_T > (101)_T > (001)_f > (111)_f$ (see **Table VII.1**) and the corresponding increasing adsorption energy trend of the hexadecanethiol on these facets can be expressed as $(111)_f > (001)_f > (101)_T > (001)_T$, as shown in **Table VII.2**. The higher adsorption energy favors the stability of the facets and thus, the treatment of hexadecanethiol enhances the crystallinity

specifically for $(111)_f$ and $(101)_f$ facets. The SXDM study in **Chapter IV** suggests that the lateral direction planes are $(002)_{bc(o,t)}$ and $(101)_{bc(o,t)}$ and therefore, the reduction in mosaicity should be related to both the increase in the intensity counts for the peaks and the enhancement in the bc(o,t) mole fraction. Therefore, the hexadecanethiol plays a pivotal role. This selectivity can also be correlated with the literature explaining the role of thiols in lifting up of the herringbone reconstruction in the Au{111} surfaces [15–20]. Although the central body and tips of the bipyramids are ~ 150-400 and ~ 100 nm thick, respectively, the generated effects can penetrate considerably deeper with the presence of high index facets and anisotropic tapered geometry. In this context, the support comes from the thiol induced deformation of a 300 nm faceted crystal where the strain could penetrate more than 20 nm deep into the crystal core, where initially there was hardly any strain [51].
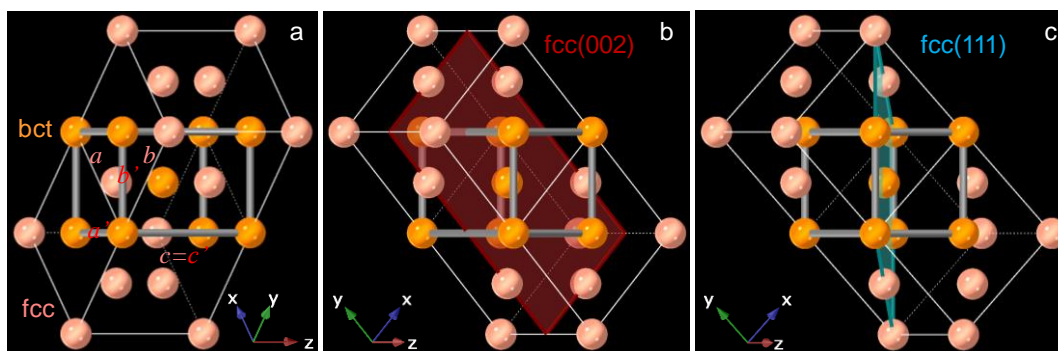
Figure VII.5. Crystallographic projection. (a) Schematic illustration of a bct lattice borne out of two face-shared fcc unit cells. x, y and z axes present the *a*, *b* and *c* axes of fcc cell, respectively. *a'*, *b'* and *c'* are axes of bct cell. Both the *c* and *c'* axes coincide and lye in the horizontal plane, while the *a* and *b* axes of the fcc are rotated by 45° with respect to the bct *a'* and *b'* axes. The orange atoms connected by the solid thicker lines represent the bct cell, derived from fcc. (b,c) Schematically projected the $(002)_f$ and $(111)_f$ planes in the fcc unit cells, respectively. The $(002)_T$ and $(101)_T$ planes coincide with the $(002)_f$ and $(111)_f$ planes, respectively.

VII.4.B Treatment with Na₂S

Similar to thiol, the literature contains studies reporting on the effect of other sulphur containing groups on metal surfaces, for example, exposure of H_2S leads to $\{100\}_f$ faceting of spherical Pt particles [21]. Here, the effect of Na_2S on the stability of the bc(o,t) Au crystallites has been studied systematically using XRD and SEM.

The bc(o,t) crystallites were subjected to Na_2S treatment with sufficient concentration and monitored using XRD. Treatment with Na_2S at 25 °C did not seem to have any effect on the crystallites similar to that seen in case of hexadecanethiol (see **Figure VII.1**c). Upon increasing the treatment temperature to 50 °C, surprisingly just after 10 min of treatment, the pattern showed a distinct feature different from that of the pristine (**Figure VII.6**a). Specifically, the satellite peak, $(101)_{bc(o,t)}$, to the left of $(111)_f$, grew in intensity while the broad intense $(002)_{bc(o,t)}$ was seen to be diminished, which together indicate a reorientation of the microcrystalline facets. On further increasing the treatment time, significant changes were seen; however, the broad shoulders or humps in the XRD pattern were still visible even after 76 min. With increasing the temperature to 100 °C, the bc(o,t) features in the pattern diminished eventually after 50 min of treatment as shown in **Figure VII.7**a. At 150 °C and 200 °C, similar but quick changes (disappearances of the bc(o,t) features) in the XRD pattern were observed with the XRD pattern appearing increasingly neat as shown in **Figure VII.6**b,c. Le Bail fitting of the patterns were performed on all the patterns collected. The fittings revealed (see **Figure VII.8**) the presence of bct, bco and fcc lattices with similar lattice parameters as in the case of the pristine. The 15 min treated pattern contained pure fcc as shown in **Figure VII.8**. The changes in the mole fraction of the crystalline phases have been quantitatively expressed in **Figure VII.7**b, where the mole fraction of the bc(o,t) is plotted against time of treatment for different temperatures. The variation in mole fraction with time follows a linear decay for all temperatures, following a zeroth-order reaction kinetics

$$A = A_0 - kt \qquad (1)$$

where, A_0 and A are the initial and residual concentrations at time, t while k is the rate constant. From the slopes, the rate constants for the bc(o,t) to fcc phase transformation have been estimated to be 48.3, 227, 355 and 869 $\mu M.s^{-1}$ for 50 °C, 100 °C, 150 °C and 200 °C, respectively.

Further, to calculate the activation energy of the transformation, the rate constant *vs.* time was plotted as shown in the inset of **Figure VII.7**b, which follows a straight line behavior. From the slope of the straight line, the activation energy calculated using the Arrhenius equation was ~ 2.8 kJ/mol,

$$k = Ae^{\frac{-E_a}{RT}} \qquad (2)$$

where k, A, E_a, R and T represent the rate constant, pre-exponential factor, activation energy, universal gas constant and the absolute temperature, respectively. The activation energy for the phase transformation is as low as 29 meV. Therefore, this observation is in contrast to the previously observed thermal stability of the phases at 400 °C. Thus, Na_2S plays a crucial role as an adsorbent in the phase transformation of Au microcrystallites.
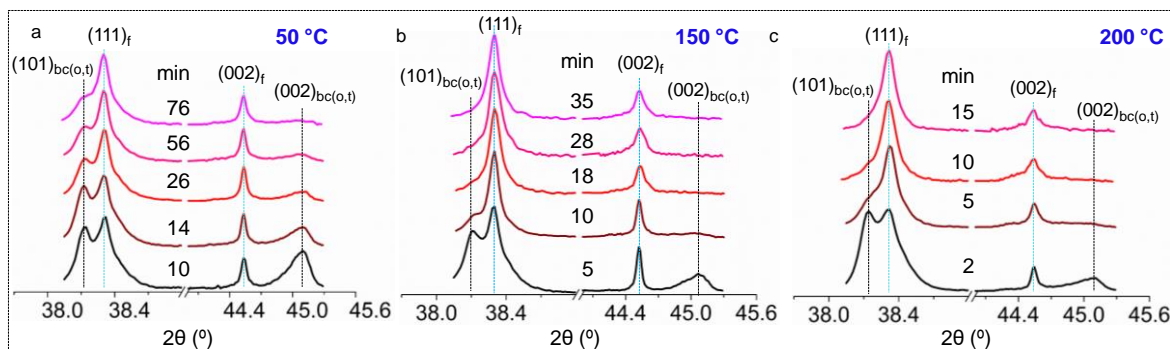
Figure VII.6. (a–c) Time dependent treatment of Na_2S on bc(o,t) microcrystallites for different temperatures.

In order to understand the phase transformation process, the values of area-II/area-I ratio (similar to hexadecanethiol, see **Figure VII.2**d) are presented with the treatment time in **Figure VII.9**, where the ratio decays sharply within a short reaction time frame (< 15 min) and reaches a plateau. The variation in the ratio is observed in all the studied temperatures, however the changes are faster with higher treatment temperatures. Therefore, it appears that the nature of the adsorbent and its kinetics together dictate the transformation, where the transfer of diffraction intensity from $(002)_{bc(o,t)}$ to $(101)_{bc(o,t)}$ is the first step followed by phase transformation as shown in **Figures VII.6** and **VII.7**a. Thus, the plausible route for the phase transformation can be expressed as $(002)_{bc(o,t)} \rightarrow (101)_{bc(o,t)} \rightarrow (111)_f$.

In order to understand the transformation, 2D atomic arrangements of the different facets are considered as shown in **Figure VII.10**. Here, the $(001)_T \rightarrow (101)_T$ transformation is nearly similar to the $(001)_f \rightarrow (111)_f$ as seen in Au sputtered films during annealing (at ~ 350 °C) [53,55]. Although, thermal annealing transforms the Au films in preferable (111) orientation, the bc(o,t) crystallites remain unaffected with $(002)_{bc(o,t)}$ orientation at ~ 400 °C. The surface energy trend exhibits the $(111)_f$ and $(101)_{bc(o,t)}$ as preferred orientations in the respective unit cells (see **Table VII.1**), however, the retention of the pristine pattern during thermal annealing is in stark contrast [56]. The presence of Na_2S introduces the energetically

preferable $(002)_{bc(o,t)} \rightarrow (101)_{bc(o,t)}$ transformation as the first step, even at a moderately low temperature ($\sim$ 50 °C). Thus, binding of adsorbents on the Au surfaces can overcome the reorientation cost, making the pattern $(101)_{bc(o,t)}$ oriented.
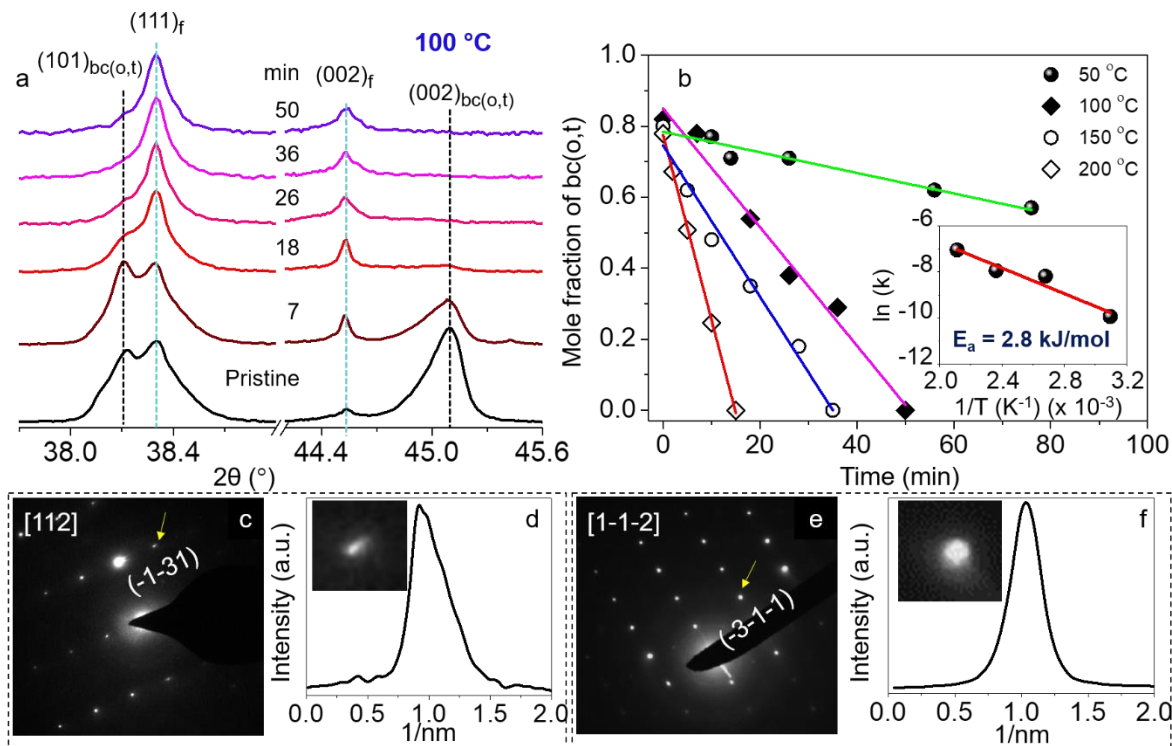
Figure VII.7. (a) Time dependent treatment of Na_2S on bc(o,t) Au microcrystallites at 100 °C. (b) Compositional changes of the bc(o,t) phases in Au bipyramids with Na_2S treatment time for different temperatures. Mole fraction of bc(o,t) phases varies linearly with time for all the temperatures, representing a zeroth-order reaction kinetics. Inset shows the plot of rate constants (k) at different temperatures (T). The temperature dependent rate constant data results linear fitting to the Arrhenius equation with activation energy of 2.8 kJ/mol. (c,e) ED patterns collected from the tip along the [112] and [1-1-2] directions and (d,f) intensity profile drawn along {113} spots for before and after Na_2S treatment, respectively.

DFT calculations have shown the effect of sulphur adsorption at the different facets of Au as shown in **Table VII.3**. The increasing adsorption energy can be represented as $(001)_f > (111)_f > (101)_T > (001)_T$. The transformation from $(002)_{bc(o,t)} \rightarrow (101)_{bc(o,t)}$ within a short reaction duration can be explained by the higher stabilization energy of the $(101)_{bc(o,t)}$ facets induced by Na_2S, which is otherwise dauntingly difficult to achieve with temperature alone as the variable. Further, the $(101)_T \rightarrow (111)_f$ conversion takes place rather at low working

temperature ($\sim$ 100 °C). The $(101)_T$ and $(111)_f$ facets exhibit nearly similar atomic arrangements and require minimal amount of expansion/contraction along the axes of $(101)_T$ to result into $(111)_f$ (see **Figure VII.10**). Thus, the overall phase transformation process is quite similar to that of polycrystalline Au film, $(100)_f$ to $(111)_f$ or that in bc(o,t) to fcc phase transformation by thermal annealing at 700 °C (the pattern is similar to (111) oriented film, see **Figure VI.16** in **Chapter VI**).
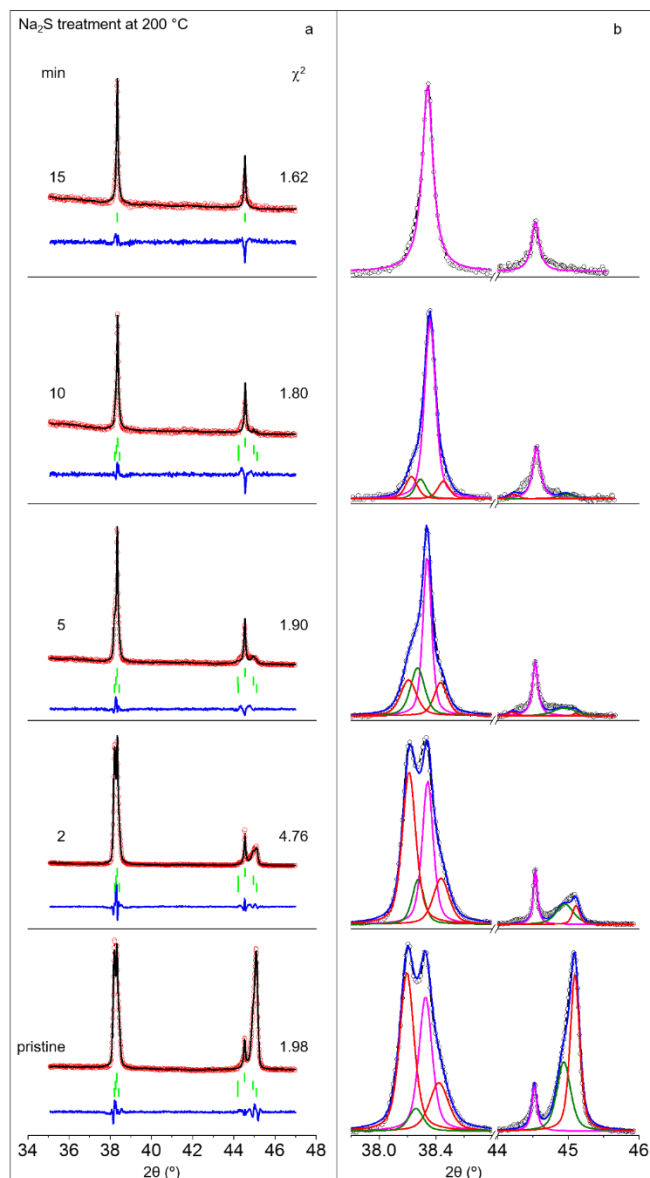
Figure VII.8. (a,b) Le Bail fitting of the XRD patterns collected post-treatment with Na_2S (at 200 °C).

Energetically, the direct conversion of $(101)_T$ to $(001)_f$ or *via* $(111)_f$ is equally probable, however, the similar atomic arrangements in the $(101)_T$ and $(111)_f$ facets favor the latter process. Although the expected next step is $(111)_f \rightarrow (001)_f$, the transformation does not proceed which explains the preferred Au(111) orientation.
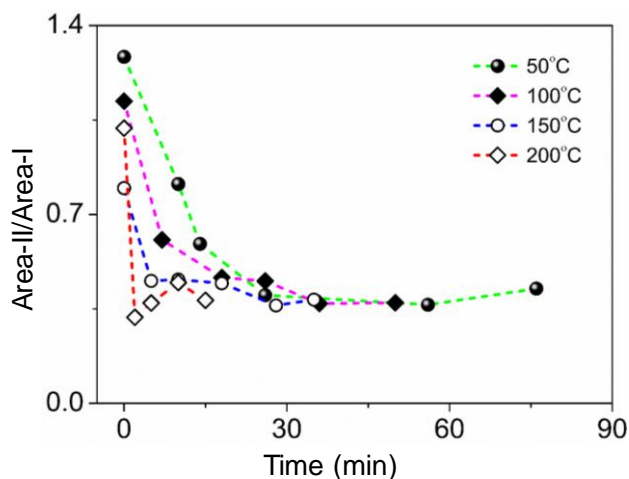
Figure VII.9. Changes in XRD area-II/area-I ratio of bc(o,t) Au with Na_2S treatment time at 50, 100, 150 and 200 °C, respectively.
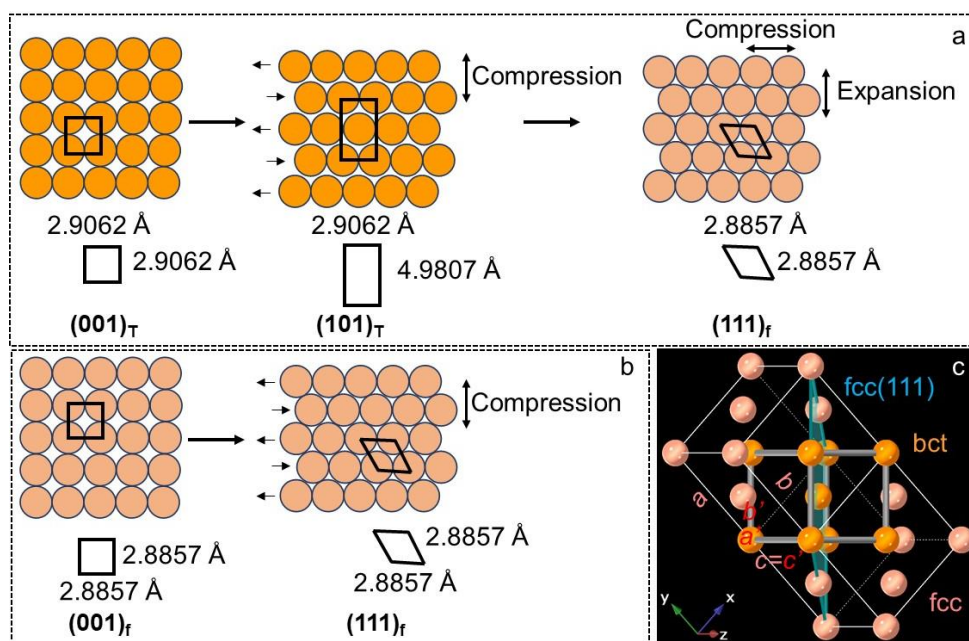
Figure VII.10. (a) Atomistic view of bct(002) to fcc(111) possible phase transformation route. The black arrows show the direction of atomic layer movement. (b) Atomistic model of fcc(001) to fcc(111) possible transformation route. (c) Schematic representation of a bct unit cell borne out of two fcc unit cells, where the bct(101) plane coincide with fcc(111) plane.

Treatment with Na_2S does not seem to induce any significant changes in the morphologies of the bipyramids, specifically to the corrugations as shown in **Figures VII.11 and VII.12**. This can be understood from the above direct bc(o,t) $\rightarrow$ fcc transformation, where the small changes in atomic positions can alter the orientation of the pattern and thereby, insignificant changes in the µm sized crystallites. However, for the similar changes observed in the pattern during annealing, the morphology deforms due to the highly mobile atoms. SAED patterns were collected from bc(o,t) and phase transferred fcc bipyramids (see **Figure VII.7**c,e) at the tip along the [112], [1-1-2] directions, where the intensity profiles drawn over the {131} spots display asymmetric and symmetric curves, respectively (see **Figure VII.7**d,f). The symmetric line profile confirms the reduction in strain in the form of fcc lattice.

Table VII.3. Binding energy of sulphur on various Au surfaces.

Surfaces	S-binding Energy (eV)
bct{001}	-2.65
bct{101}	-2.79
fcc{111}	-3.03
fcc{001}	-3.12
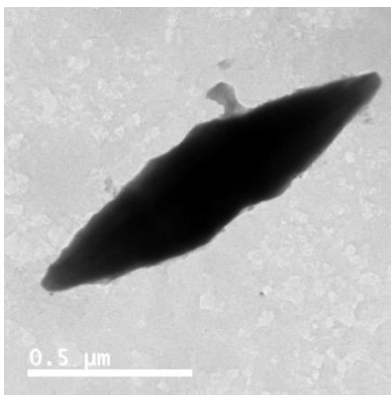
Figure VII.11. TEM image of the Au bipyramid treated with Na_2S at 200 °C.

Literature reports discuss the role of chemisorbed electronegative elements on metals, where the elements typically lead to compressive stress with a change in the range of -5 Nm^{-1} [51]. This is in coherence with the observations drawn here, a bc(o,t) to fcc

transformation (mainly compression). The effect of the hexadecanethiol was not strong enough to cause $(101)_T$ to $(111)_f$ phase transformation, whereas, Na_2S, is able to do so. Hence, one can consider the stronger the adsorbent interaction with the Au surface, the faster the observed changes, which can also be validated by the difference in energy by DFT as shown in **Table VII.3**.

Na_2S treated (at 200 °C for 10 min) sputtered Au film also exhibits a (111) oriented pattern with reduction in FWHM, similar to bc(o,t) crystallites. Other reducing agents, such as formaldehyde, sodium borohydride ($NaBH_4$) and lithium aluminium hydride ($LiAlH_4$) also introduce similar effects.
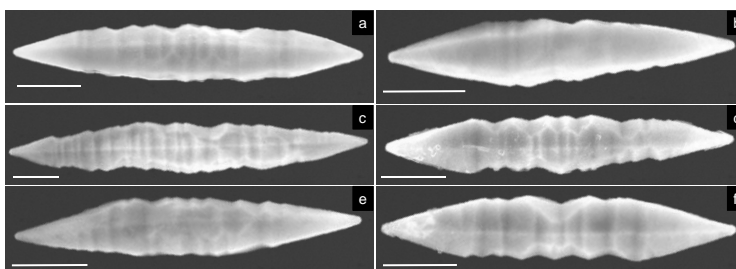
Figure VII.12. (a–f) SEM images of Na_2S treated Au bipyramid at 200 °C. Scale bar, 500 nm. The same crystallites were not examined due to the physical movement of the crystallites in the substrate while heating (since the aqueous Na_2S solution starts boiling at 100 °C and beyond with production of H_2S, therefore introduces physical disturbances to the crystallite).
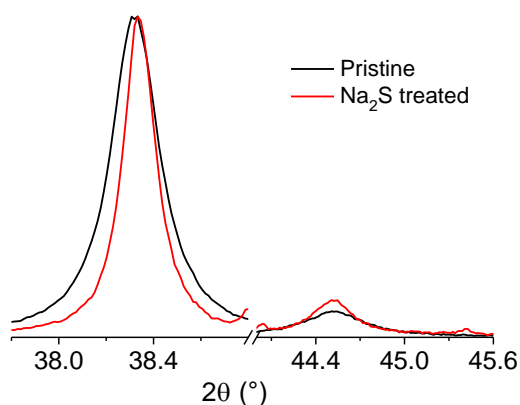
Figure VII.13. XRD patterns of the pristine Au sputtered film and Na_2S treated at 200 °C for 10 min.

VII.4.C Treatment with Quaternary Ammonium Salts

Amines are the most common surfactants used in modifying crystallites morphology/crystal structure while being present at the growth or post-growth process. For example, the ToABr facilitates the stabilization of Au in the unconventional bc(o,t) lattices

while being present during the growth process. Thus, the effect of the same surfactant on the as-synthesized bc(o,t) Au crystallites is interesting to study during post synthesis. This section deals with the effect of quaternary ammonium salts on the bc(o,t) Au crystallites.
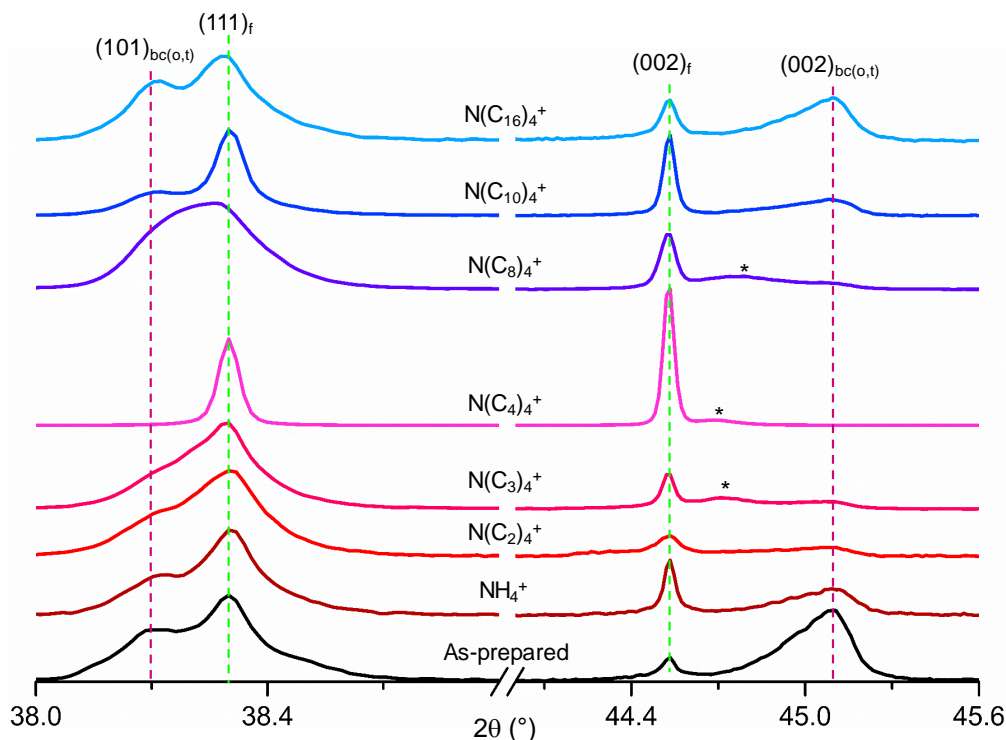
Figure VII.14. Treatment of quaternary ammonium salts on bc(o,t) Au microcrystallites at 220 °C for 7 min. Changes in the XRD pattern with treatment of different alkyl ammonium salts. * denotes a new peak. The alkyl ammonium salts are $NR_4^+X^-$, where R is the alkyl group (R = H, C_2H_5, C_3H_7, C_4H_9, C_8H_{17}, $C_{10}H_{21}$ and $C_{16}H_{31}$ and $X^- = Br^-$). $X^- = OH^-$ is only for R = C_2H_5 and C_3H_7.

The as-prepared bc(o,t) Au microcrystallites (37 µg) were treated with a 60 µL of quaternary ammonium salts (NR_4X, R being hydrogen/alkyl groups; X, the anionic counterpart, Br^-/OH^-), specifically NH_4Br, $N(C_2H_5)_4OH$, $N(C_3H_7)_4OH$, $N(C_4H_9)_4Br$, $N(C_8N_{17})_4Br$, $N(C_{10}H_{21})_4Br$ and $N(C_{16}H_{33})_4Br$ at 220 °C for 7 min. The treated crystallites are extensively studied using laboratory XRD and SEM.

The XRD patterns of the adsorbent treated crystallites are shown in **Figure VII.14** for various alkyl chain lengths of the quaternary ammonium salts. The treatment of NH_4^+ on the crystallites surface results in a sharp decrement in the intensity of $(002)_{bc(o,t)}$. Further, H being replaced with alkyl chain in NR_4X starting with C_2 to C_4, the drop in the $(002)_{bc(o,t)}$ intensities are much higher (almost vanishes) and the changes are visible at the $(101)_{bc(o,t)}$ regions as well.

Visibly, the changes are most prominent in the case of $N(C_4)_4^+$. Based on this observation, one is tempted to think that the treatment of $N(C_4)_4^+$ leads to the disappearance of the bc(o,t) lattices. Further, with increasing the chain length from C_8 to C_{16}, the intensity of the peak reduces monotonically. The extensive reduction in the $(002)_{bc(o,t)}$ intensity and increment in the $(002)_f$ prompts one to express its relation with the chain length. The ratio, P(after treatment)/P(as-synthesized) is plotted against the alkyl chain length in **Figure VII.15**a, where P is the intensity ratio of bco(002)/fcc(002). The intensity ratio decreases sharply with increasing the chain length from H to C_3 and reaches a minimum at C_4 (intensity of the $(002)_{bc(o,t)}$ is ~ 0). Further, with increasing the chain length, the intensity ratio increases sharply reflecting nearly a V-shaped curve with the minimum at C_4 which signifies the role of $N(C_4)_4^+$ in bringing down the intensity of $(002)_{bc(o,t)}$ peak.

Profile matching of the patterns was carried out and the contributions of the phases were plotted out in **Figures VII.16** and **VII.17**. Interestingly, for the case of $N(C_3)_4^+$, $N(C_4)_4^+$ and $N(C_8)_4^+$, an additional peak appears which is denoted by an asterisk in **Figure VII.14** and can be assigned to a new phase (however with different 2θ values in each case).

The profile matching of the $N(C_3)_4^+$ treated XRD pattern is shown in **Figure VII.15**b,c, which can be fitted with a combination of fcc, bct, bco and the new phase (termed as bct-I, space group *I4/mmm*) with a $\chi^2 = 4.73$, as shown in **Figure VII.16**. The cell parameters for the different lattices are $a = b = c = 4.0810$ Å for fcc; $a = b = 2.9062$ Å and $c = 4.0450$ Å for bct; $a = 2.9184$ Å, $b = 2.8931$ Å, $c = 4.0315$ Å for bco and $a = b = 2.9010$ Å and $c = 4.0630$ Å for bct-I. Similarly, the contributions of the phases in case of $N(C_4)_4^+$ could be satisfied only by fcc and bct-I (see **Figure VII.17**) while the lattice parameters of the bct-I are $a = b = 2.9010$ Å and $c = 4.0661$ Å as tabulated in **Table VII.4** along with the other parameters. Interestingly, the lattice parameters of the bct-I differ in terms of the *c* parameter, *i.e.*, 4.0630, 4.0661 and 4.0610 Å for $N(C_3)_4^+$, $N(C_4)_4^+$ and $N(C_8)_4^+$, respectively while *a* remains similar, ~ 2.9010 Å (see **Table VII.4**), indicating an expansion along *c*-direction reaching towards fcc (4.081 Å), while being maximum for $N(C_4)_4^+$.
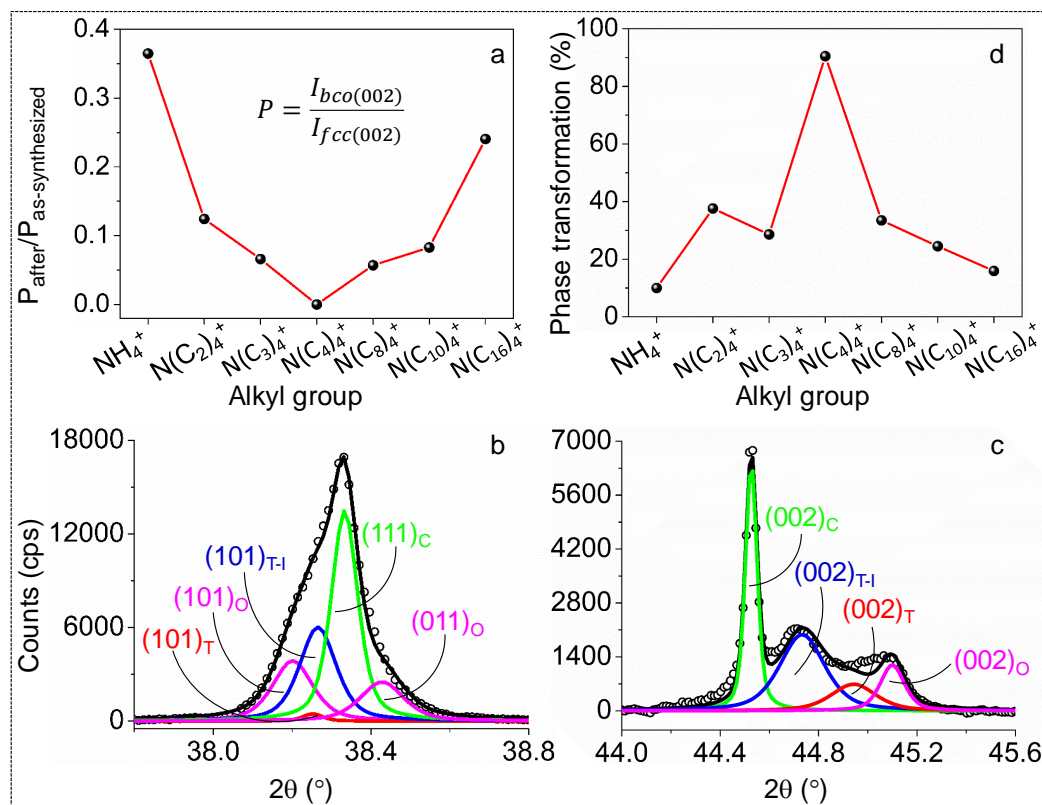
Figure VII.15. Analyzing the XRD patterns. (a) Changes in the intensity ratio of after treatment/as-synthesized with various alkyl groups for bco(002) and fcc(002) peaks. The intensity ratio is minimum at $N(C_4)_4^+$. (b,c) Profile matching of the $N(C_3)_4^+$ treated XRD pattern. Contribution of a new bct phase as identified in **Figure VII.14**c (by *) represents T-I in blue curve. (d) Rate of phase transformation for different alkyl groups. The $N(C_4)_4^+$ demonstrates a maximum transformation.
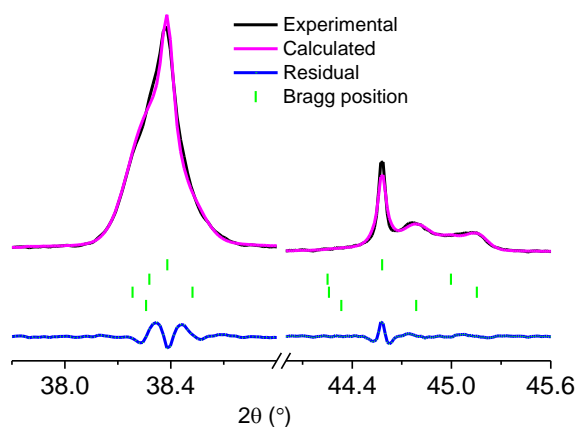
Figure VII.16. Le Bail fitting of the XRD data collected from $N(C_3)_4^+$ treated Au microcrystallites (at 220 °C).

The appearance of bct-I phase was also seen during Ar^+ exposure as reported in **Chapter V**. The XRD patterns corresponding to other chain lengths exhibit a combination of fcc, bct and bco phases (see **Figure VII.17**). The areas under the curves were considered to calculate the bc(o,t) contribution in these phases as shown in **Figure VII.17**. Surprisingly, with the treatment of alkyl ammonium salts, the bc(o,t) fraction drops while the fcc fraction increases significantly, implying a phase conversion as shown in **Figure VII.15**d. The maximum transformation is seen for $N(C_4)_4^+$, accounting to be ~ 90% with fcc(002) orientation (similar to the pristine). Thus, the occurrence of bct-I and its facile nature in accommodating varying c parameter values are the key to cause effective phase transformation, similar to the phenomena observed in Ar^+ exposed bc(o,t) crystallites in **Chapter V**. The post-treatment introduces a sharp $(002)_f$ peak in the XRD patterns as shown in **Figure VII.17**, however, the detailed changes will be addressed later (see under **Figure VII.21**).
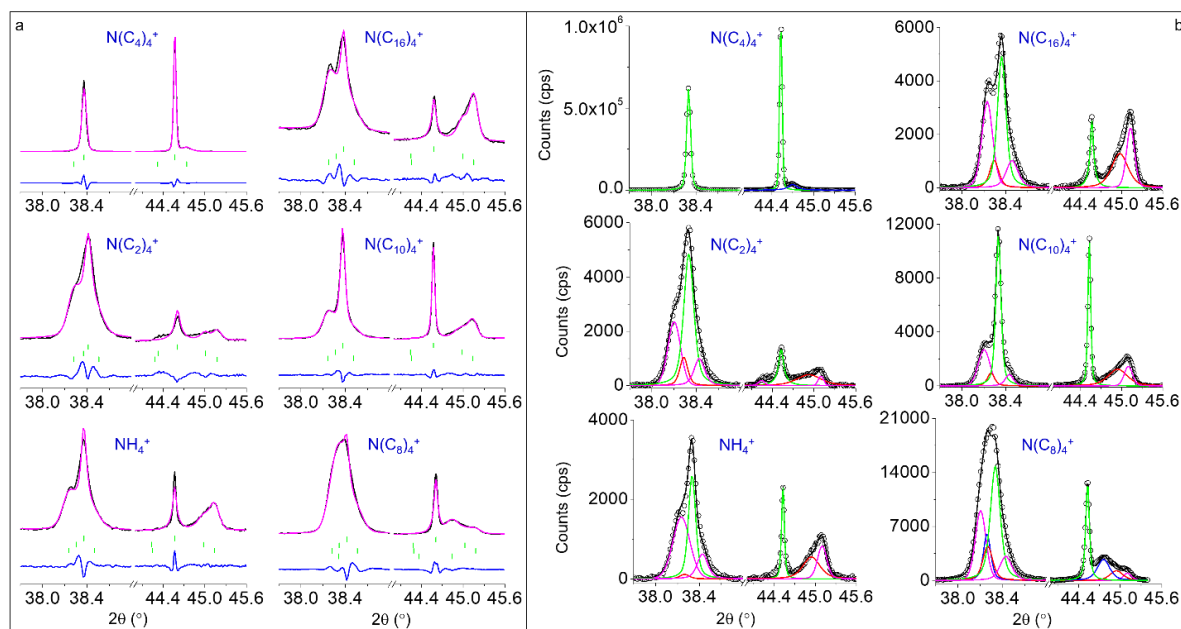
Figure VII.17. (a) Le Bail fitting of the XRD data collected from Au microcrystallites treated with various adsorbents. Black, pink, blue and green color curves indicate the experimental, calculated, residual (experimental−calculated) and Bragg position, respectively. (b) Profile matching of the XRD patterns collected post-treatment with quaternary ammonium salts at 220 °C for 7 min. The black circles represent the experimental data. The green, red, pink and blue are the contributions from fcc, bct, bco

and bct-I, respectively and their sum is shown in black color curve. The bct-I contributes toward $N(C_3)_4^+$, $N(C_4)_4^+$ and $N(C_8)_4^+$ only.

In order to understand the phase transformation process, the morphology of the crystallites has been monitored by SEM (while tracking a single crystal) as shown in **Figure VII.18**a. Visibly, the changes in the morphology of the crystallites are mainly for $N(C_4)_4^+$, where the corrugated facets and sharp tips have disappeared. The effective change in the area of the adsorbent treated crystallites morphology is ~ 0.76% lesser than pristine, indicating probable reduction in volume. The bc(o,t) lattices consist of ~ 0.1% (for bco) and 0.53% (bct) higher volume than fcc and thus, the phase transformation to fcc reduces down the overall volume. The changes in the length of the crystallites for various alkyl lengths have been plotted in **Figure VII.18**b with the maximum corresponding to $N(C_4)_4^+$ treatment (~ $14.23 \pm 0.66\%$, while monitoring 10 crystallites for each cases). The least morphological changes were observed for NH_4^+ and $N(C_2)_4^+$, although rounding of the sharp tips was seen (~ 2% shrinkage in length).

Table VII.4. Lattice parameter details

Chain length	fcc	bct		bco			bct-I	
	$a = b = c$ (Å)	$a = b$ (Å)	c (Å)	a (Å)	b (Å)	c (Å)	$a = b$ (Å)	c (Å)
NH_4^+	4.081	2.9062	4.0450	2.9184	2.8931	4.0315	-	-
$N(C_2)_4^+$	4.081	2.9032	4.0463	2.9184	2.8931	4.0315	-	-
$N(C_3)_4^+$	4.081	2.9062	4.0450	2.9184	2.8931	4.0315	2.9010	4.0630
$N(C_4)_4^+$	4.081	-	-	-	-	-	2.9010	4.0661
$N(C_8)_4^+$	4.081	2.9062	4.0450	2.9184	2.8931	4.0315	2.9010	4.0610
$N(C_{10})_4^+$	4.081	2.9062	4.0450	2.9182	2.8925	4.0317	-	-
$N(C_{16})_4^+$	4.081	2.9062	4.0450	2.9184	2.8931	4.0315	-	-

In order to understand the effect of adsorbent on the crystallites morphology as well as the crystal structure, the fcc crystallites have been used as reference and subjected to $N(C_4)_4^+$ treatment at 220 °C for 7 min, while the latter was chosen based on the performance observed in case of bc(o,t) Au (in **Figures VII.14**, **VII.15** and **VII.18**a,b). The fcc crystallites exhibit sharp tips (~ 30° angle) with nanofacets over μm length which undergo drastic deformation

upon the treatment with $N(C_4)_4^+$ as shown in **Figure VII.18**c. Briefly, the sharp tips and the corrugated nanofacets disappear with an overall reduction in the length (~ 1 μm) of ~ 22%. The overall changes in the morphology are similar in both fcc and bc(o,t) crystallites, *i.e.*, independent of the crystal structure. Additional support comes from **Figure VII.19**, where the other shaped crystallites also exhibit similar rounding effect with smooth surfaces, irrespective of the pristine crystal structures. Therefore, the reshaping is independent of the crystallographic orientation and inherent crystal structure, however, the extent of modification is curvature dependent (see **Figure VII.19**).
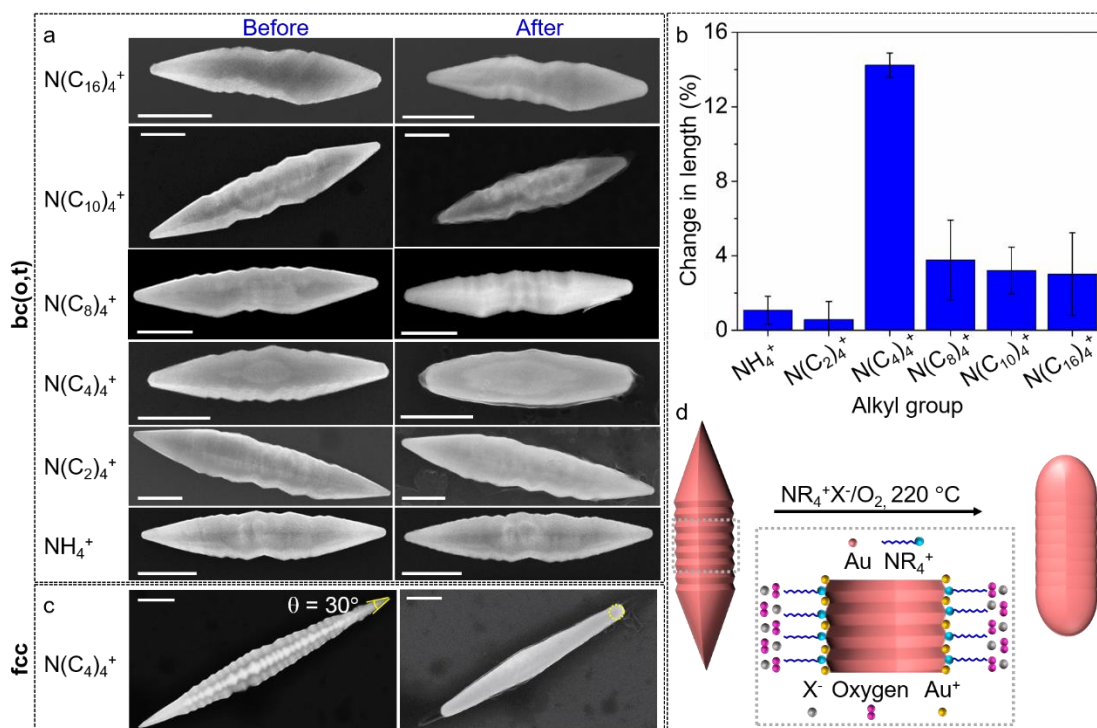
Figure VII.18. Post-treatment changes in the morphology of the crystallites. In each case the same crystallites have been tracked to monitor the changes. (a) SEM images of the pre− and post−treated bc(o,t) bipyramids. The alkyl chain details have been pointed out at the left hand side. Scale bar, 300 nm. (b) Post-treatment changes in length of the bc(o,t) bipyramids for various alkyl groups. Astonishing changes observed in case of $N(C_4)_4^+$. (c) SEM images of pre− and post−treated fcc bipyramids by $N(C_4)_4^+$ at 220 °C for 7 min. Scale bar, 500 nm. The angle and circle drawn in yellow over the crystallite tips encompass the sharp and circular (blunt) tips, respectively. (d) Schematic exposition of the shape recasting by $NR_4^+X^-/O_2$, where the reactive sites (mainly convex regions) dissolve into AuX_2^- followed by the redeposition of the latter in the form of Au at the concave regions. Schematic, not in scale.

Following the treatment, no observable extra particulates were found (**Figure VII.20**), which confirms consequent redeposition of the dissolved Au over the crystallite surface and followed by deformation in the morphology. The deformations can be expressed as shortening the length and incrementing the width of the crystallite, which are also well versed with the modified crystallites morphology (see **Figures VII.18** and **VII.19**). The extent of reduction in length is much higher in case of fcc than the bc(o,t) crystallites, because of the presence of the acute angled tips and the µm ranged nanofacets consisting of highly curved regions [48]. Additionally, the presence of defects such as twin boundaries also facilitates the reshaping process. This observation related to reshaping is in coherence with the literature discussing the role of CTAB in the rounding off the nanorods/nanoparticles by oxidative etching [23] while effectively being employed at the higher curvature regions [29,57,58], specifically, the dissolution at the convex curvatures and redeposition on the concave places [28].
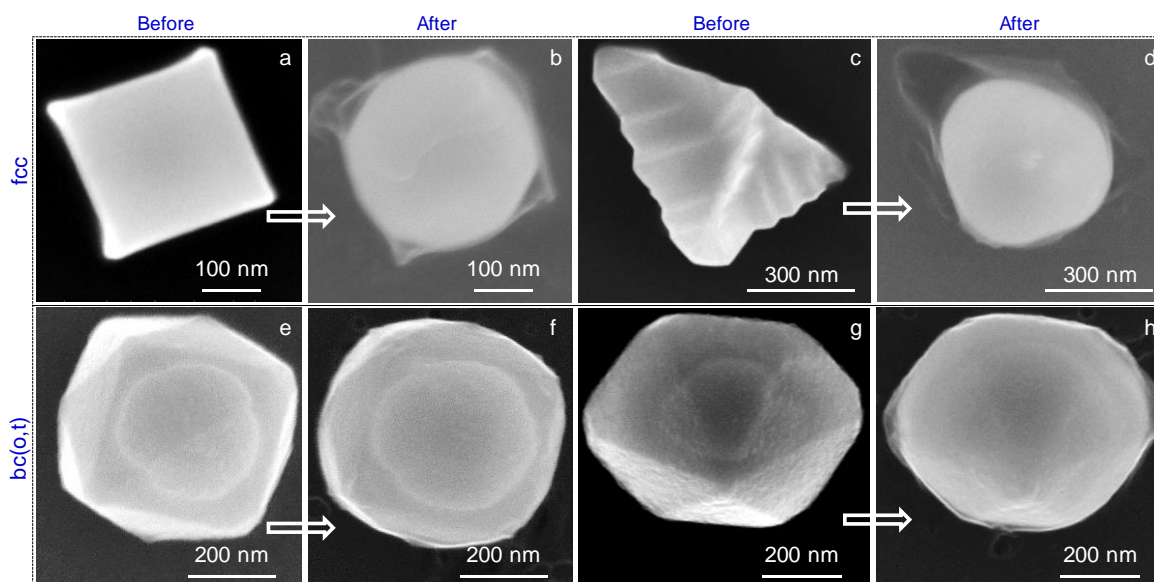
Figure VII.19. Effect of $N(C_4)_4^+$ treatment on the morphology of the Au microcrystallites. SEM images of pristine fcc (a,c) and bc(o,t) (e,g) microcrystallites and their corresponding images at the post-treatment with $N(C_4)_4^+$ in (b,d) and (f,h), respectively. The arrow shows the post-treatment effect. The as-synthesized sharper corners, edges and vertexes disappear and become nearly round in shape. The rounding effect is more prominent in the top panel with sharper corners and edges while being independent on the exposed facets. Thus, the change in morphology is governed by the curvature of the crystallite surface and not by the pristine crystal structure.

Further, $N(C_4)_4^+$ treated XRD patterns of the fcc and bc(o,t) crystallites were taken into consideration (in **Figure VII.21**), where both the patterns exhibit enhancement in the intensity

while retaining the overall orientation, $(002)_f$ as in pristine $(002)_O$. The enhancements are ~ 1.44 and 1.77 times for fcc (111) and (002) peaks, respectively, whereas are 99 and 473 times for bc(o,t). The evolution in the intensities relates to enrichment in the crystallinity, being higher at the preferred (002) directions. The retention of the orientation at the post-treatment time can be understood from the redeposition of dissolved Au in the form of energetically stable fcc lattice over the $(002)_O$ backbone (see **Figure VII.5**b). As the bc(o,t)(002) and fcc(002) planes form and orient within the crystallite volume, they exhibit a parallel relation (see in **Figure VII.5**b) and thus, the preservation of the orientation is reasonable. The other reasons for the increment in the overall intensity counts can be understood from the dissolution of the high index facets, the reduction in mosaicity/strain and further, the increase in structure factor (from bc(o,t) to fcc lattice as shown in the below calculation).

$$\text{Structure factor for fcc, } F_{hkl} = f(1 + e^{\pi i(h+k)} + e^{\pi i(k+l)} + e^{\pi i(h+l)}) \quad (3)$$

$$\text{Structure factor for body–centered lattice, } F_{hkl} = f(1 + e^{\pi i(h+k+l)}) \quad (4)$$

$$\text{Intensity of the XRD peaks, } I = F_{hkl}^2 \quad (5)$$

The allowed reflections in fcc are (111) and (200); and $I_{fcc} = F_{hkl}^2 = 16f^2$.

Similarly, the allowed reflections in body-centered lattices are (101), (011), (110), (002); and, $I_{bc(o,t)} = F_{hkl}^2 = 4f^2$.
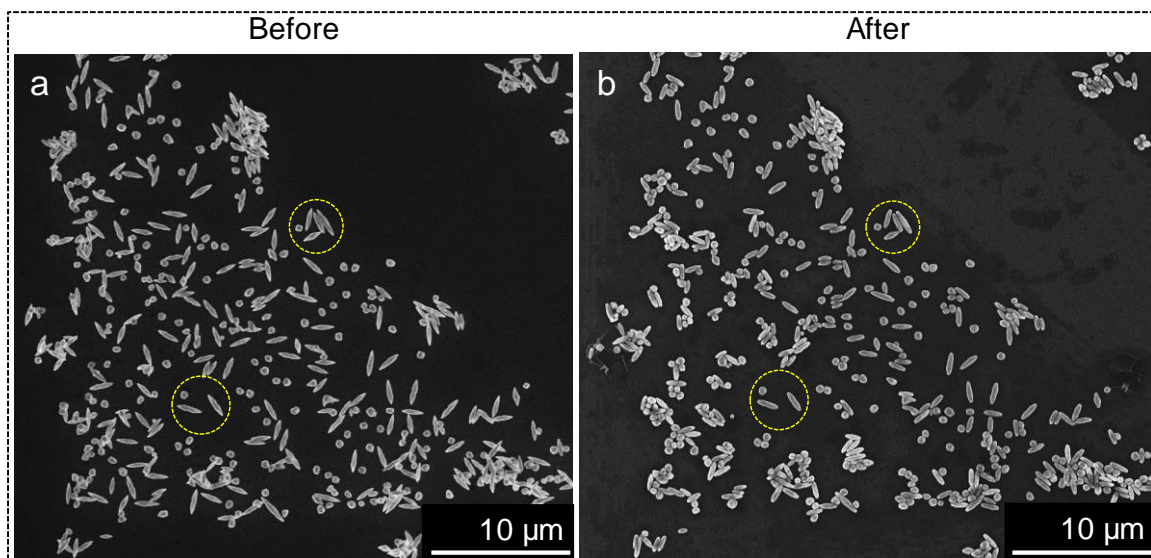
Before   After

Figure VII.20. Large area view of the $N(C_4)_4^+$ treated crystallites. SEM images of the microcrystallites (a) before and (b) after $N(C_4)_4^+$ treatment at 220 °C for 7 min. The yellow circles have been drawn for reference. During the adsorbent treatment, the crystallites are locally immobile and thus allow to

monitor the changes in the morphology of the same crystallite. No additional formation of the particulates observed in (b).

Therefore, the intensity of bc(o,t) reflection is usually lower than fcc reflections. The presence of strain in addition to lower structure factor and less number of atom in bc(o,t) (2/unit cell) than fcc unit cell (4/unit cell) may contribute to the weakening of bc(o,t) peaks intensity. The bc(o,t) crystallites annealed at 700 °C also exhibit the similar deformed morphology as in here, however with different final orientation in the XRD pattern, *i.e.*, $(111)_f$. Importantly, the role of surfactant is remarkable in the deformation of the morphology as well as the phase transformation to fcc, particularly at a moderate operating temperature (~ 220 °C).
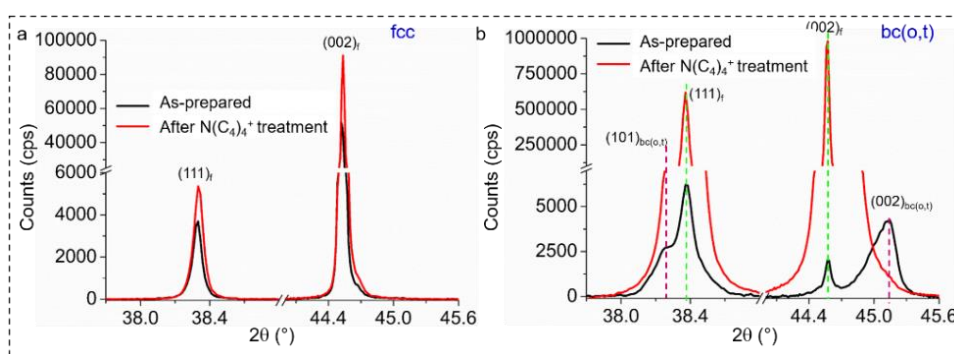
Figure VII.21. Effect of $N(C_4)_4^+$ treatment on the XRD pattern. Changes in the XRD patterns of (a) fcc and (b) bc(o,t) crystallites before and after $N(C_4)_4^+$ treatment at 220 °C for 7 min. The treated XRD patterns exhibit an overall increment in the intensities highlighting enhancement in crystallinity in both the cases, however, the astonishing enhancement observed by 493 times for $(002)_{bc(o,t)}$.
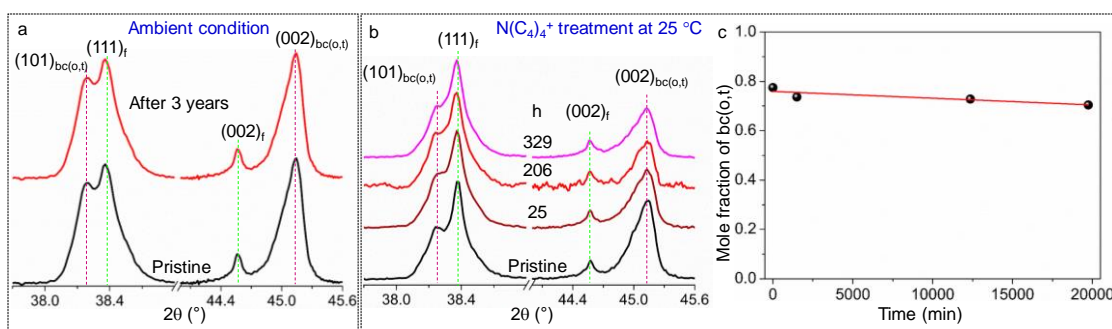
Figure VII.22. Stability of bc(o,t) Au microcrystallites studied at 25 °C at different environments, (a) ambient condition and (b,c) in $N(C_4)_4^+$ solution by monitoring changes in XRD patterns. The composition of the phases remain intact at ambient condition, while a gradual reduction in the mole fraction of the bc(o,t) phases as shown in (c), indicating phase transformation to fcc induced by the adsorbent.

The combined effects of (i) extensive modification in the morphology, (ii) reduction in $(002)_{bc(o,t)}$ intensity and (iii) fast phase transformation caused by $N(C_4)_4^+$, play prominent role in the phase transformation. Further increasing or decreasing the chain length is less effective (see **Figure VII.22**). Thus, $N(C_4)_4^+$ is the most effective and suited. The changes in the morphology can be explained by the selective oxidative etching of X^-/O_2 (see equation 6) and redeposition by Oswald ripening/thermal decomposition as shown in **Figure VII.18**a,c, however, the efficacy depends upon the chain length.

$$Au(0) + Br^- + O_2 \rightarrow AuBr_2^- \qquad\qquad (6)$$
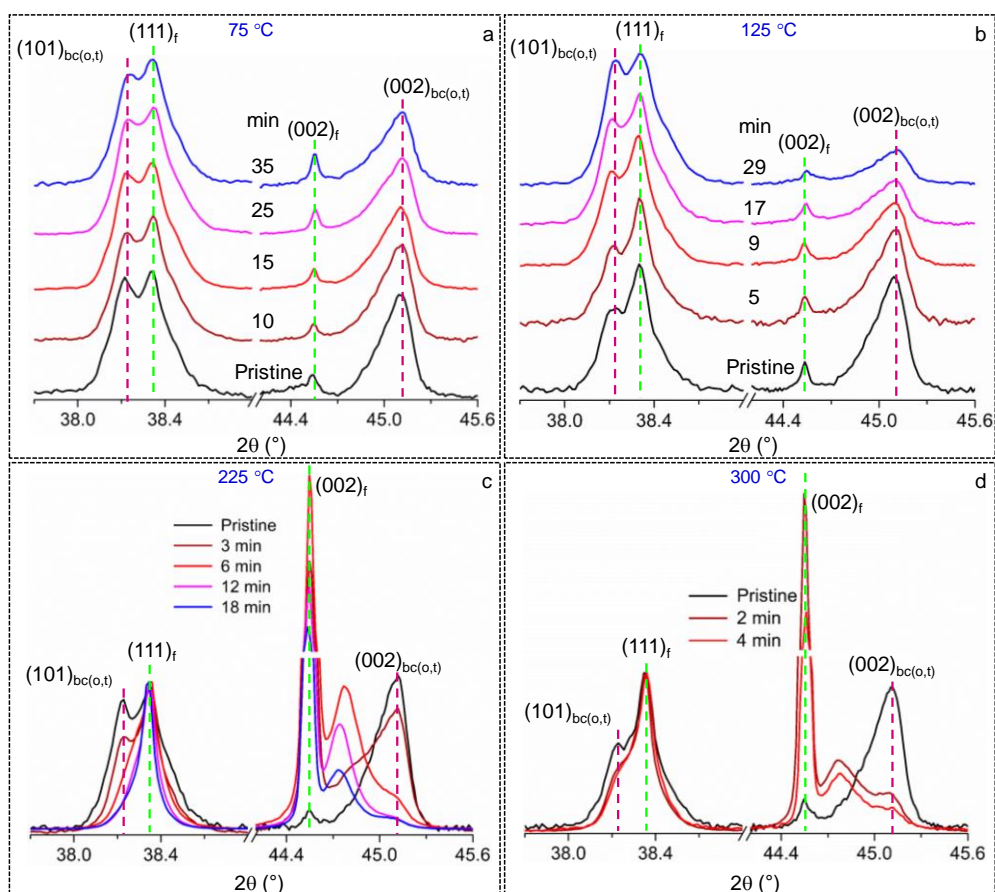
Figure VII.23. Temperature dependent $N(C_4)_4^+$ treatment on bc(o,t) Au microcrystallites. (a−d) Time dependent changes in the XRD pattern has been monitored by XRD for 75, 125, 225 and 300 °C, respectively. From the variation in the area under the peak, mole fraction of bc(o,t) have been calculated and plotted in **Figure VII.24**b.

It therefore appears that there is substantial dissolution of the Au atoms from surfaces especially in the regions of the tips and high index facets/un-coordinated sites. Due to the lower

coordination numbers at the convex facets, the stabilization energy associated with addition of extra atoms is relatively low and correspondingly, the chemical potential is higher than that on a flat surface [59]. Addition of an extra atom to a convex surface can be energy expensive. In contrast, a concave facet with a lower chemical potential offers higher stabilization for an incoming atom. In this case, atomic addition becomes favorable. Eventually, the atoms from the convex facets dissolve into the solution, and redeposit on concave surfaces (following equation 7) which is in line with the observed deformation in morphology in **Figure VII.18**a,c.
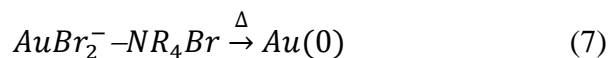
$$AuBr_2^- - NR_4Br \xrightarrow{\Delta} Au(0) \qquad (7)$$

The dissolved Au redeposits with its conventional (fcc) lattice and thereby causes the phase transformation as shown in **Figure VII.18**d. In presence of capping agents, the process is enhanced due to the formation of $AuBr_2^- - NR_4Br$ complex [28]. The stabilization of $AuBr_2^-$ complex is governed by the ionic strength of the alkyl ammonium cations [60] as previously reported in case of Au-CTAB complex. Additionally, formation of self-assembled monolayers of alkane thiolates system over metal nanostructures and formation of lamellar structure are dependent on the alkyl chain length; prevail for longer chain lengths [61]. Therefore, formation of $AuBr_2^-$ and followed by stabilization of $AuBr_2^- - NR_4Br$ complex in presence of capping agents (NR_4Br) are the rate determining steps for the deformation of Au crystallites. The longer alkyl chains prefer to form densely packed self-assembled structures [62] and thereby reduction in etching. Butyl groups being relatively shorter possess less steric hindrance and therefore increase the efficacy of binding of Au arriving from unfavorable convex positions. This leads to a shape deformation as well as phase transformation.

Most of the reshaping of the nanoparticles as discussed in the literature are observed at room temperature. Herein, the study systematically unveils the role of temperature on the $N(C_4)_4^+$ treatment, since at the higher temperatures, the probability of exposing and activating both the unstable lattices and the defects is higher. Therefore, the transformation is expected to be temperature dependent. At first, the crystallites have been treated with $N(C_4)_4^+$ at 25 °C and the collected pattern has been compared with the pristine pattern in **Figure VII.22**. Noteworthy observation, the $N(C_4)_4^+$ treatment at 25 °C results in reduction in the intensity of $(002)_{bc(o,t)}$ region, imposing a phase transformation caused by the adsorbent as shown in **Figure VII.22**c. However, the transformation is very slow, which is understandable due to the μm

length and thickness of the crystallite. The effect of temperature on the phase transformation was monitored by XRD at various temperatures, such as 75, 125, 180, 225 and 300 °C as shown in **Figures VII.23** and **VII.24**. At 75 °C, a drop in the $(002)_{bc(o,t)}$ intensity is observed after 35 min of treatment (see **Figure VII.23**a) and with increasing the temperature to 125 °C, the drop in the $(002)_{bc(o,t)}$ intensity is much higher in a relatively shorter time (29 min), as shown in **Figure VII.23**b. Further, increasing the temperature to 180 °C causes a drastic drop in the $(002)_{bc(o,t)}$ intensity (see **Figure VII.24**a). The reduction in intensity is also observed in $(101)_{bc(o,t)}$ region along with a reduction in FWHM. Interestingly, with increasing time, a new peak (at $2\theta = 44.76°$) appears at 25 min, which can be fitted with bct-I with lattice parameters of $a = b = 2.9010$ Å and $c = 4.0614$ Å (see **Table VII.5**).
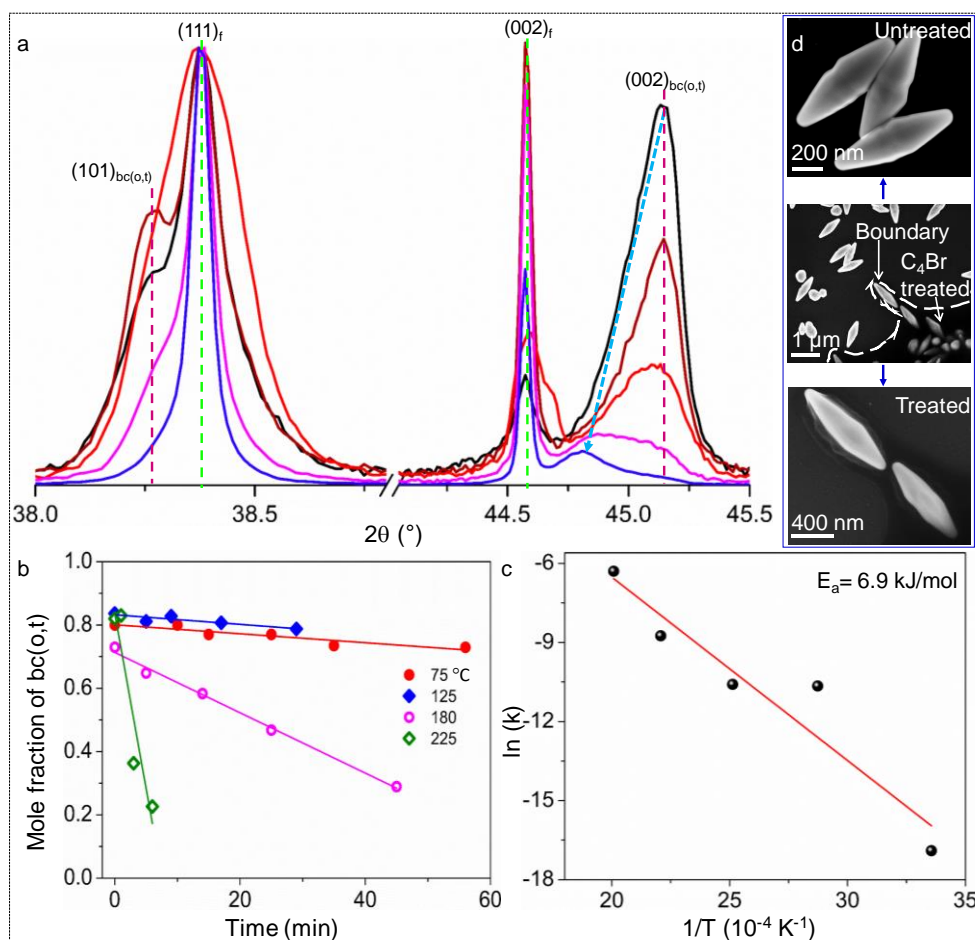
Figure VII.24. Effect of temperature on $N(C_4)_4^+$ treatment. (a) Time dependent $N(C_4)_4^+$ treatment at 180 °C on bc(o,t) Au microcrystallites and the corresponding changes in XRD patterns for 5, 14, 25 and 45 min. (b) Time dependent changes in mole fraction of bc(o,t) for different temperatures. Rate

constant obtained from the slope of the linear decrement line. (c) Activation energy calculation from temperature versus rate constant plot. (d) *In-situ* heating of the Au microcrystallites in $N(C_4)_4^+$ at 200 °C inside a SEM. In contrast to the untreated crystallites, the sharp faceting is absent in the treated ones.

Thus, the disappearance of the bc(o,t) peaks is relatively slower at lower temperatures, which can be validated by increasing the reaction temperature to 225 °C as shown in **Figure VII.23**c. At 225 °C, after a relatively short duration (6 min), the $(002)_{bc(o,t)}$ peak vanishes as though shifting its intensity to the new bct-I phase (at $2\theta = 44.77°$). On increasing the treatment time results in multiple new bct-I phases. Additional increment in the temperature (~ 300 °C) does not cause a practical disappearance of the bc(o,t) peaks (see **Figure VII.23**d) due to the fast evaporation of the solvent (supported by the thermogravimetric analysis (TGA) of the $N(C_4H_9)_4Br$ shown in **Figure VII.25**). The bct-I phase appears in the temperature range of 180 °C to 300 °C; this fact can be linked with the TGA data. Thus, the intermediate phases can be achieved through temperature controlled $N(C_4)_4^+$ treatment, which are the routes to cause effective phase transformation.

Table VII.5. Variation in the lattice parameters of the $N(C_4)_4^+$ treated Au microcrystallites in bco, bct and bct-I unit cells.

Treatment temperature (°C)	Time	bct (c/a)	bco (c/a)	bco (c/b)	bct-I (c/a)
25	25 h	1.3918	1.3862	1.3935	-
	206 h	1.3918	1.3814	1.3935	-
	329 h	1.3918	1.3814	1.3935	-
75	10 min	1.3918	1.3862	1.3935	-
	15 min	1.3918	1.3814	1.3935	-
	25 min	1.3918	1.3814	1.3935	-
	35 min	1.3918	1.3814	1.3935	-
	56 min	1.3918	1.3814	1.3935	-

Treatment temperature (°C)	Time	bct (c/a)	bco (c/a)	bco (c/b)	bct-I (c/a)
125	5 min	1.3918	1.3862	1.3935	-
	9 min	1.3918	1.3814	1.3935	-
	17 min	1.3918	1.3814	1.3935	-
	29 min	1.3918	1.3814	1.3935	-
180	5 min	1.3918	1.3862	1.3935	-
	14 min	1.3918	1.3814	1.3935	1.4000
	25 min	1.3918	1.3814	1.3935	1.4000
	45 min	1.3918	-	-	1.4000
	60 min	1.3918	-	-	1.4003
	90 min	1.3918	-	-	1.4008
	150 min	1.3918	-	-	1.4010
225	1 min	1.3918	1.3862	1.3935	-
	3 min	1.3918	1.3814	1.3935	1.4000
	6 min	1.3918	1.3814	1.3935	1.4000
	12 min	1.3918	1.3814	1.3935	1.4012
	18 min	1.3918	1.3814	1.3935	1.4005
300	2 min	1.3918	1.3819	1.3940	1.400

Time dependent changes in mole fraction of bc(o,t) crystallites are plotted for various temperatures, which follows a linear decay resulting in a zeroth-order reaction, as shown in **Figure VII.24**b. From the slope, the rate constant has been calculated for various temperatures and further used to calculate the activation energy. The ln(k) versus 1/T curve trails a straight-line decay, which can be fitted with the Arrhenius equation to estimate the activation energy (E_a = 6.9 kJ/mol), as shown in **Figure VII.24**c. The activation energy is much lower than the

energy required for the self-diffusion of bulk Au (165 kJ/mol) and the phase transformation caused by thermal annealing (120 kJ/mol) [56]. The changes in the morphology of the crystallite induced by the $N(C_4)_4^+$ treatment have been studied *via in-situ* SEM at ~ 200 °C. The morphology of the treated crystallites in **Figure VII.24**d exhibits rounding of the facets in contrast to the untreated ones, a similar observation drawn from the *ex-situ* study.
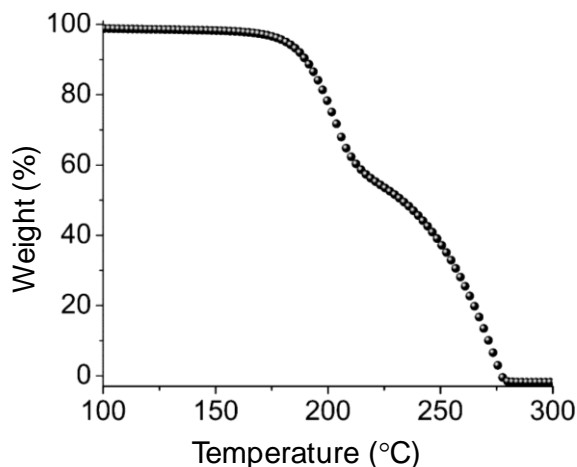
Figure VII.25. Thermogravimetric analysis (TGA) of $N(C_4H_9)_4Br$ at N_2 environment. The decomposition is very fast ~ 220 °C.

Although the difference in the activation energies (for the $N(C_4)_4^+$ and annealing) is much higher, the crystallites do not break up, as has been seen among Ag nanowires (during bct to fcc phase transformation *via* annealing). This is perhaps due to the low working temperature [63]. The appearance of bct-I in the longer due course of the treatment (or higher temperature) hints that the prolonged dissolution of the crystallite invokes the new phase and it does not appear at the immediate dissolution of the outer layer. Additionally, the phase transformation is not 100%, implying the presence of cumulative strain at the core. Therefore, the bc(o,t) phases in the crystallite volume are encapsulated with fcc lattice, *i.e.*, the core is made of bc(o,t) lattice.

VII.4.D Treatment with M-ToABr

Thermolysis of metal-ToABr precursor (M-ToABr, M = Pd, Pt, Ag and Cu) results in metal (in case of Pd and Pt) or metal bromide (Ag, Cu) particulates. In this context, the effect of the M-ToABr on the bc(o,t) Au crystallites surface is of another exciting topic, bringing out

the role of different metal anions on the stability of bc(o,t) crystallites. In order to separate out the contribution of the metal from the metal-organic precursor, ToABr (*i.e.*, $N(C_8)_4^+$) has been chosen because of its sparingly effective nature with regard to the phase transformation process (see **Figure VII.26**). Note, the ToABr has been used for the stabilization of bc(o,t) lattices in the precursor composition (*i.e.,* AuAgToABr).
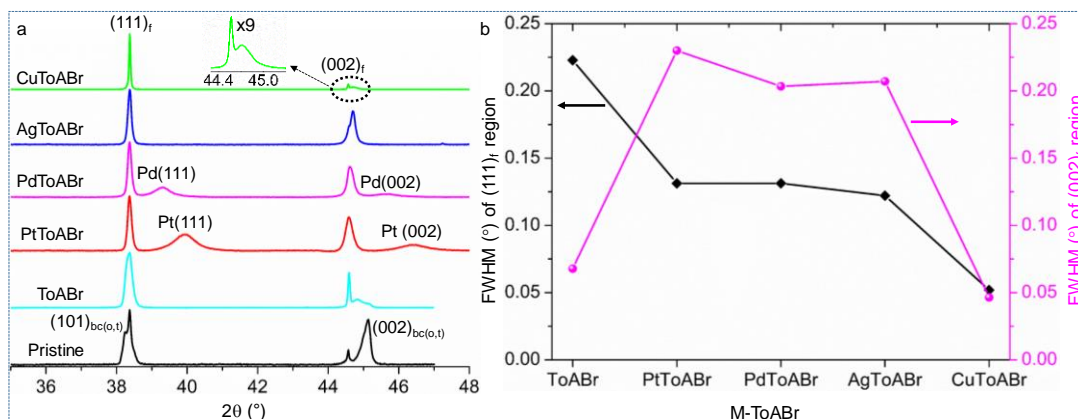
Figure VII.26. Effect of M-ToABr on the Au microcrystallites. (a) XRD patterns of the M-ToABr treated Au microcrystallites at 220 °C for 7 min, where M = Pt, Pd, Ag and Cu. Treatment with M-ToABr results in deposition of Pd and Pt over the crystallite surface, confirmed by the additional satellite peaks in the XRD patterns. No additional peaks arise due to Ag or Cu. (b) Post-treatment changes in FWHM of the $(111)_f$ and $(002)_f$ regions of the XRD patterns for various M-ToABr precursors.
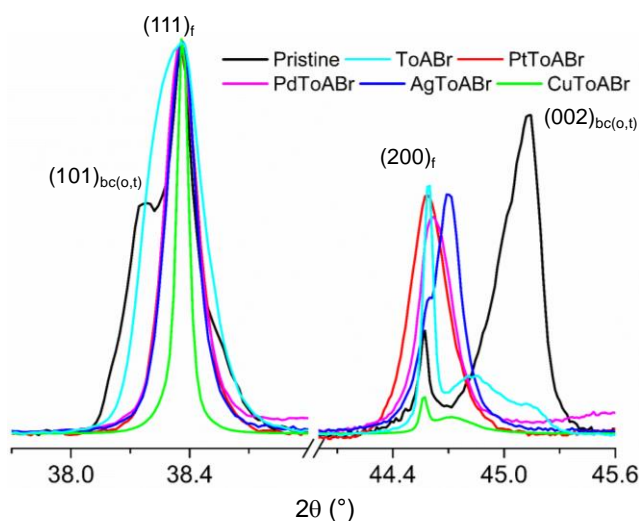
Figure VII.27. XRD patterns of the M-ToABr treated Au microcrystallites at 220 °C for 7 min. The pristine pattern is (002) oriented and so are the M-ToABr treated patterns. Surprisingly, the CuToABr

treated pattern is (111) oriented with very small FWHM, confirming the capability of facial phase transformation.

The bc(o,t) crystallites (37 µg) were treated with M-ToABr (60 µl) at 220 °C for 7 min and the corresponding changes were monitored by XRD and SEM. Upon treatment with PtToABr, the intensity of the $(002)_{bc(o,t)}$ peak vanishes as shown in **Figure VII.26**a. The changes in the pattern are even visible at the $(002)_f$ and (111) regions when compared with the pristine pattern in terms of increased broadening and reduction of the FWHM of the peaks, respectively (see **Figures VII.26**b and **VII.27**). The combined changes in the pattern altogether amount to the process of phase transformation. A similar behavior was observed in case of PdToABr. The XRD patterns collected from the Pt-/Pd-ToABr treated crystallites exhibit signals of Pt/Pd (see **Figure VII.26**a) generated from nano-/micro-particulates as seen from the respective M-ToABr thermolysis processes [64].
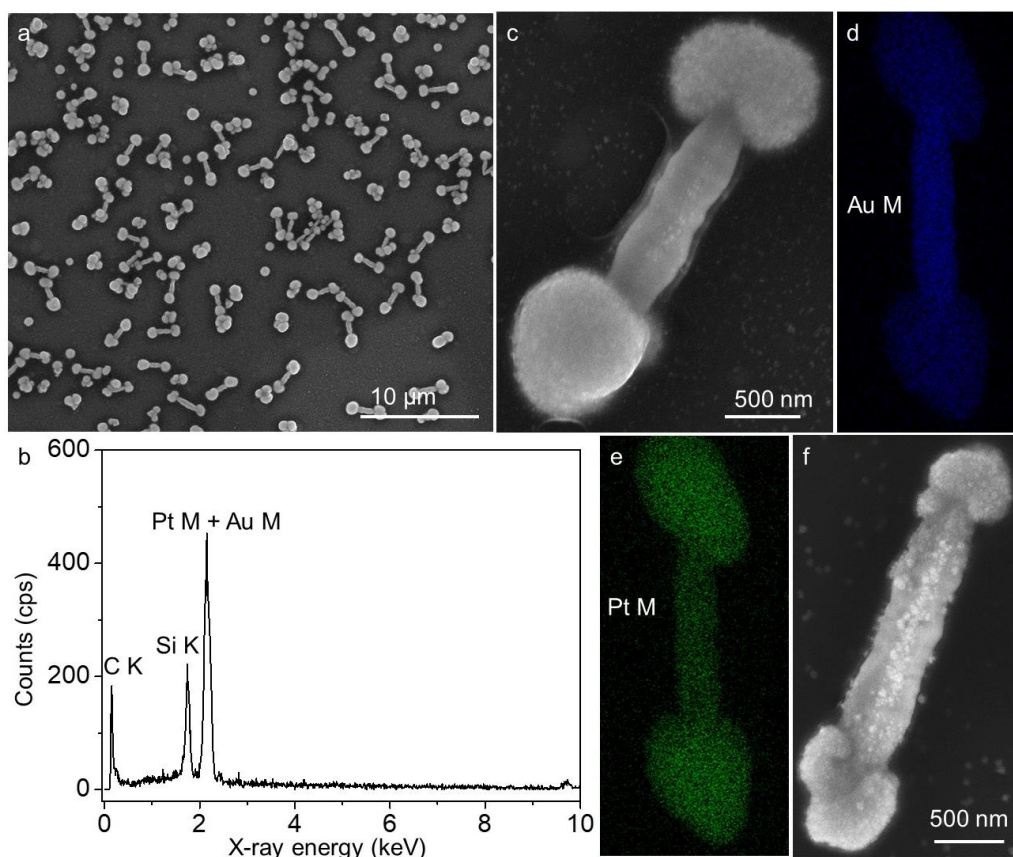
Figure VII.28. PtToABr treated Au crystallites at 220 °C. (a) SEM image of the Au-Pt crystallites exhibiting dumbbell shape. (b) EDX spectrum collected from the crystallite. (c–e) EDX elemental

mapping reveals presence of Au and Pt at the body and tips, respectively. (f) SEM image of Au-Pt crystallite depicting deposition of Pt at the body, in addition to the tips.
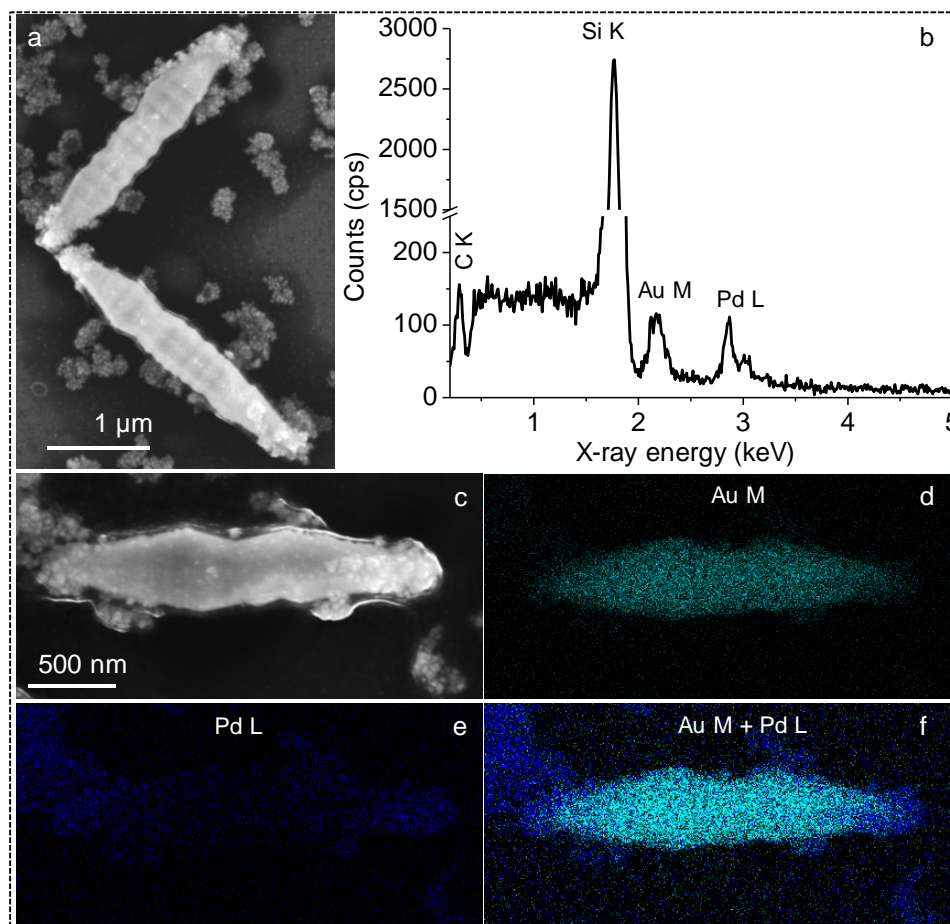
Figure VII.29. PdToABr treated Au crystallites at 220 °C. (a) SEM image of the Au-Pd crystallites exhibiting dumbbell shape. (b) EDX spectrum collected from the crystallite. (c−f) EDX elemental mapping reveals presence of Au and Pd at the body and tips, respectively.

SEM images of the PtToABr treated crystallites display dumbbell shaped features (see in **Figure VII.28**a,b). Energy Dispersive X-ray Spectroscopy (EDX) spectrum confirms the presence of Pt (see **Figure VII.2**8b). Elemental mapping reveals the presence of Pt mainly at the tips of the crystallite (~ 900 nm) and rarely at the body, as shown in **Figure VII.28**c−e. The size of the Pt dumbbell clearly shows the selective nature of the Pt growth over the surface of the bipyramid. These observations can be directly linked with the spatial distribution of the bc(o,t) lattices at the crystallite body (as observed by SXDM study, reported in **Chapter IV**). Thus, Pt deposits selectively at the fcc enriched tips (see **Figure VII.28**c). With the progress of the reaction, the bc(o,t) rich body gradually transforms to fcc and thereby, favors the

deposition of Pt, however sparingly as shown in **Figure VII.28**f. Similar to PtToABr, role of PdToABr in the bc(o,t) crystallites can be seen in **Figures VII.26–VII.29**.

The XRD pattern collected from the AgToABr treated crystallites exhibits a distinct peak at $2\theta = 44.707°$, indexable to $(002)_{T-I}$, which is analogous to the intermediate step seen in temperature dependent phase transformation induced by $N(C_4)_4^+$ in **Figures VII.23**c and **VII.24**. The AgToABr treated pattern does not host any signature of Ag since thermolysis of AgToABr results in AgBr [64]. The formation of AgBr leads to a sudden reduction in the Br^- stock, causing a halt to the phase transformation/etching process. In this scenario, the role of Ag^+ in the reshaping of the Au nanostars by blocking the Br^- ions may be referred from the literature [28]. Thus, by introducing a blocking agent (Ag^+), the phases (bct-I) can be frozen at any time by providing a range of crystal structures (with different c values and mole fractions).
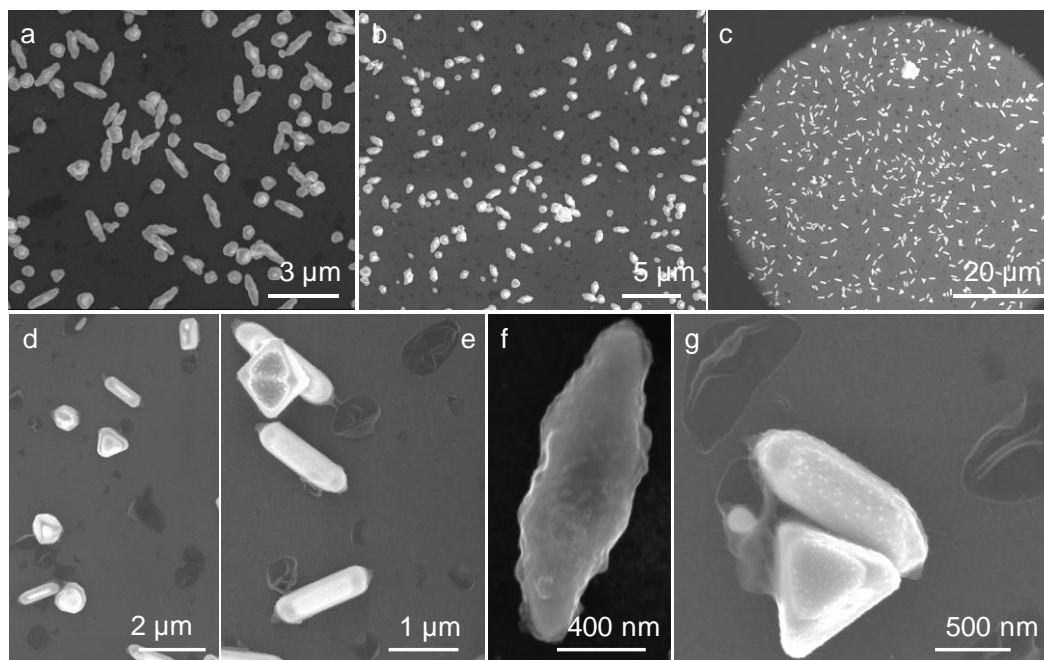
Figure VII.30. (a–g) SEM images of the CuToABr treated crystallites at 220 °C.

The CuToABr treated XRD pattern exhibits $(111)_f$ orientation with nearly disappeared $(002)_{bc(o,t)}$ peak as shown in **Figures VII.26**a and **VII.27**. Similar to AgToABr, thermolysis of CuToABr also generates CuBr [64]. Thus one would expect the phase transformation to retard at an intermediate step similar to AgToABr. However, a different pattern was seen which is well-understood from the role of shape-directing agent, Cu^{2+} stabilizing the (111) facets [65], in contrast to the pristine (002) orientation. Here, Cu^{2+} has been used to reshape the

morphology of the Au microcrystallites. As reported [30,65–67], [68,69], the Cu^{2+} ions enhance the efficacy of the oxidative etching (Br^-/O_2). Thus, the newly formed precursor redeposits at favorable orientations (such as plates) which can be confirmed by the SEM images of the treated crystallites in **Figure VII.30** displaying Au plates in addition to bipyramids and rods. The formation of plates, assisted by the Cu^{2+}, exhibits the (111) oriented XRD pattern.
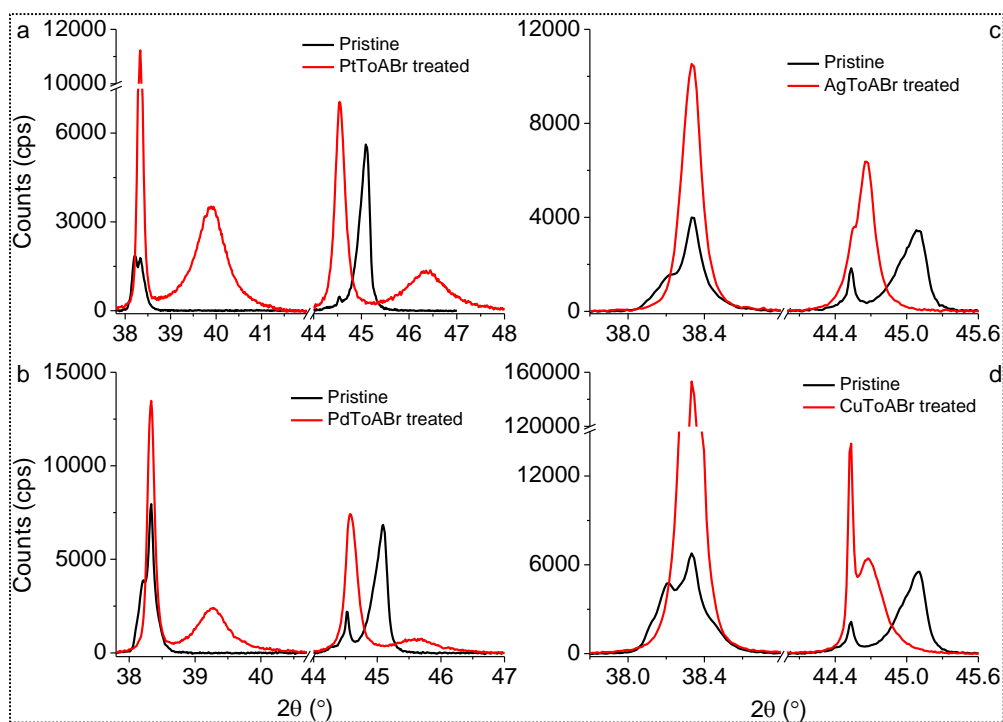
Figure VII.31. (a–d) XRD patterns of the M-ToABr treated at 220 °C for 7 min. The enhancement in intensity is maximum for CuToABr.

The position of the peak newly appeared during the post-treatment process (at 2θ ~ 44.5°, which is closer to $(002)_f$ region) follows the trend as CuToABr < PdToABr ~ PtToABr < AgToABr (see **Figure VII.27** and **VII.31**). The FWHM of the $(111)_f$ and $(002)_f$ peaks has been plotted for various M-ToABr in **Figure VII.26**b. In case of CuToABr, for both $(111)_f$ and $(002)_f$ regions, the FWHM is ~ 0.05°, highlighting nearly strain-free fcc as shown in **Figure VII.26**b. Whereas for the remaining M-ToABr, the anisotropic nature of the FWHM with broader peaks in both the (111) and (002) regions signifies that the presence of Cu^{2+} is crucial in causing the phase transformation. The intensities of the final patterns corresponding to $(111)_f$ and $(002)_f$ regions are shown in **Figure VII.31**, displaying an overall enhancement in

the intensity. Importantly, the enhancement is extensive in CuToABr treated pattern with a distinctly $(111)_f$ orientation which is in well agreement with the expected role of Cu^{2+} observed from the literature. The role of metals in phase transformation is visible as the disappearance of the $(002)_{bc(o,t)}$ peak and the reduction in FWHM at the (111) region which were otherwise unachievable by ToABr alone (see **Figure VII.32**).

The lattice mismatch between Au (fcc) and Pt, Pd are 3.87% and 4.67%, respectively. For Au in bc(o,t) crystallites, however, the lattice mismatch value with respect to Pt or Pd is only ~ ±1% along all three axes. Although the lattice mismatches are within the range (irrespective of substrate crystal structure), the selective deposition of Pt/Pd over the fcc rich tip/fcc-body (phase transferred to fcc) as outgrowth is intriguing. DFT calculations have revealed that the deposition of the hetero-atom is governed not by the lattice mismatch, rather by the atomic arrangement on the surface of the substrate [70]. As such, the isotropic nature of fcc favors over the anisotropic bc(o,t) lattices explaining the observations drawn in case of Pt/Pd deposition on bc(o,t) Au crystallites.
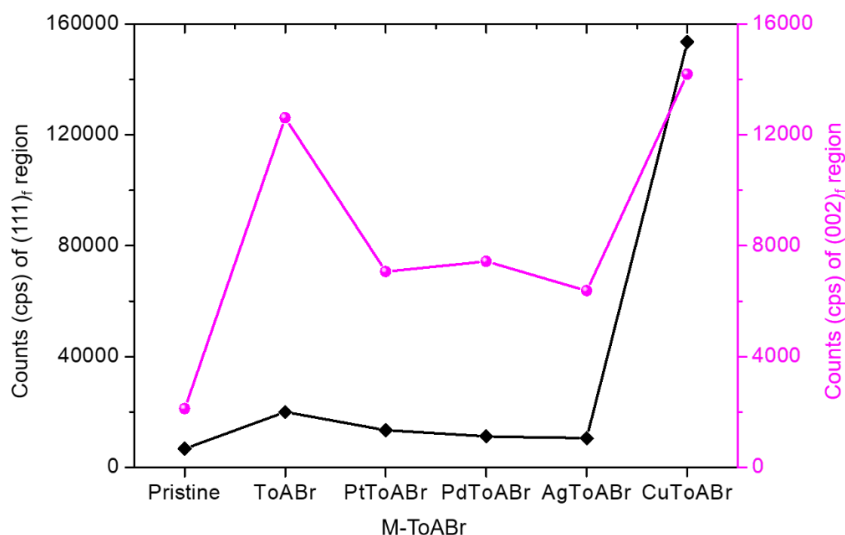
Figure VII.32. Changes in the XRD intensity of the $(111)_f$ and $(002)_f$ regions treated with different M-ToABr.

Literature reports display the role of over layers (*i.e.*, metals) epitaxially deposited on 2H/4H Au nanostructures in causing the phase transformation to fcc, due to the strain generated by the epi-layer [11,34]. The selective deposition at the fcc sites explains the insignificant role of Pt/Pd in introducing strain and thereby causing the phase transformation.

VII.4.E Treatment with Au(III)/ToABr

In order to understand the chemical stability of the bc(o,t) crystallites in other reactive environments, particularly with respect to the well-known oxidizing agent Au(III)/alkyl ammonium bromide [71–73], the crystallites are treated with the Au(III)/ToABr (*i.e.*, AuToABr) and its effects are studied systematically.

The SEM images of the AuToABr treated crystallites are shown in **Figure VII.33**a–e. The as-prepared sample in Si substrate exhibits a uniform distribution of the Au microcrystallites (see **Figure III.7**b in **Chapter III**), while the treated sample exhibits non-uniform distribution of the crystallites proportions along with poly-disperse morphologies and sizes of the crystallites as shown in **Figure VII.33**a. Thus, SEM images were collected from different regions of the substrate and one such region is shown in **Figure VII.33**a, where overall modifications in the morphology such as smoothening of the crystallites were observed. These modifications can be linked with the disappearance of the high index facets and rounding of the tips, as shown in **Figure VII.33**b. Additionally, few µms wide Au plates are visible in **Figure VII.33**a. The formation of the plates can be understood considering the thermolysis of the AuToABr as was previously seen in the literature [74]. The other parts of the substrate (see **Figure VII.33**c–e) contained crystallites with various changes in the morphologies. Note a region in **Figure VII.33**c, dissolution of the bipyramids (marked by white ellipses) was seen. Interestingly, some parts of the substrate exhibit only very few particles such as microplates (see **Figure VII.33**d) with the footprints of the pre-existed microcrystallites before the treatment, implying full dissolution of the microcrystallites. In another part, micro-rods, plates, cuboctahedrons as well as micro-decahedra crystallites may be seen (**Figure VII.33**e). Thus, the treatment of AuToABr dissolves Au microcrystallites of unconventional morphologies to give rise to energetically favorable morphologies. The modified morphologies include shortened bipyramids and other poly-dispersed particles (**Figure VII.33**a–e). It may be noted that thermolysis of only AuToABr results in majorly microplates [74–77], in contrast to the observations made here. This intriguing evolution of new morphologies can be explained by the full dissolution of the microcrystallites as was observed by the splitting of the bipyramids in **Figure VII.33**c and by the redeposition onto micro-plates and -rods as shown in **Figure VII.34**.

The as-synthesized crystallites (with bc(o,t) fraction of ~ 79%) possess a (002) orientation different from the conventional fcc Au which is always (111) oriented. The post-treated crystallites were characterized by XRD (see **Figure VII.35**a) along with the as-synthesized pattern for reference. The treated pattern exhibits a huge intensity contribution in both the fcc(111) and fcc(002) regions with $(111)_f/(002)_f$ ratio of 80.5, indicating high anisotropy with overall orientation to be (111), different from the as-synthesized pattern.
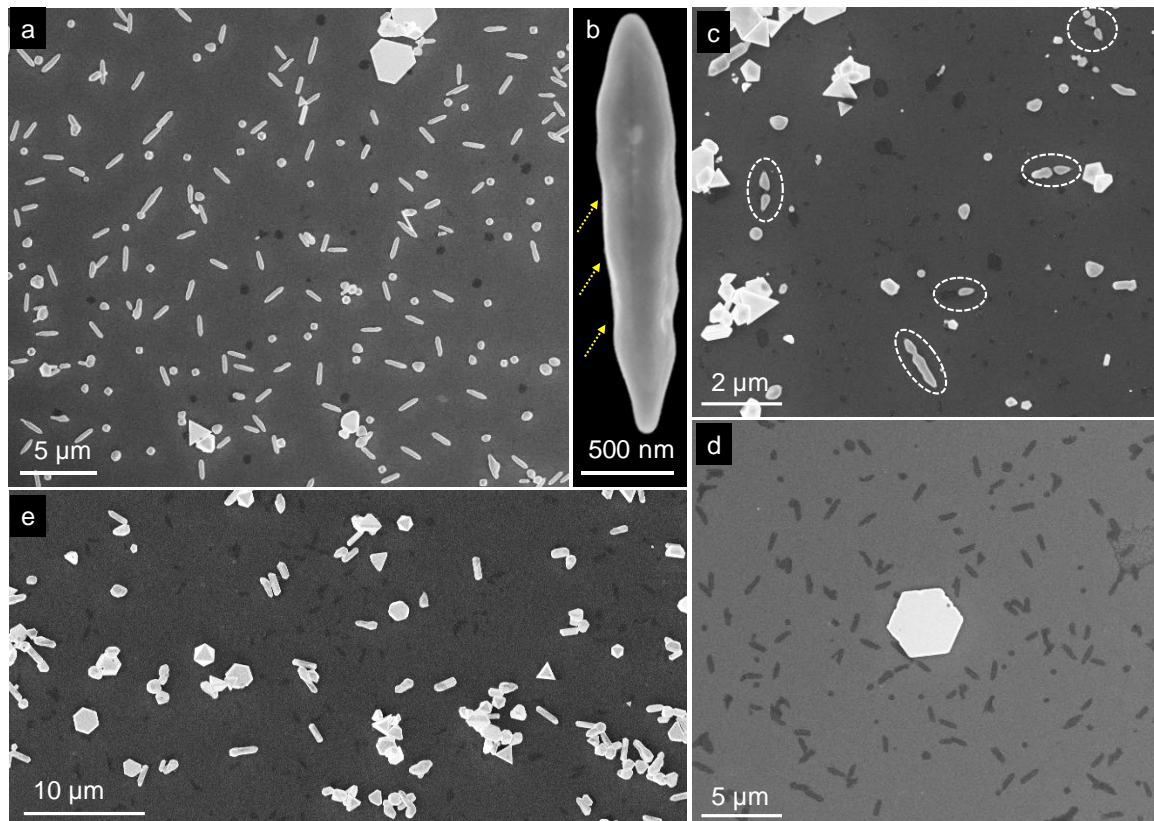
Figure VII.33. Effect of AuToABr on Au microcrystallites at 220 °C for 7 min. (a−e) SEM images of the AuToABr treated crystallites at different magnifications from different parts of the same sample. The yellow arrows in (b) indicate disappearance of the high index facets. The white ellipses in (c) are drawn to guide the eye. The black marks represent the footprint of the Au microcrystallites.

In order to understand the changes occurred in the XRD pattern in great detail, the pattern has been magnified and shown in **Figure VII.35**a−c. The magnified $(111)_f$ region in **Figure VII.35**a exhibits an increment in intensity by ~ 1538 times in the post-treated sample. Further, the increments in the intensities of the $(002)_f$ and $(002)_{bc(o,t)}$ regions are 79 and 0.45 times, respectively as shown in **Figure VII.35**b,c. The huge increment in the overall XRD pattern with favorable (111) orientation can be linked with the formation of Au micro-plates

and -rods [74], which are formed due to the thermolysis of AuToABr precursor which was added in the starting of the treatment. Interestingly, the reduction in the $(002)_{bc(o,t)}$ intensity by ~ 0.45 factor can be explained by the dissolution of the Au microcrystallites detailed described in **Figure VII.33**d. The dissolved Au acts as a precursor enhancing the Au precursor quantity, thus leading to the generation of fcc Au crystallites which in turn enhances the intensity of the overall XRD pattern. The dissolution followed by the redeposition can be explained by the comproportionation reaction [71] previously observed in the presence of Au(III) [71,73,78,79]. Thus, the reaction between the AuToABr and Au can be expressed as follows in equation (8).

$$[ToA^+][AuCl_4^-] + 2Au^0 + 2ToABr \xrightarrow{\Delta} 3[ToA^+][AuX_2^-] \qquad X^- = Cl^-/Br^- \qquad (8)$$
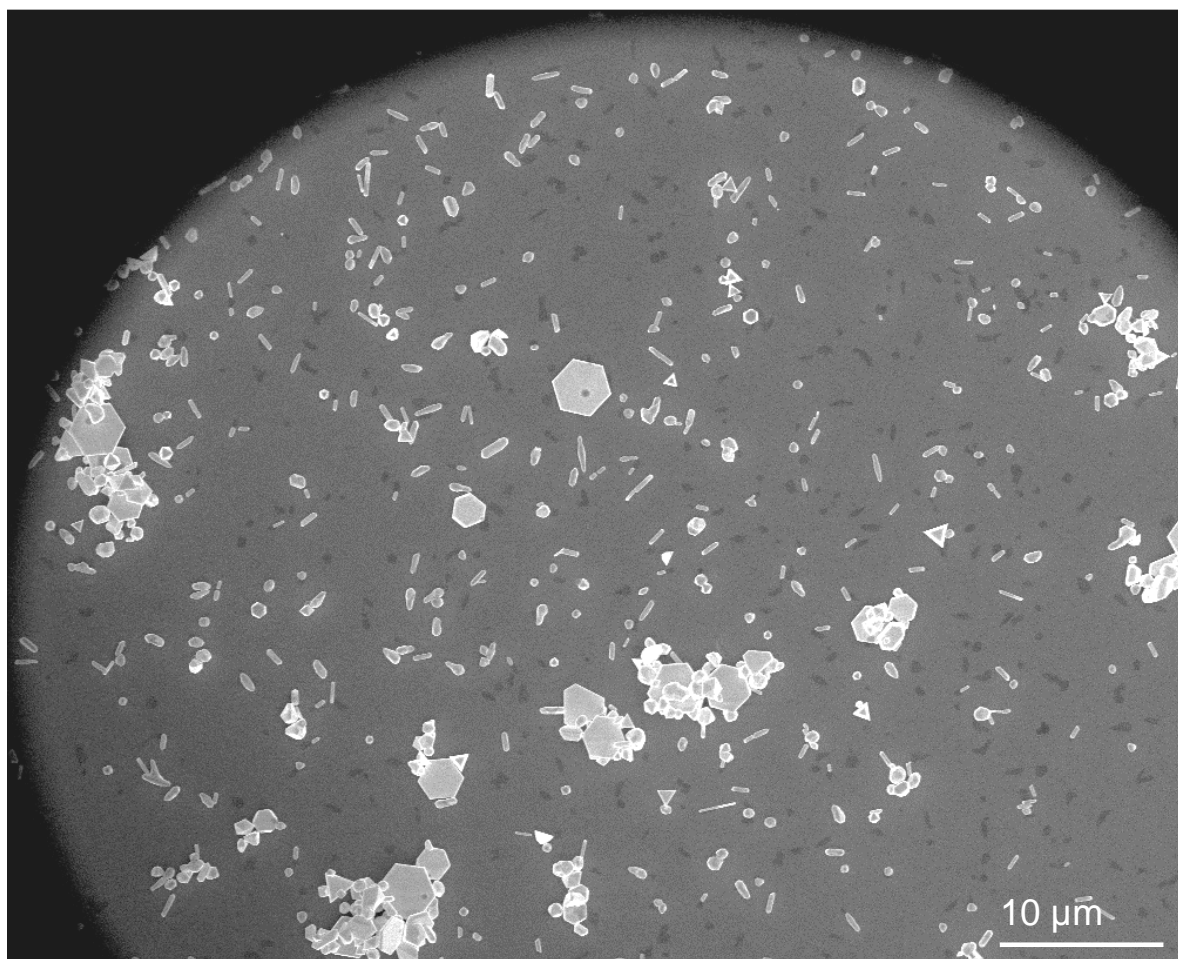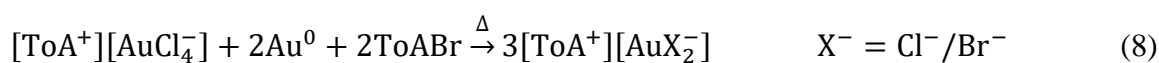
Figure VII.34. Large area SEM image of AuToABr treatment (at 220 °C for 7 min) Au microcrystallites.

In larger picture, simple thermolysis of the AuToABr at 220 °C is nearly similar to the treatment of AuToABr at 220 °C, since the precursor at the post-treatment process is a mixture of Au(I) and Au(III) ions in ToABr as shown in equation (8). The inhomogeneity in terms of the distribution of the crystallites and the corresponding geometries can be understood due to the fast reaction kinetics resulting in decomposition of the AuToABr at high temperature (220 °C) and non-uniform spreading of the AuToABr. Thus, in order to track the intermediate steps involved in the dissolution of as-synthesized Au microcrystallites, the crystallites have been treated with a lower amount of Au(III) (in AuToABr), since the comproportionation reaction is mainly governed by the presence of Au(III). Additionally, other parameters, such as reaction kinetics may also play a role. Thus, both the concentration and kinetics are varied concurrently and the effects are studied by SEM.

The crystallites were subjected to AuToABr (with lower quantity of Au(III)) at 150 °C for 5 s and washed to remove the unreacted precursor and examined under SEM as shown in **Figure VII.36**a. Surprisingly, the bipyramids with high index facets changed to dumbbell like shapes with thin layers of Au at the tips. Further, increasing the reaction time to 20 s (**Figure VII.36**b,c) leads to selective dissolution of the body of the crystallite. The extent of the dissolution of the central part of the crystallite can be compared with the size of the crystallite (see **Figure VII.37**). The dissolution of the bipyramids is an oxidation process and can be understood from the high magnified SEM images in **Figure VII.36**d–h. Specifically, the reaction starts at the central part of the crystallite (clearly distinguishable by the residual precursor in black at **Figure VII.36**e) and with the progress of the reaction, the dissolution is selective to the central part of the body along with a very slow reaction at the tips. In the total reaction time frame, most bipyramids tend to loose the central thick region, leaving the tips nearly unaffected as though the core got dissolved leaving the shell. Although the central part is thicker than the tips, the tips are the only remainder towards the end of the reaction. This is an interesting observation as it relates to the reactivity of local region in the crystallite (morphology) and not simply with the mass available locally. SXDM study on an as-prepared crystallite revealed the spatial distribution of the different lattices in the crystallite volume, specifically bc(o,t) rich body and fcc rich tips (described in **Chapter IV**). Considering the effect of comproportionation reaction to be the most active at the higher Gibbs energy site, the central body consisting high-index facets and metastable bc(o,t) lattices offers the most

reactive sites (see the black patches in **Figure VII.36**e). Thus, it appears that a thin fcc shell covers the whole crystallite with the bc(o,t) rich core as was also observed during $N(C_4H_9)_4Br$ treated phase transformation process (reported in section **VII.4.C**). In the given reaction time frame, the dissolution of the central body is dependent on the size of the crystallite; larger the size, longer is the time taken to dissolve away the central bc(o,t) region.
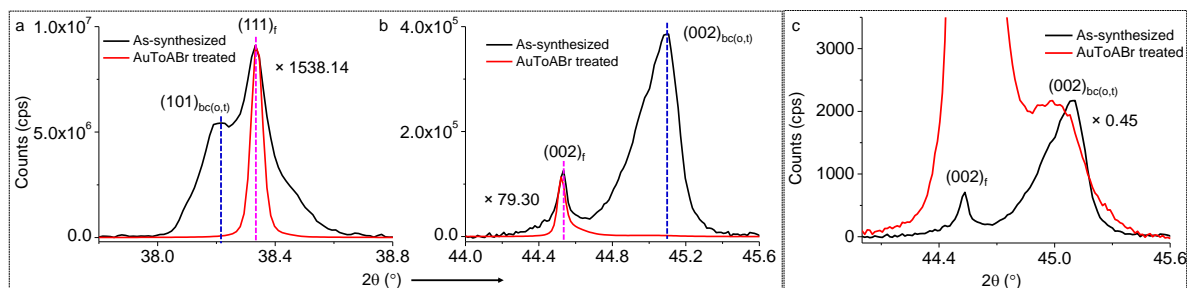
Figure VII.35. XRD pattern collected from the AuToABr treated (at 220 °C for 7 min) crystallites along with the as-synthesized pattern have been shown. (a–c) The as-synthesized pattern has been magnified by factor of 1538.14, 79.30 and 0.45, respectively and shown along with the actual intensity count of the AuToABr treated pattern.
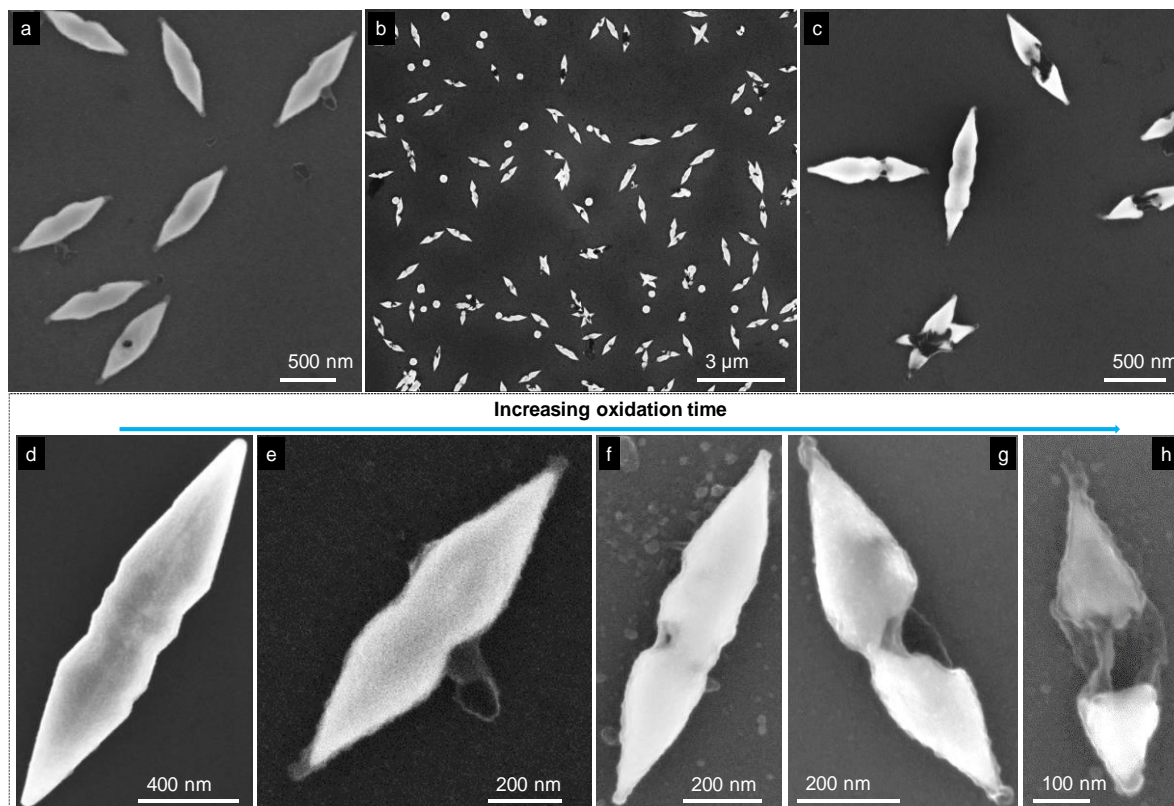
Figure VII.36. Effect of AuToABr on Au microcrystallites at 150 °C. SEM images of AuToABr treated Au microcrystallites for (a) 5 and (b,c) 20 s, respectively. (d–h) High-magnified SEM images of AuToABr treated Au microcrystallites at 150 °C at different intermediate stages, depicting the possible dissolution pathway of the bipyramids by the AuToABr. The central part of the crystallite affects at first and followed by the tips. Thus, hinting the higher reactivity at the central part followed by the tips.

The desolation dissolution of such large crystallites is intriguing. The literature describes the probability of the oxidation of Au(0) by Au(III) to Au(I) of being higher for small sized particles due to the lowering of the negative redox potential and the higher curvatures involved [80], which is clearly not applicable to the present scenario as the crystallites, in the present study, are rather large. Therefore, the observed trend must be related to thermodynamically metastable bc(o,t) lattices which primarily reside in the central core. The sharp tips made of fcc, on the other hand, take much longer to dissolve (**Figure VII.36**a–e).
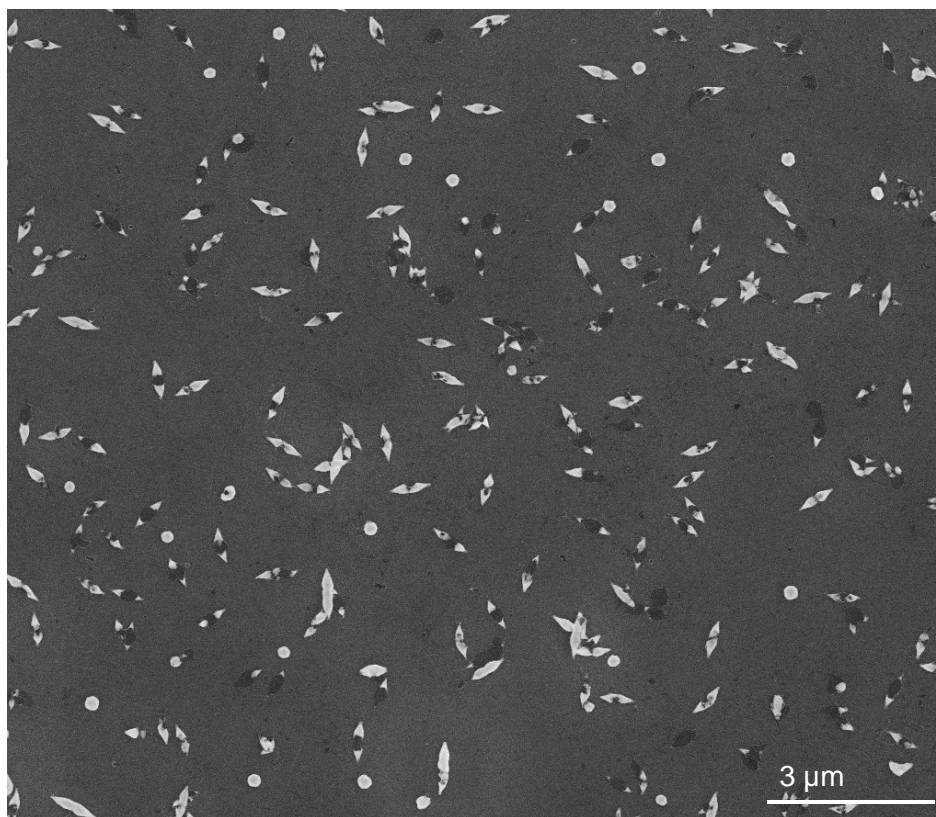
Figure VII.37. SEM image of the large area view of AuToABr treated crystallites at 150 °C for 20 s. One immediate observation is the selective dissolution of the core while leaving the tips in most of the cases. The extent of dissolution is length dependent, bigger the crystallite lesser is the extent of dissolution. Thus, the dissolution is mass dependent at the central part of the crystallite.

The role of ammonium salts are well-known in stabilizing anisotropic morphologies (such as rods, wires and plates) as well as unconventional lattices (bc(o,t) [48,81], hcp [10,12]) of Au. The same capping agent (ToABr) forming the AuToABr precursor dissolves the as-synthesized bc(o,t) lattices, selectively. However, in larger picture, the treatment of AuToABr results in anisotropic morphologies (micro-plates/-rods) as shown in **Figure VII.38**a which are in fcc lattice (see **Figure VII.38**b). Thus, treatment of AuToABr is capable to cause irreversible conversion of unconventional anisotropic 1D morphologies (in bc(o,t) lattices) to anisotropic 2D+1D morphologies (in fcc lattice).
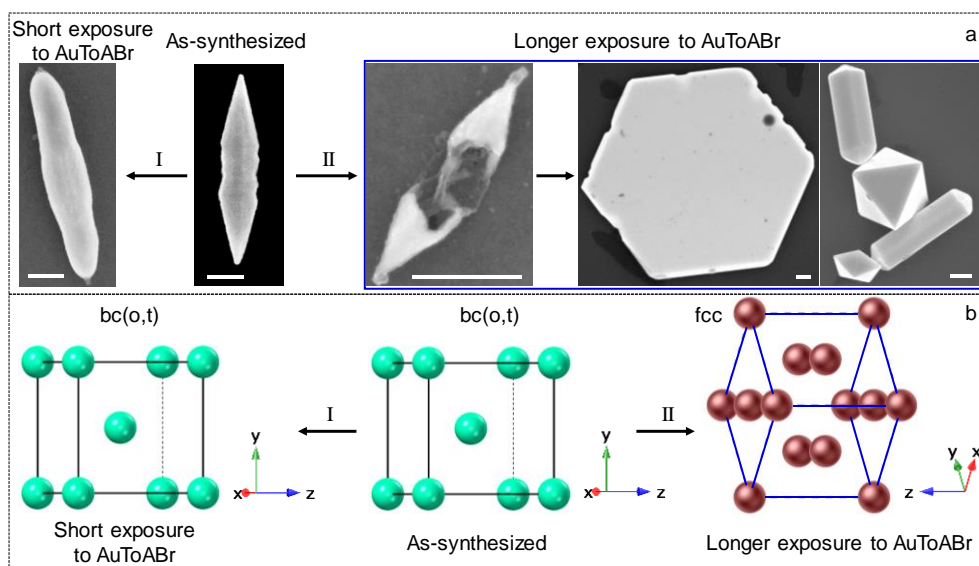
Figure VII.38. (a) SEM images of AuToABr treated Au microcrystallites captured at different intermediates, explaining the possible changes observed in their morphologies and corresponding crystal structures in (b). Scale bar, 300 nm. At a very short reaction time frame, the very high reaction kinetics result in disappearances of the high-index facets and sharp tips of the bipyramids while retaining the bc(o,t) crystal structures (pathway I), however at longer reaction time, dissolution of the crystallites followed by formation of micro-plates, -rods, decahedra, cuboctahedra *etc*., in fcc lattice prevail (pathway II).

In the present study, AuToABr acts as an oxidizing agent and dissolves the Au microcrystallites to form Au(I). The dissolution is crystal structure dependent, more reactive at the bc(o,t) rich central part of the crystallite, followed by the fcc rich tips. Furthermore, the dissolution is more favorable for the geometrically unfavorable morphologies. Therefore, the presence of high index facets and the metastable lattices, synergistic agents allows to dissolve the crystallite within a short reaction time. Thus, the AuToABr can be used to switch between

the energetically expensive facets/morphologies and crystal structures to the most favorable morphologies and the crystal structures.

SXDM study of a bc(o,t) Au bipyramid has unveiled the presence of large mosaicity along the length of the bc(o,t) rich body capped with the fcc rich tips, while the growth directions are bco<010> and fcc<110> (see details in **Chapter IV**). The results described in this chapter validate the role of adsorbents on the geometry, stability and reactivity of the bc(o,t) crystallites. For example, a treatment with hexadecanethiol heals the mosaicity irreversibly to a great extent with preferential adsorption at the $(101)_{bc(o,t)}/(111)_f$ facets. The Na_2S, a reducing agent, causes irreversible phase transformation to fcc with (111) as preferred orientation, through a strong Au-S interaction. The quaternary ammonium bromide, an oxidizing agent, evinces phase transformation to fcc with $(002)_f$ orientation, through a set of new phases (bct-I) *via* the uniaxial expansion. The Lewis acid dissolves Au(0) by converting it into Au(I) and the latter redeposits in fcc lattice with (002) orientation. The phase conversion depends on the alkyl chain length. The conversion is maximum for the butyl group. Importantly, the process of lattice transformation in case of Na_2S (final pattern is fcc(111) orientated) and quaternary ammonium medium (fcc(002) orientated) is different in each case and so are the corresponding changes in the morphology of the crystallites. Specifically, in case of Na_2S, a direct conversion from bc(o,t) to fcc occurs, whereas for quaternary ammonium surfactants, the transformation occurs *via* the generation of intermediate bct-I phases. Although the calculated activation energies are in the similar order, the values do not match exactly. The performance of an alkyl group can be improved by incorporating metal cations such as M-ToABr. The epitaxial deposition of metals over the fcc enriched tips elucidates the crystal structure dependent deposition of the foreign metals on the bc(o,t) Au crystallite. Such a system is interesting in terms of mapping (by SEM) of the spatial distribution of the different lattices in the crystallite volume. Additionally, the presence of synergistic agents, such as Cu^{2+} can enhance the etching process with the full dissolution of the crystallite and therefore, redepositing them in fcc(111) oriented morphologies. Surprisingly, the crystal structure dependent dissolution of Au was observed in Au(III) medium, leading to higher instability of bc(o,t) than fcc. The oxidizing agents such as the ones used here, bring out the observation that the bc(o,t) rich core is encapsulated with the fcc sheath in the form of a core-shell geometry.

In spite of the co-presence of large compressive and tensile strains in the μm sized crystallite, the ambient stability of the crystallite for indefinite period of time is commendable! The stability can be understood from the core-shell geometry. The thickness of the sheath is non-uniform throughout the body of the crystallite, especially higher at the tips. The fraction of fcc concentrates over the penta-twinned tips made of 10 {111} facets, which explain the selective deposition of Pt/Pd at the tips. Therefore, the study resolves the spatial distribution of the different phases in the entire crystallite volume and the corresponding reactivity patterns under different chemical environments.

VII.5. Conclusions

In conclusion, treatments with various adsorbents on the bc(o,t) Au crystallites were studied. The study reports a chemical window in terms of stability of the phases as well as their morphologies. The consequences include enhancement in crystallinity by reducing the mosaicity with a preferential orientation to the $(101)_{bc(o,t)}$ or $(111)_f$ facet (for hexadecanethiol) and phase transformation to fcc. The process of phase transformation is distinct for different adsorbents. In case of Na_2S, a bc(o,t) to fcc direct conversion is observed with a preferential $(111)_f$ orientation, whereas, treatment with $N(C_4H_7)_4Br$ introduces a set of new bct-I phases *via* uniaxial expansion, followed by the phase transformation to fcc with (002) orientation. The extent of transformation and the corresponding final orientation (in the case of quaternary ammonium cations) can be tailored by the additional synergistic or blocking agent. The study demonstrates the geometrical locations of different lattices in the crystallite volume, fcc rich tips and bc(o,t) rich body. The crystal structure dependent anisotropic deposition of Pd/Pt enables the mapping of the multi-phased system. Importantly, the crystal structure dependent dissolution in Au(III) oxidizing medium discloses the higher reactivity of bc(o,t) than fcc due to the higher Gibbs free energy of the former. Surprisingly, the study unravels a core-shell geometry, *i.e.*, the metastable bc(o,t) core is being protected under the thermodynamically stable fcc sheath. The observations drawn from the study explain the extraordinary stability of the bc(o,t) Au crystallite at the ambient condition, and their reactivities under various chemical environments, which may be useful in applications related to catalysis.

References

[1] Z. Fan and H. Zhang, *Crystal Phase-Controlled Synthesis, Properties and Applications of Noble Metal Nanomaterials*, Chem. Soc. Rev. **45**, 63 (2016).

[2] T.-H. Yang, Y. Shi, A. Janssen, and Y. Xia, *Surface Capping Agents and Their Roles in Shape-Controlled Synthesis of Colloidal Metal Nanocrystals*, Angew. Chem. Int. Ed. **59**, 15378 (2020).

[3] J. Gao, C. M. Bender, and C. J. Murphy, *Dependence of the Gold Nanorod Aspect Ratio on the Nature of the Directing Surfactant in Aqueous Solution*, Langmuir **19**, 9065 (2003).

[4] B. Nikoobakht and M. A. El-Sayed, *Preparation and Growth Mechanism of Gold Nanorods (NRs) Using Seed-Mediated Growth Method*, Chem. Mater. **15**, 1957 (2003).

[5] T. K. Sau and C. J. Murphy, *Room Temperature, High-Yield Synthesis of Multiple Shapes of Gold Nanoparticles in Aqueous Solution*, J. Am. Chem. Soc. **126**, 8648 (2004).

[6] L. Gou and C. J. Murphy, *Fine-Tuning the Shape of Gold Nanorods*, Chem. Mater. **17**, 3668 (2005).

[7] N. R. Jana, L. Gearheart, and C. J. Murphy, *Seed-Mediated Growth Approach for Shape-Controlled Synthesis of Spheroidal and Rod-like Gold Nanoparticles Using a Surfactant Template*, Adv. Mater. **13**, 1389 (2001).

[8] X. Lu, M. S. Yavuz, H.-Y. Tuan, B. A. Korgel, and Y. Xia, *Ultrathin Gold Nanowires Can Be Obtained by Reducing Polymeric Strands of Oleylamine-AuCl Complexes Formed via Aurophilic Interaction*, J. Am. Chem. Soc. **130**, 8900 (2008).

[9] Z. Huo, C. K. Tsung, W. Huang, X. Zhang, and P. Yang, *Sub-Two Nanometer Single Crystal Au Nanowires*, Nano Lett. **8**, 2041 (2008).

[10] X. Huang, S. Li, Y. Huang, S. Wu, X. Zhou, S. Li, C. L. Gan, F. Boey, C. A. Mirkin, and H. Zhang, *Synthesis of Hexagonal Close-Packed Gold Nanostructures*, Nat. Commun. **2**, 292 (2011).

[11] Z. Fan, M. Bosman, X. Huang, D. Huang, Y. Yu, K. P. Ong, Y. A. Akimov, L. Wu, B. Li, J. Wu, Y. Huang, Q. Liu, C. Eng Png, C. Lip Gan, P. Yang, and H. Zhang, *Stabilization of 4H Hexagonal Phase in Gold Nanoribbons*, Nat. Commun. **6**, 7684 (2015).

[12] C. Wang, X. Li, L. Jin, P.-H. Lu, C. Dejoie, W. Zhu, Z. Wang, W. Bi, R. E. Dunin-Borkowski, K. Chen, and M. Jin, *Etching-Assisted Route to Heterophase Au Nanowires with Multiple Types of Active Surface Sites for Silane Oxidation*, Nano Lett. **19**, 6363 (2019).

[13] Z. Fan, M. Bosman, Z. Huang, Y. Chen, C. Ling, L. Wu, Y. A. Akimov, R. Laskowski, B. Chen, P. Ercius, J. Zhang, X. Qi, M. H. Goh, Y. Ge, Z. Zhang, W. Niu, J. Wang, H. Zheng, and H. Zhang, *Heterophase Fcc-2H-Fcc Gold Nanorods*, Nat. Commun. **11**, 3293 (2020).

[14] C. Wang, Y. Hu, C. M. Lieber, and S. Sun, *Ultrathin Au Nanowires and Their Transport Properties*, J. Am. Chem. Soc. **130**, 8902 (2008).

[15] A. Friedrich, C. Shannon, and B. Pettinger, *A Study of the Influence of Halide Adsorption on a Reconstructed Au (111) Electrode by Second Harmonic Generation*, Surf. Sci. **251/252**, 587 (1991).

[16] Y. Liu and V. Ozolins, *Self-Assembled Monolayers on Au (111): Structure, Energetics, and Mechanism of Reconstruction Lifting*, J. Phys. Chem. C **116**, 4738 (2012).

[17] J. Wang, B. M. Ocko, A. J. Davenport, and H. S. Isaacs, *In Situ X-ray-Diffraction and - Reflectivity Studies Ofthe Au(111)/Electrolyte Interface: Reconstruction and Anion Adsorption*, Phys. Rev. B **46**, 10321 (1992).

[18] A. D. Jewell, H. L. Tierney, and E. C. H. Sykes, *Gently Lifting Gold's Herringbone Reconstruction: Trimethylphosphine on Au (111)*, Phys. Rev. B **82**, 205401 (2010).

[19] G. Andreasen, C. Vericat, M. E. Vela, and R. C. Salvarezza, *Dynamics of Sulfur Adlayer Transformations at Metal/Electrolyte Interfaces*, J. Chem. Phys. **111**, 9457 (1999).

[20] P. Maksymovych and J. T. Yates, *Au Adatoms in Self-Assembly of Benzenethiol on the Au (111) Surface*, J. Am. Chem. Soc. **130**, 7518 (2008).

[21] P. J. F. Harris, *Sulphur-Induced Faceting of Platinum Catalyst Particles*, Nature **323**, 792 (1986).

[22] G. Mettela and G. U. Kulkarni, *Facet Selective Etching of Au Microcrystallites*, Nano Res. **8**, 2925 (2015).

[23] C. K. Tsung, X. Kou, Q. Shi, J. Zhang, M. H. Yeung, J. Wang, and G. D. Stucky, *Selective Shortening of Single-Crystalline Gold Nanorods by Mild Oxidation*, J. Am. Chem. Soc. **128**, 5352 (2006).

[24] H. Pan, S. Low, N. Weerasuriya, and Y.-S. Shon, *Graphene Oxide-Promoted Reshaping and Coarsening of Gold Nanorods and Nanoparticles*, ACS Appl. Mater. Interfaces **7**, 3406 (2015).

[25] M. B. Mohamed, K. Z. Ismail, S. Link, and M. A. El-Sayed, *Thermal Reshaping of Gold Nanorods in Micelles*, J. Phys. Chem. B **102**, 9370 (1998).

[26] R. Zou, Q. Zhang, Q. Zhao, F. Peng, H. Wang, H. Yu, and J. Yang, *Thermal Stability of Gold Nanorods in an Aqueous Solution*, Colloids Surf. A Physicochem Eng. Asp. **372**, 177 (2010).

[27] A. S. A. M. Al-Sherbini, *Thermal Instability of Gold Nanorods in Micellar Solution of Water/Glycerol Mixtures*, Colloids Surf. A Physicochem Eng. Asp. **246**, 61 (2004).

[28] L. Rodríguez-Lorenzo, J. M. Romo-Herrera, J. Pérez-Juste, R. A. Alvarez-Puebla, and L. M. Liz-Marzán, *Reshaping and LSPR Tuning of Au Nanostars in the Presence of CTAB*, J. Mater. Chem. **21**, 11544 (2011).

[29] C. M. Aguirre, T. R. Kaspar, C. Radloff, and N. J. Halas, *CTAB Mediated Reshaping of Metallodielectric Nanoparticles*, Nano Lett. **3**, 1707 (2003).

[30] J. Pérez-Juste, I. Pastoriza-Santos, L. M. Liz-Marzán, and P. Mulvaney, *Gold Nanorods: Synthesis, Characterization and Applications.*, Coord. Chem. Rev. **249**, 1870 (2005).

[31] H. Zhang, B. Gilbert, F. Huang, and J. F. Banfield, *Water-Driven Structure Transformation in Nanoparticles at Room Temperature*, Nature **424**, 1025 (2003).

[32] M. Epifani, E. Pellicer, J. Arbiol, N. Sergent, T. Pagnier, and J. R. Morante, *Capping Ligand Effects on the Amorphous-to-Crystalline Transition of CdSe Nanoparticles*, Langmuir **24**, 11182 (2008).

[33] Y. Liu, C. Wang, Y. Wei, L. Zhu, D. Li, J. S. Jiang, N. M. Markovic, V. R. Stamenkovic, and S. Sun, *Surfactant-Induced Postsynthetic Modulation of Pd Nanoparticle Crystallinity*, Nano Lett. **11**, 1614 (2011).

[34] Z. Fan, X. Huang, Y. Han, M. Bosman, Q. Wang, Y. Zhu, Q. Liu, B. Li, Z. Zeng, J. Wu, W. Shi, S. Li, C. L. Gan, and H. Zhang, *Surface Modification-Induced Phase Transformation of Hexagonal Close-Packed Gold Square Sheets*, Nat. Commun. **6**, 6571 (2015).

[35] H. Cheng, N. Yang, Q. Lu, Z. Zhang, and H. Zhang, *Syntheses and Properties of Metal Nanomaterials with Novel Crystal Phases*, Adv. Mater. **30**, 1707189 (2018).

[36] I. Chakraborty, S. N. Shirodkar, S. Gohil, U. V. Waghmare, and P. Ayyub, *A Stable, Quasi-2D Modification of Silver: Optical, Electronic, Vibrational and Mechanical Properties, and First Principles Calculations*, J. Phys. Condens. Matter **26**, 025402 (2014).

[37] K. Kusada, H. Kobayashi, T. Yamamoto, S. Matsumura, N. Sumi, K. Sato, K. Nagaoka, Y. Kubota, and H. Kitagawa, *Discovery of Face-Centered-Cubic Ruthenium Nanoparticles: Facile Size-Controlled Synthesis Using the Chemical Reduction Method*, J. Am. Chem. Soc. **135**, 5493 (2013).

[38] L. Dubrovinsky, N. Dubrovinskaia, W. A. Crichton, A. S. Mikhaylushkin, S. I. Simak, I. A. Abrikosov, J. S. De Almeida, R. Ahuja, W. Luo, and B. Johansson, *Noblest of All Metals Is Structurally Unstable at High Pressure*, Phys. Rev. Lett. **98**, 045503 (2007).

[39] R. Briggs, F. Coppari, M. G. Gorman, R. F. Smith, S. J. Tracy, A. L. Coleman, A. Fernandez-Pañella, M. Millot, J. H. Eggert, and D. E. Fratanduono, *Measurement of Body-Centered Cubic Gold and Melting under Shock Compression*, Phys. Rev. Lett. **123**, 45701 (2019).

[40] S. M. Sharma, S. J. Turneaure, J. M. Winey, Y. Li, P. Rigg, A. Schuman, N. Sinclair, Y. Toyoda, X. Wang, N. Weir, J. Zhang, and Y. M. Gupta, *Structural Transformation and Melting in Gold Shock Compressed to 355 GPa*, Phys. Rev. Lett. **123**, 45702 (2019).

[41] D. Huo, Z. Cao, J. Li, M. Xie, J. Tao, and Y. Xia, *Seed-Mediated Growth of Au Nanospheres into Hexagonal Stars and the Emergence of a Hexagonal Close-Packed Phase*, Nano Lett. **19**, 3115 (2019).

[42] Y. Chen, Z. Fan, Z. Luo, X. Liu, Z. Lai, B. Li, Y. Zong, L. Gu, and H. Zhang, *High-Yield Synthesis of Crystal-Phase-Heterostructured 4H/Fcc Au@Pd Core–Shell Nanorods for Electrocatalytic Ethanol Oxidation*, Adv. Mater. **29**, 1701331 (2017).

[43] Q. Wang, Z. L. Zhao, C. Cai, H. Li, and M. Gu, *Ultra-Stable 4H-Gold Nanowires up to 800 °C in a Vacuum*, J. Mater. Chem. A **7**, 23812 (2019).

[44] Q. Lu, A. L. Wang, Y. Gong, W. Hao, H. Cheng, J. Chen, B. Li, N. Yang, W. Niu, J. Wang, Y. Yu, X. Zhang, Y. Chen, Z. Fan, X. J. Wu, J. Chen, J. Luo, S. Li, L. Gu, and H. Zhang, *Crystal Phase-Based Epitaxial Growth of Hybrid Noble Metal Nanostructures on 4H/Fcc Au Nanowires*, Nat. Chem. **10**, 456 (2018).

[45] W. Niu, J. Liu, J. Huang, B. Chen, Q. He, A.-L. Wang, Q. Lu, Y. Chen, Q. Yun, J. Wang, C. Li, Y. Huang, Z. Lai, Z. Fan, X.-J. Wu, and H. Zhang, *Unusual 4H-Phase Twinned Noble Metal Nanokites*, Nat. Commun. **10**, 2881 (2019).

[46] G. Mettela, M. Bhogra, U. V. Waghmare, and G. U. Kulkarni, *Ambient Stable Tetragonal and Orthorhombic Phases in Penta-Twinned Bipyramidal Au Microcrystals*, J. Am. Chem. Soc. **137**, 3024 (2015).

[47] G. Mettela, N. Mammen, J. Joardar, S. Narasimhan, and G. U. Kulkarni, *Non-Fcc Rich Au Crystallites Exhibiting Unusual Catalytic Activity*, Nano Res. **10**, 2271 (2017).

[48] G. Mettela, R. Boya, D. Singh, G. V. P. Kumar, and G. U. Kulkarni, *Highly Tapered Pentagonal Bipyramidal Au Microcrystals with High Index Faceted Corrugation: Synthesis and Optical Properties*, Sci. Rep. **3**, 1 (2013).

[49] M. Yu, N. Bovet, C. J. Satterley, S. Bengió, K. R. J. Lovelock, P. K. Milligan, R. G. Jones, D. P. Woodruff, and V. Dhanak, *True Nature of an Archetypal Self-Assembly System: Mobile Au-Thiolate Species on Au(111)*, Phys. Rev. Lett. **97**, 166102 (2006).

[50] D. Jiang, M. L. Tiago, W. Luo, and S. Dai, *The "Staple" Motif: A Key to Stability of Thiolate-Protected Gold Nanoclusters*, J. Am. Chem. Soc. **130**, 2777 (2008).

[51] M. Watari, R. A. McKendry, M. Vögtli, G. Aeppli, Y. A. Soh, X. Shi, G. Xiong, X. Huang, R. Harder, and I. K. Robinson, *Differential Stress Induced by Thiol Adsorption on Facetted Nanocrystals*, Nat. Mater. **10**, 862 (2011).

[52] Q. Li, W. Niu, X. Liu, Y. Chen, X. Wu, X. Wen, Z. Wang, H. Zhang, and Z. Quan, *Pressure-Induced Phase Engineering of Gold Nanostructures*, J. Am. Chem. Soc. **140**, 15783 (2018).

[53] J. C. Love, L. A. Estroff, J. K. Kriebel, R. G. Nuzzo, and G. M. Whitesides, *Self-Assembled Monolayers of Thiolates on Metals as a Form of Nanotechnology*, Chem. Rev. **105**, 1103 (2005).

[54] Z. Fan, X. Huang, Y. Han, M. Bosman, Q. Wang, Y. Zhu, Q. Liu, B. Li, Z. Zeng, J. Wu, W. Shi, S. Li, C. L. Gan, and H. Zhang, *Surface Modification-Induced Phase Transformation of Hexagonal Close-Packed Gold Square Sheets*, Nat. Commun. **6**, 6571 (2015).

[55] Z. Hou, N. L. Abbott, and P. Stroeve, *Electroless Gold as a Substrate for Self-Assembled Monolayers*, Langmuir **14**, 3287 (1998).

[56] G. Mettela, Y. A. Sorb, A. Shukla, C. Bellin, V. Svitlyk, M. Mezouar, C. Narayana, and G. U. Kulkarni, *Extraordinarily Stable Noncubic Structures of Au: A High-Pressure and*

-Temperature Study, Chem. Mater. **29**, 1485 (2017).

[57] P. J. Straney, N. A. Diemler, A. M. Smith, Z. E. Eddinger, M. S. Gilliam, and J. E. Millstone, *Ligand-Mediated Deposition of Noble Metals at Nanoparticle Plasmonic Hotspots*, Langmuir **34**, 1084 (2018).

[58] H. Yuan, K. P. F. Janssen, T. Franklin, G. Lu, L. Su, X. Gu, H. Uji-I, M. B. J. Roeffaers, and J. Hofkens, *Reshaping Anisotropic Gold Nanoparticles through Oxidative Etching: The Role of the Surfactant and Nanoparticle Surface Curvature*, RSC Adv. **5**, 6829 (2015).

[59] Y. Xia, Y. Xiong, B. Lim, and S. E. Skrabalak, *Shape-Controlled Synthesis of Metal Nanocrystals: Simple Chemistry Meets Complex Physics?*, Angew. Chem. Int. Ed. **48**, 60 (2009).

[60] J. Pérez-Juste, L. M. Liz-Marzán, S. Carnie, D. Y. C. Chan, and P. Mulvaney, *Electric-Field-Directed Growth of Gold Nanorods in Aqueous Surfactant Solutions*, Adv. Funct. Mater. **14**, 571 (2004).

[61] P. John Thomas, A. Lavanya, V. Sabareesh, and G. U. Kulkarni, *Self-Assembling Bilayers of Palladiumthiolates in Organic Media*, Proc. Indian Acad. Sci. (Chem. Sci.) **113**, 611 (2001).

[62] K. Soliwoda, E. Tomaszewska, B. Tkacz-Szczesna, E. Mackiewicz, M. Rosowski, A. Bald, C. Blanck, M. Schmutz, J. Novák, F. Schreiber, G. Celichowski, and J. Grobelny, *Effect of the Alkyl Chain Length of Secondary Amines on the Phase Transfer of Gold Nanoparticles from Water to Toluene*, Langmuir **30**, 6684 (2014).

[63] Z. Li, J. S. Okasinski, J. D. Almer, Y. Ren, X. Zuo, and Y. Sun, *Quantitative Determination of Fragmentation Kinetics and Thermodynamics of Colloidal Silver Nanowires by in Situ High-Energy Synchrotron X-ray Diffraction*, Nanoscale **6**, 365 (2014).

[64] B. Radha, S. Kiruthika, and G. U. Kulkarni, *Metal Anion-Alkyl Ammonium Complexes as Direct Write Precursors to Produce Nanopatterns of Metals, Nitrides, Oxides, Sulfides, and Alloys*, J. Am. Chem. Soc. **133**, 12706 (2011).

[65] T. Wen, H. Zhang, X. Tang, W. Chu, W. Liu, Y. Ji, Z. Hu, S. Hou, X. Hu, and X. Wu, *Copper Ion Assisted Reshaping and Etching of Gold Nanorods: Mechanism Studies and Applications*, J. Phys. Chem. C **117**, 25769 (2013).

[66] W. Liu, H. Zhang, T. Wen, J. Yan, S. Hou, X. Shi, Z. Hu, Y. Ji, and X. Wu, *Activation of Oxygen-Mediating Pathway Using Copper Ions: Fine-Tuning of Growth Kinetics in Gold Nanorod Overgrowth*, Langmuir **30**, 12376 (2014).

[67] T. Wen, Z. Hu, W. Liu, H. Zhang, S. Hou, X. Hu, and X. Wu, *Copper-Ion-Assisted Growth of Gold Nanorods in Seed-Mediated Growth: Significant Narrowing of Size Distribution via Tailoring Reactivity of Seeds*, Langmuir **28**, 17517 (2012).

[68] T. S. Sreeprasad, A. K. Samal, and T. Pradeep, *Body- or Tip-Controlled Reactivity of Gold Nanorods and Their Conversion to Particles through Other Anisotropic Structures*, Langmuir **23**, 9463 (2007).

[69] T. S. Sreeprasad, A. K. Samal, and T. Pradeep, *Reactivity and Resizing of Gold Nanorods in Presence of Cu2+*, Bull. Mater. Sci. **31**, 219 (2008).

[70] D. H. Lim, S. Aboud, and J. Wilcox, *Investigation of Adsorption Behavior of Mercury on Au(111) from First Principles*, Environ. Sci. Technol. **46**, 7260 (2012).

[71] J. Rodríguez-Fernández, J. Pérez-Juste, P. Mulvaney, and L. M. Liz-Marzán, *Spatially-Directed Oxidation of Gold Nanoparticles by Au(III)-CTAB Complexes*, J. Phys. Chem. B **109**, 14257 (2005).

[72] B. P. Khanal and E. R. Zubarev, *Chemical Transformation of Nanorods to Nanowires: Reversible Growth and Dissolution of Anisotropic Gold Nanostructures*, ACS Nano **13**, 2370 (2019).

[73] P. J. G. Goulet, A. Leonardi, and R. B. Lennox, *Oxidation of Gold Nanoparticles by Au(III) Complexes in Toluene*, J. Phys. Chem. C **116**, 14096 (2012).

[74] B. Radha, M. Arif, R. Datta, T. K. Kundu, and G. U. Kulkarni, *Movable Au Microplates as Fluorescence Enhancing Substrates for Live Cells*, Nano Res. **3**, 738 (2010).

[75] B. Radha and G. U. Kulkarni, *Giant Single Crystalline Au Microplates*, Curr. Sci. **102**, 70 (2012).

[76] B. Radha and G. U. Kulkarni, *A Real Time Microscopy Study of the Growth of Giant Au Microplates*, Cryst. Growth Des. **11**, 320 (2011).

[77] G. U. Kulkarni, G. Mettela, and S. Kiruthika, *Synthesis of Nano- and Microcrystallites of Metals Using Metal-Organic Precursors*, in *Molecular Materials: Preparation, Characterization, and Applications* (2017), pp. 213–237.

[78] Y. J. Lee, N. B. Schade, L. Sun, J. A. Fan, D. R. Bae, M. M. Mariscal, G. Lee, F. Capasso, S. Sacanna, V. N. Manoharan, and G. R. Yi, *Ultrasmooth, Highly Spherical Monocrystalline Gold Particles for Precision Plasmonics*, ACS Nano **7**, 11064 (2013).

[79] B. P. Khanal and E. R. Zubarev, *Purification of High Aspect Ratio Gold Nanorods: Complete Removal of Platelets*, J. Am. Chem. Soc. **130**, 12634 (2008).

[80] O. S. Ivanova and F. P. Zamborini, *Electrochemical Size Discrimination of Gold Nanoparticles Attached to Glass/Indium-Tin-Oxide Electrodes by Oxidation in Bromide-Containing Electrolyte*, Anal. Chem. **82**, 5844 (2010).

[81] G. Mettela and G. U. Kulkarni, *Site Selective Cu Deposition on Au Microcrystallites: Corners, Edges versus Planar Surfaces*, CrystEngComm **17**, 9459 (2015).

*   *   *

Chemical Stability and Reactivity of the non-Cubic Au Microcrystallites[*]

Summary

Well known to chemists and metallurgists, the nobility of Au is challenged by reagents such as aqua regia, which dissolve Au to form salt solutions. Among metals, Hg blends with Au to form amalgam, otherwise transition metals such as Cu, tend to interact with Au surfaces in electrochemical media. In this chapter, an experimental investigation of the stability of Au microcrystallites bearing unconventional crystal lattices is reported. The results show that non-cubic Au exhibits enhanced stability towards Hg and aqua regia and practically no interaction with Cu during electroless plating. This unconventional Au is undoubtedly nobler.

VIII.1 Introduction

For ages, bulk Au has been treasured for its brilliant unfading yellow luster [1]. Chemically, Au is known for its extraordinary oxidation resistance making it a standard protecting material in a variety of applications from household jewellery to satellite parts [2]. The surface stability of Au has been the subject matter of numerous experimental and theoretical studies in the last few decades [3,4]. Strangely, reagents such as Hg [5], CN⁻ [6], and aqua regia [7] are well known for their reactivities with Au. Various mechanisms have also been proposed for the dissolution of Au in such media [7–9]. Although noble, Au is known to exhibit a strong affinity towards other transition metals in general (Ag, Pd, Pt, Cu *etc.*) under galvanic conditions. Growth of metals on various crystallographic surfaces of Au is often studied in order to understand the relation between the substrate and the epi-layer [10,11]. For instance, despite high lattice difference (11.4%), Cu can grow epitaxially on Au surfaces [12] due to high Au−Cu bond strength favoring underpotential deposition (UPD) [10,13].

The above discussion pertains to bulk Au which is stable in fcc crystal structure. Importantly, it retains its fcc lattice even at high temperatures and pressures [14]. It has been a daunting difficulty to crystallize bulk Au in unconventional crystal lattices. Rarely, Au crystallizes in unconventional lattices at high temperatures and pressures, also under certain synthetic conditions [14,15]. Hitherto, the catalytic activity of fcc Au is known only in the

form of nanocrystallites and clusters [16,17]. Like bulk Au, these nanoparticles readily react with Hg [16] and aqua regia [18].

VIII.2 Scope of the Investigation

The bc(o,t) crystallites exhibit unprecedented stability under harsh physical and chemical conditions as reported in **Chapters V−VII**. Extraordinary chemical and physical stabilities of Au pertaining to the non-reactivity in most of the harsh chemical environments and retention of the fcc crystal structure under very high-temperatures and -pressures crown Au to be the noblest of all metals. However, the traditional Au reacts with Hg, aqua regia, CN⁻ and transition metals. Hitherto, crystal structure dependent reactivity of Au is not known. A knowledge of the reactivity of Au with different crystal structures in these harsh chemicals will be interesting. The chapter deals with the effect of Hg, aqua regia and transition metals on fcc and bc(o,t) Au crystallites, which are harsh to fcc Au.

VIII.3 Experimental Details

Chemicals. Copper sulphate pentahydrate ($CuSO_4. 5H_2O$, 99.5%), sodium potassium tartrate ($KNaC_4H_4O_6 \cdot 4H_2O$, 99%), sodium hydroxide (NaOH, 98%), formaldehyde solution (HCHO, 37.2 wt%) and mercury (Hg) purchased from SD Fine Chemicals, India. All reagents and solvents were used as received without further purification. Double-distilled water was used throughout this investigation.

Cu electroless deposition. Copper plating solution is a mixture of solution A and B. Solution A was prepared by dissolving 3g of $CuSO_4$, 14 g of sodium potassium tartrate and 4 g of NaOH in 100 mL of distilled water. Aqueous solution of formaldehyde (37.2 wt%) is solution B. 5 mL of solution A and 1 mL of solution B were mixed for Cu electroless deposition. Au microcrystallites comprised of different crystals structures (fcc and bc(o,t)) were dipped in plating solution. The process was halted at different times by taking out the sample from the solution and then washed with water, ethanol and finally dried under N_2 gas.

VIII.4 Results and Discussion

As detailed in the earlier studies from the group, the Au crystallites prepared at 135 and 220 °C exhibit fcc and bc(o,t) crystal structures, respectively (**Figure VIII.1**) [19–21]. From the elemental analysis, the fcc and bc(o,t) crystallites are found to be of Au only, free of capping agents (**Figure VIII.2**). SEM analysis has revealed that the major product, irrespective

of the synthetic temperature, is the penta-twinned bipyramid (see **Figure VIII.1**). Briefly, the crystallites comprising the fcc phase (135 °C synthesis) show sharp and symmetric peaks in the XRD pattern (see **Figure VIII.1**a) with fcc(002) reflection relatively more pronounced due to preferred orientation of the corresponding facet [21]. Contrary to fcc, the bc(o,t) crystallites exhibit broad, asymmetric as well as split peaks related to bc(o,t) phases as shown in **Figure VIII.1**e. These occur as shoulders to fcc(111) and well separated peaks from fcc(002). The bipyramids prepared at 135 °C (fcc) are typically longer. The crystallite shown in SEM image in **Figure VIII.3**a measured ~ 17 µm along the length with central diameter of ~ 1.5 µm tapering into penta-twinned tips of diameter ~ 50 nm. The surface is seen highly corrugated enclosed by facets of high miller indices (**Figure VIII.1**c). Contrary to fcc, the Au crystallites prepared at 220 °C (predominantly bc(o,t)) are much shorter (~ 2.2 µm, **Figure VIII.3**f) but do host similar surface corrugations (also see **Figure VIII.1**g).
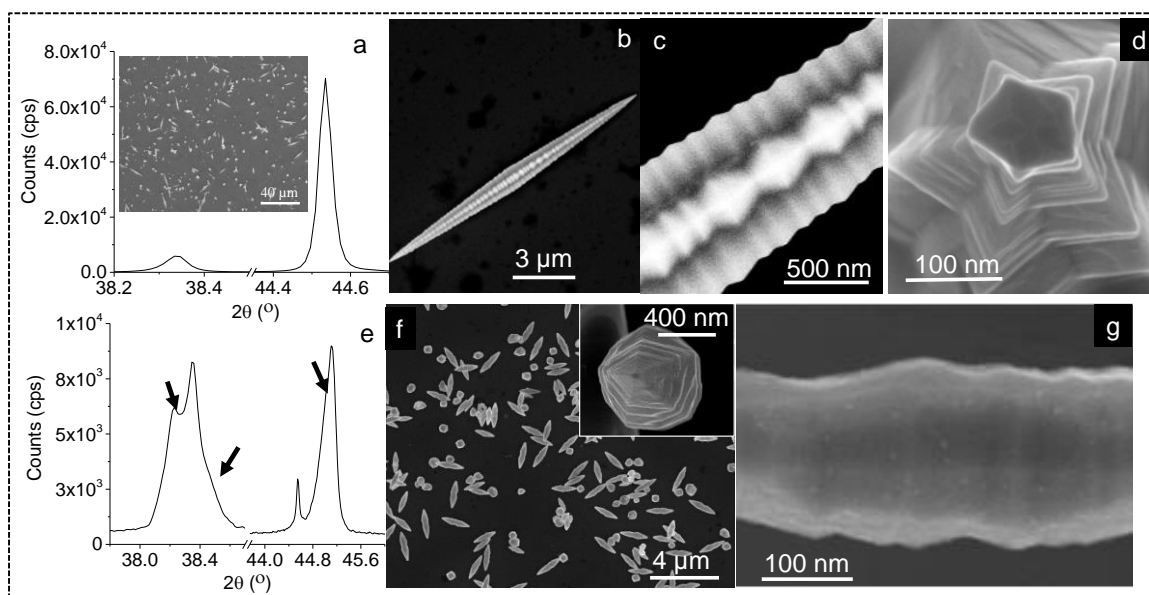
Figure VIII.1. (a,e) XRD patterns and (b−d and f,g) SEM images of fcc and bc(o,t) Au bipyramids. Arrow marks indicate the peaks corresponding to bc(o,t) phase. Inset in (a) is a low magnified SEM image of fcc Au crystallites.

VIII.4.A Electroless Deposition of Cu

Here, Cu growth on bc(o,t) Au crystallites was chosen to monitor from electroless plating, while using fcc Au as reference by following a previous report from the laboratory [12]. In spite of higher lattice mismatch between fcc Au and Cu, rapid growth of Cu on the fcc crystallites was noticed due to the underpotential deposition and strong binding

energy of Cu-Au [10,13]. The electroless deposition in presence of Au catalyst can be written by the following equation.

$$HCHO + OH^- \rightarrow HCOO^- + \frac{1}{2} H_2 + 2e^- \qquad (1)$$

$$Cu(II) + 2e^- \rightarrow Cu(0) \qquad (2)$$
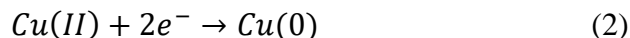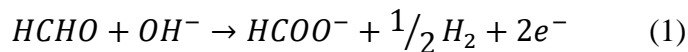
For Cu electroless deposition, the as-prepared Au crystallites were immersed in a Cu-plating solution for 10 min. As expected, the microcrystallites bearing fcc lattice got coated with Cu all over the surface. Microscopy images and the associated elemental analysis (see **Figure VIII.3**b–d) revealed hexagonally shaped Cu outgrowths so conspicuous that the overall size increased noticeably (also see **Figure VIII.4**). Such hexagonal growth has commonly been observed on various Au surfaces [12,23]. In case of bc(o,t) bipyramids on the other hand, the Cu deposition took place only at the tips, in the form of thin flakes (**Figure VIII.3**f–i). The elemental line profile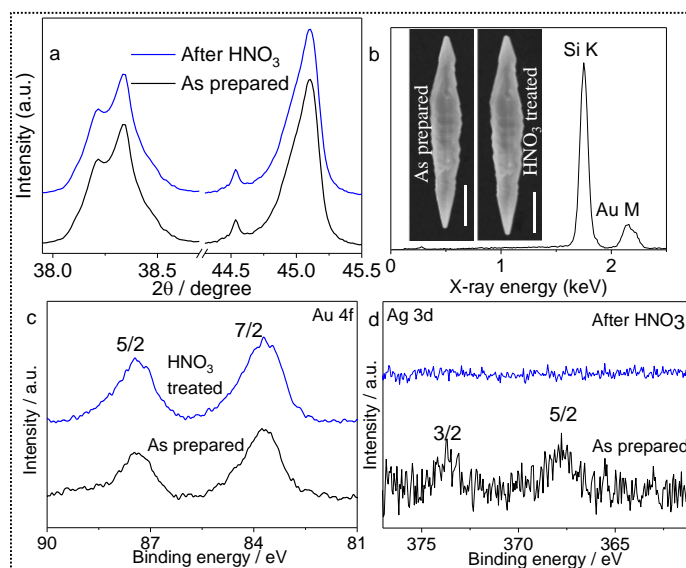 showed clearly that there is no measurable trace of Cu on the central portion of the bc(o,t) bipyramids (**Figure VIII.3**j,k), but the Cu signal at the tips is visible above the noise level in the EDX map (**Figure VIII.3**h). Obviously, this minimal Cu plating was not enough to cause any detectable changes in the XRD pattern of the bc(o,t) bipyramids (**Figure VIII.3**l).

Figure VIII.2. (a) XRD patterns collected from Au bipyramids before and after HNO₃ treatment. (b) EDX spectrum collected from bc(o,t) Au bipyramids. (c,d) XPS spectra for Au 4f and Ag 3d levels collected from pristine and HNO₃ treated Au bipyramids. Inset in (b) shows the SEM images of Au bipyramids before and after HNO₃ treatment. Scale bar, 500 nm.
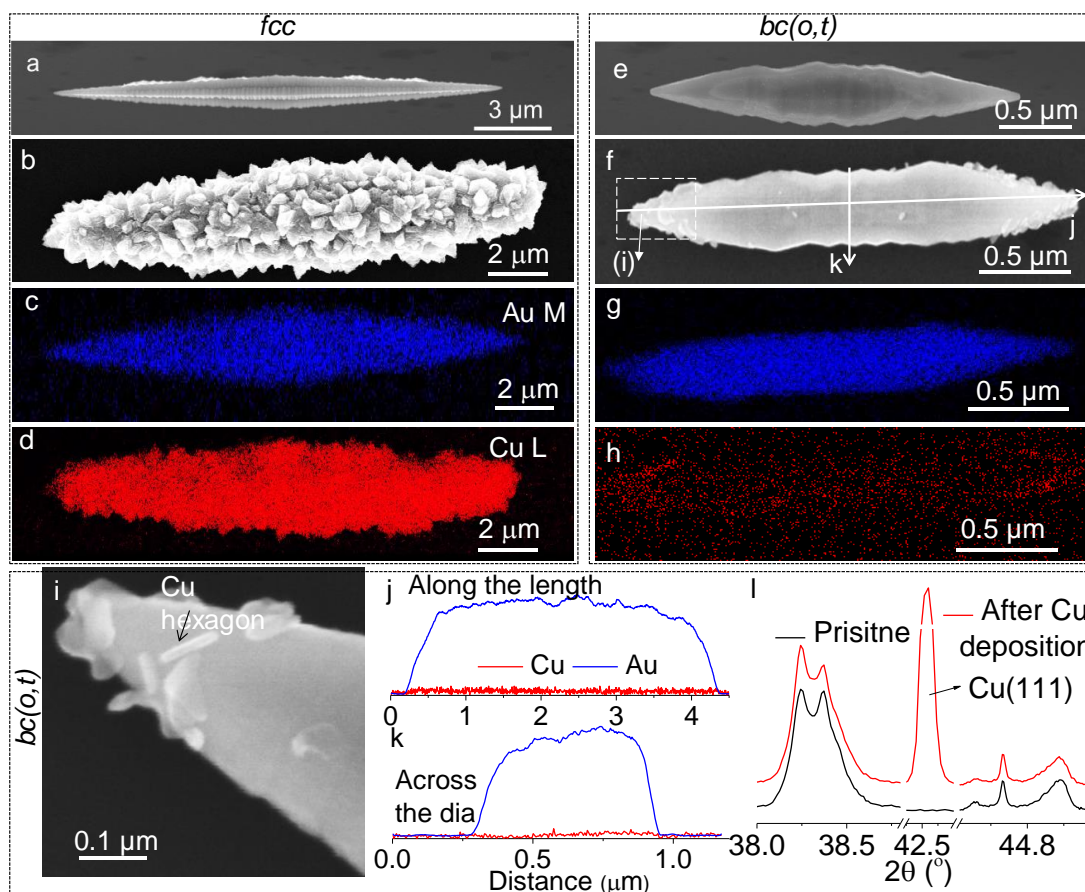
Figure VIII.3. (a,e) SEM images of uncoated typical fcc and bc(o,t) Au bipyramids. SEM images and elemental maps following Cu plating on fcc (b–d) and bc(o,t) Au (f–h) bipyramids, respectively. (i) A high magnification image of the tip region (dashed square) indicated in (f). (j,k) EDX intensity profiles of Cu and Au along the length (top) and across the diameter of the crystallite shown in (f). A common arbitrary intensity scale has been used. (l) XRD patterns collected from Au microcrystallites before and after Cu plating for 10 min.

Cu growth on fcc Au microcrystallites was monitored by halting the process at different times of plating (**Figure VIII.5**). The SEM image reveals that Cu nanoislands of ~ 40 nm were formed on the Au bipyramids after 3 min of plating which grew to ~ 300 nm in 6 min to finally form a Cu film beyond 10 min (**Figure VIII.5**a–d), regardless of size of the fcc bipyramids (see **Figure VIII.6**). On bc(o,t) bipyramids, there is no detectable Cu plating on the central portion of the bipyramids even after 45 min, while the size of the Cu islands at the tips increased to few hundreds of nm (**Figure VIII.5**e–k). This was the case irrespective of the size of the bc(o,t) bipyramid (**Figure VIII.7**).   Back-scattered-electron (BSE) images also reveal
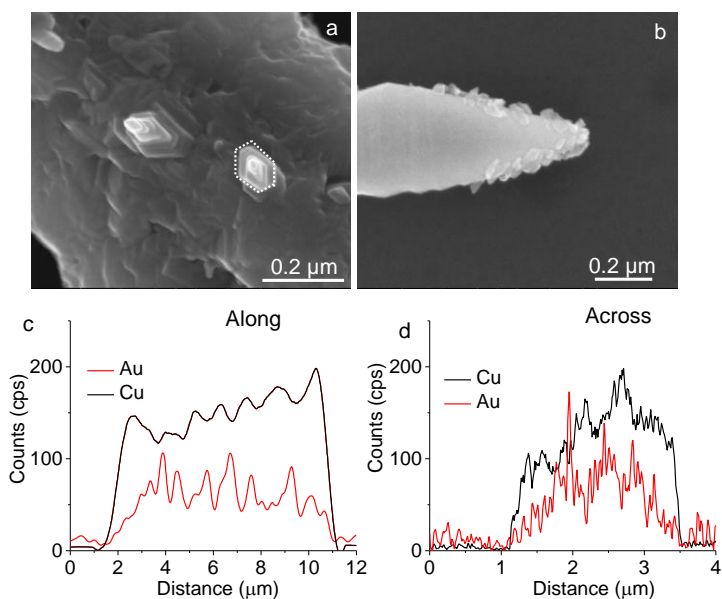
Figure VIII.4. SEM images of magnified portions of (a) fcc and (b) bc(o,t) bipyramids after Cu deposition. (c,d) EDX line profiles along and across the fcc Au bipyramid.
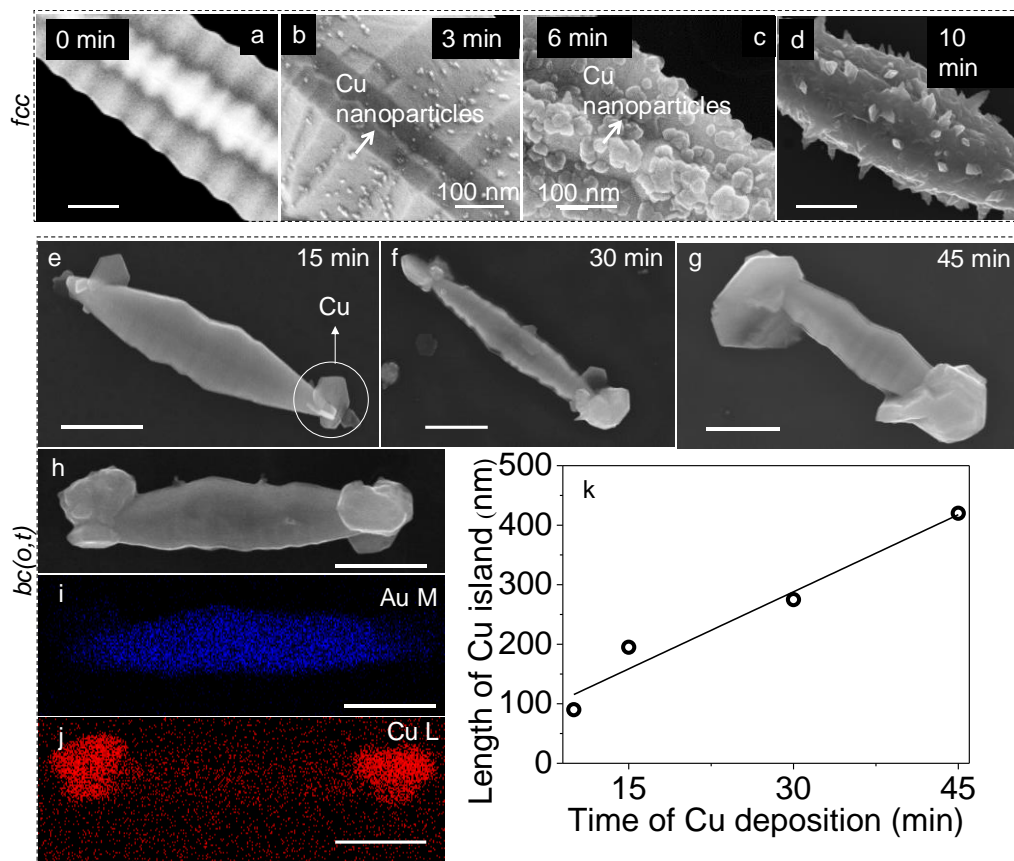
Figure VIII.5. SEM images of fcc (a–d) and bc(o,t) Au bipyramids (e–g) after different times of Cu electroless plating. (h–j) SEM image and elemental maps of bc(o,t) Au bipyramid after 30 min of Cu

electroless plating. (k) Average length (along the bipyramid length) of the Cu cap as a function of electroless deposition time. Scale bar where not mentioned is 500 nm.

the selective plating of Cu on tips of the bipyramids (**Figure VIII.8**). The deposition of Cu on the fcc crystallites is similar to the previous observations drawn by the group [12]. Interestingly, Cu deposition did not occur on the bc(o,t) Au surfaces, although the latter has similar lattice mismatch with Cu as do fcc surfaces. The calculated lattice mismatches of bct Au with respect to Cu along the *a(b)* and *c*-axes are 13.5% and 11.89%, while the lattice mismatches of bco Au along the *a*, *b* and *c*-axes are 13.9%, 12.9% and 11.4% respectively. Thus, the lattice mismatch of bct and bco cells are ~ 2% higher along the *a* and *b* axes. This compares with the value observed in the case of Ni-Au system (~ 13.6%), which however does not seem to hinder epitaxial growth of Ni on fcc Au [22]. Thus, the lattice mismatch alone cannot explain the unfavoured growth of Cu on bc(o,t) Au surfaces. This anisotropic deposition of Cu is similar to the selective deposition of Pt on the bc(o,t) crystallites in section **VII.4.D** in **Chapter VII.** In contrast to the PtToABr treatment at 220 °C (with high rate of phase transformation), here, the selective deposition of Cu on the fcc rich tips in the bc(o,t) microcrystallites occurs at room temperature.
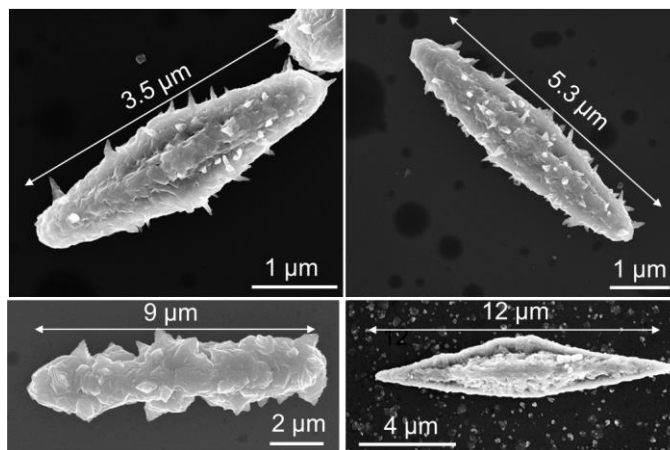
Figure VIII.6. SEM images of fcc Au bipyramids with variable sizes after Cu plating for 10 min.

VIII.4.B Treatment with Hg

Encouraged by the striking behavior (in Cu electroplating medium), the stability of bc(o,t) Au microcrystallites was investigated under the known corrosive reagent, Hg, while constantly comparing with fcc crystallites. Here, the fcc Au was prepared in different forms, as films (*via* electroless deposition) and anisotropic particles (triangles, hexagons *etc.*). Both

the fcc and bc(o,t) microcrystallites were separately immersed in 20 grams of Hg and taken out at different times to study the morphological changes (**Figure VIII.9**). The fcc bipyramids treated for 3 min appear highly deformed as the corrugated surfaces got dissolved away in Hg (**Figure VIII.9**a,b), the residuals showing the presence of Hg along with Au (**Figure VIII.9**e–g). Indeed, the amalgamation process is so effective that since long it is widely used for Au extraction from ores [22]. After 6 min of Hg treatment (**Figure VIII.9**c), the residuals were reduced to sub-micrometer sizes and after 10 min, they simply disappeared (**Figure VIII.9**d) as also evident from the XRD data in **Figure VIII.9**h. Indeed, fcc Au microcrystallites of different sizes (micron and submicron) and various polygonal shapes as well as thin films have been similarly tried out (**Figures VIII.10–VIII.13**). The bc(o,t) bipyramids were also subjected to a similar treatment. Interestingly, no morphological changes were noticed even after 27 hours of Hg contact (**Figures VIII.9**i–l and **VIII.10–VIII.13**), and accordingly, no significant changes were seen in the XRD pattern (**Figure VIII.9**m). To make a reliable comparison, a mixture of fcc and bc(o,t) microcrystallites was placed alongside on a substrate and treated with Hg simultaneously (**Figure VIII.9**n–q). During the Hg treatment, the fcc crystallites were dissolved selectively while the bc(o,t) bipyramids were found to be intact, bringing out the extraordinary stability of bc(o,t) Au in Hg environment.
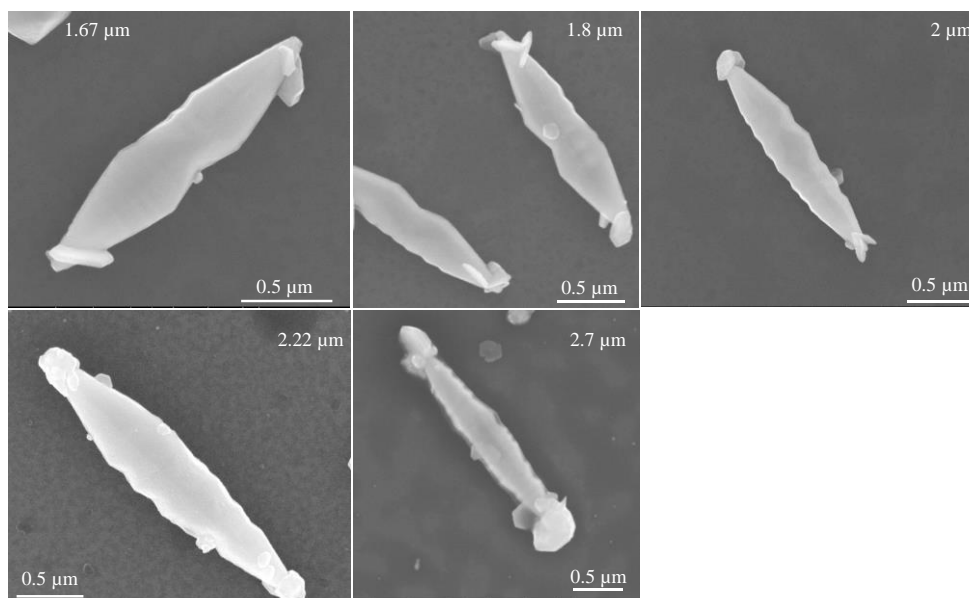
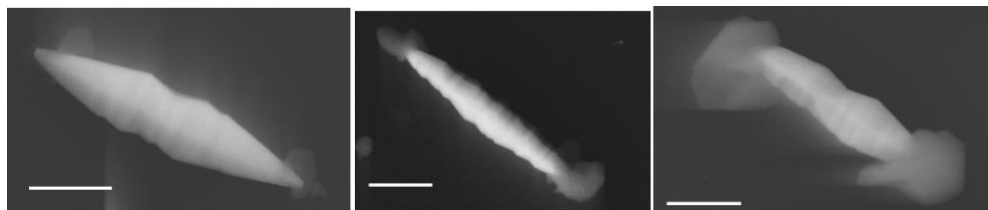**Figure VIII.7.** SEM images of bc(o,t) Au bipyramids with variable sizes after Cu plating for 10 min.

Figure VIII.8. Back-scattered-electron (BSE) images of Au/Cu bipyramids prepared from 15, 30 and 45 min of Cu electroless plating. Scale bar, 500 nm.
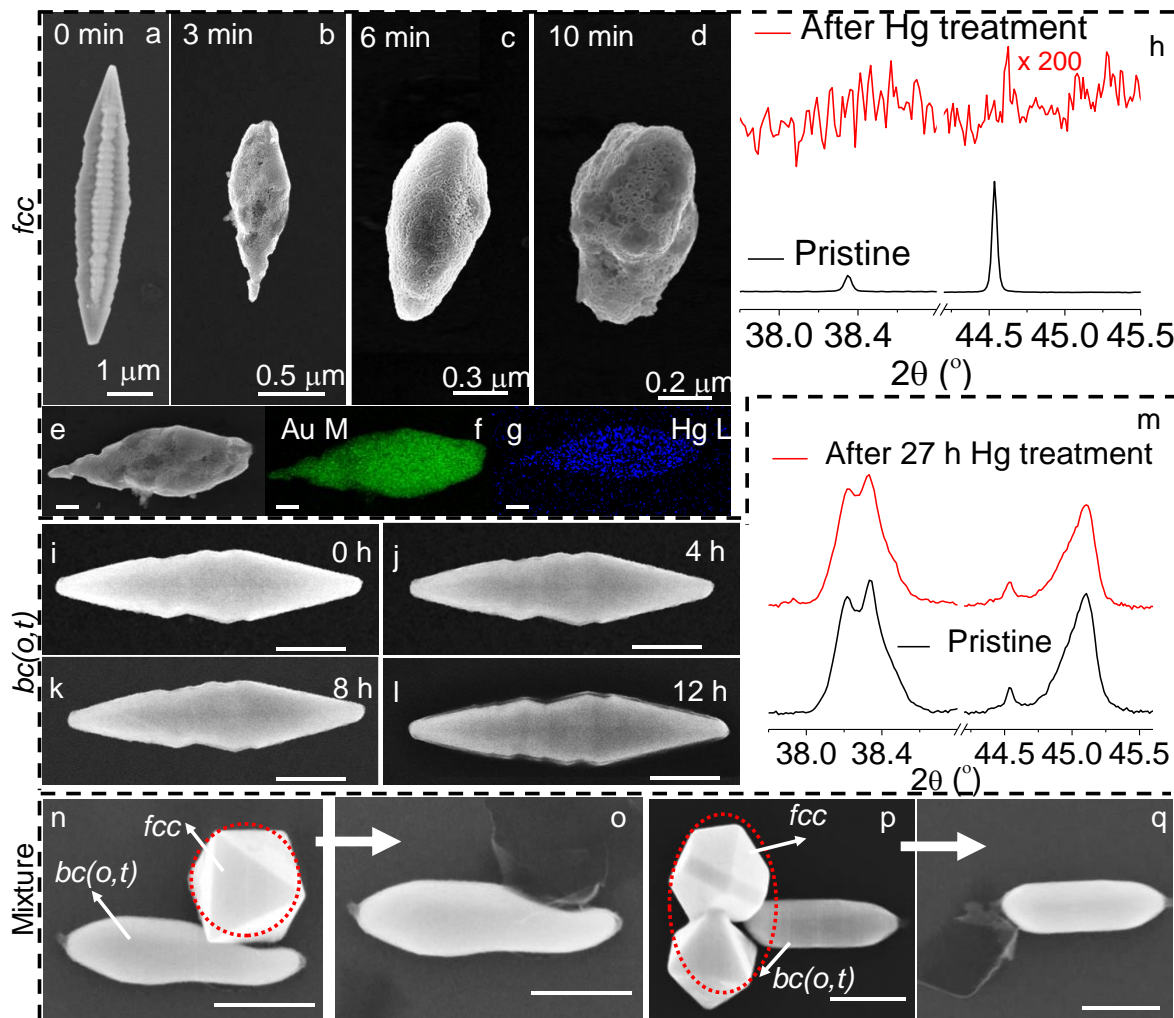
Figure VIII.9. SEM images of fcc Au bipyramids before (a) and after (b−d) Hg treatment. (e) SEM image of fcc Au bipyramid after Hg treatment. (f,g) Elemental mapping of Au M and Hg L energy levels. (h) XRD patterns collected from fcc Au crystallites before and after Hg treatment (i−l) SEM images of bc(o,t) Au bipyramids after Hg treatment. (m) XRD patterns collected from bc(o,t) bipyramids before and after Hg treatment. Mixture of fcc and bc(o,t) Au bipyramids before (n,p) and after Hg treatment (o,q). Scale bar, 500 nm.
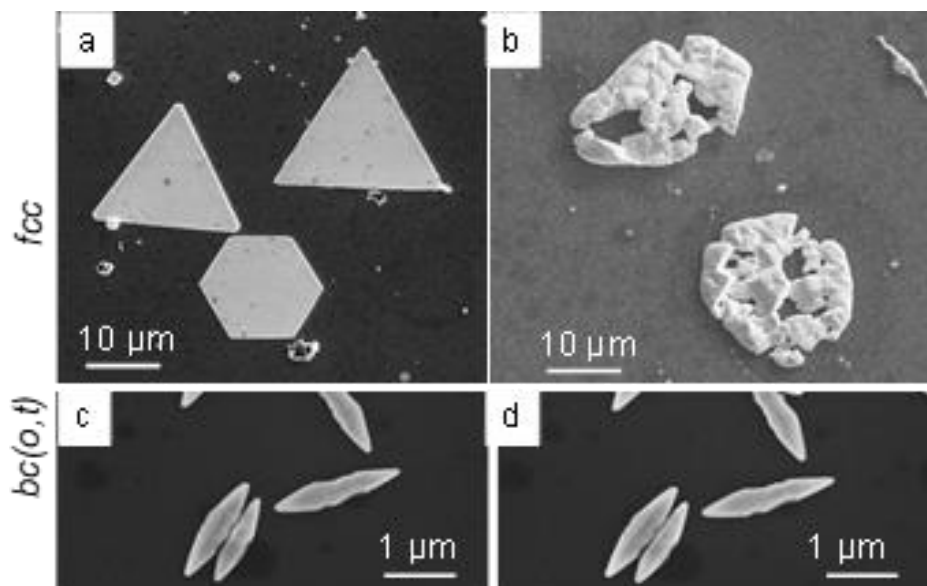
Figure VIII.10. (a,b) SEM images of fcc Au plates before and after Hg treatment. (c,d) SEM images of bc(o,t) Au bipyramids before and after Hg treatment.
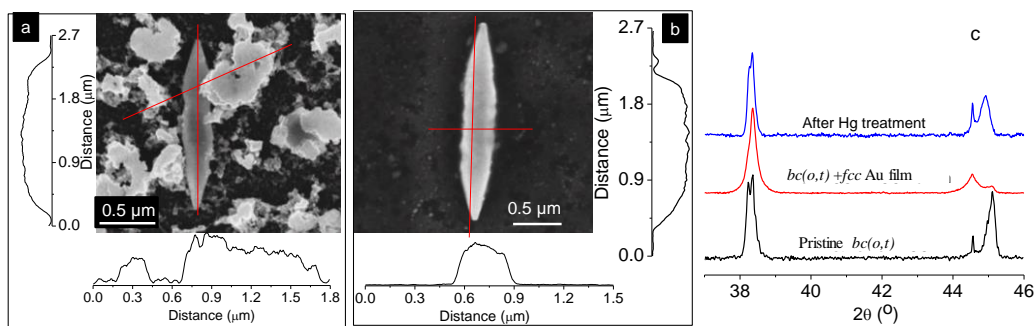
Figure VIII.11. (a,b) SEM images of bc(o,t) Au bipyramid with fcc film; before and after Hg treatment. (c) XRD patterns collected from mixture of fcc and bc(o,t) Au before and after Hg treatment.
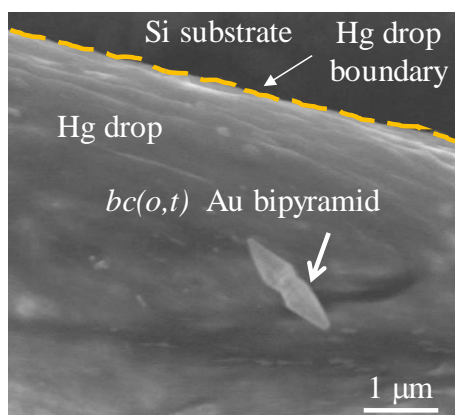
Figure VIII.12. SEM image of a bc(o,t) Au bipyramid floating on Hg drop.
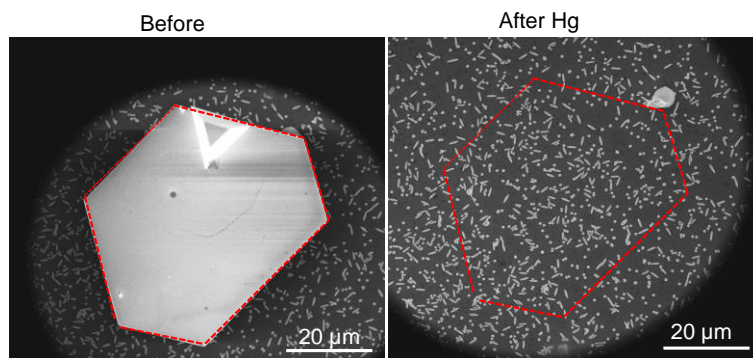
Figure VIII.13. SEM images of fcc and bc(o,t) mixture before and after Hg treatment. Prior to Hg treatment, hexagonal and triangular crystallites exhibited smooth surfaces over large areas. As expected, these fcc polygons were damaged under Hg environment.

VIII.4.C Treatment with Aqua regia

Aqua regia is another well-known reagent to dissolve Au. Although independently incapable, the NO_3^- and Cl^- combination works well, with the former oxidizing metal atoms and leading further to the formation of $AuCl_4^-$ complex. The fcc bipyramids dissolved gradually in aqua regia solution (mixture of HNO_3 and HCl in 1:3 molar ratio, 10% v/v in water), and disappeared after 1 h treatment. **Figure VIII.14**a–c shows the intermediate stages during the fcc Au dissolution. The fcc reflections in the XRD pattern disappeared after 70 min of treatment. A similar trend is noticed with the fcc Au films (**Figure VIII.15**). On the other hand, trivial morphological changes (evident from the SEM images) have been noticed in the bc(o,t) Au crystallites under these conditions (**Figure VIII.14**d,e). For ready comparison, a mixture of fcc and bc(o,t) Au crystals were placed on a given substrate and treated together with aqua regia. Similar to the observations made in respect of Hg, the fcc crystallites got dissolved while the bc(o,t) bipyramids were undamaged (**Figure VIII.14**f,g and **VIII.16**). However, the bc(o,t) Au dissolves much faster in high concentrations of aqua regia (**Figure VIII.17**). For a constant aqua regia concentration, the amount of Au decreases exponentially as a function of time for both fcc and bc(o,t) phases, indicating a first order reaction kinetics (**Figure VIII.14**h)

$$A = A_0 e^{-kt} \hspace{3cm} (3)$$

where A_0 and A represent pristine and residual Au at time t with rate constant k, respectively. The calculated values of the dissolution rate constant of fcc and bc(o,t) Au are 20×10^{-4} and 2×10^{-4} s^{-1}, respectively (inset, **Figure VIII.14**h), at 10% v/v aqua regia concentration. The

bc(o,t) Au exhibits a dissolution rate constant nearly one order lower is indeed striking. At lower concentrations of aqua regia, the rate constant is even lower (see inset of **Figure VIII.14**h).
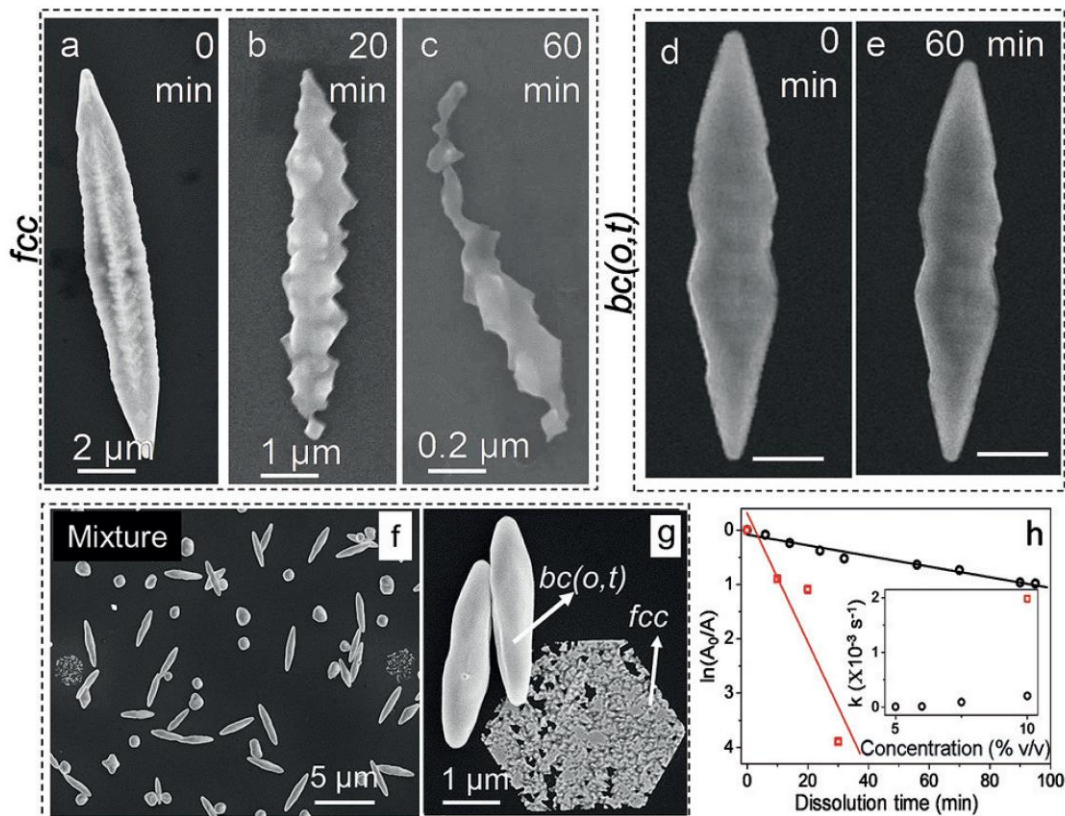
Figure VIII.14. SEM images of fcc (a–c), bc(o,t) (d,e) and mixture of fcc and bc(o,t) Au (f,g) after treatment with aqua regia for various times. Scale bar, 1 μm. (h) Aqua-regia treatment on 80 nm fcc electroless film (red squares) and bc(o,t) Au microcrystallites (black circles). Variation in ln(A$_0$/A) with dissolution time for fcc and bc(o,t) Au microcrystallites at 10% v/v aqua regia concentration. Inset shows the variation in the rate constant with aqua regia concentration (% v/v).

Thus, the effect of aqua regia in the morphology of the crystallite was carefully studied by SEM at different time intervals. The dissolution is throughout the body of the fcc plates and bipyramids (see **Figures VIII.14**a–c and **VIII.16**). In case of bc(o,t) crystallites, at an interval of ~ 618 min (in 5% v/v aqua regia) the bipyramids exhibit reduction in the length while the width is unaltered, *i.e.*, the selective dissolution of the tips as shown in **Figure VIII.18**a. This observation can be correlated with the spatial distribution of the lattices as discussed in **Chapter IV**, *i.e.*, the selective dissolution of the fcc rich tips while retaining the bc(o,t) rich core from being affected. With the progress of the reaction, the dissolution is mainly in one

direction, longitudinal direction, leading to the reduction in aspect ratio. The bc(o,t) bipyramids also consist of sharp tips and high-index nanofacets which are much similar to the fcc bipyramids. Thus, in case the dissolution was curvature dependent, then the higher curvature regions should have also experienced the dissolution. However, the bare dissolution at the high index facets implies the selective nature of the dissolution towards fcc lattice.
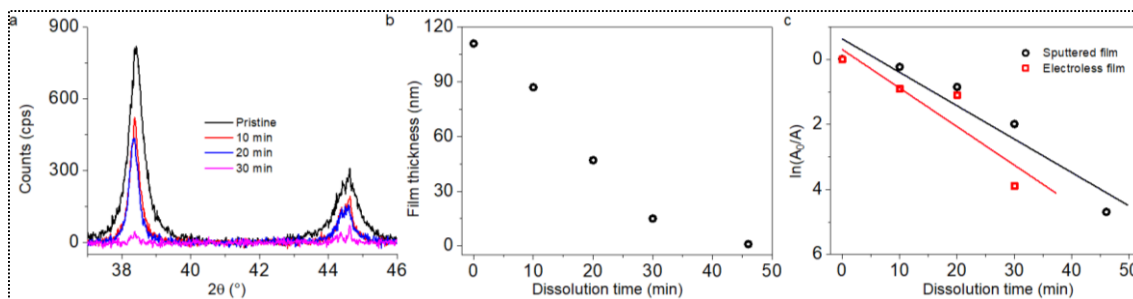
Figure VIII.15. (a) Time dependent changes in XRD patterns with aqua regia (10% v/v) treatment for electrolessly grown 80 nm thick film. With the treatment time, the dissolution of Au film occurs which leads to changes in the total area under the XRD peaks. (b) Treatment of 10% v/v aqua regia on sputtered 110 nm fcc Au film and corresponding changes in the thickness of the film monitored by using Dektak surface profilometer. (c) Variation in $\ln(A_0/A)$ with dissolution time for fcc film (by sputtered and electrolessly grown), which can be fitted to first order reaction kinetics.
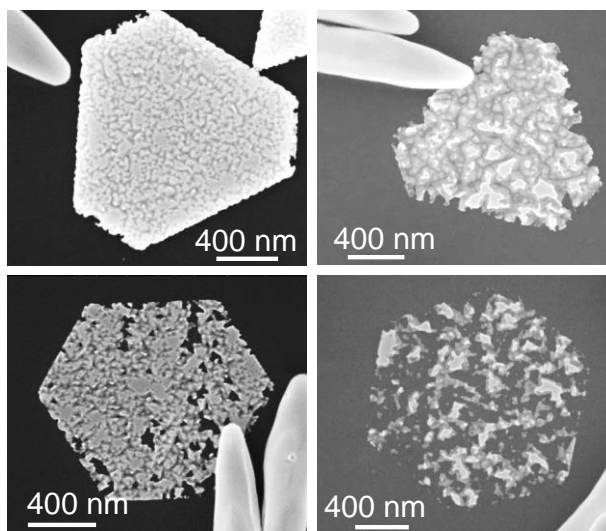
Figure VIII.16. SEM images of etched fcc Au polygons after aqua regia treatment.

The time dependent XRD patterns of the aqua regia treated bc(o,t) crystallites exhibit a noticeable shift in the (002) region, towards the $(002)_f$, *i.e.*, expansion along the *c*-direction (see **Figure VIII.18**b). The emerged peak can be assigned to $(002)_{T-I}$ with the new phase, bct-

I. A similar observation was seen during thermal annealing of the crystallite (see **Figure VI.15** and **VI.16** in **Chapter VI**). With the progress of the reaction, the position of the emerging peak distributes along with enlarged broadening (see **Figures VIII.19** and **VIII.20**), similar to the thermal annealing at ~ 500-700 °C. Thus, in addition to the fcc and bc(o,t) phases, series of bct-I phases can be accommodated, representing the broadening in the XRD pattern. The intensity of the phases alters and finally reaches to fcc. The dissolution could have been occurred through two possibilities: (a) a direct formation of bc(o,t) Au to $AuCl_4^-$ or (b) *via* phase transformation to fcc and the followed by formation of $AuCl_4^-$. Here, the latter process prevails, which can be confirmed by the presence of the series of bct-I phases which are the direction towards fcc and thereby, the dissolution (see **Figures VIII.19** and **VIII.20**).
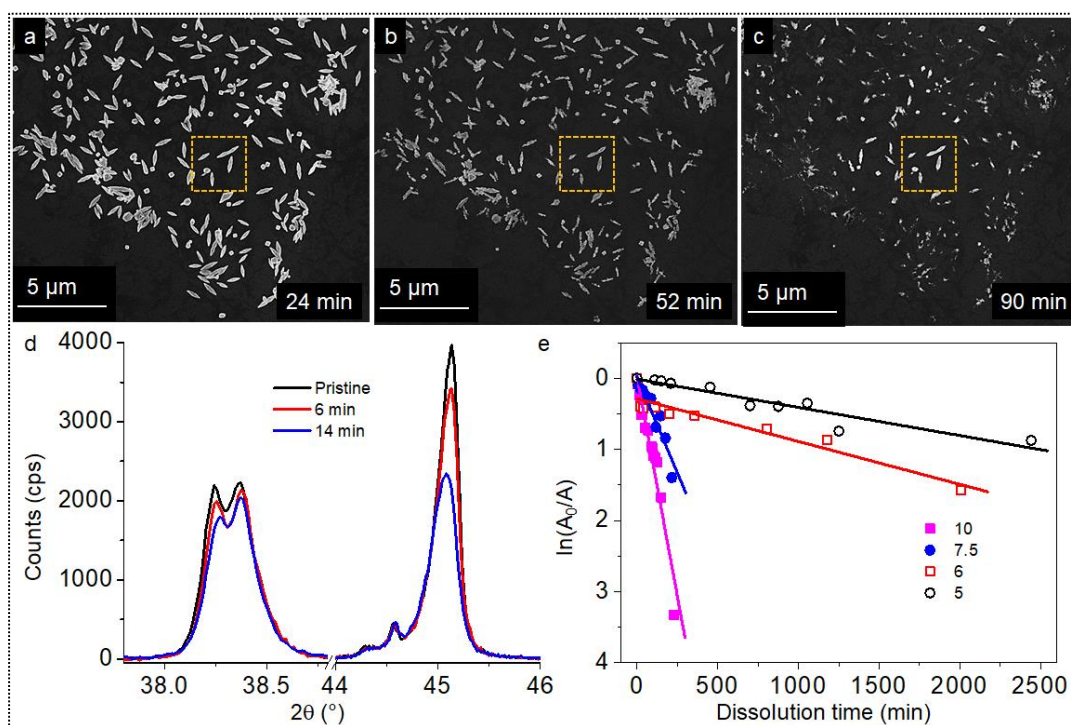
Figure VIII.17. (a–c) SEM images of the time dependent aqua regia (10% v/v) treatment on bc(o,t) Au microcrystallites. The same sample area has been examined after every treatment. There was no visible particle movement or loss due to treatment and observed no physical movement of particles, where the reference microcrystallites are marked by yellow dotted box. (d) Time dependent aqua regia treatment on bc(o,t) Au microcrystallites and the corresponding changes in XRD patterns (for 10% v/v aqua regia treatment). With increasing treatment time, the area under the XRD peak decreased due to the dissolution of Au microcrystallites which has been monitored and plotted for the rate constant calculation. (e) Variation in the $\ln(A_0/A)$ has been plotted with dissolution time for different

concentrations of aqua regia. With time, the $\ln(A_0/A)$ decreases following a linear behavior which can be fitted to first order reaction kinetics. The value of the rate constant was calculated from the slope. With increasing aqua regia concentration, the dissolution is much faster.
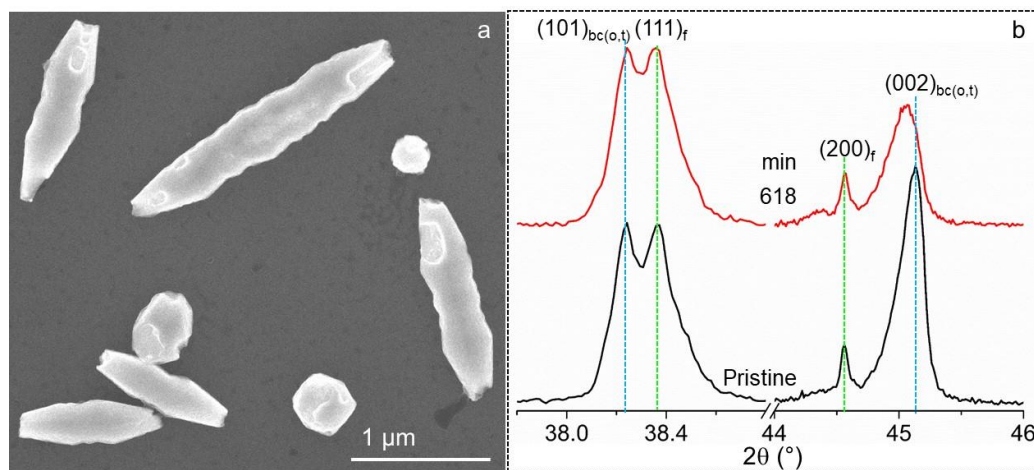
Figure VIII.18. (a) SEM image and (b) XRD pattern of the bc(o,t) microcrystallites after 5% v/v aqua regia treatment.
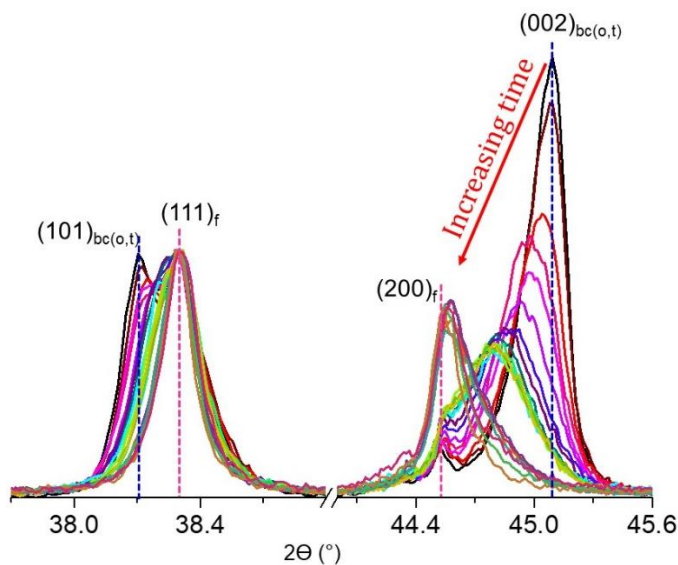
Figure VIII.19. Time dependent XRD pattern of the aqua regia (10% v/v) treated Au microcrystallites.

The SEM images and the XRD patterns exhibit a beautiful correlation pertaining to the bct-I phase, briefly, the dissolution at the tips results in the first recording of bct-I by XRD, as shown in **Figure VIII.18**b (also see **Figure VIII.21**). The dissolution of the fcc rich tips exposes the bc(o,t) core in the aqua regia medium which drives the phase transformation from the exposed bc(o,t) to bct-I. The bc(o,t) core prefers to phase transform to fcc and followed by dissolution in presence of aqua regia. In the prolonged exposure, the existence of series of

bct-I phases and the reduced size of the crystallite further validate that the phase transformation is the path to cause dissolution. The dissolution of the bc(o,t) lattices is well-controlled (in lower concentration) due to the presence of limiting step, the phase transformation which systematically allows to monitor the changes in aspect ratio as well as crystal structure (see **Figure VIII.22**).
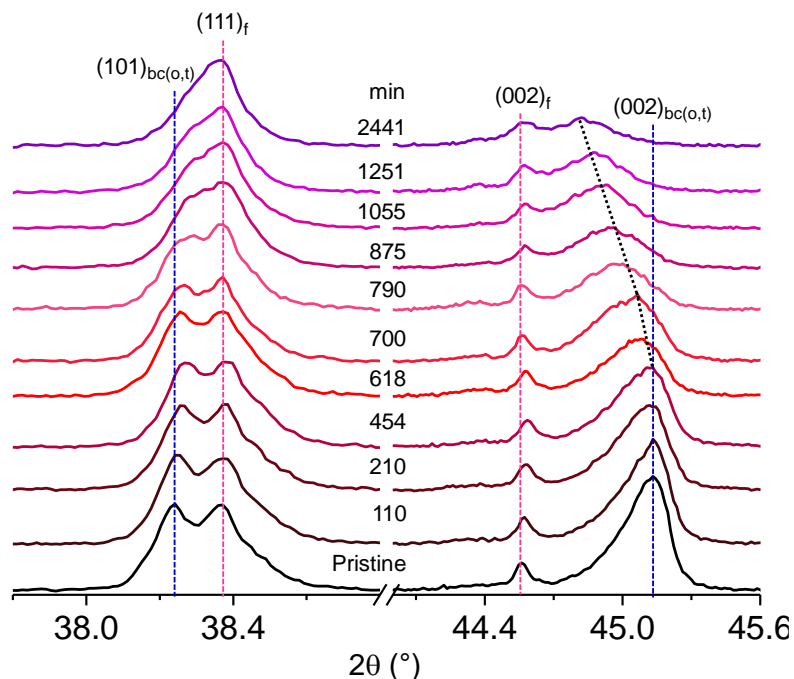
Figure VIII.20. Time dependent changes in XRD pattern of the aqua regia (5% v/v) treated Au microcrystallites.
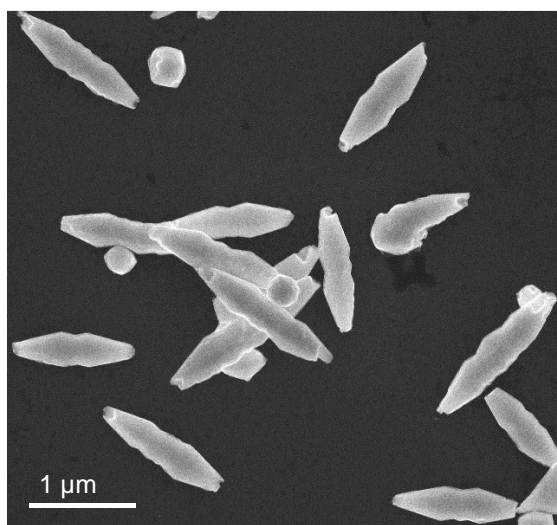
Figure VIII.21. Mapping the spatial distribution of the bco lattices in the Au microcrystallites by aqua regia treatment. The tips of the crystallites behave differently in contrast to the central body.
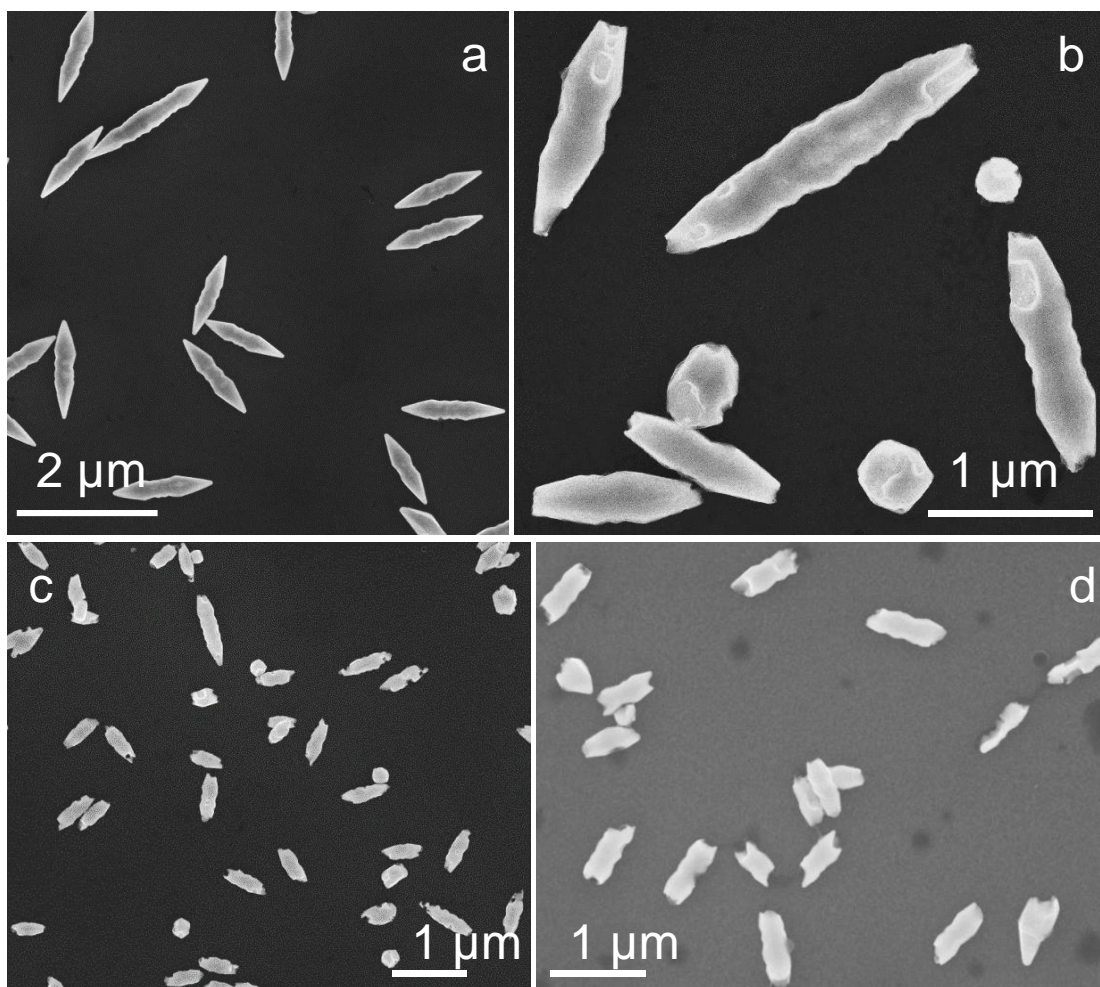
Figure VIII.22. (a–d) Time dependent dissolution trend of bc(o,t) Au microcrystallites in aqua regia. Tip selective oxidation of Au. Treatment time increases from (a) to (d).

In general, any hetero-atom interaction and subsequent deposition, however tolerant of lattice mismatch, does crucially depend on the configurational arrangement of the atoms forming the surface. DFT studies have shown that the local structure rearrangement due to the presence of vacancies at Au surface plays a significant role in stabilizing a foreign adatom (say Cu or Hg) [24]. In the case of Cu on Au for instance, more than the lattice mismatch, it appears that the lattice anisotropy at the bc(o,t) facets makes surface deposition of Cu unfavorable. Similar arguments may be made in respect of other hetero-atoms requiring definitive surface geometries for adsorption and, in general, for extended interaction.

The emergence of the new bct-I phase can be understood from the large disturbances in the atomic positions in the crystallite volume as seen in the **Chapters V–VIII**. The etching assisted phase transformation observed in case of $N(C_4H_9)_4Br$ is similar to the dissolution by

aqua regia, where both of the processes introduce atomic rearrangement. Similarly, the thermal annealing introduces sufficient kinetic energy to rearrange the atoms in the favorable configuration. In the process of the rearrangement, the various c/a values associated with the bct-I phases can be achieved. The observation prevails in all the three cases. Thus, the conversion from bc(o,t) to fcc through the intermediate bct-I phases is an easy and favorable path. During the phase transformation, ranges of bct-I are present along with fcc and bc(o,t), which are somewhat different to the observation made in **Chapter V**, where Ar^+ irradiation induced disappearance of bc(o,t) and generation of a distinct bct-I were seen.

The energy barrier associated with the kinetically arrested metastable bc(o,t) and thermodynamically stable fcc lattices is high (activation energy ~ 120 kJ/mol at thermal annealing). The direct crossover of this energy barrier in a single jump is possible only in the presence of Na_2S by drastically reducing down the activation energy to ~ 3 kJ/mol which can be related with the strong binding affinity of Au-S. On the contrary, in other cases, either annealing or chemical etching, the transformation seems to be a continuous process. Therefore, in the path of the bc(o,t) to fcc transformation, multiple local minima exist which can be attributed to the bct-I lattices. The energy differences between the bc(o,t) and bct-I are small enough to overcome by those perturbants. Although the energy barrier is small, it is considerably high to overcome at the ambient conditions or under high energy X-ray (15 keV) or under e-beam (200 keV).

The effects of chemical adsorption in reducing down the energy barrier also explain why the transformation is nearly complete in Na_2S while is incomplete for rest of the cases. The untwisting of the domains in the crystallite volume occurs in presence of hexadecanethiol and annealing. Additional presence of twist along the length adds up to the energy barrier and thus, the studied crystallites are at the kinetically arrested state both in terms of morphology (including twist and bipyramidal shape) and crystal structure. Therefore, the first step for crossing the barrier is untwisting followed by phase transformation which consequences in the morphological deformation. In case of Na_2S, the morphological changes were not observed, however, the (111) oriented final pattern explains the cross over involved with the metastable lattice.

VIII.5 Conclusions

In conclusion, experimental results presented in this chapter show that the bc(o,t) Au is unusually stable under harsh chemical conditions in which conventional fcc Au is known to lose its nobility. Three different cases were considered; epitaxial growth of Cu, alloying with Hg and dissolution in aqua regia. Though Cu epitaxial growth is facile on fcc Au surfaces, no Cu epitaxial growth took place on bc(o,t) Au even after prolonged plating. Though the fcc Au forms amalgam rapidly with Hg, no such reaction was noticed with the bc(o,t) Au crystallites. Similarly with aqua regia, no morphological changes were visible on the surface of bc(o,t) crystallites. These observations are attributed to anisotropic bc(o,t) surface sites that render adsorption of adatoms sensitive to local geometry, ineffective.

References

[1] X. Yang, M. Yang, B. Pang, M. Vara, and Y. Xia, *Gold Nanomaterials at Work in Biomedicine*, Chem. Rev. **115**, 10410 (2015).

[2] J. Miró and C. Del Pozo, *Fluorine and Gold: A Fruitful Partnership*, Chem. Rev. **116**, 11924 (2016).

[3] P. Pyykkö, *Theoretical Chemistry of Gold*, Angew. Chem. Int. Ed. **43**, 4412 (2004).

[4] B. Hammer and J. K. Nørskov, *Why Gold Is the Nobelest of All the Metals*, Nature **376**, 238 (1995).

[5] T. Hou, M. Chen, G. W. Greene, and R. G. Horn, *Mercury Vapor Sorption and Amalgamation with a Thin Gold Film*, ACS Appl. Mater. Interfaces **7**, 23172 (2015).

[6] W. J. Martin, *The Cyanide Method of Extracting Gold from Its Ores*, J. Am. Chem. Soc. **18**, 309 (1896).

[7] P. Johnston, N. Carthey, and G. J. Hutchings, *Discovery, Development, and Commercialization of Gold Catalysts for Acetylene Hydrochlorination*, J. Am. Chem. Soc. **137**, 14548 (2015).

[8] W. Lin, R. Zhang, S.-S. Jang, C.-P. Wong, and J.-I. Hong, *" Organic Aqua Regia "— Powerful Liquids for Dissolving Noble Metals*, Angew. Chem. Int. Ed. **49**, 7929 (2010).

[9] G. Mettela and G. U. Kulkarni, *Facet Selective Etching of Au Microcrystallites*, Nano Res. **8**, 2925 (2015).

[10] K. D. Gilroy, A. Ruditskiy, H.-C. Peng, D. Qin, and Y. Xia, *Bimetallic Nanocrystals: Syntheses, Properties, and Applications*, Chem. Rev. **116**, 10414 (2016).

[11] H. D. Y. Bian, Ting Zhang, Hui Jiang, Yingying Jin, Chuanhong Wu, Jianbo Yang, *Epitaxial Growth of Twinned Au−Pt Core−shell Star-Shaped Decahedra as Highly Durable Electrocatalysts*, Nano Lett. **15**, 7808−7815 (2015).

[12] G. Mettela and G. U. Kulkarni, *Site Selective Cu Deposition on Au Microcrystallites: Corners, Edges versus Planar Surfaces*, CrystEngComm **17**, 9459 (2015).

[13] M. Nishizawa, T. Sunagawa, and H. Yoneyama, *Underpotential Deposition of Copper on Gold Electrodes through Self-Assembled Monolayers of Propanethiol*, Langmuir **13**, 5215 (1997).

[14] L. Dubrovinsky, N. Dubrovinskaia, W. A. Crichton, A. S. Mikhaylushkin, S. I. Simak, I. A. Abrikosov, J. S. De Almeida, R. Ahuja, W. Luo, and B. Johansson, *Noblest of All Metals Is Structurally Unstable at High Pressure*, Phys. Rev. Lett. **98**, 045503 (2007).

[15] X. Huang, S. Li, Y. Huang, S. Wu, X. Zhou, S. Li, C. L. Gan, F. Boey, C. A. Mirkin, and H. Zhang, *Synthesis of Hexagonal Close-Packed Gold Nanostructures*, Nat. Commun. **2**, 292 (2011).

[16] I. Ojea-Jiménez, X. López, J. Arbiol, and V. Puntes, *Citrate-Coated Gold Nanoparticles as Smart Scavengers for Mercury(II) Removal from Polluted Waters*, ACS Nano **6**, 2253 (2012).

[17] H. Y. Kim, H. M. Lee, and G. Henkelman, *CO Oxidation Mechanism on CeO2-Supported Au Nanoparticles*, J. Am. Chem. Soc. **134**, 1560 (2012).

[18] S. R. King, J. Massicot, and A. M. McDonagh, *A Straightforward Route to Tetrachloroauric Acid from Gold Metal and Molecular Chlorine for Nanoparticle Synthesis*, Metals (Basel). **5**, 1454 (2015).

[19] G. Mettela, M. Bhogra, U. V. Waghmare, and G. U. Kulkarni, *Ambient Stable Tetragonal and Orthorhombic Phases in Penta-Twinned Bipyramidal Au Microcrystals*, J. Am. Chem. Soc. **137**, 3024 (2015).

[20] G. Mettela, N. Mammen, J. Joardar, S. Narasimhan, and G. U. Kulkarni, *Non-fcc Rich Au Crystallites Exhibiting Unusual Catalytic Activity*, Nano Res. **10**, 2271 (2017).

[21] G. Mettela, R. Boya, D. Singh, G. V. P. Kumar, and G. U. Kulkarni, *Highly Tapered Pentagonal Bipyramidal Au Microcrystals with High Index Faceted Corrugation: Synthesis and Optical Properties*, Sci. Rep. **3**, 1793 (2013).

[22] M. Tsuji, D. Yamaguchi, M. Matsunaga, and K. Ikedo, *Epitaxial Growth of Au@Ni Core-Shell Nanocrystals Prepared Using a Two-Step Reduction Method*, Cryst. Growth Des. **11**, 1995 (2011).

[23] K. D. Gilroy, R. A. Hughes, and S. Neretina, *Kinetically Controlled Nucleation of Silver on Surfactant-Free Gold Seeds*, J. Am. Chem. Soc. **136**, 15337 (2014).

[24] D. H. Lim, S. Aboud, and J. Wilcox, *Investigation of Adsorption Behavior of Mercury on Au(111) from First Principles*, Environ. Sci. Technol. **46**, 7260 (2012).

*   *   *

Crystal Structure Dependent Cu Deposition on Au microcrystallites; A Versatile Template to Deposit Metals and Metal Sulfide Overlayers[*]

Summary

Identification of the crystal phases domain in a given crystallite requires a high resolution electron microscopy and selected area diffraction techniques. However, it is an immense challenge to prepare the samples and to identify the polymorphic domains in a crystallite, specifically when the size of the domains is in μm regime. Here, the well-known Cu electroless process has been used to map the fcc lattice domains from a group of mixed phases. The Cu growth was selective on the fcc domains, while the other lattice regions remained free of Cu. In spite of the similar lattice mismatches, the Cu deposition is mainly governed by isotropic geometry of the fcc surfaces. The obtained Au-Cu structures are served as seeds to grow metal-semiconductors/hetero-structures (Au-CuS and Au-Cu$_2$O) and bimetals (Au-Ag, Au-Pd and Au-Pt) with anisotropic geometry.

IX.1 Introduction

Crystal structure plays an important role in altering the physiochemical properties of metal nanoparticles. In the recent years, crystal structure dependent chemical stability, electronic and catalytical properties of the metal nanocrystallites are established. The unusual atomic arrangements of the atoms in the lattices attribute to such interesting properties. The examples include reduction in the metallicity for hcp Ag nanorods (in contrast to conventional fcc) [1] and enhancement in the catalytic activity for fcc Ru (in contrast to hcp) [2].

In the past few decades, there has been an immense growth in size- and shape-controlled synthesis of metal nanocrystallites [3]. Thanks to the efforts from various groups for the development of myriad synthetic routes. The properties of metal nano and microcrystallites have been widely explored. Size- and shape-influenced reactivity of the metal nanocrystallites have also been explored [4–6]. Various techniques such as HRTEM [7,8] and coherent X-ray diffraction (CXD) [9] have been used to address the reactivity of various sites (corners, edges and planar surfaces) on metal nano- and micro-structures. The above all examples pertain to monophase of the metals.

---

[*] Paper based on part of this study: Bull. Mater. Sci. **43**, 323 (2020).

On the other hand, very limited synthetic routes are available for the preparation of noble metal nanocrystallites in their metastable crystal structures. Au in hcp lattice is reported in square sheet form [10], though it is not stable under the high energy e-beam. A synthetic route to prepare Au microcrystallites baring bc(o,t) phases has been reported from the group [11]. The synthetic conditions are very suitable to prepare Au microcrystallites with different amount of bc(o,t) phases [11–13]. Crystal structure dependent catalytic properties of Au microcrystallites have been explored; bc(o,t) Au shows higher catalytic activity than the fcc Au [13]. Sun *et al.* have used selected area nanodiffraction to identify the fcc and bct regions in bct enriched Ag nanowires (thickness ~ 100 nm) with a prerequisite sample preparation step, *i.e.*, sectioning using a sophisticated and destructive FIB technique [14].

Template driven anisotropic growth of bimetallic, metal-semiconductors are much studied in the literature [15–17]. However, the role of crystal structure of the template in driving the anisotropic structures is not yet validated well. For example, the 4H Au nanoribbons/nanorods are served as templates for the growth of 4H phase of various other metals such as Ag, Pd, Pt, Ru, Cu and Os [18–20]. The growth is mainly isotropic in nature and driven by the epitaxial relations. Similarly, the template has also been used for the growth of semiconductors [21]. In all cases, the growth is isotropic.

IX.2 Scope of the Investigation

The bc(o,t) Au microcrystallites are indeed interesting systems to study because they exhibit immense structural stability under high pressures and high temperatures. Also the ease of phase control just depends upon the variation of the reaction kinetics [11,13]. The crystallites are ~ half a μm thick and not suitable to study their spatial distribution of the phases by HRTEM and SAED. The preparation of a specimen by the well-known FIB is also not suitable since the process is destructive (as discussed in **Figure IV.2, Chapter IV**), time consuming and cumbersome. Thus, a simple and effective route is required to quantify the contribution of the different lattices as well as map the spatial distribution in an individual bc(o,t) crystallite among a collection of crystallites. Additionally, the effect of pristine crystal structure in template based growth of overlayers of metal (such as Pd, Pt, Ag and Au), metal sulfide (CuS) and oxide (Cu_2O) needs to be explored.

IX.3 Experimental Details

Formation of Au-CuS. The as-synthesized Au-Cu crystallites were dipped in freshly prepared Na_2S solution (by dissolving 128 mg in 5 mL distilled water) and kept for different time intervals. After that, the samples were cleaned with water and IPA and dried under N_2.

IX.4 Results and Discussion

IX.4.A Identification of Geometrical Location of Polymorphs

Au microcrystallites with variable fractions of bc(o,t) were synthesized by thermal decomposition of metal organic AuAgToABr precursor by following the previously developed recipe reported by the group [11–13]. The obtained Au crystallites consist of 0%, 10%, ~ 25%, ~ 53% and ~ 80% of bc(o,t) phases, as can be seen from the XRD patterns in **Figure IX.1**a. SEM analysis has revealed that the bipyramid shaped crystallites are the major product while tetrahexahedral and hexagram shaped ones are the minor (see **Figure IX.1**b–f) [11]. The size of the Au crystallites decreases at higher thermolysis temperature, for instance, bipyramids prepared at ~ 220 °C are of ~ 3 µm long whereas at 130 °C are of ~ 8 µm long, which is consistent with the previous reports from the group [11,12]. Although the sizes of Au crystallites are different for different thermolysis temperatures, the surface corrugations are present in all the cases.

It is shown in **Chapters VII** and **VIII** that Pt/Pd/Cu deposition is sensitive to the local geometry of the Au crystallites, specifically deposition is favored at the fcc rich tips while leaving the bc(o,t) rich body unaffected. Here, Cu deposition has been used as a probe to identify the fcc and bc(o,t) regions of Au crystallites. The main reason to choose Cu over other metals such as Pd and Pt is the higher lattice mismatch of the former with the Au. To grow Cu epitaxially on Au microcrystallites, electroless plating method is used as it can be performed at the ambient conditions without aids of any external electric field or inert atmospheric conditions. Au microcrystallites hosting different amounts of bc(o,t) phases (0 to ~ 85%) were dipped in Cu platting solution for 10 min. Samples were washed with plenty of water followed by acetone and were dried under N_2 gas. The obtained samples were characterized by XRD, SEM, EDX, TEM and AFM techniques. Further, the SEM analysis of the Au-Cu crystallites revealed the morphological aspects of the grown Cu as shown in **Figure IX.2**. The Au microcrystallites bearing fcc lattice are uniformly covered by Cu while obtained Au-Cu core-

shell crystallites persist the shape of Au crystallites. The surface of Au-Cu crystallites is covered with rod like morphologies which have grown out of the Cu film (see **Figure IX.3**a,b).
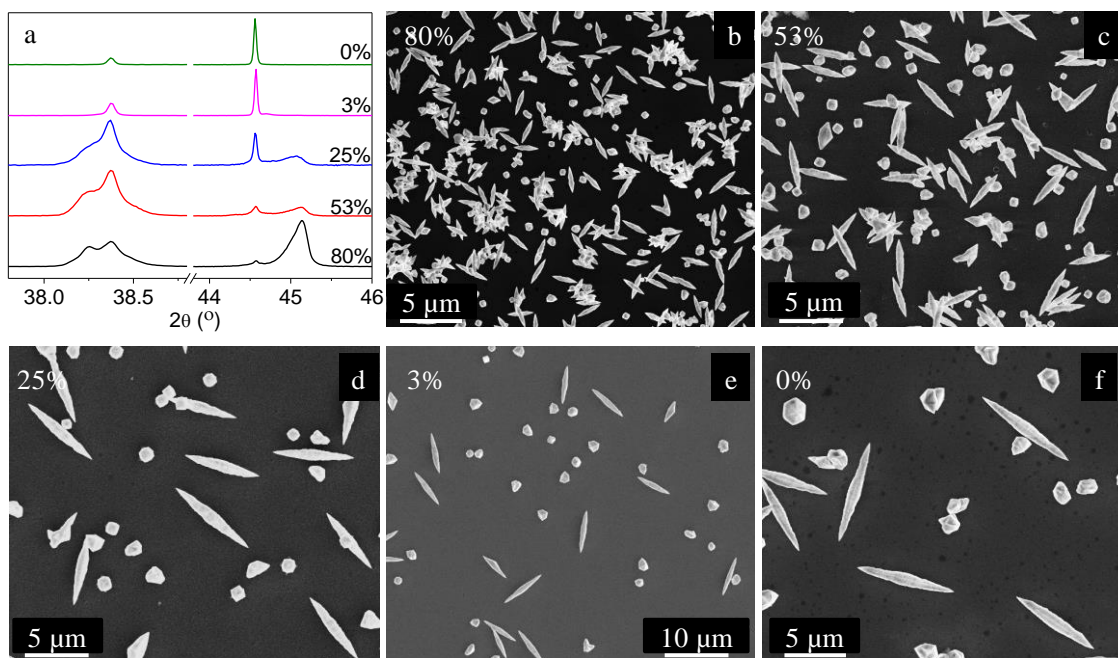

Figure IX.1. XRD patterns (a) and SEM images (b–f) collected from the Au microcrystals with variable amounts of bc(o,t) phases fraction.

Interestingly unlike the former case, the Cu deposition is non-uniform on Au microcrystals hosting bc(o,t) lattices as discussed in **Figure VIII.3**f, **Chapter VIII**. Difference in Cu deposition is clear even at low fractions of bc(o,t) ($<$ 5%) in Au crystallites (**Figure IX.4**). Discontinued Cu islands made of Cu hexagons have grown on Au bipyramids. For 10% bc(o,t), Cu deposition became even less; only tips and ridges of the bipyramids were covered with Cu, while no deposition was seen at other places of Au bipyramids (see **Figure IX.2**d–f). The Cu hexagons are parallel to the tips of the bipyramids, which hints the epitaxial growth of Cu on the Au surfaces as shown in **Figure IX.3**c,d. Cu growth became minimal on body of the ~ 25% bc(o,t) Au crystallites while tips were covered with Cu (see **Figure IX.2**g–i). Further increasing the bc(o,t) proportion to ~ 50%, only tips of the bipyramids were covered, while no detectable Cu was seen on body (in **Figure IX.2**j–l). At higher content of bc(o,t) (*i.e.*, 85%), the Cu deposition has become very minimal even at the tips of the bipyramids as shown in **Figure IX.2**m–o. Even after prolonged exposure, Cu is mainly deposited on the tips of the bipyramids, while size of the Cu islands has grown upto few hundreds of nm (**Figure IX.5**).

Interestingly, the Cu growth on bc(o,t) bipyramids is epitaxially driven irrespective of the bc(o,t) proportions (see **Figures IX.3** and **IX.4**).
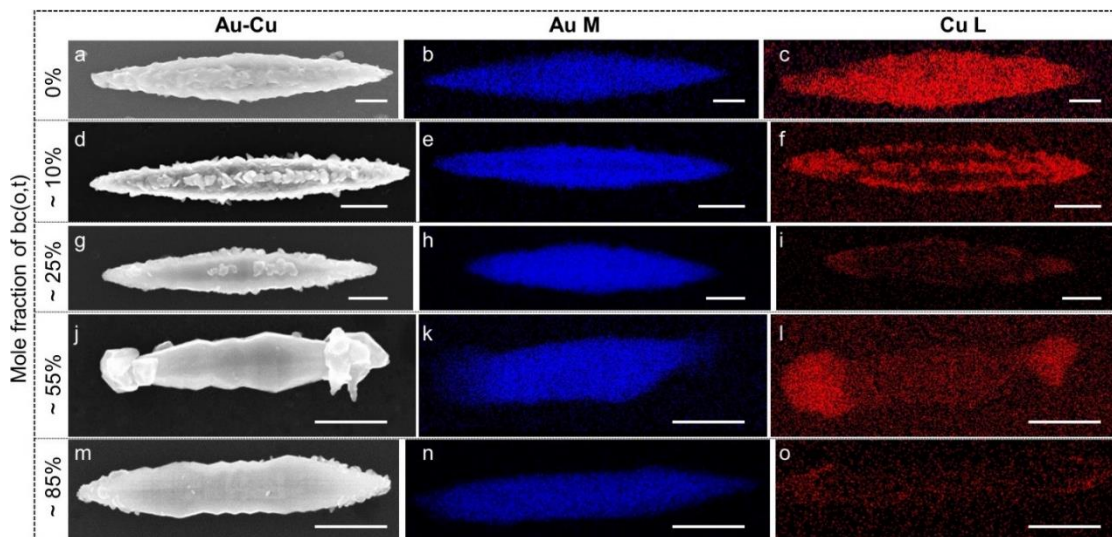

Figure IX.2. (a,d,g,j,m) SEM images of Au bipyramids consist of variable fraction of bc(o,t) lattices covered with Cu grains. Elemental mapping for Au M (b,e,h,k,n) and Cu L levels (c,f,i,l,o) are shown. Scale bars are 3 μm, 1 μm and 500 nm for (a–c), (d–i) and (j–o), respectively.

The Au plates (in fcc lattice) possessing single crystalline {111} oriented anisotropic morphology were also dipped in the Cu plating medium (see **Figure IX.6**a) [22], which resulted in the deposition of Cu on throughout the surface of the microplate (see **Figure IX.6**b) [23]. EDX mapping of the Au-Cu plate confirms the conformal coating of Cu on the Au template, resulting in Au-Cu core-shell structure as shown in **Figure 1X.6**c–e, while retaining the overall morphology similar. Thus, the Cu deposition is uniform on fcc crystallites, irrespective the shape of the crystallite.

Therefore, Cu growth takes place only on fcc regions while no detectable Cu is seen on bc(o,t) Au surfaces. Indeed, it is a versatile and simple route to synthesize site-selective growth of Cu on Au crystallites. In spite of higher lattice mismatch between fcc Au and Cu *i.e.*, 11.4%, the spontaneous UPD of Cu on Au surfaces and the presence of reactive high index corrugated surfaces have facilitated the rapid growth of Cu on Au surfaces. Though the calculated mismatch between bc(o,t) Au and Cu is nearly same of fcc Au, the growth of Cu on bc(o,t) regions is not seen (see details under section **VIII.4.A in Chapter VIII**). In case of bc(o,t) Au, probably the large strain associated within the crystal may add up to the lattice strain which makes the Cu deposition almost impossible on bc(o,t) Au surfaces. It clearly indicates that

lattice structure influences the epitaxial growth phenomenon more than lattice mismatch in case of Au (as reported in section **VIII.4.1** in **Chapter VIII**).
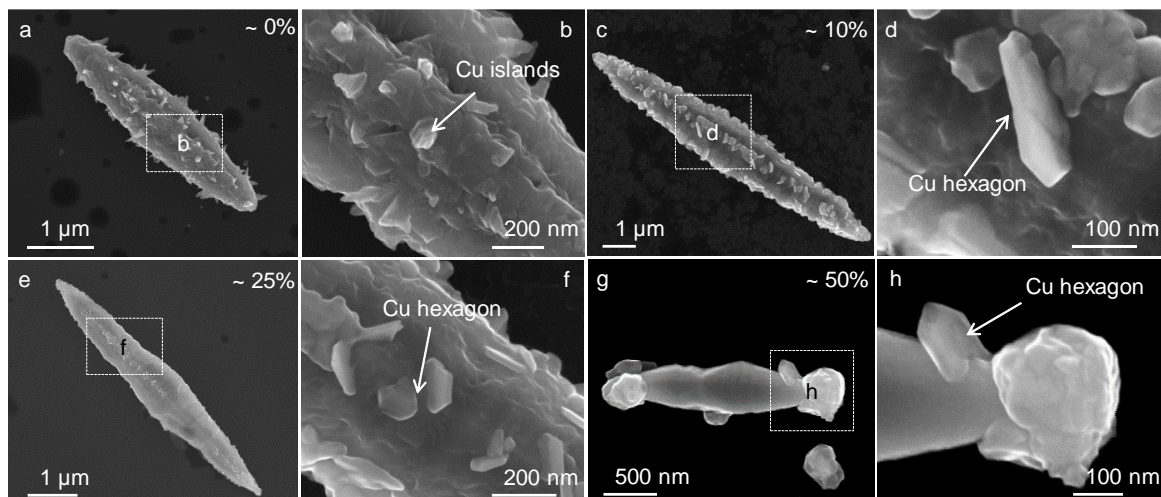
Figure IX.3. (a,c,e,g) Cu growth on various mole fraction of bc(o,t) Au bipyramids and the (b,d,f,h) magnified view of the Cu polygons.
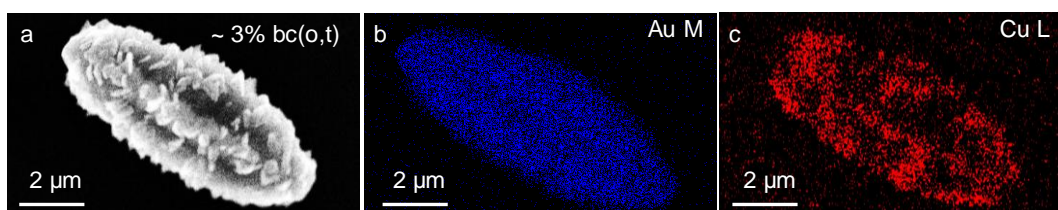
Figure IX.4. (a) Cu growth on nearly fcc Au bipyramids and the corresponding EDX mapping in (b,c). The non-uniform deposition of Cu depicts the influence of templates crystal structure in identifying the presence of bc(o,t).
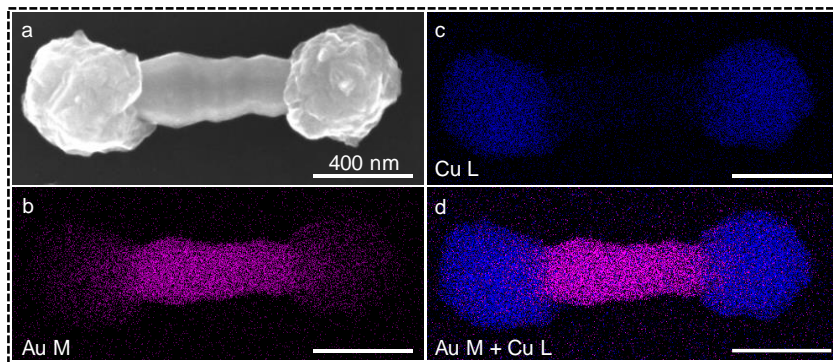
Figure IX.5. (a−d) SEM image and elemental maps of Au microcrystallite with electroless deposition of Cu for prolonged period of time. Here, Cu selectively deposits over the tips (fcc rich), leaving the central part (bco rich) uncoated. Scale bar, 400 nm.
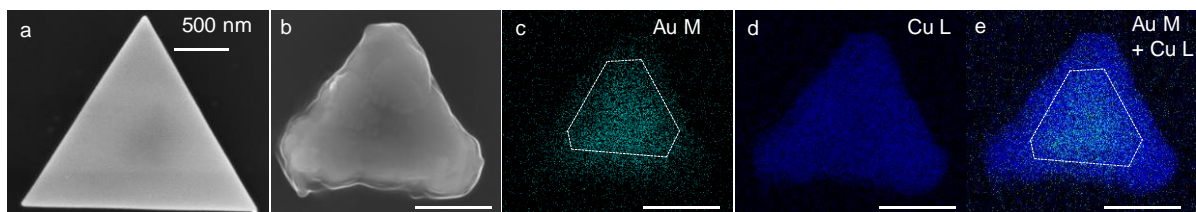
Figure IX.6. (a) SEM image of as-synthesized Au plate. (b) SEM image and the corresponding (c–e) EDX mapping of the Au-Cu crystallite. Scale bar, 500 nm. The contour of the Au crystallite has been shown in white dotted hexagon. The crystallites are movable and does not to allow to image the same crystallites prior to and after Cu deposition.
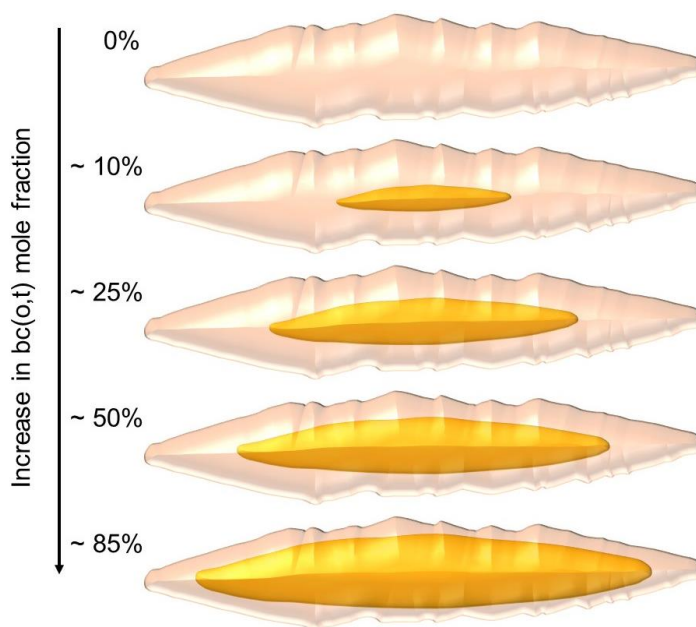
Figure IX.7. Schematic illustration of bc(o,t)-fcc core-shell geometry for various bc(o,t) mole fractions. Light pink and dark orange represent fcc and bc(o,t), respectively.

The spatial distribution of the phases as described in **Chapters IV** and **VII** reveals the crystallite is composed of fcc rich tips and bc(o,t) rich body with a bc(o,t)-fcc core-shell geometry. From the resisting behavior of Cu deposition and the corresponding anisotropic deposition among the various bc(o,t) contents, the spatial distribution of the bc(o,t) lattices can be explained by **Figure IX.7**. Selective deposition of Cu at the tips (for ~ 85% bc(o,t)) and over the entire body (~ 0% bc(o,t)) of the bipyramids confirms the presence of fcc lattices at the tips of the former. The intermediate mole fractions of bc(o,t) exhibit a preference towards anisotropic deposition which can be interlinked with the core-shell geometry, *i.e.*, the bc(o,t) core being encapsulated with the fcc sheath may introduce strain to the fcc situated at the outer

surface and thus, the sheath behaves differently. This observation can clearly be seen when the bc(o,t) fraction is as small as ~ < 5%, the shell starts to get affected (see **Figure IX.4**). The selective deposition of Cu towards the tips (~ 55% bc(o,t)) hints the non-uniform shell thickness (*i.e.*, fcc) over the entire length, specifically higher at the tips. The presence of penta-twinned tips with 10 {111} facets allows the anisotropic (*i.e.*, higher) shell thickness at the tips, leading to the deposition of Cu petals at the tips of ~ 85% bc(o,t) contained crystallites (see **Figure IX.2**m–o).
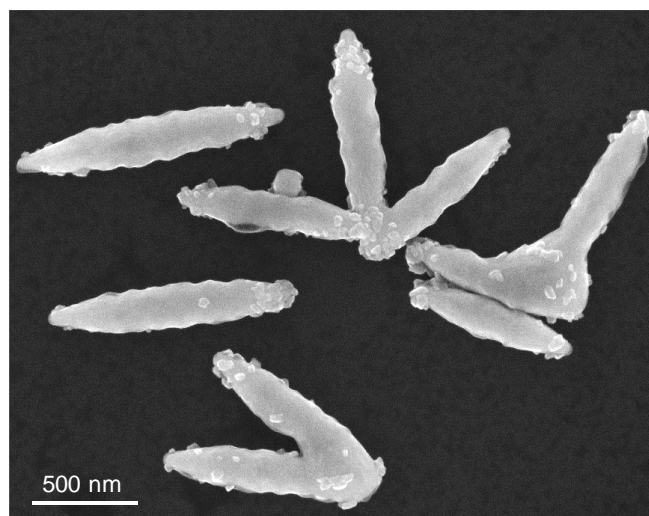
Figure IX.8. Mapping the spatial distribution of the bc(o,t) lattices in the Au microcrystallites by electroless deposition of Cu. The tips of the crystallites behave differently in contrast to the central body.

In contrast, the 4H Au nanoribbons/nanorods serve as template for the epitaxial growth of 4H phase of other metals followed by their semiconductors, where the deposition is nearly uniform [21]. Therefore, the Cu deposition can be used as a chemical probe to identify the polymorphic domains in a multi-phased crystallite and even to separate out from a collection of crystallites as shown in **Figure IX.8** and thus, this unique approach is followed in this work.

IX.4.B Cation Exchange Induced Anisotropic Growth of Au-M (where M = Pd, Pt, Ag and Au) from Au-Cu

The obtained Au-Cu crystallites have been used as starting seeds to grow various noble metals (Ag, Pd, Pt and Au) selectively on fcc regions of Au microcrystallites (**Figure IX.9**a,b,d–f). Being very reactive, Cu can be replaced by various noble metals such as Au, Ag,

Pd and Pt by following the galvanic displacement reaction. Below are the possible chemical reactions.

$$Cu(0) + 2Ag(I) \rightarrow 2Ag(0) + Cu(II) \qquad (1)$$

$$Cu(0) + Pd(II) \rightarrow Pd(0) + Cu(II) \qquad (2)$$

$$2Cu(0) + Pt(IV) \rightarrow Pt(0) + 2Cu(II) \qquad (3)$$

$$3Cu(0) + 2Au(III) \rightarrow 2Au(0) + 3Cu(II) \qquad (4)$$
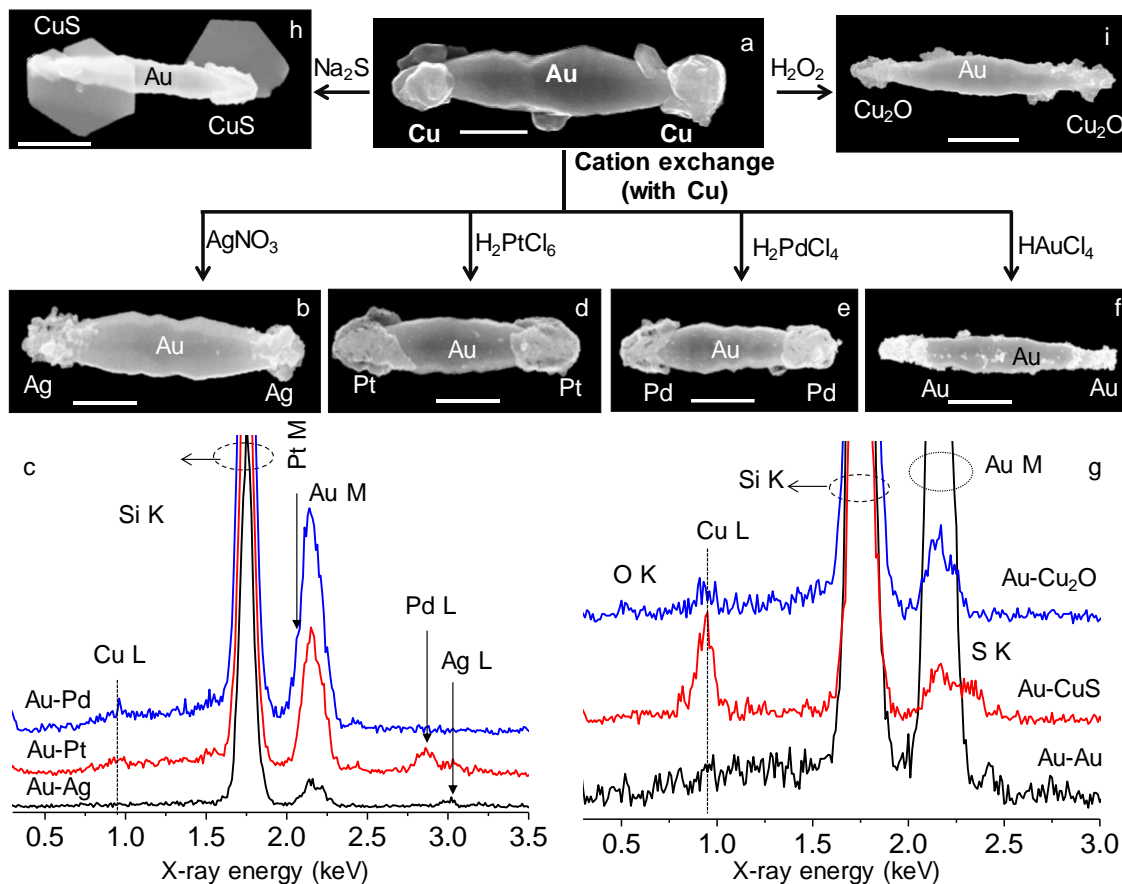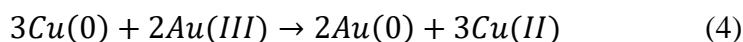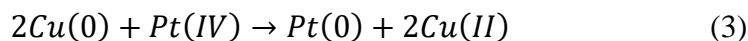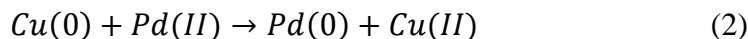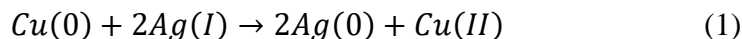
Figure IX.9. SEM images of various (a,b,d–f) metal, (h) metal sulphide and (i) metal oxide overlayers obtained from Au-Cu bipyramids in (a). (c,g) EDX spectra obtained from the as-grown overlayers. Scale bar, 500 nm.

The obtained dumbbell shaped Au-Cu microcrystallites were treated with 5 mL AgNO$_3$ (0.5 mM) for 10 min. Even the dumbbell shape was preserved after replacing Cu with Ag. The high magnified image shows that the Ag film formed at the tips of Au bipyramid is nanoporous and consists of Ag nanoparticles of ~ 20-100 nm (see **Figure IX.9**b). No detectable Cu was observed in EDX spectra after being replaced with Ag as shown in **Figure IX.9**c. Similarly,

Au-Cu dumbbells were treated with H_2PdCl_4, H_2PtCl_6 and $HAuCl_4$ to replace Cu with Pd, Pt and Au, respectively (see in **Figure IX.9**d–f). Likewise Ag, the other noble metals (Pd, Pt and Au) have also formed nanoporous films at the tips of Au bipyramids. In case of Pd and Pt, much small nanoparticles have been observed (see **Figure IX.9**d,e).

IX.4.C Template Driven Growth of Metal Sulfide Overlayers

Ultrathin 2D metal sulfide nanostructures have revealed extraordinary properties, applications and thus, the subject matter of current research. However, synthesis of shape-controlled large sized (~ few μms) plates/sheets are not well-known, specifically due to the colloidal synthesis process resulting in distribution of shape/size.

This work is focused on 2D CuS plates growth on bc(o,t) Au microcrystallites. Prior to the discussion, it is worthwhile to look into the growth of CuS on fcc Au plates. The wet chemical synthesis processes of CuS triangular/Hexagonal nanoplates include solvothermal methods [24], soft templating [25], seed mediated [26] or surfactant assisted [27] non-aqueous growth. However, shape-controlled growth of large 2D CuS nanoplates is yet to be investigated. In this direction, ultrathin size tunable triangular/hexagonal nanoplates upto 3 μm in lateral length have been fabricated [28,29]. However, a general and facile route for the synthesis of surfactant free aqueous process of well-dispersed shape-controlled large plates has not been validated.

The as-prepared Au−Cu [23] plates were dipped in Na₂S solution (as schematically represented in **Figure IX.10**a) for 10 min and washed with water followed by IPA. Following the Na₂S treatment, nanoplate-like features distributed all over the substrate were seen as shown in **Figure IX.10**b. The magnified view of a plate in **Figure IX.10**c shows a bright feature at the centre surrounding by a hexagonal plate-like morphology, and such features arranged at different angles (majorly ~ 0° and 90°) with respect to the Si substrate are seen (see **Figure IX.10**b). Elemental mapping of the plate reveals that the nanoplates are made of Cu and S, whereas the bright feature in the center is of Au, Cu and S (see **Figure IX.10**d–f). The mapping also unveiled that the central bright portion consists of Cu deposited over a much smaller sized Au (**Figure IX.10**c). Interestingly, the sides of the Au crystallite and the CuS nanoplate are parallel, hinting the growth to be a template-driven process, while the template is the Au nanoplate crystallite. BSE imaging confirms the formation of a core−shell structure

as shown in **Figure IX.10**g,h, where a tiny core made of Au encapsulated with the Cu shell facilitates the growth of ~ μm long plates (evincing three different contrast regions). The treatment of Na_2S to the Au–Cu crystallites results in CuS nanoplates following the below reaction.

$$Cu(0) + Na_2S + 2H_2O \rightarrow CuS + H_2 + 2NaOH \qquad (5)$$
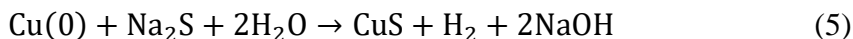
EDX spectrum collected from the Au-CuS crystallites elucidates the presence of Cu/S ~ 54/45 as in **Figure IX.10**i. XRD data collected from the same crystallites in **Figure IX.10**j exhibits an anisotropic pattern with a highly intense peak at ~ 38.16° assignable to Au{111} and the second intense peak at ~ 32.94° ascribed to the (006) peak of CuS hexagonal phase (JCPDS Card no. 65-0603) with lattice parameters of $a = b = 3.785$ Å, $c = 16.297$ Å in the space group, $P6_3/mmc$. Thus, the lattice mismatch from the two intense peaks can be calculated which is ~ 15.23%. The spontaneous reaction between Cu and S^{2-} (Gibbs free energy, ΔG_{CuS} = -53.6 kJ/mol) allows the formation of CuS while the orientation is to be dictated by the small Au at the core. Thus, in spite of huge lattice mismatch, the hetero-epitaxial growth is facilitated, where the key lies in epitaxial deposition of Cu. Similar anisotropic (006) oriented XRD pattern was observed in 1-2 μm large CuS triangular/hexagonal plates [29]. By comparing the SEM and XRD in **Figure IX.10**c and **10**j, one may conclude that the hexagonal plates are {001} oriented similar to the Au crystallites which are {111} oriented. In addition to the intense (006) peak in XRD, many small peaks are also seen which are possibly arising from varied stoichiometry known for the Cu-S system [30]. AFM image collected from a plate shows that the thickness is ~ 23 nm with a surface roughness of ~ 4 nm (see **Figure IX.10**k,l). In the example shown, the height of the Au-Cu crystallite is ~ 93 nm with respect to the CuS plate. The length and thickness of the plates possess distributions, ~ few μms and ~ 20-200 nm, respectively.

The Au-CuS growth process (as discussed above) can be implemented on bc(o,t) crystallites of Au as well, where the deposition of Cu is anisotropic (see section **IX.4.A**). A study of the growth of CuS from such as a seed would be worthwhile. Hitherto, numerous methods have been developed for the selective growth of semiconducting materials on metal tips. However, these methods are strongly dependent on many of the synthetic conditions.
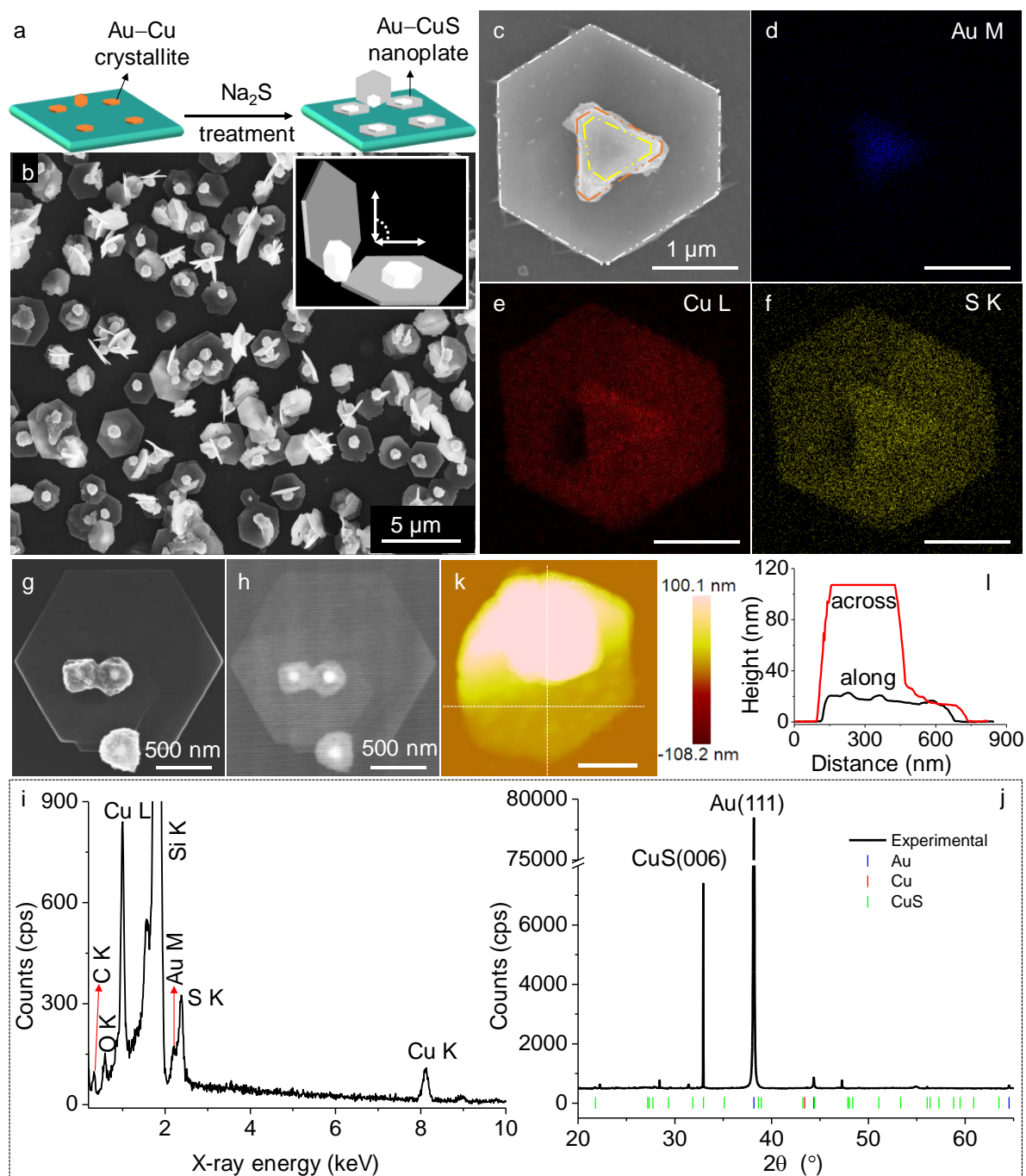
Figure IX.10. (a) Schematic representation of Au-CuS nanoplates formation starting from Au-Cu. Treatment of Na_2S (for 10 min) on the Au-Cu crystallites (10 min Cu deposition) results the Au-CuS nanoplates. (b) SEM image of as-synthesized Au-CuS nanoplates and in the inset schematically projected the orientation of the plates. (c) SEM image of a single nanoplate along with the contours of the pristine Au (yellow dot dashed lines), Cu (orange) and overgrown CuS nanoplate (white) drawn to visualize the relation between them. (d–f) EDX mapping of the Au-CuS nanoplate shown in (c). Scale bar, 1 µm. EDX mapping confirms the very small Au core and CuS shell. (g) SEM and (h) the

corresponding BSE images of a nanoplate. (i) EDX spectrum and (j) XRD pattern collected from the collection of the Au-CuS nanoplates. The BSE image reveals the core-shell geometry. The lines in the BSE image are due to the noise in the detector. (k) AFM image of a nanoplate and the corresponding line profiles drawn along and across the lengths of the nanoplate in (l). Scale bar, 200 nm.

The obtained Au-Cu bipyramids have been used as starting seeds to grow various sulfides (CuS) and oxides (Cu_2O) selectively on fcc regions of Au microcrystallites (**Figure IX.10**). The high Gibbs free energy ($\Delta G_{Cu2O} = -146.0$ kJ/mol) and high affinity of Cu towards chalcogens allow the rapid formation of Cu-chalcogenides. The Au-Cu dumbbells were treated with 5 mL of Na_2S (320 mM) solution for 10 min, and SEM image of the obtained product is shown in **Figure IX.9**h,i. Hexagonal plate like crystallites have emerged from the tips regions, similar to the CuS plates grown *via* Au-Cu plates in **Figure IX.9**. The atomic percentage of Cu and S in hexagonal plates is 52:48 obtained from the EDX spectra in **Figure IX.9**g. Similarly, the Au-Cu dumbbells were treated with H_2O_2 solution for 10 min (see **Figure IX.10**d). Nanocrystalline Cu_2O films have formed at the tips (with Cu:O atomic ratio of 68:32 as shown in **Figure IX.9**g) following the below reaction.

$$2Cu(0) + H_2O_2 \rightarrow Cu_2O + H_2O \qquad (6)$$
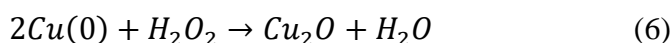
The Au-M anisotropic morphologies can be employed for the growth of other Au-sulfides (similar to Au-CuS)/Au-oxides (similar to Au-Cu_2O), specifically for the anisotropic structures and will be interesting to monitor their properties when the template is in multi-phased domain.

IX.5 Conclusions

In conclusion, a simple solution based route is investigated to identify the fcc and bc(o,t) regions in a given Au crystallite by UPD of Cu. The Cu deposition is selective to the fcc region. Interestingly, even the small proportions of bc(o,t) can also be identified with Cu plating. The anisotropic deposition confirms the presence of a fcc-bc(o,t) core-shell geometry. The unique epitaxial relation of Au-Cu facilitates the growth of ~ few μms large flat CuS hexagonal plates. The Au-Cu dumbbells also act as substrate for the growth of semiconducting materials CuS and Cu_2O, selectively at the tips. Besides, the Au-Cu crystallites can be used as a template to grow noble metals (Au, Ag, Pd and Pt) by cation exchange (with Cu). A simple, wet chemical process in identifying the polymorphic domains in a given crystallite was thus far not known and hence, the results reported should lead the way to future understanding.

References

[1]   I. Chakraborty, S. N. Shirodkar, S. Gohil, U. V Waghmare, and P. Ayyub, *A Stable, Quasi-2D Modification of Silver: Optical, Electronic, Vibrational and Mechanical Properties, and First Principles Calculations*, J. Phys. Condens. Matter **26**, 025402 (2014).

[2]   K. Kusada, H. Kobayashi, T. Yamamoto, S. Matsumura, N. Sumi, K. Sato, K. Nagaoka, Y. Kubota, and H. Kitagawa, *Discovery of Face-Centered-Cubic Ruthenium Nanoparticles: Facile Size-Controlled Synthesis Using the Chemical Reduction Method*, J. Am. Chem. Soc. **135**, 5493 (2013).

[3]   T.-H. Yang, Y. Shi, A. Janssen, and Y. Xia, *Surface Capping Agents and Their Roles in Shape-Controlled Synthesis of Colloidal Metal Nanocrystals*, Angew. Chem. Int. Ed. **59**, 15378 (2020).

[4]   V. Bansal, V. Li, A. P. O'Mullane, and S. K. Bhargava, *Shape Dependent Electrocatalytic Behaviour of Silver Nanoparticles*, CrystEngComm **12**, 4280 (2010).

[5]   N. Tian, Z.-Y. Zhou, S.-G. Sun, Y. Ding, and Z. L. Wang, *Synthesis of Tetrahexahedral Platinum Nanocrystals with High-Index Facets and High Electro-Oxidation Activity*, Science **316**, 732 (2007).

[6]   Q. Zhang and H. Wang, *Facet-Dependent Catalytic Activities of Au Nanoparticles Enclosed by High-Index Facets*, ACS Catal. **4**, 4027 (2014).

[7]   S. Han, G. Xia, C. Cai, Q. Wang, Y. Wang, M. Gu, and J. Li, *Gas-Assisted Transformation of Gold from fcc to the Metastable 4H Phase*, Nat. Commun. **11**, 552 (2020).

[8]   M. J. Walsh, K. Yoshida, A. Kuwabara, M. L. Pay, P. L. Gai, and E. D. Boyes, *On the Structural Origin of the Catalytic Properties of Inherently Strained Ultrasmall Decahedral Gold Nanoparticles*, Nano Lett. **12**, 2027 (2012).

[9]   M. Watari, R. A. McKendry, M. Vögtli, G. Aeppli, Y. A. Soh, X. Shi, G. Xiong, X. Huang, R. Harder, and I. K. Robinson, *Differential Stress Induced by Thiol Adsorption on Facetted Nanocrystals*, Nat. Mater. **10**, 862 (2011).

[10]   X. Huang, S. Li, Y. Huang, S. Wu, X. Zhou, S. Li, C. L. Gan, F. Boey, C. A. Mirkin, and H. Zhang, *Synthesis of Hexagonal Close-Packed Gold Nanostructures*, Nat. Commun. **2**, 292 (2011).

[11]   G. Mettela, M. Bhogra, U. V. Waghmare, and G. U. Kulkarni, *Ambient Stable Tetragonal and Orthorhombic Phases in Penta-Twinned Bipyramidal Au Microcrystals*, J. Am. Chem. Soc. **137**, 3024 (2015).

[12]   G. Mettela, R. Boya, D. Singh, G. V. P. Kumar, and G. U. Kulkarni, *Highly Tapered Pentagonal Bipyramidal Au Microcrystals with High Index Faceted Corrugation: Synthesis and Optical Properties*, Sci. Rep. **3**, 1793 (2013).

[13]   G. Mettela, N. Mammen, J. Joardar, S. Narasimhan, and G. U. Kulkarni, *Non-fcc Rich Au Crystallites Exhibiting Unusual Catalytic Activity*, Nano Res. **10**, 2271 (2017).

[14] Y. Sun, Y. Ren, Y. Liu, J. Wen, J. S. Okasinski, and D. J. Miller, *Ambient-Stable Tetragonal Phase in Silver Nanostructures*, Nat. Commun. **3**, 971 (2012).

[15] F. Wang, S. Cheng, Z. Bao, and J. Wang, *Anisotropic Overgrowth of Metal Heterostructures Induced by a Site- Selective Silica Coating*, Angew. Chem. Int. Ed. **52**, 10344 (2013).

[16] B. Wu, D. Liu, S. Mubeen, T. T. Chuong, M. Moskovits, and G. D. Stucky, *Anisotropic Growth of TiO2 onto Gold Nanorods for Plasmon- Enhanced Hydrogen Production from Water Reduction*, J. Am. Chem. Soc. **138**, 1114 (2016).

[17] M.-M. Chen, C.-H. Xu, W. Zhao, H.-Y. Chen, and J. Xu, *Observing the Structure-Dependent Electrocatalytic Activity of Bimetallic Pd–Au Nanorods at the Single-Particle Level*, Chem. Commun. **56**, 3413 (2020).

[18] Z. Fan, Z. Luo, Y. Chen, J. Wang, B. Li, Y. Zong, and H. Zhang, *Synthesis of 4H/fcc - Au@M (M = Ir, Os, IrOs) Core-Shell Nanoribbons for Electrocatalytic Oxygen Evolution Reaction*, Small **12**, 3908 (2016).

[19] Z. Fan, Y. Chen, Y. Zhu, J. Wang, B. Li, Y. Zong, Y. Han, and H. Zhang, *Epitaxial Growth of Unusual 4H Hexagonal Ir, Rh, Os, Ru and Cu Nanostructures on 4H Au Nanoribbons*, Chem. Sci. **8**, 795 (2016).

[20] Z. Fan, M. Bosman, X. Huang, D. Huang, Y. Yu, K. P. Ong, Y. A. Akimov, L. Wu, B. Li, J. Wu, Y. Huang, Q. Liu, C. Eng Png, C. Lip Gan, P. Yang, and H. Zhang, *Stabilization of 4H Hexagonal Phase in Gold Nanoribbons*, Nat. Commun. **6**, 7684 (2015).

[21] Z. Fan, X. Zhang, J. Yang, X.-J. Wu, Z. Liu, W. Huang, and H. Zhang, *Synthesis of 4H/fcc-Au@metal Sulfide Core-Shell Nanoribbons*, J. Am. Chem. Soc. **137**, 10910 (2015).

[22] B. Radha, M. Arif, R. Datta, T. K. Kundu, and G. U. Kulkarni, *Movable Au Microplates as Fluorescence Enhancing Substrates for Live Cells*, Nano Res. **3**, 738 (2010).

[23] G. Mettela and G. U. Kulkarni, *Site Selective Cu Deposition on Au Microcrystallites: Corners, Edges versus Planar Surfaces*, CrystEngComm **17**, 9459 (2015).

[24] W. Du, X. Qian, M. Xiaodong, Q. Gong, H. Cao, and J. Yin, *Shape-Controlled Synthesis and Self-Assembly of Hexagonal Covellite (CuS) Nanoplatelets*, Chem. Eur. J. **13**, 3241 (2007).

[25] Y. Du, Z. Yin, J. Zhu, X. Huang, X. J. Wu, Z. Zeng, Q. Yan, and H. Zhang, *A General Method for the Large-Scale Synthesis of Uniform Ultrathin Metal Sulphide Nanocrystals*, Nat. Commun. **3**, 1177 (2012).

[26] S. W. Hsu, C. Ngo, W. Bryks, and A. R. Tao, *Shape Focusing during the Anisotropic Growth of CuS Triangular Nanoprisms*, Chem. Mater. **27**, 4957 (2015).

[27] Y. Xie, L. Carbone, C. Nobile, V. Grillo, S. D'Agostino, F. Della Sala, C. Giannini, D. Altamura, C. Oelsner, C. Kryschi, and P. D. Cozzoli, *Metallic-like Stoichiometric Copper Sulfide Nanocrystals: Phase- and Shape-Selective Synthesis, near-Infrared*

Surface Plasmon Resonance Properties, and Their Modeling, ACS Nano **7**, 7352 (2013).

[28] W. van der Stam, Q. A. Akkerman, X. Ke, M. A. van Huis, S. Bals, and C. de Mello Donega, *Solution-Processable Ultrathin Size- and Shape-Controlled Colloidal $Cu_{2-x}S$ Nanosheets*, Chem. Mater. **27**, 283 (2015).

[29] R. Lesyuk, E. Klein, I. Yaremchuk, and C. Klinke, *Copper Sulfide Nanosheets with Shape-Tunable Plasmonic Properties in the NIR Region*, Nanoscale **10**, 20640 (2018).

[30] C. Coughlan, M. Ibáñez, O. Dobrozhan, A. Singh, A. Cabot, and K. M. Ryan, *Compound Copper Chalcogenide Nanocrystals*, Chem. Rev. **117**, 5865 (2017).

*   *   *

Summary and Outlook

The thesis is essentially a detailed description of the stabilization of unconventional bc(o,t) (bco and bct) lattices of Au in the form of microcrystallites and unraveling of their spatial distribution. Using simple wet chemistry, it has been shown that the crystallites can serve as templates for anisotropic growth of metals and semiconductors. The thesis defines a practical boundary for the crystallite stability with regard to varied chemical and physical environments.

Chapter I summarizes various synthetic methods from the literature for metal nano- and micro-structures hosting unconventional morphology. A few interesting examples of nanomaterials in unconventional lattices exhibiting crystal structure dependent properties are cited. **Chapter II** details out the characterization techniques used in the context of the thesis work to study the occurrences, spatial distribution and stabilities of unconventional lattices.

Chapter III has showcased the possibility of increasing the proportion of the bc(o,t) lattices by varying the precursor composition with great reproducibility and yield. A by-product of the study is the stabilization of large sized decahedra (~ few μms) with prominent ridges and twin boundaries. **Chapter IV** has dealt with the spatial distribution of the multi-phases in a μm sized non-cubic Au bipyramid with a non-destructive scanning X-ray diffraction microscopy (SXDM) technique with nano beam. The study has provided insights into the growth aspects of the different lattices, the presence of the 5-fold symmetry leading to twin boundaries as well as the peculiar final geometry. The technique can be used for understanding the growth of the multi-phase nano-/micro-structures.

Chapter V discussed the stability of the bc(o,t) lattices under ion beam irradiation, a physical perturbant. The irradiation of Ar^+ ion at the low beam energy (1.2-5 keV) stabilizes ranges of new bct-I phases by uniaxial expansion along c-direction which eventually causes a phase transformation to fcc. **Chapter VI** deals with releasing the crystallite strain by *in-situ* thermal annealing while monitoring using SXDM with a nano-beam. The study allowed visualization of the domain untwisting within the crystallite volume.

Chapter VII describes the stability of the crystallites and of the bc(o,t) lattices with various adsorbents. The latter were chosen from the commonly used reagents for stabilization of unconventional morphologies of nanomaterials. Treatment with hexadecanethiol was seen

to enhance the crystallinity by the reduction in crystal mosaicity along the length. The bc(o,t) Au undergoes phase transformation to fcc in presence of Na_2S and quaternary ammonium salts with preferential fcc(111) or fcc(002) orientation, respectively. The metal cations influence the reaction rates acting as synergistic/blocking agents during the phase transformation process. Following the comproportionation reaction, Au(III) in ToABr could dissolve the ~ 200-400 nm thick crystallites with the rate of dissolution being relatively higher at the metastable bc(o,t) lattices due to higher Gibbs free energies associated with them. The observations made in this context point to a bc(o,t)-fcc core-shell geometry of the crystallites, while lending support to the observed extraordinary stability under ambient conditions. **Chapter VIII** has brought out the extraordinary chemical stability of bc(o,t) Au, in contrast to fcc Au, with respect to electrolessly deposited Cu, Hg and aqua regia environments. The unusual stability refers to the geometrical anisotropy associated with the bc(o,t) lattices which does not favor the adsorption of the foreign atoms.

Chapter IX describes a wet chemical route to characterize the multi-phase system. The electroless deposition of Cu acts as a chemical probe and unravels the bc(o,t)-fcc core-shell geometry-in line with the observations made in Chapter VII. The general applicability of the method was also shown. The anisotropically deposited Cu on the bc(o,t) crystallite has been used for the deposition of other metals by galvanic replacement *via* template assisted growth. Such anisotropic morphologies can be used for optical, catalytic and sensing purposes. Further, anisotropic growth of metal sulfide overlayers was explored on the Au-Cu template.

Moving forward, upscaling of the bc(o,t) Au crystallites in larger quantity (mg to g scale) can be targeted using this modified synthetic recipe. Upscaling the growth of the crystallites will enable to study crystal structure dependent electrical, mechanical and magnetic properties of bc(o,t) Au. Further, the growth mechanism of the crystallites morphology both in fcc and bc(o,t) will be interesting to study. Crystal structure dependent studies for the crystallites hosting ranges of bct-I as well as the distinct bct-I will also be interesting. Additionally, understanding the role of Ag^+ ions on the growth of other shaped crystallites may also bring out some surprises. The role of excess ions (such as from excess of HCl) would be another aspect worth studying. Future work should focus on single crystallite catalysis, importantly, by combining it with SXDM measurements. Similar to the fine-tuned X-ray beam

of SXDM, the confocal Raman beam should be able to map out the catalytic sites at various locations of the microcrystallite. Strain associated with solid angle gap in a decahedra is expected to increase with its size and therefore, the large sized decahedra can be used as model system to understand the strain relaxation processes.

<p align="center">*   *   *</p>

List of Publications

From this thesis

[1] **C. Sow**, G. Mettela, and G. U. Kulkarni, *Shape-Controlled Template-Driven Growth of Large CuS Hexagonal Nanoplates,* Bull. Mater. Sci. **43**, 323 (2020).

[2] **C. Sow**,* A. Sarma,* A. Schropp, D. Dzhigaev, T. F. Keller, C. G. Schroer, M. K. Sanyal, and G. U. Kulkarni, *Unraveling the Spatial Distribution of Catalytic Non-Cubic Au Phases in a Bipyramidal Microcrystallite by X-ray Diffraction Microscopy*, ACS Nano **14**, 9456 (2020). (* Equal contribution)

[3] G. Mettela, S. Kouser,* **C. Sow**,* S. T. Pantelides, and G. U. Kulkarni, *Nobler than the Noblest: Noncubic Gold Microcrystallites*, Angew. Chem. Int. Ed. **57**, 9018 (2018). (* Equal contribution)

[4] **C. Sow**, and G. U. Kulkarni, *Non-Cubic to Cubic Structural Change in Au Microcrystallites by Oxidative Etching,* (2021). (Submitted)

[5] **C. Sow**, R. Jana, A. Datta, and G. U. Kulkarni, *Adsorbent Induced Phase Transformation in Non-Cubic Au Microcrystallites,* (2021). (Submitted)

[6] **C. Sow**, G. Mettela, G, P. Suchithra, and G. U. Kulkarni, *Crystal Structure Dependent Cu Deposition on Au Microcrystallites; A Versatile Template to Deposit Metals and Metal Sulfide Overlayers,* (2021). (Under preparation)

[7] **C. Sow**, M. Bhogra, U. V. Waghmare, and G. U. Kulkarni, *Persistent Body-Centered Tetragonal Phases in Non-Cubic Au Microcrystallites Induced by Ar^+ Ion Irradiation,* (2021). (Under preparation)

[8] **C. Sow**, and G. U. Kulkarni, *Crystal Structure Dependent Dissolution of Non-Cubic Au Bipyramids by Lewis Acids,* (2021). (Under preparation)

[9] **C. Sow**, A. Sarma, A. Schropp, T. F. Keller, C. G. Schroer, M. K. Sanyal, and G. U. Kulkarni, *In-situ Monitoring the Non-Cubic to Cubic Phase Transformation under High Temperatures in a Au Bipyramid by X-ray Diffraction Microscopy*, (2021). (Under preparation)

[10] **C. Sow**, and G. U. Kulkarni, *Maximization of Non-Cubic Phases in Ambient Stable Au Microcrystallites,* (2021). (Under preparation)

[11]   **C. Sow**, and G. U. Kulkarni, *Thermal Stability of the Strained Body-Centered Tetragonal Phases in Non-Cubic Au Microcrystallites,* (2021). (Under preparation)

Co-authored publications

[12]   S. Kiruthika, **C. Sow**, and G. U. Kulkarni, *Transparent and Flexible Supercapacitors with Networked Electrodes*, Small **13**, 1701906 (2017).

[13]   P. Suchithra, R. Raj, **C. Sow** and G. U. Kulkarni, *Crystal struture dependent Optical Properties of Au microcrystallites,* (2021). (Under preparation)

Review

[1]   **C. Sow**, P. Suchithra, G. Mettela, and G. U. Kulkarni, *Noble Metal Nanomaterials with Nontraditional Crystal Structures*, Annu. Rev. Mater. Res. **50**, 345 (2020). (Invited)

*   *   *